

Final Report to the  
Office of Naval Research

**EFFECTS OF A CROSS-TAIL MAGNETIC FIELD  
ON THE EQUILIBRIUM STRUCTURE OF THE  
QUIET-TIME MAGNETOTAIL**

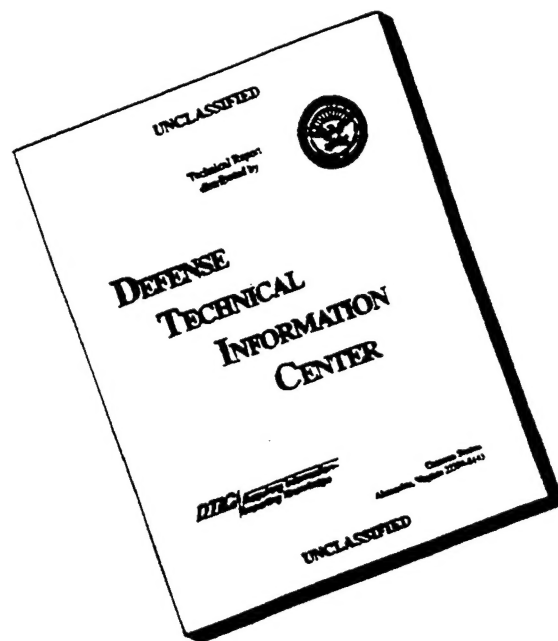
Dr. Daniel L. Holland  
Illinois State University  
Department of Physics  
Normal, Illinois 61790-4560  
(309) 438-3243  
holland@entropy.phy.ilstu.edu

**DISSEMINATION STATEMENT A**

Approved for public release;  
Distribution Unlimited

19970219 022

# DISCLAIMER NOTICE



**THIS DOCUMENT IS BEST  
QUALITY AVAILABLE. THE  
COPY FURNISHED TO DTIC  
CONTAINED A SIGNIFICANT  
NUMBER OF PAGES WHICH DO  
NOT REPRODUCE LEGIBLY.**

## TABLE OF CONTENTS

SUMMARY OF RESEARCH ACTIVITIES	3
PROGRAMMATIC TRAVEL	5
PUBLICATIONS AND PRESENTATIONS	6
I. Grant Related	
Refereed Journals	
Conference Proceedings	
NRL Reports	
Abstracts	
Departmental Presentations	
Manuscripts in Preparation	
II. Non-Grant Related	8
Abstracts	
Departmental Presentations	
UNDERGRADUATE STUDENT INVOLVEMENT	9

## SUMMARY OF RESEARCH ACTIVITIES

As the publication record suggests, during the tenure of the grant we have investigated a number of topics relevant to nonlinear dynamics and equilibrium structures in the magnetotail. Some of the initial goals of the program were modified so as to allow for more active participation of undergraduate students in the research. We are still in the process of completing some of the self-consistent magnetotail equilibrium calculations. A brief discussion of the major accomplishments of the research program is presented in the following paragraphs.

### I. Effects of a Constant Cross-Tail Magnetic Field on the Particle Dynamics in the Magnetotail.

In this project we have examined the effects of a constant cross-tail magnetic field,  $B_y$ , on the phase space structures and the observational signatures of nonlinear particle dynamics in the quiet-time magnetotail. We have found that the separation of phase space into dynamically distinct regions (transient, stochastic and integrable) persists, albeit with considerable complications. Since the equation of motion for charged particle in the model magnetic field is not symmetric under the replacement of  $\$Z\$$  with  $\$-Z\$$  we must use two surfaces of section to describe the system; one for north-to-south crossings and one for south-to-north crossings. The subdivision of the entry regions into transient and stochastic entry regions has been described in detail.

With respect for potential observational signatures, we have shown that if  $B_y$  is less than the normal component to the magnetic field,  $B_z$  component, the resonant coherent chaotic scattering of particles and the resulting distribution function features persist. If  $|B_y|$  is greater than  $B_z$ , on the other hand, the majority of the particles are forward scattered through the current sheet and there is no discernible signature of the resonance in the phase and pitch-angle averages distribution function. This is significant in that the presence or absence of the resonance effect in observed distribution functions can constrain the magnitude of  $B_y$ . More recent results using pitch-angle resolved distribution functions indicate that even in the regime of  $B_y > B_z$  there may be a pitch angle bunching effect which can be used an indicator of the magnitude of  $B_y$ .

### II. Characterization of Collisional Effects on Magnetotail Particle Dynamics

This project is a continuation of work which was initially begun with Dr. James Chen at the Naval Research Laboratory. Here we have performed a number of numerical experiments using a test particle code with an ad hoc collision operator to quantify the effects of collisions on the phase space boundaries and resulting distribution function signatures in "magnetotail-like" magnetic fields. We have found that the phase space partitions persist for small to moderate scattering amplitudes. In particular, we find that the KAM surfaces break up, thus allowing orbits to diffuse into and out of the previously integrable regions; however, the separation in time scales between the stochastic and integrable regions remains. The separation between the transient and stochastic regions remains prominent in both phase space and time scales. Using simple analytic approximations we have shown that the collisions are well modeled as a random walk process in both pitch-angle and energy.

In addition, using the coherence factor as a measure of the effectiveness of collisions in modifying phase space, we have shown that for the collisions to have a significant effect they must be of a sufficiently large amplitude or of a high enough frequency to transport a large number of particles across the stochastic-transient boundary. As one might expect, a constant amplitude of energy scattering will tend to destroy the low energy peaks but will not significantly affect the high energy peaks. Constant amplitude pitch-angle scattering on the other hand tends to suppress all of the peaks equally. These results are significant in that they help to explain the robust nature of the phase space structures and the resulting observed signatures of the ion distribution function.



### III. A Finite $\beta$ , Kinetic Equilibrium Model of the PSBL-lobe Interface

In this project we developed a fully self-consistent, finite  $\beta$ , kinetic model of the boundary layer which forms between the plasma sheet boundary layer (PSBL) and the lobe in the earth's magnetotail. The model is based on two basic observations. The first is that the plasma density in the PSBL tends to be much higher than the plasma density in the lobe. The second is that the transition between the lobe and the PSBL occurs on a scale length which is on the order of an ion gyroradius. In a series of papers, Romero et al. constructed a model of this interface and evaluated its stability in the limit of zero  $\beta$ , where  $\beta$  is the ratio of the plasma pressure to the magnetic field pressure. In their analysis they found that plasma density variations on such a short scale length resulted in large electrostatic potentials ( $e\phi \approx T_e$ ) in order to maintain quasineutrality. In addition, strong plasma flows perpendicular to the magnetic field develop in both the electrons and ions. Furthermore, these flows, which carry a net current, were shown to be a source of free energy in driving broadband electrostatic noise. The growth rate of the noise is found to be determined the parameter  $\alpha_\sigma = (1/\Omega_\sigma)(dV_\sigma/dx)$  where  $\sigma = i, e$ ,  $\Omega_\sigma$  the cyclotron frequency of the particle species, and  $(dV_\sigma/dx)$  is the gradient in the cross-field velocity flows.

In our model we choose particle distributions functions which in the limit of  $\beta=0$  reduce to those suggested by Romero et al., but which also allow us to investigate the large  $\beta$  regime. In the low  $\beta$  limit we find that we reproduce the results of Romero et al. In the high  $\beta$  regime we find a general steepening of the plasma profiles and a substantial change in the magnetic field across the boundary. In particular, we find that the magnetic field may vary by a factor of two for physically reasonable parameters, in good agreement with observations. It is interesting to note that the shear parameter,  $\alpha_\sigma$ , is independent of  $\beta$  at least in the regime  $0 < \beta < 300$ . Since the growth rate of the electrostatic noise depends upon  $\alpha_\sigma$ , this indicates that the much simpler  $\beta=0$  results provide a reasonable approximation to the wave spectrum.

### IV. Observational Signatures of Global Magnetospheric Structures in GEOTAIL Satellite Data

Based on the theoretical/numerical results from this grant and tentative identification of the energy resonance phenomena in ISEE-1 satellite data, I have obtained a grant through the NASA-JOVE program to examine the GEOTAIL Comprehensive Plasma Instrument data for more experimental verification. We have found several examples of the predicted signature in the ion distribution function for cases in which the satellite is in the proper region (i.e. the central plasma sheet) and the magnetotail is quiet ( $K_p \sim 1$ ). It is found that the peaks can exist for long periods of time (tens of minutes) with little change in the signature between measurements. We have also performed simulations which produce pitch-angle resolved distribution functions in support of this work. These simulations have put the theoretical interpretation of the peaks on a much firmer foundation.

### PROGRAMMATIC TRAVEL

During the the tenure of the grant I have made seven trips either to work with collaborators on related topics or to present papers at conferences. The trips are listed below in chronological order.

- 1) Travel to the Naval Research Laboratory in Washington, DC to work with Dr. James Chen, Dr. Peter Cargill and Dr. James Harold on topics related to magnetotail equilibrium and stability. 1/10/94 - 1/16/94
- 2) Spring meeting of the American Geophysical Union in Baltimore, MD; 5/23/94 - 5/27/94
- 3) Annual meeting of the American Physical Society, Division of Plasma Physics in Mineapolois, MN; 11/7/94 - 11/11/94
- 4) Spring meeting of the American Geophysical Union in Baltimore, MD; 5/30/95 - 6/2/95
- 5) Annual meeting of the American Physical Society Division of Plasma Physics in Louisville, KY; 11/6/95 - 11/10/95
- 6) Spring meeting of the American Geophysical Union in Baltimore, MD; 5/20/96 - 5/24/96
- 7) Fall meeting of the American Geophysical Union in San Francisco, CA; 12/15/96 - 12/19/96

## PUBLICATIONS AND PRESENTATIONS RELATED TO GRANT

Listed below are all of the publications and presentations which are related to magnetospheric physics which were completed during the grant period. Copies of each of these papers are attached.

### Refereed Journals

1. Daniel L. Holland, James Chen and Alex Agranov, *Effects of a Constant Cross-Tail Magnetic Field on the Particle Dynamics in the Magnetotail*, J. Geophys. Res., **101**, 24997, 1996.
2. Glenn Joyce, James Chen, Steven Slinker, and Daniel L. Holland, *Particle Energization Near an X-line in the Magnetotail based on Global MHD Fields*, J. Geophys. Res., **100**, 19167, 1995.
3. James Chen and Daniel L. Holland, *Reply to Burkhart, Spieser and Dusenbery*, Phys. Plasmas, **1**, 801, 1994

### Conference Proceedings

1. Daniel L. Holland and James Chen, *Self Consistent Current Sheet Structures in the Quiet Time Magnetotail*, 1993 MIT Symposium and Cambridge Workshop on the Physics of Space Plasmas.
2. James Chen and Daniel L. Holland, *Nonlinear Dynamics of Particles in the Magnetosphere: A Tutorial Review*, 1993 MIT Symposium and Cambridge Workshop on the Physics of Space Plasmas.
3. Glenn Joyce, James Chen, Steven Slinker, and Daniel L. Holland, *Particle Energization Near an X-line in the Magnetotail based on Global MHD Fields*, 1993 MIT Symposium and Cambridge Workshop on the Physics of Space Plasmas.
4. James Chen and Daniel L. Holland, *Global Consequences of Nonlinear Particle Dynamics in the Magnetotail*, Geophysical Monograph **86**, 205, 1995

### Reports

1. Daniel L. Holland and James Chen, *A Current Calculation Algorithm for Test Particle Simulations of the Magnetotail*, NRL Internal Report #7168
2. D Walker, D., J. Chen, C. Siefing, D. Duncan, J. Stracka, J. Antoniadis, J. Bowles and D. Holland, *Nonlinear particle dynamics in the magnetotail; a laboratory study 1. the experimental configuration and numerical simulation*, NRL Memorandum #7734

### Abstracts

(\* – indicates student coauthor)

1. D. L. Holland, W.R. Paterson and L. A. Frank, *Observational Signatures of Global Magnetospheric Structures in GEOTAIL Satellite Data*, EOS, **77**, F625, (1996).
- 2.\* D. L. Holland and P. W. Valek, *Equilibrium Structure of the PSBL – Lobe Interface*, EOS, **77**, 253, (1996).
- 3.\* D. L. Holland and D. J. King, *Distribution function signatures of the global topology of the quiet-time magnetotail*, Bull. Am. Phys. Soc., **40**, 1844, 1995.

4. D. L. Holland, J. Chen, *Effects of a Constant Cross-Tail Magnetic Field on the Particle Dynamics in the Magnetotail*, EOS, **76**, 245, 1995.
- 5.\* D. J. King, D. L. Holland, and J. Chen, *Characterization of Collisional Effects on Magnetotail Particle Dynamics*, EOS, **76**, 246, 1995.
- 6.\* P. W. Valek and D. L. Holland, *A Finite  $\beta$ , Kinetic Equilibrium Model of the PSBL*. Bull. Am. Phys. Soc., **39**, 1719, (1994).
7. D. L. Holland, P. J. Cargill, J. Chen, and J. B. Harold, *Hybrid Simulations of  $B_y$  Fields in the Magnetotail*, EOS, **75**, 302, 1994.
- 8.\* P. W. Valek and D. L. Holland, *A Finite  $\beta$ , Kinetic Equilibrium Model of the PSBL*, EOS, **75**, 302, 1994.
9. J. Chen, J. B. Harold, D. L. Holland and A.T.Y. Lui, *Kinetic Coupling of the Auroral Region and the Near-Earth Current Sheet*, EOS, **75**, 302, 1994.

#### Departmental Presentations

1. D. L. Holland, *On the parametrization of chaotic particle dynamics in the magnetotail*, December 7, 1994, ISU Physics Department Informal Seminar.
2. Holland, Daniel, *Kinetic modeling of plasma equilibria*, March 6, 1995, ISU Physics Department Informal Seminar.
3. Holland, Daniel, *Equilibrium structures of boundary layers in the magnetosphere*, September 7, 1995, ISU Physics Department Informal Seminar.
4. Daniel Holland, *Magnetic Substorms*, Twin Cities Amateur Astronomy Club, October 1996.
5. Daniel Holland, *Magnetic Substorms*, Lecture Series for High School Physics Students, Illinois State University, September 1996.

#### Manuscripts in Preparation

These manuscripts are based on work performed during the grant period and will be submitted for publication this year.

1. D. L. Holland, W. R. Paterson and L. A. Frank, *Observational Signatures of Global Magnetospheric Structures in GEOTAIL Satellite Data*, to be submitted to Geophysical Research Letters.
2. D. L. Holland, D. J. King, and J. Chen, *Characterization of Collisional Effects on Magnetotail Particle Dynamics*, to be submitted to the Journal of Geophysical Research.
3. D. L. Holland and P. W. Valek, *A Finite  $\beta$ , Kinetic Equilibrium Model of the PSBL-Lobe Interface*, to be submitted to the Journal of Geophysical Research.

## PUBLICATIONS AND PRESENTATIONS NOT RELATED TO GRANT

In addition to my work in magnetospheric physics, I also have an ongoing program studying plasma wall interactions in magnetized plasmas. Listed below are all of the publications and presentations which are related to sheath physics which were completed during the grant period. I recently received a grant through the Research Corporation to continue this work.

### Abstracts

(\* – indicates student coauthor)

- 1.\* S. W. Powell and D. L. Holland, *Sheath Structure in a Weakly Magnetized Plasma*, Bull. Am. Phys. Soc., **39**, 1758, (1994).

### Departmental Presentations

1. D. L. Holland, *Sheath structures in a magnetized plasma*, Seminar given to Mark Kushner's Plasma Processing Group in the Electrical Engineering Department at the University of Illinois, July 1994.
2. Holland, Daniel, *An analytic model of sheath structures in an obliquely incident magnetized plasma*, Argonne National Laboratory Fusion Power Program Seminar, April 28, 1995.
2. Daniel Holland, *Sheath Structures in a Magnetized Plasma*, ISU Colloquium, April 28, 1996.

## UNDERGRADUATE STUDENT INVOLVEMENT

A primary objective of the physics program at Illinois State University is to get our students actively involved in the departments research programs. Thus far I have had four undergraduate students involved in my magnetospheric physics projects. The students and a brief description of their contributions are given below.

student	Year(s)	Accomplishments
Phil Valek	1993-94	Investigated the equilibrium structure of the PSBL-lobe interface including the effects of finite plasma $\beta$ .
David King	1994-96	Investigated the effects of "collisions" on phase space structures and distribution function signatures due to nonlinear particle dynamics in the magnetotail. Began an investigation of pitch-angle resolved distribution functions.
Aaron Starkey	1994	Extended the analysis begun by Phil Valek to include more realistic effects including a diffuse rather than a sharp boundary.
Ann Witmer	1996	Assisted in the analysis of ion data from the GEOTAIL satellite.

The work that these students performed resulted in 4 presentations at predominately undergraduate research symposiums. These are listed below. In addition, much of the work was presented at national/international conferences. These presentations are listed above in the section on presentations related to the grant and are marked with an asterisk.

1. David King and Daniel Holland, *Characterization of collisional effects on the nonlinear particle dynamics in the magnetotail*, 1994 Argonne Undergraduate Research Symposium.
2. P. W. Valek and D. L. Holland, *A finite  $\beta$ , kinetic equilibrium model of the PSBL-lobe interface*, 1994 Spring Meeting of the Illinois Section of the Society of Physics Students at Illinois Wesleyan University.
3. P. W. Valek and D. L. Holland, *A finite  $\beta$ , kinetic equilibrium model of the PSBL-lobe interface*, 1994 Illinois State University Undergraduate Research Symposium.
4. David King and Daniel Holland, *Characterization of Collisional Effects on the Nonlinear Particle Dynamics in the Magnetotail*. 1995 ISU undergraduate research symposium

A measure of the success of the students participation in the research program is what the students are currently doing. Phil Valek is a graduate student doing work in space physics at Auburn University, David King is a graduate student in electrical engineering at the University of New Mexico and Aaron Starkey is employed in industry in the Chicago area. Ann Witmer is still actively involved in the project. Note also the David King was awarded a DoD fellowship for graduate study.

## Effects of a constant cross-tail magnetic field on the particle dynamics in the magnetotail

Daniel L. Holland

Department of Physics, Illinois State University, Normal

James Chen and Alex Agranov

Beam Physics Branch, Plasma Physics Division, Naval Research Laboratory, Washington, D.C.

**Abstract.** The effects of a constant cross-tail magnetic field  $B_y$  on the phase space structures and the observational signatures of nonlinear particle dynamics in the quiet time magnetotail are examined. The separation of phase space into dynamically distinct regions (transient, stochastic and integrable) is found to persist, albeit with considerable complications. In addition, it is shown that if  $|B_y|$  is less than the  $B_z$  component, the resonant coherent chaotic scattering of particles and the resulting distribution function features persist. If  $|B_y| \gtrsim B_z$ , on the other hand, the majority of the particles are forward scattered through the current sheet, and there is no discernible signature of the resonance in the distribution function. This is significant in that the presence or absence of the resonance effect in observed distribution functions can constrain the magnitude of  $B_y$ .

### Introduction

In the collisionless plasmas of the magnetosphere, properties of particle distributions can carry a wealth of information regarding the global system. For example, *West et al.* [1978] suggested that pitch angle distributions of energetic electrons can be used to distinguish between dipolar and tail-like fields near Earth during quiet time. *Lyons and Speiser* [1982] argued that the “kidney bean” shaped  $v_{\perp}$ – $v_{\parallel}$  distributions [*DeCoster and Frank*, 1979] indicated evidence of current sheet acceleration. *Curran and Goertz* [1989] suggested that depletion in the model distribution can be a signature of  $X$  lines. *Martin and Speiser* [1988] found that particle acceleration in the  $X$ -type neutral line can be manifested as a ridge structure in the phase-angle-averaged distribution functions.

In the quasi-neutral sheet geometry relevant to the central plasma sheet, *Chen et al.* [1990] presented observational evidence for the nonlinear particle dynamics and a phase space resonance effect [*Burkhart and Chen*, 1991]. The signature appears as peaks and valleys in ion distribution functions with separation scaling as  $\tilde{H}^{1/4}$  where  $\tilde{H} = H/m\Omega_z^2 b_z^2 \delta^2$  is the normalized energy,  $m$  is the ion mass,  $\delta$  is the scale length of the field reversal,  $\Omega_z$  is the ion cyclotron frequency in the constant magnetic field normal to the current sheet  $B_z$ , and  $b_z$  is the ratio of the  $B_z$  and the asymptotic value to the primary field component  $B_x$ . The resonance scaling has also been calculated for the general field dependence of  $B_x(z) \propto z^s$ , yielding a  $\tilde{H}^{\chi}$  resonance scaling where  $\chi = (1/2)s/(s+1)$  [*Chen*, 1992, 1993]. Thus the resonance in locally observed distribution functions can serve as a measurable diagnostic of the magnetic field profile as seen by particles on the scale of  $(\rho_z \delta)^{1/2}$  inside the current sheet. Here  $\rho_z$  is the gyroradius in the constant  $B_z$  field. The resonance effect

arises from the existence of distinct classes of orbits (differential memory) which can give rise to similar distribution function features in different field models [*Ashour-Abdalla et al.*, 1991, 1993].

It was further suggested [*Chen et al.*, 1990] that particle and magnetometer data from a single satellite could be used to infer the current sheet thickness. More recently, *Lui* [1993] presented a different but complementary procedure to extract global information about the current sheet from local spacecraft measurements. Since satellite measurements are local in space and time, the ability to infer global properties from local measurements would be valuable.

In the above suggestions, a number of assumptions are made regarding the global magnetic field. One is that the cross-tail  $B_y$  component of the magnetic field is negligible. In reality, there exist periods when  $B_y$  is not negligible in the magnetotail [e.g., *McComas et al.*, 1986]. In this paper, we quantify the effects of a constant nonzero  $B_y$  on the nonlinear particle dynamics and the  $\tilde{H}^{1/4}$  resonance effect. This constant  $B_y$  field is assumed to be caused by the interplanetary magnetic field and is different from the antisymmetric (i.e. an odd function of  $z$ )  $B_y$  field found in hybrid simulations of the current sheet [*Pritchett and Coroniti*, 1993; *Burkhart et al.*, 1993; *Cargill et al.* 1994]. For antisymmetric  $B_y$  fields of this type the equations of motion retain the same symmetries as those with  $B_y = 0$ . Thus the basic phase space partitioning and distribution function signatures are not greatly modified so long as we retain a tail-like topology, that is provided that the maximum value of  $B_y \ll B_0$ . This result is born out by test particle codes in model fields.

A recent paper by *Zhu and Parks* [1993] examined the effects of a constant cross-tail component of the magnetic field on individual particle orbits. In this paper, we concentrate on the generic properties of classes of orbits. We find that the resonance effect and the resulting distribution function signature persists for  $B_y \lesssim B_z$  but becomes undiscernible for  $B_y \gtrsim B_z$ . This can serve as a diagnostic signature by allowing one to infer limits on the relative

magnitude of  $B_y$  and  $B_z$  and as a quantitative criterion for judging the influence of  $B_y$  on the particle dynamics.

### Dynamical System

We use a modified Harris model with a superimposed constant cross-tail magnetic field  $B_y$

$$\mathbf{B}(z) = B_0 \tanh(z/\delta) \hat{\mathbf{x}} + B_y \hat{\mathbf{y}} + B_z \hat{\mathbf{z}}. \quad (1)$$

The equations of motion in this field are given by

$$\frac{d^2 X}{d\tau^2} = \frac{dY}{d\tau} - \epsilon \frac{dZ}{d\tau} \quad (2a)$$

$$\frac{d^2 Y}{d\tau^2} = \frac{d}{d\tau} \left[ b_z^{-2} \ln(\cosh(b_z Z)) - X \right] \quad (2b)$$

$$\frac{d^2 Z}{d\tau^2} = \epsilon \frac{dX}{d\tau} - b_z^{-1} \tanh(b_z Z) \frac{dY}{d\tau} \quad (2c)$$

where  $b_z \equiv B_z/B_0$ ,  $\epsilon \equiv B_y/B_z$  and we have used the standard normalized variables, that is,  $X \equiv (x - P_y/m\Omega_z)/b_z\delta$ ,  $Y \equiv (y + C_x/m\Omega_z)/b_z\delta$ ,  $Z \equiv z/b_z\delta$  and  $\tau = \Omega_z t$ . Here  $P_y \equiv mv_y + (q/c)A_y$  is the canonical momentum in the  $y$  direction,  $A_y = B_0\delta \ln[\cosh(z/\delta)]$  is the vector potential, and  $C_x \equiv m(v_x + \Omega_z y)$  is a constant associated with the  $x$  motion. Note that if we let  $\epsilon \rightarrow 0$  (i.e.,  $B_y \rightarrow 0$ ), we recover (5), (6), and (7) of *Chen and Palmadesso* [1986]. Also note that these equations may not be used to approach the integrable limit  $b_z \rightarrow 0$ , since we have explicitly divided by  $b_z$  in our normalizations.

Equations (2a), (2b), and (2c) are invariant under the simultaneous replacements of  $Z \rightarrow -Z$  and  $\epsilon \rightarrow -\epsilon$  and the simultaneous replacements of  $Y \rightarrow -Y$ ,  $\tau \rightarrow -\tau$ , and  $\epsilon \rightarrow -\epsilon$ . As in the  $B_y = 0$  case, these symmetries have a profound influence on the phase space structure. For our purposes here, the symmetry  $Z \rightarrow -Z$  with  $\epsilon \rightarrow -\epsilon$  implies that a source distribution of particles coming from  $Z < 0$  with  $\epsilon < 0$  will behave in the same way as a source distribution of particles coming from  $Z > 0$  with  $\epsilon > 0$ .

As in the  $B_y = 0$  case, we will describe the dynamical system using Poincaré maps at the midplane,  $Z = 0$ , emphasizing the generic and topological properties of families of solutions. The Poincaré surface of section is the first return map of (2a), (2b), and (2c) at the midplane ( $Z = 0$ ). In previous studies [*Chen and Palmadesso*, 1986], one Poincaré section at  $Z = 0$  has been used to describe the dynamics for each value of  $\hat{H}$  in field geometries with reflection symmetry about the midplane. If, however, the system is not symmetric under  $Z \rightarrow -Z$ , then the two directions of midplane crossing must be distinguished. Thus the system will be described using two phase space surfaces, one for  $\dot{Z} > 0$  and one for  $\dot{Z} < 0$  evaluated at  $Z = 0$ . A typical example of the surface of section plots is given in Figure 1 for the case  $\hat{H} = 187$ ,  $b_z = 0.1$ , and  $\epsilon = 1$ . Figure 1a gives the  $Z = 0$  crossing with  $\dot{Z} > 0$ , designated south-to-north (S-N), and Figure 1b gives the surface of section at  $Z = 0$  for  $\dot{Z} < 0$ , designated north-to-south (N-S). This should be compared with Figure 2 of *Holland and Chen* [1991] which corresponds to the same values of  $\hat{H}$  and  $b_z$  with  $\epsilon = 0$ . (The previous result includes collisions which will not be discussed in the present work. The primary effect of the collisions is to destroy the Kolmogorov-Arnol'd-Moser (KAM) surfaces in the integrable region.) The important dynamical property for our

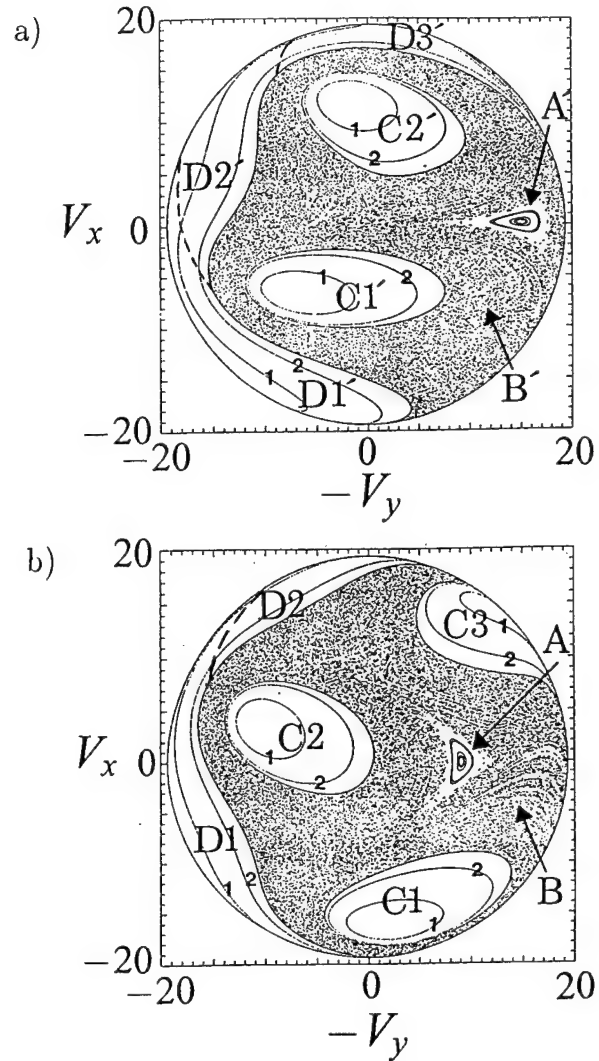


**Figure 1.** Surface of section plots for the case in which the particles are launched from  $Z \gg 1$  with  $\hat{H} = 187.4$ ,  $b_z = 0.1$ , and  $\epsilon = 1$ . (a) South-to-north crossings are shown. (b) North-to-south crossings are shown. Regions A and A' are the integrable regions; B and B' are the stochastic regions; and C, C', D and D' are transient regions. The curves labeled 1 and 2 in the transient regions correspond to particle swith asymptotic pitch angles of 30° and 60°, respectively.

discussion here, as in the  $B_y = 0$  case, is that the partitioning of phase space into transient, stochastic, and integrable regions persists, albeit with considerable additional complexities.

Referring to Figure 1, (where we have taken  $\epsilon > 0$ ) the regions A and A' are the integrable regions of phase space. In this region, orbits are confined to KAM surfaces for all time in the absence of noise. A few representative integrable orbits are shown as nested closed curves. Note that A and A' correspond to one set of orbits, crossing the midplane with  $\dot{Z} > 0$  and  $\dot{Z} < 0$ , respectively. All particles approaching the midplane from the north will first cross midplane in region C1 (N-S crossing). The particles will then cross the midplane again in region C1' (S-N crossing) followed by region C2, C2', and C3. Some particles then escape to infinity (transient orbits), whereas others will reenter the phase space in region B (stochastic orbits). Similarly, those particles approaching the midplane from the south will first enter the midplane in region





**Plate 1.** Color coded break down of the entry and exit regions of Figure 1 according to the type of particle: red, transient orbits with an odd number of crossings; green, transient orbits with an even number of crossings; yellow, stochastic orbits with an odd number of crossings; and blue, stochastic orbits with an even number of crossings.

D1' (S-N crossing). The particles will then cross the midplane again in region D1 (N-S crossing), D2', D2 and so forth. Again some particles will escape to infinity after one traversal of the midplane (transient orbits), whereas others will reenter the phase space in region B and make multiple traversals of the midplane

(stochastic orbits). The above discussion is true for  $\epsilon > 0$ . For  $\epsilon < 0$  the same basic consideration hold true, however, particles approaching from the north will now enter into the D regions and particles approaching from the south will enter into the C regions. Owing to the symmetries of the equations of motion, the

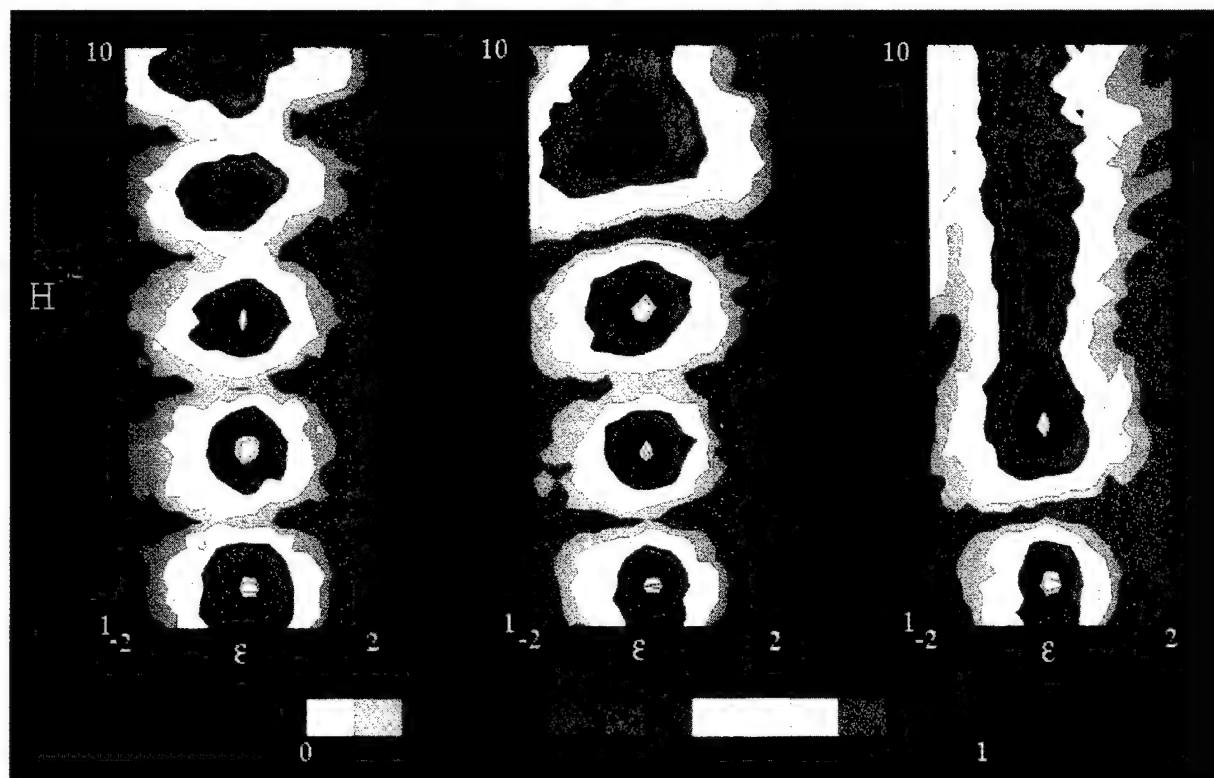


**Plate 2.** Forward scattering probability for  $1 \leq \dot{H}^{1/4} \leq 10$ ,  $-2 \leq \epsilon \leq 2$  and (left)  $b_z = 0.05$ , (center)  $b_z = 0.1$ , and (right)  $b_z = 0.2$ .

last crossing point for a given orbit must fall within the mirror image (about  $V_x = 0$ ) of the entry regions, either C1 or D1'. (This is discussed in detail below for a particular example.) As in the  $B_y = 0$  case, the number of midplane crossings for one traversal, that is, the number of C and D regions, increases with  $\hat{H}$ . The boundary between the transient regions C and D, and the stochastic region B corresponds to those particles with pitch angle  $90^\circ$  in the asymptotic regions. The curves labeled 1 and 2 in the transient regions correspond to orbits with asymptotic pitchangle of  $30^\circ$  and  $60^\circ$ , respectively. An interesting difference between the two types of transient regions (C and D) is that orbits with a given asymptotic pitch angle fall on closed curves in regions C, whereas the constant pitch angle curves in regions D are not closed but are instead finite length line segments. This difference is understood by the fact that regions of type C are isolated and completely surrounded by the stochastic regions. In order to have a boundary defined by the orbits with an asymptotic pitch angle of  $90^\circ$ , orbits with constant asymptotic pitch angles must fall on concentric closed curves. In contrast, the regions of type D are not completely surrounded by the stochastic region but are in fact in contact with each other. Hence the constant pitch angle curves are no longer closed but instead form a continuous curve between the successive regions. An interesting aspect of this is that the boundary between two adjacent regions of type D (e.g. D1' and D2') is not defined by a single asymptotic pitch angle but instead has particles with all asymptotic pitch angles. (The boundaries between the regions of type D are the dashed curves in Figure 1.) Note that the mapping of the contours from one D region to another, say, those in D1 to D2, gives continuous curves across the boundary, but the points in D1 and D2 are separated by intervening crossings in D1' on a different Poincare surface of section.

As in the  $B_y = 0$  case, the entry regions, C1 and D1', may be subdivided into the entry regions for transient and stochastic orbits [Chen, 1992]. This is done by examining the intersection of the "time reversed" entry regions of phase space with the regions C, C', D, and D'. Again, owing to the symmetries of the equations of motion, the time reversed entry regions are simply the mirror image in  $V_x$  of the normal entry regions. (In the following, the mirror image of a region refers to reflection about  $V_x = 0$ .)

As a particular example, in Plate 1a we show the entry and exit regions for particles approaching the midplane from the south with  $\hat{H} = 187$  and  $B_y = B_z = 0.1B_0$ . Plate 1b shows the entry and exit regions for particle approaching the midplane from the north, with the same parameters. The points shown in red represent transient orbits which cross the midplane an odd number of times and therefore leave the midplane region from the same surface of section on which they entered, for example, if the particle initially enters the midplane from the north, it leaves to the south and vice versa. Note that in Plate 1a the red particles initially enter the region through the intersection of regions D1' and the mirror image of D2' and D3'. These particles cross the midplane for the last time in the mirror image of D1'. The red particles in Plate 1b enter through the intersection of region C1 and the mirror image of C3 and leave the system in the mirror image of region C1.

Green points represent transient orbits which cross the midplane an even number of times and therefore leave the midplane on the opposite surface of section from which they entered. In Plate 1a, the green orbits initially enter through the intersection of D1' and mirror image of C2' and leave the system in the mirror image of C1. In Plate 1b the green orbits enter through the intersection of region C1 and the mirror image of region D2 and leave the system in the mirror image of region D1'.

Blue (yellow) points represent stochastic orbits which cross the midplane even (odd) numbers of times. In Plate 1a, these orbits enter through the intersection of region D1' and the mirror image of region B'. Those orbits that cross the midplane even (odd) numbers of times eventually leave the system through the mirror image of region C1 (D1'). In Plate 1b, the stochastic orbits enter the system through the intersection of region C1 and the mirror image of region B. Those orbits which cross the system an even (odd) number of times eventually leave through the mirror image of D1' (C1).

If we now regard the current sheet as a chaotic scattering system, we may calculate the forward and backward scattering probability as a function of  $\hat{H}^{1/4}$  and  $\epsilon$  for given values of  $b_z$ . This is done by launching an isotropic, constant energy shell of particles for a given magnetic field ( $b_z$  and  $\epsilon$ ) from a fixed value of  $Z$  in the asymptotic region of the magnetic field ( $|Z| \gg 1$ ) and determining the location of the particle when it escapes from the system. We then vary  $\hat{H}$  and  $\epsilon$  for fixed values of  $b_z$  to build up a plot of the forward scattering probability. The results of this calculation are shown in Plate 2 for  $1 \leq \hat{H}^{1/4} \leq 10$ ,  $-2 \leq \epsilon \leq 2$  and (left)  $b_z = 0.05$ , (center)  $b_z = 0.1$  and (right)  $b_z = 0.2$ . The forward scattering probability for particles launched from the north ( $\sigma_{nf}$ ) is plotted according to the color bar shown:  $\sigma_{nf} = 0$  means that all particles launched from the northern asymptotic source ( $Z > 0$ ) are backscattered while  $\sigma_{nf} = 1$  means that all particles from the north escape to the  $Z = -\infty$ . Both limits correspond to coherent scattering. The most significant feature of these plots is the presence of well-defined regions (gray to purple) in which the majority of the particles are backscattered. For small values of  $\epsilon$ , these are separated by regions (orange to red) in which the majority of the particles are forward scattered. As in the  $B_y = 0$  case, these correspond to energy levels in which the phase space structure is very symmetric. For  $\epsilon > 1$ , essentially all of the particles are forward scattered. If we look at the cut along the  $\epsilon = 0$  plane, we recover the results of Chen *et al.* [1990]. Note that we only need to calculate the forward scattering probability for particles which are launched from above the midplane since we may use the symmetry property  $Z \rightarrow -Z$  and  $\epsilon \rightarrow -\epsilon$  to determine those from below.

## Construction of the Distribution Function

In this section, we generalize the previous analysis of coherent chaotic scattering [Chen *et al.*, 1990] to construct the distribution function in the presence of the cross-tail field component. Suppose that the northern and southern particle sources are given by  $f_n(\hat{H})$  and  $f_s(\hat{H})$ , respectively. Furthermore, suppose that we have an observer located in the northern hemisphere between the current sheet and the source region. Such a situation, depicted in Figure 2, may be considered to be a satellite located in the central plasma sheet far from the plasma sheet boundary layer but outside the current sheet. Since self-consistent calculations indicate a current sheet thickness of the order of one Earth radius [Pritchett and Coroniti, 1992; Burkhardt *et al.*, 1993; Holland and Chen, 1993], any point a few Earth radii away from the midplane will suffice. This corresponds well to the ISEE 1 data shown by Chen *et al.* [1990]. The distribution function that the observer sees will consist of three parts: (1) particles coming directly from the northern source region, (2) particles from the northern source region that are backscattered at the current sheet, and (3) particles from the southern source region that are forward scattered by the current sheet. Mathematically this is written as

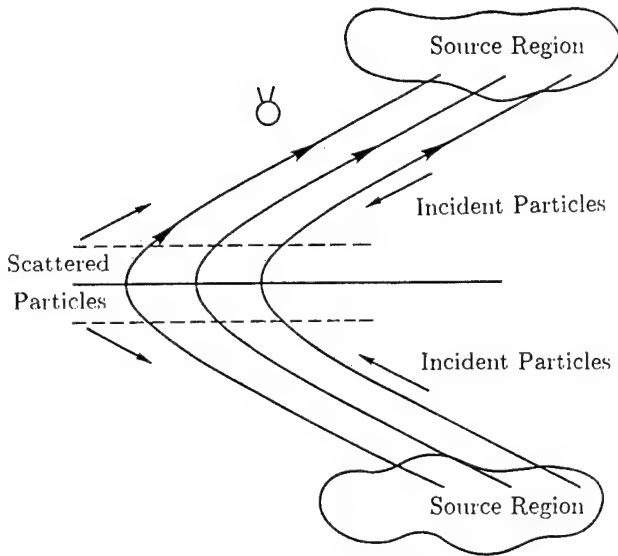


**Figure 2.** Schematic diagram of distribution function calculation.

$$f_{ob}(\hat{H}) = [1 + \sigma_{nb}(\hat{H}, \epsilon)]f_n(\hat{H}) + \sigma_{sf}(\hat{H}, \epsilon)f_s(\hat{H}) \quad (3)$$

where  $f_{ob}(\hat{H})$  is the observed, pitch angle averaged distribution function,  $\sigma_{nb}(\hat{H}, \epsilon)$  is the backscattering probability of a particle launched from the northern hemisphere with given  $\hat{H}$  and  $\epsilon$ , and  $\sigma_{sf}(\hat{H}, \epsilon)$  is the forward scattering probability of a particle launched from the southern hemisphere. Owing to the symmetry  $Z \rightarrow -Z$  with  $\epsilon \rightarrow -\epsilon$  and using  $\sigma_f = 1 - \sigma_b$ , (3) may be rewritten as

$$f_{ob}(\hat{H}) = [2 - \sigma_{nf}(\hat{H}, \epsilon)]f_n(\hat{H}) + \sigma_{nf}(\hat{H}, -\epsilon)f_s(\hat{H}). \quad (4)$$

Thus we only need the northern (or southern) forward scattering probability, but we must have it for both positive and negative values of  $\epsilon$ .

As an illustration, we show in Figure 3 two model distribution functions constructed using the above formulation assuming that  $b_z = 0.1$ . Both the northern and southern source distributions are taken to be Maxwellians with a normalized thermal energy,  $\hat{H}_{th} = 3000$ . In addition, we have assumed that  $f_s = 1.5f_n$ . In the first case (Figure 3a), we have chosen  $\epsilon = 0.2$  and in the second (Figure 3b) we have chosen  $\epsilon = 1$ . Note that for the small  $\epsilon$  case, the characteristic peaks and valleys of the coherent chaotic scattering are quite distinct, whereas in the second case there are no obvious signatures of the phase space resonance. Owing to the symmetry of the scattering probability for particles launched from above and below the current sheet, if  $f_s = f_n$  the peaks and valleys in the pitch angle averaged distribution function will not be present even for small  $\epsilon$ . (This is also true for the  $B_y = 0$  case discussed by *Chen et al.* [1990].) If, on the other hand,  $f_s \neq f_n$ , the resulting observed distribution function need not be Maxwellian even though the sources may be. For more general magnetic field of the form  $B_x = B_0 z^s$ , we expect the corresponding resonance  $N \sim \hat{H}^s$  should similarly persist since it is based on similar phase space partitioning.

## Discussion

In this paper, we have examined the modifications to the phase space structures due to the addition of a constant cross-tail mag-

netic field. We have found that the basic phase space partitioning into transient, stochastic, and integrable regions persists. Since we no longer have the symmetry  $Z \rightarrow -Z$ , however, we must use two surfaces of section to describe the motion; one for north-to-south crossing points and one for south-to-north crossing points. In addition, we have identified a new type of transient regions (regions D in Figure 1) which are distinguished from the traditional type of transient regions (regions C in Figure 1) by the fact that they are not completely surrounded by stochastic regions.

We have also examined the effects of the constant cross-tail magnetic field on the distribution function signatures as reported by *Chen et al.* [1990]. We have found that provided  $|\epsilon| \lesssim 1$ , the coherent chaotic scattering of particles is robust, and hence the resulting peaks and valleys in the ion distribution function persist. If, on the other hand, we have  $|\epsilon| > 1$ , then the majority of the particles are forward scattered through the current sheet and there is no structure in the calculated distribution function. This result is significant in that if the peaks and valleys are observed in particle data from a satellite, it places limits on the magnitude of any cross-tail component to the magnetic field. If the peaks and valleys are not observed, on the other hand, then little can be said regarding the magnetic field topology. This is because the absence of the signature could be the result of the violation of other approximations, for example, time stationarity, one-dimensionality, etc. In conclusion, this paper presents another example of how local data from a single satellite may be used to infer global information on the current sheet structure.

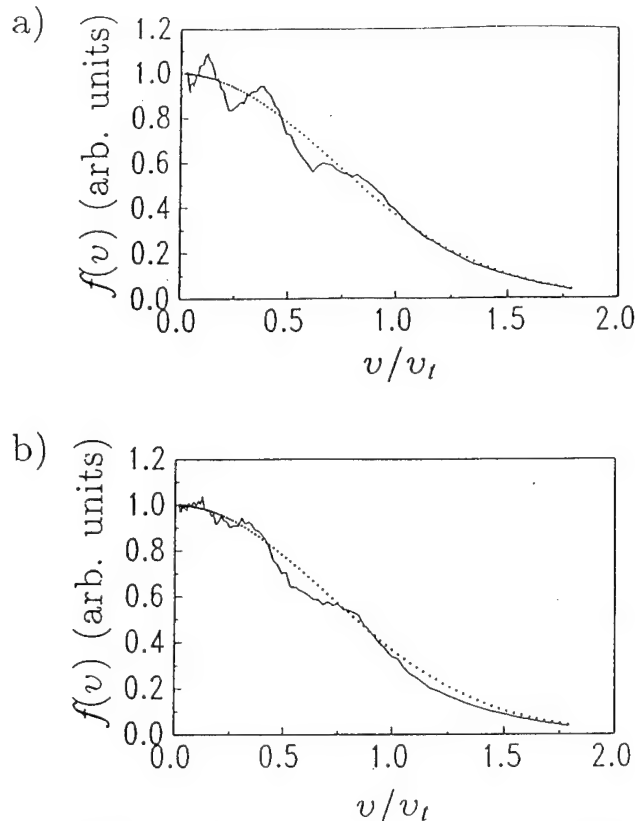


**Figure 3.** Two model ion distribution functions calculated in the region  $Z \gg 1$  with  $b_z = 0.1$ . Here  $f_s > f_n$  is assumed. (a)  $\epsilon = 0.2$ , and (b)  $\epsilon = 1$ . Dotted curves represent Maxwellian distributions of the same temperature.

**Acknowledgments.** This work was supported by the National Aeronautics and Space Administration (W-16,991) and the Office of Naval Research.

The Editor thanks O.W. Lennartsson and another referee for their assistance in evaluating this paper.

## References

- Ashour-Abdalla, M., J. Berchem, J. Büchner, and L. M. Zelenyi, Large and small scale structures in the plasma sheet: A signature of chaotic motion and resonance effects, *Geophys. Res. Lett.*, **18**, 1603, 1991.
- Ashour-Abdalla, M., J. P. Berchem, J. Büchner, and L. M. Zelenyi, Shaping of the magnetotail from the mantle: Global and local structuring, *J. Geophys. Res.*, **98**, 5651, 1993.
- Burkhart, G. R., and J. Chen, Differential memory in the Earth's magnetotail, *J. Geophys. Res.*, **96**, 14,033, 1991.
- Burkhart, G. R., and J. Chen, Particle motion in  $x$ -dependent Harris-like Magnetotail models, *J. Geophys. Res.*, **98**, 89, 1993.
- Burkhart, G. R., P. B. Dusenbery, T. W. Speiser, and R. E. Lopez, Hybrid simulations of thin current sheets, *J. Geophys. Res.*, **97**, 13,799, 1992.
- Burkhart, G. R., J. F. Drake, P. B. Dusenbery, and T. W. Speiser, A particle model for the magnetotail neutral sheet equilibria, *J. Geophys. Res.*, **98**, 21,373, 1993.
- Cargill, P. J., J. Chen, and J. B. Harold, One-dimensional hybrid simulations of current sheets in the quiet magnetotail, *Geophys. Res. Lett.*, **21**, 2251, 1994.
- Chen, J., Nonlinear dynamics of charged particles in the magnetotail, *J. Geophys. Res.*, **97**, 15,011, 1992.
- Chen, J., Physics of the magnetotail current sheet, *Phys. Fluids B*, **5**, 2663, 1993.
- Chen, J., and P. J. Palmadesso, Chaos and nonlinear dynamics of single-particle orbits in a magnetotail-like magnetic field, *J. Geophys. Res.*, **91**, 1499, 1986.
- Chen, J., G. R. Burkhart, and C. Y. Huang, Observational signatures of nonlinear magnetotail particle dynamics, *Geophys. Res. Lett.*, **17**, 2237, 1990.
- Curran, D. B., and C. K. Goertz, Particle distributions in a two-dimensional reconnection field geometry, *J. Geophys. Res.*, **94**, 11,521, 1989.
- DeCoster, R. J., and L. A. Frank, Observations pertaining to the dynamics of the plasma sheet, *J. Geophys. Res.*, **84**, 5099, 1979.
- Holland, D. L., and J. Chen, Effects of collisions on the nonlinear particle dynamics in the magnetotail, *Geophys. Res. Lett.*, **18**, 1579, 1991.
- Holland, D. L., and J. Chen, Self-consistent current sheet structures in the quiet time magnetotail, *Geophys. Res. Lett.*, **20**, 1775, 1993.
- Lui, A. T. Y., Inferring global characteristics of current sheet from local measurements, *J. Geophys. Res.*, **98**, 13,423, 1993.
- Lyons, L. R., and T. W. Speiser, Evidence of current sheet acceleration in the geomagnetic tail, *J. Geophys. Res.*, **87**, 2276, 1982.
- Martin, R. F., and T. W. Speiser, A predicted energetic ion signature of a neutral line in the geomagnetic tail, *J. Geophys. Res.*, **93**, 11,521, 1988.
- McComas, D. J., C. T. Russel, R. C. Elphic, and S. J. Bame, The near-Earth cross-tail current sheet: Detailed ISEE 1 and 2 case studies, *J. Geophys. Res.*, **91**, 4287, 1986.
- Pritchett, P. L., and F. V. Coroniti, Formation and stability of the self-consistent one-dimensional tail current sheet, *J. Geophys. Res.*, **97**, 16,773, 1992.
- Pritchett, P. L., and F. V. Coroniti, A radiating one-dimensional current sheet, *J. Geophys. Res.*, **98**, 15,355, 1993.
- West, H. I., R. M. Buck, and M. G. Kivelson, On the configuration of the magnetotail near midnight during quiet and weakly disturbed periods: Magnetic field modeling, *J. Geophys. Res.*, **83**, 3819, 1978.
- Zhu, Z., and G. Parks, Particle orbits in model current sheets with a nonzero  $B_y$  component, *J. Geophys. Res.*, **98**, 7603, 1993.
- A. Agranov and J. Chen, Beam Physics Branch, Plasma Physics Division, Naval Research Laboratory, Washington, DC 20375-5000. (e-mail: chen@ppdu.nrl.navy.mil)
- D. L. Holland, Department of Physics, 311 Moulton Hall, Illinois State University, Normal, IL 61790-4560. (e-mail: holland@entropy.phy.ilstu.edu)

(Received March 7, 1995; revised July 21, 1995; accepted July 24, 1995.)

## Particle energization near an X line in the magnetotail based on global MHD fields

G. Joyce, J. Chen, S. Slinker, D. L. Holland,<sup>1</sup> and J. B. Harold

Beam Physics Branch, Plasma Physics Division, Naval Research Laboratory, Washington, D. C.

**Abstract.** Particle acceleration near an X line in the magnetotail and the resulting ion distribution functions in the central plasma sheet are studied by using  $2\frac{1}{2}$ -dimensional test particle simulations. The electric and magnetic fields are taken from a three-dimensional global magnetohydrodynamic (MHD) simulation model describing the solar wind-magnetosphere interaction. A southward interplanetary magnetic field is chosen as the input solar wind condition. Test particles are generated from a model ion source distribution consistent with the macroscopic MHD parameters in the lobe region. The particles are calculated earthward and tailward of the X line. It is found that ion distributions consist of two main components: a low-energy population similar to the input distribution and a high-energy population. The former corresponds to particles that do not cross the region in which the  $B_x$  field reverses direction, while the latter consists of particles which cross the midplane, gaining energies on the order of keV. The spatial dependence of the relative population of low-energy versus high-energy components is discussed. The details of the acceleration process are determined from the motion of test particles in the simulation.

### 1. Introduction

The magnetotail consists of a number of distinct regions characterized by different plasma properties. The central plasma sheet (CPS) contains hot (keV) ions, and the surrounding lobe plasma is cold (tens of eV). It is presumed that the lobe particles gain energy upon entering the CPS. Accordingly, particle acceleration mechanisms and distribution functions in the CPS have been investigated for a number of magnetic configurations relevant to the magnetotail. For example, Cowley [1978] and Lyons and Speiser [1982] modeled the "current sheet acceleration" in the magnetotail, using noninteracting Speiser orbits. More recently, Horton and Tajima [1990, 1991] and Holland and Chen [1992] investigated particle energization incorporating the nonlinear dynamics of charged particles in the magnetotail [Chen and Palmadesso, 1986], and ion distribution functions have been modeled by using test particles [Lyons and Speiser, 1982; Chen et al., 1990a, b; Burkhardt and Chen, 1991; Ashour-Abdalla et al., 1991, 1993]. Particle energization and distribution functions in X line magnetic field configurations have also received extensive attention [Wagner et al., 1981; Curran et al., 1987; Curran and Goertz, 1989; Martin and Speiser, 1988; Doxas et al., 1990; Burkhardt et al., 1990; Moses et al., 1993]. In these studies, test particle trajectories were calculated in prescribed X line configurations. Burkhardt et al. [1991] carried out a test particle study of reconnection

region in which the current and magnetic field were iterated until they were self-consistent, satisfying  $\mathbf{J} = (c/4\pi)\nabla \times \mathbf{B}$ .

In the above works, uniform cross-tail electric fields ( $E_y$ ) are imposed, which can be transformed away in simple one-dimensional cases. In a different approach, Sato et al. [1982] investigated the acceleration of test particles using electric and magnetic fields obtained from a magnetohydrodynamic (MHD) simulation of an X-type reconnection region. This work used an isolated X line structure, and reconnection was forced by injecting magnetized plasma toward the neutral line. Scholer and Jamitzky [1989] and Birn and Hesse [1994] calculated test particle trajectories and their energetics in time-dependent fields during plasmoid formation in two and three dimensions, respectively. In the work of Scholer and Jamitzky [1989], reconnection is triggered in an initial current sheet by a localized resistivity. In the work of Birn and Hesse [1994], a plasmoid is formed in a model magnetotail in response to introducing anomalous resistivity. Test particle trajectories are then calculated in the simulated electric and magnetic fields. In order to incorporate large-scale fields encompassing different regions, Ashour-Abdalla et al. [1993] used a two-dimensional reduction of the Tsyganenko [1989] model in steady state with an imposed uniform cross-tail electric field,  $E_y$ . The Tsyganenko model gives a description of the magnetic field under various geomagnetic conditions and is constructed from a statistical composite of satellite measurements. In this "large-scale kinetic" approach, the magnetic field and imposed electric field are not self-consistently determined for the model magnetosphere.

The objective of the present paper is to investigate how ion distribution functions are formed in a model CPS with an X line. The essential ingredient in connecting the CPS, X line, and the rest of the magnetotail is the fields that are

<sup>1</sup>Now at Physics Department, Illinois State University, Normal.



consistent with the global magnetosphere under given solar wind conditions. This provides a significant extension of the previous approach in which an isolated X line is treated with an imposed uniform  $E_y$  field. We use the electric and magnetic fields given by an MHD model of the magnetosphere and use test particle simulations to model kinetic properties in the MHD fields. It is clear that MHD can only approximate the actual solar wind-magnetosphere system based on macroscopic energy and momentum balance. However, the fields are self-consistent within the set of basic MHD equations, and the use of a global model allows one to relate the region of interest to the solar wind conditions in a quantitative way. In particular, the energy and momentum flux, i.e., the Poynting vector  $\mathbf{E} \times \mathbf{B}$  and the particle motion, are consistent with the global system in near steady state. The present study represents an initial step toward obtaining a kinetic model consistent with the global solar wind-magnetosphere system. In this paper, we focus on the physical process of particle energization and entry from the lobes into the CPS through an X line region and the resulting ion distribution functions in the CPS.

As the model global magnetosphere, we will use the electric and magnetic fields from an MHD simulation model [Fedder et al., 1995]. We will focus on the magnetotail determined by a southward interplanetary magnetic field (IMF) and study particle energization and ion distribution functions for this configuration. In our calculations, the lobes, the X line, and the CPS form a coupled region. The significant new features of the field model are (1) electric and magnetic fields that are self-consistent within the MHD approximations, (2) asymmetric X line and CPS configurations, and (3) perhaps most important, magnetospheric configurations given in relation to IMF conditions. The present calculation is time independent, and the consistency between the current and magnetic field will not be treated.

## 2. MHD Model of the Magnetosphere

We will first describe the three-dimensional (3D) global simulation model of Fedder et al., which will constitute the MHD framework, a surrogate global magnetosphere, to be used in our work. We will focus on the electric and magnetic fields in the magnetotail and the lobes.

The model uses ideal MHD equations to describe the solar wind and the magnetosphere. The model contains an ionosphere represented as a spherical region with the boundary at  $3.5 R_E$ , allowing an active interaction between the resistive ionosphere and the rest of the magnetosphere. The model ionosphere has a time-varying conductance with a "solar" component to represent photoionization and an auroral conductance that is calculated from the magnetospheric properties. This allows the model to distinguish between the nightside and dayside. The model ionosphere provides a means of relating  $J_{\parallel}$  to  $B$  in the near-Earth region. The ionospheric currents determine an electrostatic potential that is mapped outward to the simulation boundary at  $3.5 R_E$ . The potential is used to derive an electric field used in the temporal integration of Faraday's law to update the magnetic field on that boundary. The simulation domain consists of a cylindrical region of radius  $60 R_E$  aligned along the Earth-Sun line. The ends of the cylinder extend from  $30 R_E$  sunward

to  $\sim 300 R_E$  tailward with no waves propagating back toward the Earth. Simulations are driven by either observed or model solar wind parameters at the dayside boundaries.

The MHD algorithm has been developed to minimize numerical dissipation, but like other models of this class, the representation of current sheet reconnection is determined, in part, by numerical effects; when two oppositely directed magnetic field lines are closer than the grid spacing, the code connects the lines. The reconnection process in the simulation is determined from a combination of the influence of the model ionosphere and, to a lesser extent, from numerical properties. (Reconnection per se is outside the ideal MHD formalism.)

The state of the global magnetosphere is critically determined by the solar wind/IMF. For example, geomagnetic disturbances are associated with southward turning of the IMF at the dayside magnetopause. The current paradigm is that a southward IMF leads to reconnection at the dayside magnetopause, allowing injection of magnetic flux and solar wind particles into the magnetosphere. This overall picture is qualitatively reproduced by the global MHD model of Fedder et al. In our paper, we focus on a particular time period and investigate the kinetic properties of ions. The configuration used throughout this paper was obtained by starting with a steady initial state with a northward IMF at  $+5$  nT and turning the IMF southward, which is subsequently held constant at  $-5$  nT. Several interesting properties have been observed in this model system including the formation and disruption of neutral lines and, at times, the occurrence of near steady state reconnection. In particular, we have found a quasi-steady configuration after the IMF turns southward with an X line. Unless the IMF is turned northward, the neutral line remains nearly stationary. This appears to be the longtime solution for the given southward IMF condition. We have used the model MHD fields and flows from this period to provide a framework for studying the dynamics of charged particles near the neutral line. These fields allow us to study a portion of the magnetosphere that is consistent with the near equilibrium of the global system including the IMF. The simulation model is discussed in detail by Fedder et al. [1995] and Fedder and Lyon [1995].

For our test particle simulation, we have isolated a region given by  $-50 < x < -20$  and  $-4 < z < +4$ , where the coordinates are in units of Earth radii ( $R_E$ ),  $x$  is the Sun-Earth line pointing sunward,  $y$  is the cross-tail direction with  $y = 0$  (the noon-midnight plane), and  $z$  points north. Throughout the present paper, spatial variables will be expressed in units of  $R_E$ . Figures 1a and 1b show the contours of the  $B_x$  and  $B_z$  components in the  $y = 0$  plane, taken from the MHD model. In all contour plots, we use solid (dotted) lines to denote positive (negative) values. The  $B_x$  component varies from  $-12$  nT to  $12$  nT ( $x \approx -20$ ) and changes sign across a distance of approximately  $3 R_E$  centered around  $z \approx 0$ . This field reversal region, of course, corresponds to a current sheet. However, ideal MHD does not treat the current sheet region accurately because the motion of current carriers (ions) is highly nonadiabatic [Sonnerup, 1971], and the computational grid is too sparse to resolve the region well. In order to accurately describe the magnetotail current sheet, ions must be treated kinetically as described in the introduction.

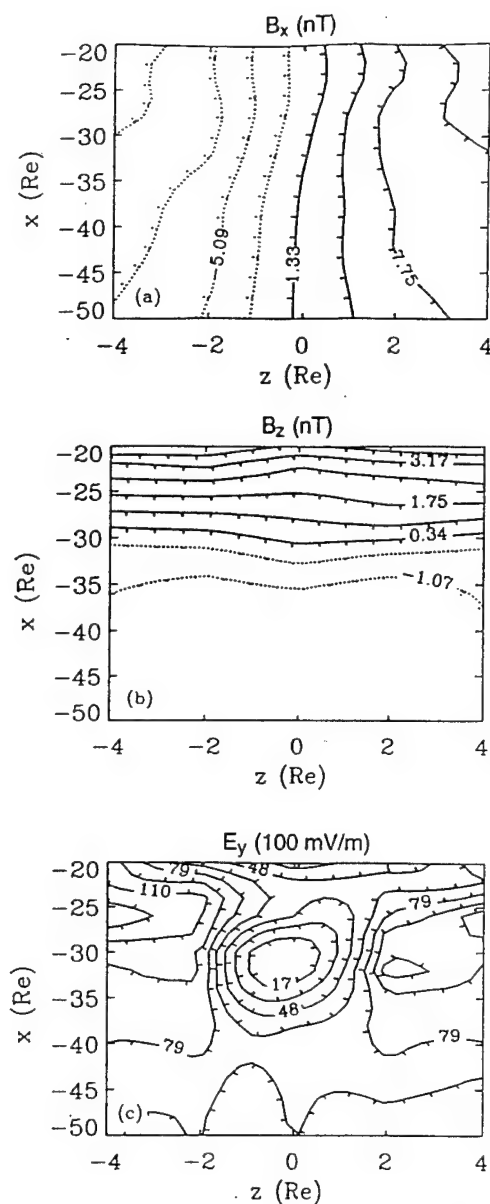


**Figure 1.** Contour plots of fields from the MHD simulation for a southward IMF. The fields are taken in the noon-midnight plane,  $y = 0$ . (a)  $B_x$  component. (b)  $B_z$  component in nT. (c) Cross-tail  $E_y$  component in units of 100 mV/m. There is an X line at  $x \approx -32$  and  $z \approx 0$ .

Figure 1b shows contours of  $B_z$ , which passes through zero at about  $x = -32$ . In conjunction with Figure 1a, we see that there is an X line at  $x \approx -32$  and  $z \approx 0$ . Earthward from the X line, the  $B_z$  field becomes stronger and dipolar. Tailward of the X line, the field is negative and nearly uniform at approximately  $-2$  nT. In the simulation box used in our work, the  $B_y$  component is roughly  $-0.1$  nT for  $z < 0$  and  $+0.2$  nT for  $z > 0$ , so that  $|B_y| \ll |B_x|, |B_z|$ . There is no significant  $B_y$  field in and near the X line. Figure 1c shows the y component of the electric field (in units of 100 mV/m) which is inferred from MHD through the relation  $\mathbf{E} = -(1/c)\mathbf{V} \times \mathbf{B}$ . The value of  $E_y$  is typically 0.5 to 1

mV/m but is smaller in the immediate vicinity of the X line because the magnetic field is weak. It is clear that the cross-tail  $E_y$  in this quasi-steady configuration is not uniform. The other components of the electric field are weaker; the  $E_x$  component is typically  $-0.03$  mV/m, and  $E_z \sim 0.5$ – $1$  mV/m for  $z < 0$ , reversing near the midplane. Figures 2a and 2b describe the  $V_z$  and  $V_x$  components of the MHD flow velocity, respectively. These figures show the classic flow patterns near a reconnection region: Incoming particles earthward of the neutral line tend to be convected earthward, while incoming particles tailward of the neutral line tend to be convected tailward. Figure 2b shows that the average tailward flow is faster than the earthward flow. This is because the magnitude of the  $B_z$  component tailward of the X line is weaker, approximately one third that on the earthward side. Particles enter the X line region from the lobes by  $\mathbf{E} \times \mathbf{B}$  drift. We point out, however, that the individual orbits need not follow the average fluid motion: a given population of particles can consist of subpopulations moving along or in opposite directions to the local average flow. This is a significant difference between MHD and a kinetic description.

With the IMF held northward at  $+5$  nT, we have also examined the configuration of the magnetotail. We find that the flow speeds are considerably slower than in the southward IMF case, giving a weaker electric field. As a result, the particle energy gain is less. This is consistent with the generally accepted notion that magnetic and particle energy

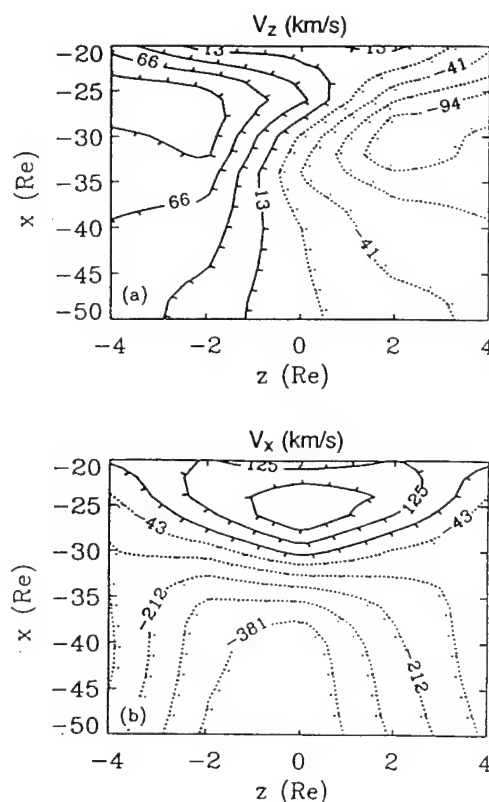


**Figure 2.** Flow velocity from the MHD simulation model. Solid (dotted) lines denote positive (negative) flows. (a)  $V_z$  component. The plasma flows toward the midplane. (b)  $V_x$  component. The plasma flows outward from the X line.

input into the magnetosphere is less during northward than southward IMF periods. With a weaker electric field, individual particles remain in the simulation region for longer periods of time, and the orbits are similar to stochastic orbits that have been studied in quasi-neutral sheets (see *Chen* [1992] for a review). In the present paper, we focus on the magnetospheric condition determined by a southward IMF.

### 3. Test Particle Simulation Model

Figures 1 and 2 show that the gradient scale lengths in the electric and magnetic fields, away from the immediate vicinity of the X line, are of the order of 5–10  $R_E$ . This is consistent with observational estimates near the Earth [*Huang and Frank*, 1994] and in the distant tail [*Behannon*, 1968]. In the  $y$  direction centered around the noon-midnight plane ( $y = 0$ ), the spatial variation in the MHD fields is also weak on the scale of several Earth radii (not shown). In comparison, the  $y$  excursion distance of particles is significantly smaller. For example, a 1-keV proton has an excursion distance of approximately  $2\rho_z \simeq 1 R_E$  if  $B_z = 1$  nT, where  $\rho_z$  is the ion Larmor radius in the  $B_z$  field. Thus the protons that are accelerated near the noon-midnight plane typically see weak spatial dependence in the  $y$  direction. (Particle orbits will be illustrated later.) In our calculations, we simplify the electric and magnetic fields by assuming that they are translationally invariant in the  $y$  direction. This allows us to follow the orbits of a large number (230,000) of ions on a two-dimensional grid (in the  $x$ - $z$  plane) at  $y = 0$ . The orbits, however, are calculated in three dimensions with all the components of the MHD fields. We also limit the source of particles to the low-temperature lobe population. Our calculation captures three-dimensional effects of particle acceleration near the noon-midnight plane ( $\pm 2 R_E$ ) but does not include particles that may come from outside this region (e.g., the flanks). The magnetic and electric fields are taken from the MHD code and interpolated to this grid from the cylindrical grid of the global model, and are frozen in time.

As discussed above, the electric field is obtained from the macroscopic flows and magnetic field and is nonuniform (Figure 1c). In order to illustrate the effect of using a uniform  $E_y$ , we have replaced the  $E_y$  field with a constant field of 0.5 mV/m, while requiring that  $\mathbf{E} \cdot \mathbf{B} = 0$ . (Note that there is no general way to impose a uniform  $E_y$  field with no  $E_{\parallel}$  unless  $B_y = 0$  is also imposed, which typically leads to  $\nabla \cdot \mathbf{B} \neq 0$ .) Not surprisingly, we find that the velocity patterns with a uniform  $E_y$  are significantly different from those of the global model. In particular, the average  $V_y$  near the X line is significantly greater for uniform  $E_y$  since the magnetic field is weak. Overall, we find that the amount of energy gained is a factor of 2 to 3 greater than that using the field in Figure 1c. The latter point is consistent with the finding of *Karimabadi et al.* [1990], who reported unrealistically high energy gain by test particles in two-dimensional magnetic fields with imposed uniform  $E_y$ . Thus, using ad hoc fields would not be consistent with the quasi-equilibrium force balance determined by the global model. In terms of individual particles, this implies that the  $\mathbf{E} \times \mathbf{B}$  drift paths and the electric field as seen by particles would be different from those in a globally consistent system. Conceptually,

$\mathbf{S} = (c/4\pi)\mathbf{E} \times \mathbf{B}$  gives the energy flux in the system so that an ad hoc uniform  $E_y$  would not produce momentum flux consistent with the assumed steady state configuration.

The particle pushing algorithm uses a standard method in which the velocities are taken on the half time steps and the positions are on the full time steps. The gyromotion is calculated by using the procedure introduced by Boris [*Boris*, 1970; *Birdsall and Langdon*, 1991]. The particles are injected into the system from the lobe region. For the simulation, this consists of injecting particles at random points along the line  $-45 < x < -25$  at  $z = \pm 4$  and  $y = 0$ . This line segment is approximately centered at the X line ( $x \simeq -32$ ). The injection planes at  $z = \pm 4$  are inside the actual simulation box and represent, in this simple model, the beginning of the lobe regions, and the injected particles have a relatively low kinetic temperature. The input particles are chosen to have an isotropic Maxwellian distribution characterized by an input temperature  $T$  and no bulk drift. We follow the orbits of the particles until they leave the system. Several velocity moments are calculated while the particles are in the system. They are the particle density, the three components of the particle velocity,  $V_x$ ,  $V_y$ ,  $V_z$ , and six components of the products of the velocity,  $V_x^2$ ,  $V_y^2$ ,  $V_z^2$ ,  $V_x V_y$ ,  $V_x V_z$ , and  $V_y V_z$ . These quantities are calculated by using standard particle-in-cell laydown techniques. The second velocity moments are necessary for the calculation of the kinetic pressure. In addition, we have averaged the kinetic pressure terms to obtain a kinetic temperature defined by

$$kT = (m/3) \int (\mathbf{v} - \langle \mathbf{V} \rangle)^2 f d^3\mathbf{v} / \int f d^3\mathbf{v}, \quad (1)$$

where  $k$  is the Boltzmann constant, the normalization is such that  $n(x, z) = \int f d^3\mathbf{v}$  is the density, and  $\langle \mathbf{V} \rangle$  is the average velocity vector. This quantity is a measure of the plasma internal energy.

The positions and velocities of the particles leaving the simulation region through the ends are recorded and are later analyzed to determine the velocity distributions. Distribution functions are obtained as a function of  $v_{\parallel}$  and  $v_{\perp}$  (where parallel and perpendicular subscripts indicate the directions relative to the local magnetic field) in various regions in  $z$ . Finally, a number of particles are tracked throughout their orbits, and the energization process for these particles is investigated. These diagnostics will be used to understand the formation of energetic particles in the magnetotail.

In our calculations, we input a Maxwellian distribution with  $T = 200$  eV to model lobe sources of particles. The kinetic temperature of the resulting test particle distribution is shown in Figure 3. Near the simulation boundaries ( $z \simeq \pm 4$ ) where  $B_x$  is strong, the temperature remains comparable to the injection temperature. In the central plasma sheet, the temperature is higher, ranging from about 600 eV in the vicinity of the X line to about 1 keV both earthward and tailward of the X line. This represents continual heating of the plasma particles in the current sheet, consistent with the observed property that the CPS contains hot (keV) ions in comparison with the low-temperature lobe plasmas and with the generally accepted notion that energization in the current sheet can make a significant contribution to the heating of the CPS plasma [e.g., *Cowley*, 1978; *Lyons and Speiser*, 1982].



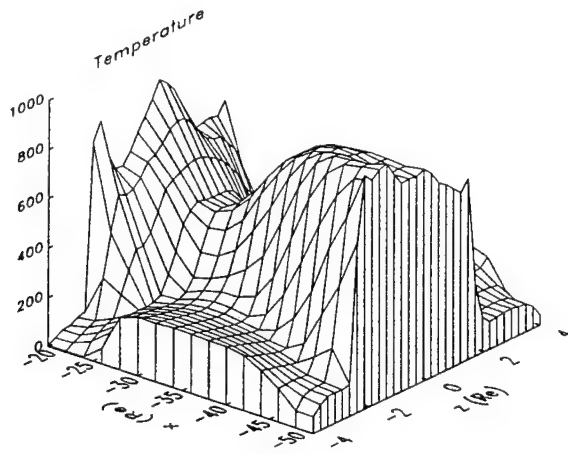


**Figure 3.** Surface plot of the kinetic temperature determined from the test particles using equation (1). The input temperature is assumed to be 200 eV. Including directed velocity, the kinetic energy reaches a maximum of 3 keV in the vicinity of  $x = -50$ .

The new feature here is that the electric field responsible for the energization and the transport of energized particles throughout the simulation region are consistent with the global configuration of the magnetosphere under the specified southward IMF condition.

### 3.1. Distribution Functions

We have analyzed the distribution of particles leaving the system through the ends of the simulation region. These distributions are computed as follows. We divide the boundary surfaces at  $x = -20 R_E$  and  $x = -50 R_E$  into segments of width  $1 R_E$  each. The distribution functions consist of particles escaping through these segments. We have examined the four segments between  $z = 0$  and  $z = 4$ . We did not compute distribution functions for  $z < 0$  because the system is relatively symmetric about the midplane. The distribution functions are given in terms of  $v_{\parallel}$  and  $v_{\perp}$ , where the perpendicular and parallel directions are determined from the magnetic field seen by each particle. Figure 4 shows the contours of  $f(v_{\parallel}, v_{\perp})$  as the particles leave the simulation box in the tailward direction. The units are such that when velocities are squared, the results are in electron volts (eV).

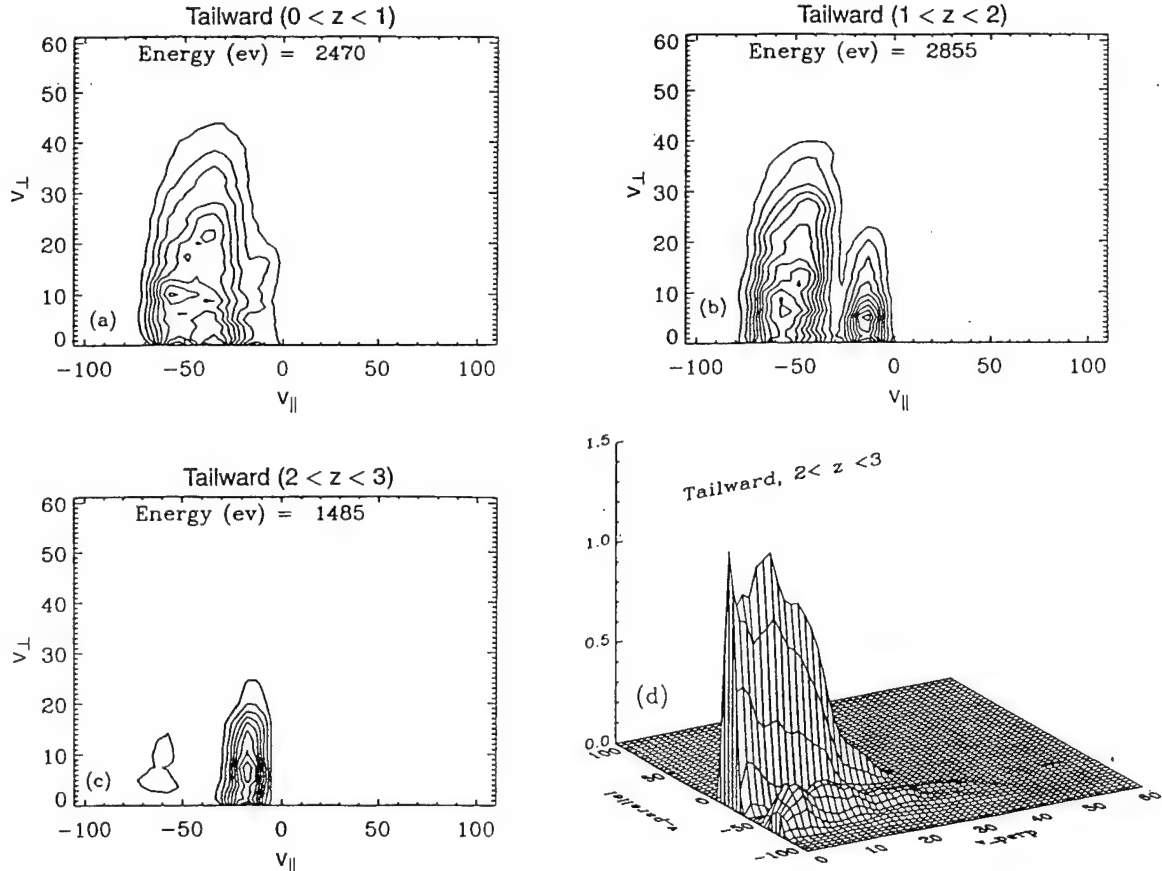


**Figure 4.** Distribution function of particles leaving the system at  $x = -50$  and different  $z$  values. The units are such that  $v^2$  is in electron volts (eV). (a) Near the midplane,  $0 < z < 1$ . The low-energy component is insignificant. (b) Here,  $1 < z < 2$ . The low-energy component is more prominent. (c) Here,  $2 < z < 3$ . The low-energy component is dominant. (d) Surface plot of the distribution shown in Figure 4c. Most particles have not crossed the midplane and have an average energy of 545 eV.

The most notable property of each distribution function is that it has two components: A low-energy component which has an energy comparable to the energy of the incoming particles (200 eV) and a high-energy component with the energy in the range of a few keV. Figure 4a is for  $0 < z < 1$  and shows that most of the particles have gained about 2.5 keV. For  $1 < z < 2$ , described in Figure 4b, the low-energy component is more evident, although the average energy is somewhat higher than that in the midplane region. As one moves away from the midplane, the cold component becomes more prominent. Figure 4c gives the distribution function for  $2 < z < 3$ . The average energy at  $\sim 1.5$  keV is significantly lower than the two distributions closer to the midplane. This distribution is dominated by a low-energy component as illustrated in Figure 4d. For  $3 < z < 4$  (not shown), the bulk of the distribution consists of low-energy particles with the average energy at  $\sim 500$  eV. The particles comprising the low-energy distribution are those that have reached the end of the system without ever crossing the midplane. The particles in the high-energy distribution have made at least one crossing of the midplane. The nature of the high- and low-energy components of the distribution functions does not change significantly in the various  $z$  regions. However, the relative sizes of the two components vary with  $z$  because of the number of particles that have made crossings of the midplane. That is, the ratio of accelerated to unaccelerated particles decreases with distance from the axis until at  $z = 4$ , there is no significant population of accelerated particles. In Figure 5, we show the fraction of particles that gain more than 1 keV (solid line) versus the fraction of particles that gain less than 1 keV (dashed line).

The results suggest that an observable ion signature tailward of the interaction with an X line is the simultaneous presence of two energy distributions with the hot component dominating near the midplane and the cold component prevailing toward the lobes. This signature is complementary to the signatures proposed previously by *Martin and Speiser* [1988] (the ridge structure) and *Curran and Goertz* [1989] (a depletion of omnidirectional fluxes near the midplane). In the particular snapshot of fields used in our paper, the distribution of particles leaving the system on the earthward side differs somewhat from that of the tailward distribution

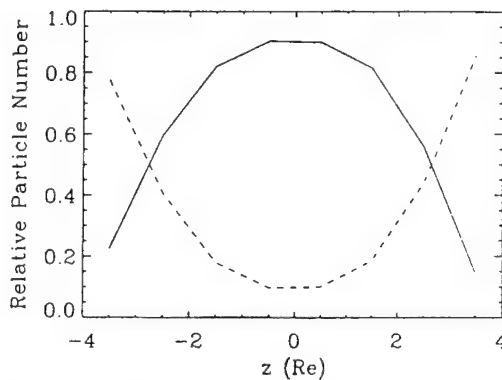


**Figure 5.** Spatial ( $z$ ) dependence of the hot versus cold components. Solid line: the fraction of particles gaining 1 keV or more. Dashed line: the fraction of particles gaining less than 1 keV.

described above. Toward the Earth, the energy gain of the particles is of the order of 1 keV as opposed to  $\sim 3$  keV (Figure 4b), and the division of particles into two energy groups is less pronounced. We attribute the differences to the fact that at the earthward boundary,  $x = -20$ , the dipole field is the dominant magnetic field, so that the field-aligned direction has a large  $z$  component, unlike that of the tailward region. The  $B_z$  component is stronger (Figure 1b), and  $E_y$  is slightly weaker (Figure 1c). In the current sheet away from the X line, the energy gain of a particle with initial kinetic energy  $H$  is given (in one dimension) by  $\Delta H \sim mc(E_y/B_z)(2H/m)^{1/2}$  [Cowley, 1978], where  $H$  is the kinetic energy of the incoming particle, so that we expect the energy gain near  $x = -20$  to be lower than that near  $x = -50$ .

As an example, Figures 1b and 1c show that  $E_y \approx 0.6$  mV/m and  $B_z \approx 1$  nT in the vicinity of  $x = -40$  and  $z = 0$  so that incoming particles drift in at approximately  $v_D \equiv c(E_y/B_z) \approx 7 \times 10^7$  cm/sec, corresponding to 2.6 keV protons. Since this energy is much greater than 200 eV, the incoming kinetic energy is  $H \approx (1/2)mv_D^2$ , and we obtain the typical energy gain  $\Delta H \approx 4$  keV, which is consistent with the simulation results. Note that a 4 keV proton has a Larmor radius of approximately  $1.4 R_E$ , somewhat smaller than the gradient scale lengths away from the X line. (In the above expression for  $\Delta H$ , we have suppressed the particle pitch angle dependence for simplicity.)

As a qualitative comparison, we consider the ion distribution functions obtained during the GALILEO crossing of the magnetotail [Frank et al., 1994]. One salient feature of the observed distribution functions, both earthward and tailward of a neutral line, is the two-component structure, consisting of cold and warm components. Our calculated distribution functions closely resemble those observed during the GALILEO encounter. In addition, the hot components of the computed distributions tend to be elongated in the  $v_\perp$  direction (Figure 4), consistent with the "lima bean" distortions in the observed distribution functions. Such distortions (but not the two-component structure) have been reported in observed distributions [DeCoster and Frank, 1979] as well as calculated distributions [Martin and Speiser, 1988]. Frank et al. [1994] attributed the hot component to the current sheet acceleration, which is supported by our simulations. We point out, however, that the present results model a generic process rather than a specific observation.

In order to understand the energization process in detail, we have studied the orbits of some randomly selected particles. Figure 6 shows a typical orbit and its kinetic energy. The orbit is injected at  $x = -40$  and  $z \approx 4$ , crosses the midplane at  $x \approx -36$ , and leaves the simulation region. This orbit has the nature of transient orbits [Chen and Palmadesso, 1986] with two midplane crossings. The initial motion is primarily  $\mathbf{E} \times \mathbf{B}$  drift toward the midplane. All the orbits we analyzed exhibited this generic behavior. When the particle reaches the vicinity of  $z = 0$ , it is accelerated in the  $+y$  (dawn-dusk) direction over the distance  $\Delta y \approx 2\rho_z$ . After leaving the current sheet, it moves in the  $x$  direction and eventually reaches the simulation boundary at  $x = 50$ . Particle orbits generally do not conserve adiabatic invariants. The kinetic energy of this particle is plotted along the trajectory. We see that the energy simply oscillates about the

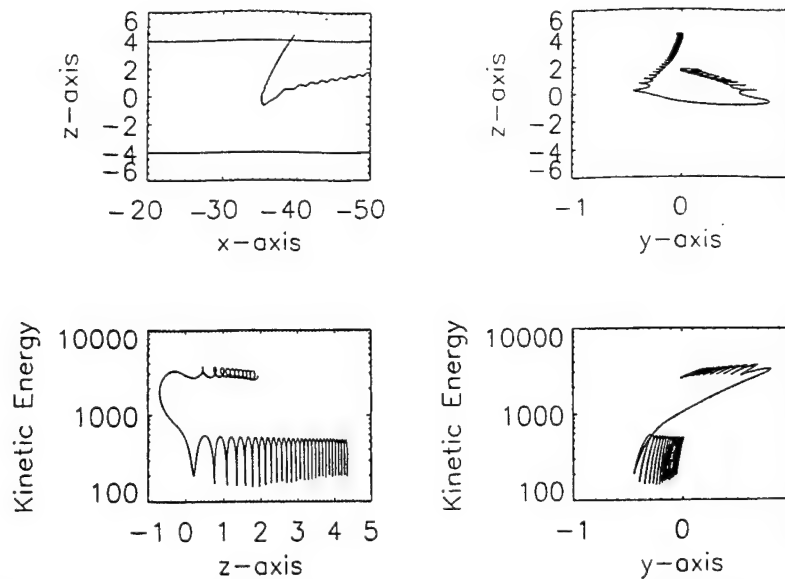


**Figure 6.** A representative midplane crossing orbit and its kinetic energy. Spatial coordinates are in units of  $R_E$ : (a)  $z$  versus  $x$  for the particle, (b)  $z$  versus  $y$  for the particle, (c) kinetic energy versus  $z$ , and (d) kinetic energy versus  $y$ .

initial energy of 200 eV until the particle enters the midplane near the neutral line, where this particle gains  $\sim 3$  keV in one traversal of the midplane. (Repeated "interaction" with the current sheet does not yield simply additive energy gain because the particle loses energy while returning to the midplane. The energy is roughly determined by the electric and magnetic fields as seen by the particle during the last interaction or midplane traversal.) There is no significant energy gain associated with the  $x$  motion. The specific number of midplane crossings can vary over a wide range, but the basic behavior described here is generic to orbits that cross the midplane. This current sheet acceleration process has been discussed in a simpler geometry [Cowley, 1978; Lyons and Speiser, 1982]. Similar orbits have been reported previously [Wagner *et al.*, 1981; Sato *et al.*, 1982; Burkhardt *et al.*, 1990; Birn and Hesse, 1994] and will not be discussed in further detail.

In contrast to orbits of the type discussed above, there are particles that do not cross the neutral line or the midplane. Such particles simply  $\mathbf{E} \times \mathbf{B}$  drift across the magnetic separatrix and move out of the simulation region without coming near the midplane and without gaining significant amounts of energy. This explains the property described in Figure 5, showing large fractions of energized particles near the midplane and low-energy particles away from the midplane. Note that particle acceleration in a neutral line or current sheet in the presence of an electric field is to be expected. The significance of our results is that the electric and magnetic fields are obtained self-consistently from a global MHD model for a given IMF condition, that the resulting energy gain of a few keV is quantitatively consistent with the observed temperature of the CPS, and that the distribution functions in various regions can be determined in relation to the global system.

In our model, the fields are based on ideal MHD, so that the electric field at the X line vanishes. In addition, the struc-

ture of the X line in our model is influenced by numerical diffusion. Thus we expect these deviations from reality to be greatest in the immediate vicinity of the neutral line. However, the particles need not cross the neutral line itself to gain energy. In fact, we found that few particles actually pass through the immediate vicinity of the X line. This is because the  $\mathbf{E} \times \mathbf{B}$  drift tends to divert particles away from the X line and the particle confinement time is short [e.g., Stern, 1979; Wagner *et al.*, 1981]. The hot component of the distribution functions described in Figure 4 primarily results from the usual current sheet acceleration as described above. Thus, in our model, the X line is the location of particle entry, but its precise structure does not significantly alter the accelerated component of the resulting distribution functions. Energy gain in this mechanism is determined by the  $y$  traversal near the midplane where the magnetic field is weak and  $E_y$  is significant. The orbit in Figure 6 has a  $y$  excursion distance of approximately  $1 R_E \sim 6.4 \times 10^8$  cm near the midplane at  $x \approx -36$  where  $E_y \sim 0.4$  mV/m. This gives the energy gain of roughly 2.5 keV. The initial particle kinetic energy (200 eV in this study) is a small fraction of the net energy gained so that the hot component of the distribution function is insensitive to the initial energy. Note that the MHD simulation fields, as well as the fields encountered by GALILEO [Frank *et al.*, 1994], are not smooth, so that the results are evidently dependent on the macroscopic properties of the fields integrated over particle trajectories rather than on local details. We argue that the existence of two-component distribution functions and the energy gain of the order of keV are robust.

To assess the relative contribution to energization by the X line itself, we have examined the number of particles crossing the plane at  $x = -32$  bounded by  $z = \pm 1 R_E$  and found that approximately 5% of all injected particles cross this planar region. These particles include those that do not approach the X line further. Such particles do not gain significant amounts of energy unless they subsequently cross the midplane some

distance away from the  $X$  line. Because the MHD simulation resolution does not allow us to examine a much smaller region around the  $X$  line, we conclude that, at most, 5% of particles randomly injected in our simulation could have experienced significant energization at the  $X$  line per se. In actuality, this is an optimistic upper bound because we were unable to find examples of orbits that gained most of their energy in the immediate vicinity of the  $X$  line.

It is interesting to note that non-Maxwellian, multicomponent distributions are generated during the energization process. The key reason is that the nonlocal motion of charged particles can take them along different paths, so that particle populations are segregated in energy and space, as illustrated in Figure 5. In the magnetosphere the typical distribution function has the form of a  $\kappa$  function with a nearly Maxwellian low-energy component and a power law high-energy component [Christon *et al.* 1989]. In our simulation, inadequate statistics prevent us from making quantitative conclusions, but the simulated distributions shown in Figures 4a–4d, which contain accelerated components, drop off more slowly than Maxwellian at the higher energies, while the distribution function in Figure 4d, which contains little accelerated component, is more nearly Maxwellian. Our results suggest that, independently of the precise acceleration site(s) and mechanisms, the multicomponent structure is a reflection of the nonlocal motion of particles following different paths and experiencing different amounts of acceleration before arriving at a given point of observation. Furthermore, if acceleration near an  $X$  line and in the current sheet contributes a significant amount of particle energy, the power law component may exhibit a  $z$  dependence similar to that shown in Figure 5, decreasing in relative importance toward the lobes.

The ion distribution functions in Figure 4 are qualitatively similar to those discussed by Onsager *et al.* [1991, Figure 4], having a cold component and a hot component with the hot component decreasing as  $|z|$  increases toward the lobes. Our work supports the conclusion of Onsager *et al.* that the cold component consists of those particles that simply  $\mathbf{E} \times \mathbf{B}$  drift across the separatrix while the hot component consists of those that cross the midplane. The specific process invoked is that only particles with particular  $v_{\parallel}$  values can reach a given point of observation while executing equatorward drifting motion (the velocity filter effect). This process, which is governed by the usual equation of motion, clearly segregates particles from any given source point. If the source has a large spatial extent in  $x$ , then an observer should intercept particles with a range of  $v_{\parallel}$  originating from the full spatial extent of the source. Figures 5 and 6 show that midplane-crossing (i.e., accelerated) particles can reach large  $z$  values. Thus, in addition to  $v_{\parallel}$ , the relative fraction of cold versus accelerated particles detected at a given point depends on the distance to and the spatial distribution of the source and on the field geometry.

### 3.2. Pressure Tensor

We have examined the kinetic pressure tensor for the test particle distributions defined by

$$P(x, z) = m \int (\mathbf{v} - \langle \mathbf{V} \rangle)(\mathbf{v} - \langle \mathbf{V} \rangle) f d^3 \mathbf{v}. \quad (2)$$

The pressure tensor is an important quantity because it determines the macroscopic force balance. For example, the pressure balance in current sheets has been discussed extensively; it was shown [Rich *et al.*, 1972] that a one-dimensional equilibrium current sheet must satisfy the marginal fire hose condition outside the current sheet,  $p_{\parallel}/p_{\perp} - 1 = B^2/4\pi$ , where the pressure tensor is taken to be anisotropic but diagonal. More recently, one-dimensional self-consistent test particle simulations have shown [Burkhart *et al.*, 1992; Holland and Chen, 1993] that  $x$ -independent equilibria with nonzero  $B_z$  exist and that the pressure tensor is generally nondiagonal in order to balance the Lorentz force  $J_y B_z$  inside the current sheet, while the usual marginal fire hose condition is satisfied outside the current sheet. The degree of nondiagonality and anisotropy depends on the input distribution functions. In an  $x$ -dependent system, the above marginal fire hose condition, which is a one-dimensional force balance requirement, may be modified. In particular, the force balance equation  $(1/c)J_y B_z - \partial p_{xx}/\partial x - \partial p_{xz}/\partial z = 0$  shows that a divergent tail ( $\partial p_{xx}/\partial x$ ) would reduce the requirement of nondiagonal elements and anisotropy. Fluidlike 2D magnetotail equilibria with isotropic pressure of the form  $p \propto |x|^{-\alpha}$  can be obtained [Bird and Beard, 1972]. Nevertheless, the recent observation of Frank *et al.* [1994] indicates that the plasma distribution is generally far from isotropic or Maxwellian.

These one-dimensional results assume uniform cross-tail electric field and are intended to model localized regions with high resolutions. For a more global model, the electric field should be determined to be consistent with a global structure. As mentioned earlier in section 3, this is because the Poynting vector  $(c/4\pi)\mathbf{E} \times \mathbf{B}$  describes the momentum and energy flux in the system. Our fields obtained from a global MHD simulation model represent a relatively stationary configuration with the macroscopic forces nearly balanced. The test particle distributions discussed above are determined by such fields but are not self-consistent in the sense of satisfying  $\mathbf{J} = (c/4\pi)\nabla \times \mathbf{B}$ . We have calculated the pressure tensor, using the test particle distribution functions, and Figure 7 shows the results in the coordinate system in which one axis is aligned with the local magnetic field. Figure 7a shows  $(p_{\parallel}/p_{\perp} - 1)$  where  $p_{\perp} = (p_{11} + p_{22})/2$  and  $p_{\parallel} = p_{33}$ . Figures 7b and 7c show  $p_{\parallel}$  and  $p_{\perp}$ , respectively. A comparison of Figure 3 and Figures 7b and 7c shows that the pressure enhancement in the current sheet is mainly due to the temperature enhancement but that there is a somewhat higher particle density. Nondiagonal pressure tensors have also been found by using Tsyganenko magnetic field [Horton *et al.*, 1993; Ashour-Abdalla *et al.*, 1993]. These calculations use large-scale two-dimensional fields but do not impose self-consistency in fields or currents.

Finally, we note that the electric and magnetic fields shown in Figure 1 are not smooth. Although the jaggedness in these MHD fields is primarily due to discreteness of the simulation cells, the real fields are not likely to be smooth over many Earth radii. We have also constructed distribution functions and velocity moments, using a smaller number of particles, and found no significant difference. Thus the two-component distribution functions obtained in our test particle calculations are evidently insensitive to the details of the fields and are expected to be a robust feature.

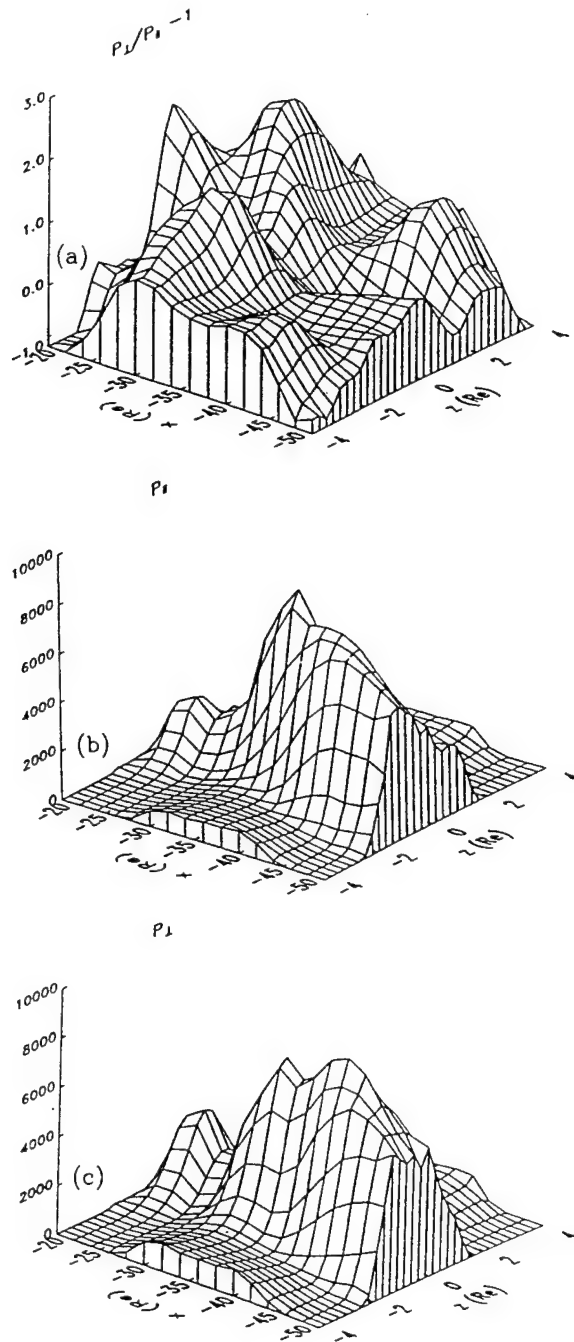


Figure 7. The diagonal pressure tensor elements. (a)  $P_{\perp}/P_{\parallel} - 1$  as a function of  $x$  and  $z$ . (b) Surface plot of  $P_{\parallel}$ . (c) Surface plot of  $P_{\perp}$ .

#### 4. Summary and Discussion

We have used the global framework provided by the Naval Research Laboratory (NRL) MHD simulation model to investigate charged particle dynamics and energization in the current sheet region of the magnetosphere during steady state reconnection near a neutral line. The main theme is to examine particle transport from the lobes to the CPS, energization

in the vicinity of the X line and current sheet, and the resulting particle distributions in the CPS. The key aspect of the work is that the global electric and magnetic fields, which connect the different regions of the model magnetosphere, are consistent with a given IMF condition, which is held constant at  $-5$  nT in the present work. The salient results are energization consistent with the observed CPS temperature and the formation of two-component distribution functions qualitatively resembling observed distribution functions. The two-component distribution functions and their spatial dependence are due to the nonlocal particle motion along different paths leading to a given point of observation. Although the magnetotail current sheet is not a region where the assumptions of the MHD model are satisfied, the general features of the larger system generated by the code are consistent with those expected in the magnetotail. In the collisionless magnetotail current sheet, scale sizes are determined by particle dynamics as governed by the global electric and magnetic fields and may be significantly less than those inferred from MHD. This suggests that one needs to develop a more self-consistent interaction between a kinetic current sheet with the larger system.

Detailed distribution function information can be obtained from particle tracking by using static fields from the MHD code. By analyzing selected orbits, we have determined that the largest energy gain occurs over a small portion of their orbits, namely, during crossings of the midplane ( $z = 0$ ). Energy gains tailward of the neutral line for the imposed southward IMF are of the order of a few keV while the energy gained by particles in the earthward direction is somewhat smaller because of the stronger magnetic field. In the tailward region, the distribution function divides naturally into two energy components, one for particles that have crossed the midplane and one for those that have not. The latter component remains cold.

In our calculations, the test particle results are not self-consistent with the fields. The present work is intended to be a first step toward a more comprehensive kinetic understanding of the global magnetosphere as determined by the solar wind. As such, we distinguish between our present "global kinetic" approach, in which the fields are determined self-consistently from a set of model (MHD) equations, from the previous "large-scale kinetic" approach, where the fields are not required to be consistent with model equations which constitute a "surrogate" global system to model the physical solar wind-magnetosphere interaction. We identify the self-consistent electric field, which is generally nonuniform, as a key quantity in determining particle distributions in a global system. From our experience, it appears that the three-dimensional MHD model can be used to track particles between various regions of the magnetotail, and can provide a basis to extend our knowledge of the role of charged particles in the formation of magnetosphere structure.

**Acknowledgments.** We would like to thank Joel Fedder and John Lyon for making the results of their study of the southward IMF case available to us. This work was supported by the National Aeronautics and Space Administration under grant W-16,991, the Office of Naval Research, and a grant of computer time from the DoD HPC Computer Center at the Naval Research Laboratory. The



work of D. L. Holland and J. B. Harold was performed as NRC/NRL Postdoctoral Research Associates.

The Editor thanks A. Otto and another referee for their assistance in evaluating this paper.

## References

- Ashour-Abdalla, M., J. Büchner, and L. M. Zelenyi, The quasi-adiabatic ion distributions in the central plasma sheet and its boundary layer, *J. Geophys. Res.*, **96**, 1601, 1991.
- Ashour-Abdalla, M., J. P. Berchem, J. Büchner, and L. M. Zelenyi, Shaping of the magnetotail from the mantle: Global and local structuring, *J. Geophys. Res.*, **98**, 5651, 1993.
- Behannon, K. W., Mapping of the Earth's bow shock and magnetic tail by Explorer 33, *J. Geophys. Res.*, **73**, 907, 1968.
- Bird, M. K., and D. B. Beard, The self-consistent geomagnetic tail under static conditions, *Planet. Space Sci.*, **20**, 2057, 1972.
- Birdsall, C. K., and A. B. Langdon, *Plasma Physics via Computer Simulation*, Adam Hilger, New York 1991.
- Birn, J., and M. Hesse, Particle acceleration in the dynamic magnetotail: Orbits in self-consistent three-dimensional MHD fields, *J. Geophys. Res.*, **99**, 109, 1994.
- Boris, J. P., Relativistic plasma simulation-optimization of a hybrid code, in *Proceedings of the Fourth Conference on Numerical Simulation of Plasmas*, pp. 3-67, Naval Research Laboratory, Washington, D. C., 1970.
- Burkhart, G. R., and J. Chen, Differential memory in the Earth's magnetotail, *J. Geophys. Res.*, **96**, 14,033, 1991.
- Burkhart, G. R., J. F. Drake, and J. Chen, Magnetic reconnection in collisionless plasmas: Prescribed fields, *J. Geophys. Res.*, **95**, 18,833, 1990.
- Burkhart, G. R., J. F. Drake, and J. Chen, The structure of the dissipation region during magnetic reconnection in collisionless plasma, *J. Geophys. Res.*, **96**, 11,539, 1991.
- Burkhart, G. R., J. F. Drake, P. B. Dusenbery, and T. W. Speiser, A particle model for the magnetotail neutral sheet equilibria, *J. Geophys. Res.*, **97**, 13,799, 1992.
- Chen, J., Nonlinear dynamics of charged particles in the magnetotail, *J. Geophys. Res.*, **97**, 15,011, 1992.
- Chen, J. and P. J. Palmadesso, Chaos and nonlinear dynamics of single-particle orbits in a magnetotail-like magnetic field, *J. Geophys. Res.*, **91**, 1499, 1986.
- Chen, J., G. R. Burkhart, and C. Y. Huang, Observational signatures of nonlinear magnetotail particle dynamics, *Geophys. Res. Lett.*, **17**, 2237, 1990a.
- Chen, J., H. G. Mitchell, and P. J. Palmadesso, Differential memory in the trilinear model magnetotail, *J. Geophys. Res.*, **95**, 15,141, 1990b.
- Christon, S. P., D. J. Williams, D. G. Mitchell, L. A. Frank, and C. Y. Huang, Spectral characteristics of plasma sheet ion and electron populations during undisturbed geomagnetic conditions, *J. Geophys. Res.*, **94**, 13,409, 1989.
- Cowley, S. W. H., A note on the motion of charged particles in one-dimensional magnetic current sheet, *Planet. Space Sci.*, **26**, 539, 1978.
- Curran, D. B., and C. K. Goertz, Particle distributions in a two-dimensional reconnection field geometry, *J. Geophys. Res.*, **94**, 272, 1989.
- Curran, D. B., C. K. Goertz, and T. A. Whelan, Ion distributions in a two-dimensional reconnection field geometry, *Geophys. Res. Lett.*, **14**, 99, 1987.
- DeCoster, D., and L. A. Frank, Observations pertaining to the dynamics of the plasma sheet, *J. Geophys. Res.*, **84**, 5099, 1979.
- Doxas, I., W. Horton, K. Sandusky, T. Tajima, and R. Steinolfson, Numerical study of the current sheet and PSBL in a magnetotail model, *J. Geophys. Res.*, **95**, 12,033, 1990.
- Fedder, J. A., and J. G. Lyon, Reconnection voltage as a function of IMF clock angle, *Geophys. Res. Lett.*, **18**, 1047, 1991.
- Fedder, J. A. and J. G. Lyon, The Earth's magnetosphere is 165  $R_E$  long: Self-consistent currents, convection, magnetospheric structure and processes for northward interplanetary magnetic field, *J. Geophys. Res.*, **100**, 3623, 1995.
- Fedder, J. A., J. G. Lyon, S. P. Slinker, and C. M. Mobarry, Topological structure of the magnetotail as a function of interplanetary magnetic field direction, *J. Geophys. Res.*, **100**, 3613, 1995.
- Frank, L. A., W. R. Paterson, and M. G. Kivelson, Observations of nonadiabatic acceleration of ions in Earth's magnetotail, *J. Geophys. Res.*, **99**, 14,877, 1994.
- Holland, D. L., and J. Chen, On chaotic conductivity in the magnetotail, *Geophys. Res. Lett.*, **19**, 1231, 1992.
- Holland, D. L., and J. Chen, Self-consistent current sheet structures in the quiet-time magnetotail, *Geophys. Res. Lett.*, **20**, 1775, 1993.
- Horton, W., and T. Tajima, Decay of correlations and the collisionless conductivity in the geomagnetic tail, *Geophys. Res. Lett.*, **17**, 123, 1990.
- Horton, W., and T. Tajima, Collisionless conductivity and stochastic heating of the plasma sheet in the geomagnetic tail, *J. Geophys. Res.*, **96**, 15,811, 1991.
- Horton, W., L. Cheung, J.-Y. Kim, and T. Tajima, Self-consistent plasma tensors from the Tsyganenko magnetic field models, *J. Geophys. Res.*, **98**, 17,327, 1993.
- Huang, C. Y. and L. A. Frank, Magnitude of  $B_z$  in the neutral sheet of the magnetotail, *J. Geophys. Res.*, **99**, 73, 1994.
- Karimabadi, H., P. L. Pritchett, and F. V. Coroniti, Particle orbits in two-dimensional equilibrium models for the magnetotail, *J. Geophys. Res.*, **95**, 17,153, 1990.
- Lyons, L. R., and T. W. Speiser, Evidence of current sheet acceleration in the geomagnetic tail, *J. Geophys. Res.*, **87**, 2276, 1982.
- Martin, R. F., and T. W. Speiser, A predicted energetic ion signature of a neutral line in the geomagnetic tail, *J. Geophys. Res.*, **93**, 11,521, 1988.
- Moses, R. W., J. M. Finn, and K. M. Ling, Plasma heating by collisionless magnetic reconnection: Analysis and computation, *J. Geophys. Res.*, **98**, 4013, 1993.
- Onsager, T. G., M. F. Thomsen, J. T. Gosling, and S. J. Bame, Electron distributions in the plasma sheet boundary layer: Time-of-flight effects, *Geophys. Res. Lett.*, **17**, 1837, 1990.
- Onsager, T. G., M. F. Thomsen, R. C. Elphic, and J. T. Gosling, Model of electron and ion distributions in the plasma sheet boundary layer, *J. Geophys. Res.*, **96**, 20,999, 1991.
- Rich, F. J., V. M. Vasyliunas, and R. A. Wolf, On the balance of stresses in the plasma sheet, *J. Geophys. Res.*, **77**, 4670, 1972.
- Sato, T., H. Matsumoto, and K. Nagai, Particle acceleration in time-developing magnetic reconnection process, *J. Geophys. Res.*, **87**, 6089, 1982.
- Scholer, M., and F. Jamitzky, Plasmoid-associated energetic ion bursts in the deep magnetotail: Numerical modeling of the boundary layer, *J. Geophys. Res.*, **94**, 2459, 1989.
- Sonnerup, B. U. Ö., Adiabatic particle orbits in a magnetic null sheet, *J. Geophys. Res.*, **76**, 8211, 1971.
- Stern, D. P., The role of O-type neutral lines in magnetic merging during substorms and solar flares, *mm J. Geophys. Res.*, **84**, 63, 1979.
- Tsyganenko, N. A., A magnetospheric magnetic field model with a warped tail current sheet, *Planet. Space Sci.*, **37**, 5, 1989.
- Wagner, J. S., P. C. Gray, J. R. Kan, T. Tajima, and S. I. Akasofu, Particle dynamics in reconnection field configurations, *Planet. Space Sci.*, **29**, 391, 1981.

J. Chen, J. B. Harold, G. Joyce, and S. Slinker, Naval Research Laboratory, Code 6790, Washington, DC 20375.

D. L. Holland, Physics Department, Illinois State University, Normal, IL 61761.

(Received December 6, 1994; revised February 27, 1995; accepted March 20, 1995.)

## COMMENTS

Comments refer to papers published in *Physics of Plasmas* and are subject to a length limitation of two printed pages. The Board of Editors will not hold itself responsible for the opinions expressed in the Comments.

### Comment on "Physics of the magnetotail current sheet" [Phys. Fluids B 5, 2663 (1993)]

G. R. Burkhart, P. B. Dusenbery, and T. W. Speiser

APAS Department, University of Colorado and NOAA Space Environment Laboratory, Boulder, Colorado 80303

(Received 16 September 1993; accepted 10 November 1993)

The purpose of this Comment is to correct the discussion given in Ref. 1 (Sec. III B) on the "current sheet catastrophe."<sup>2</sup> In Ref. 1 it is stated that in Ref. 2, no current sheet equilibria could be found in the regime of  $v_D \ll v_T$ , and that Ref. 2 attributed this to a catastrophic loss of equilibrium. It was then implied that because Ref. 3 found equilibria in the regime  $v_D \ll v_T$ , the authors of Ref. 2 were incorrect in their conclusion. In fact, in Ref. 2, it was a different parameter,  $\kappa_A$  (defined below) rather than  $v_D/v_T$  that controlled the current sheet catastrophe, and a physical explanation of the current sheet catastrophe in terms of previously published results was given. Furthermore, in Ref. 2, configurations with  $v_D/v_T \ll 1$  were found, and many of the results which were attributed to Ref. 3 by Ref. 1 had already been discussed in Ref. 2. In the following, we give a brief description of the current sheet catastrophe including the relevance and definition of the parameter  $\kappa_A$ . We then comment in more detail upon the discussion in Ref. 1 on the current sheet catastrophe.

For this discussion, it is useful to consider an example of a current sheet magnetic field,  $B_x = B_0 \tanh(z/a)$ ,  $B_z = \text{const.}$ , and  $B_y = 0$ . The Hamiltonian describing particle motion in the above configuration can be written as follows:<sup>4</sup>

$$1 = \tilde{p}_x^2 + \tilde{p}_z^2 + \{\tilde{a}^2 \ln[\cosh(\tilde{z}/\tilde{a})] - \kappa \tilde{x}\}^2, \quad (1)$$

where  $\tilde{a} = (a/\rho_0)^{1/2}$  [ $\rho_0 = v/\Omega_0$ , where  $\Omega_0 = eB_0/mc$ ,  $v = (2E/m)^{1/2}$ , and  $E$  is the particle energy],  $\kappa = (R/\rho_0)^{1/2}$  ( $R = aB_z/B_0$  is the field-line radius of curvature at  $z=0$  and  $\rho_0 = v/\Omega_0$ , where  $\Omega_0 = eB_z/mc$ ),  $\tilde{x} = x/(a\rho_0)^{1/2}$ ,  $\tilde{z} = z/(a\rho_0)^{1/2}$ ,  $\tilde{p}_x = d\tilde{x}/dt$  and  $\tilde{p}_z = d\tilde{z}/dt$  ( $t = \Omega_0 t$ ). While many normalization schemes can be chosen, the Hamiltonian must depend on at least two parameters that are related to  $\tilde{a}$  and  $\kappa$ . For example, the parameters  $\tilde{H}$  and  $b_n$  used in Ref. 1 are related to  $\tilde{a}$  and  $\kappa$  through  $\kappa = (2\tilde{H})^{-1/4}$  and  $\tilde{a} = b_n(2\tilde{H})^{-1/4}$ . The advantage of the normalization scheme given above is that for small  $\tilde{z}$  the Hamiltonian no longer depends upon  $\tilde{a}$ . This same advantage holds for the normalization used in Ref. 1 with respect to the parameter  $b_n$ . Because the small  $\tilde{z}$  regime usually controls the interaction with the current sheet, previous researchers have suggested that the parameter  $\kappa$  (or else  $\tilde{H}$ ) is most relevant to the particle motion.<sup>4</sup>

In Ref. 1, it is stated that  $\kappa \rightarrow 0$  is not an integrable limit. On the contrary, it is easy to see that in the above Hamiltonian,  $\kappa \rightarrow 0$  removes the  $x$  dependence, which causes motion in the Hamiltonian to become globally integrable.

A further advantage of the normalization given above is that  $\tau_x/\tau_z$  scales with  $\kappa$ ,<sup>4</sup> where  $\tau_z$  is the time scale of motion along  $z$  and  $\tau_x$  is the time scale for motion in the  $x$ - $y$  plane. For either small or else large values of  $\kappa$ , the two motions are decoupled and an adiabatic invariant is approximately conserved. Also, the ratio between the two time scales is manifested in the resonance energies<sup>1,5</sup> which satisfy the equation  $N = 0.84/\kappa - 0.6$  with  $N$  an integer. For  $\kappa < 1$ , all particle trajectories other than trapped, integrable orbits can be decomposed into sequential segments of crossing and noncrossing (of  $z=0$ ) motion. The number of half-oscillations of the fast  $z$  motion during a crossing segment is greater than  $N$ . For  $\kappa \geq 1$ ,  $N$  is less than one and particles cease their oscillation near  $z=0$ . For  $\kappa > 1$ , motion is the usual guiding center motion. It has been suggested that the particle trajectories are most chaotic near  $\kappa \sim 1$  because the two time scales are commensurate in that regime,<sup>4</sup> but this view has been recently questioned.<sup>6</sup> Regardless of the final resolution of the chaos question, the fact remains that near  $\kappa \sim 1$  (or else  $\tilde{H} \sim 1$ ) the character of untrapped particle trajectories changes; motion near  $z=0$  is oscillatory for  $\kappa < 1$  but it is not oscillatory for  $\kappa > 1$ . We have suggested that this change in the character of particle trajectories will result in the current sheet catastrophe described below.

In the presence of  $E_y \neq 0$ , equilibrium current sheet configurations can often be found, even under the assumption of uniformity in the  $x$  and  $y$  directions. If the incoming portion of the distribution function is specified to be a drifting Maxwellian, then the configuration is controlled by two parameters: the normalized drift velocity  $\tilde{v}_D = cE_y/B_z v_T$  and the normalized magnetic field  $B_z = B_0/(4\pi n_0 m_i v_T^2)^{1/2}$ , where  $n_0$  is the number density outside of the current sheet and  $v_T$  is the thermal spread of the injected Maxwellian. For an equilibrium, two magnetic forces must be balanced self-consistently by the particle motion: the field-line tension force,  $B_z(\partial B_x/\partial z)/4\pi$ , in the positive  $x$  direction and the gradient of the magnetic pressure  $(\partial B_x^2/\partial z)/8\pi$  which is directed toward the current

sheet center. The first of the two forces is balanced by the ejection along field lines of ions that were accelerated by the electric field within the current sheet. Equating these two forces results in the relation  $\hat{v}_D \approx B_0 / (4\pi n_0 m_i v_T^2)^{1/2}$  if it is assumed that pitch-angles are conserved in the deHoffmann-Teller frame.<sup>7,8</sup> Pitch-angle scattering due to the current sheet interaction can reduce the current somewhat.<sup>2</sup>

In Ref. 2, the parameter  $\kappa_A$  was defined to be the value of  $\kappa$  corresponding to ions of average energy:

$$\kappa_A = \frac{1}{(2\hat{E}_A)^{1/4}} \frac{\hat{B}_z}{|\hat{j}_0|^{1/2}}, \quad (2)$$

where  $\hat{E}_A = \int d^3v f(v) (v/v_T)^2$  and  $|\hat{j}_0|$  is the magnitude of the current density at the current sheet midplane normalized to  $en_0v_T$ . The drift velocity,  $\hat{v}_D$  primarily enters Eq. (2) through  $|\hat{j}_0|$ , with the current increasing for increasing  $\hat{v}_D$ .

In the regime of  $\kappa_A < 1$ , the magnetic pressure gradient can be balanced by the effective pressure due to the oscillation of the ions near the current sheet center. Equating these two forces results in the scaling for the current sheet thickness  $a \sim \hat{v}_D^{-4/3} \lambda_0$ , where  $\lambda_0 = c/\omega_{pi}$  outside the current sheet.<sup>8</sup> This scaling was verified by numerical calculation.<sup>2</sup>

On the other hand, if it is assumed that particles conserve magnetic moment exactly (i.e.,  $\kappa_A \gg 1$ ), a population of trapped particles must be included in the distribution function.<sup>9</sup> The necessity for trapped particles arises because magnetic moment invariant particles do not perform the oscillations in  $z$  required to balance the magnetic pressure (they do not set a length scale in the  $z$  direction).

Let us then assume an equilibrium in the  $\kappa_A < 1$  regime, and imagine quasistatically adjusting one of the controlling parameters,  $\hat{v}_D$  or  $\hat{B}_z$ , in such a way that  $\kappa_A$  increases. This can be accomplished by either reducing  $\hat{v}_D$  or else increasing  $\hat{B}_z$ . At some critical value of this controlling parameter, the value of  $\kappa_A$  will have increased to such a point that the particles no longer oscillate near  $z=0$ . Because the oscillation was required to balance the magnetic pressure, at this critical point the magnetic pressure will no longer be balanced and equilibrium will be lost.

In Ref. 2 it was discovered that no equilibria could be found for  $\kappa_A \gtrsim 0.7$ . In light of the forgoing considerations, it was suggested that this inability to find equilibria corresponds to a catastrophe, the physical basis for which is given above. Since  $\kappa_A$  depends upon both  $\hat{v}_D$  and  $\hat{B}_z$ , according to this suggestion, for any value of  $\hat{v}_D$ , some value

of  $\hat{B}_z$  can be found for which  $\kappa_A = 0.7$ . Likewise, if  $\hat{B}_z$  is fixed, the value of  $\hat{v}_D$  corresponding to the catastrophe will depend upon the value of  $\hat{B}_z$ .

In Ref. 1, it was incorrectly reported that in Ref. 2 no equilibria could be found with  $\hat{v}_D < 1$ . In fact, however, Ref. 2 reported equilibria with  $\hat{v}_D$  as small as 0.35. Furthermore, it was already shown in Ref. 2 that as  $\hat{v}_D$  was reduced below one with constant  $\hat{B}_z$ , the density enhancement at the center of the current sheet became negligible and that the current sheet thickened (see Fig. 5 of Ref. 2). The scaling for the current sheet thickness (given above) was verified numerically in Ref. 2.

These results were obtained for a small value of  $\hat{B}_z$  (0.1) so that even for  $\hat{v}_D = 0.35$ ,  $\kappa_A$  remained less than 0.4. For a larger value of  $\hat{B}_z$  (0.5), it was discovered that equilibria could not be found for  $\kappa_A > 0.7$ . The critical value of  $\hat{v}_D$  in this case was 1.2.

In Ref. 1, it is stated that in Ref. 2 the lack of equilibria arose because the input distributions were constrained to be drifting Maxwellians. The choice of the term constraint may be somewhat misleading because it implies that the catastrophe occurs because of overspecification. What is meant here is that, in Ref. 2, the boundary conditions were chosen such that the incoming portion of the distribution function is a drifting Maxwellian. We maintain that even in the case of a distribution function with a high-energy tail (as is chosen by Ref. 3) and a fixed value of  $\hat{v}_D$ , there will be some value of  $\hat{B}_z$  beyond which no equilibria can be found. Because  $\hat{B}_z$  is small, even though  $\hat{v}_D$  is small in the calculations of Ref. 3, the values of  $\kappa$  are significantly less than 0.7 for most particles in the distribution functions used and therefore it is expected that equilibria can be found. (Reference 3 did not publish values for  $\kappa_A$  or for any similar parameter, we arrive at the above numbers through estimates based on other published quantities.) Thus, in spite of the implication to the contrary in Ref. 1, the results of Ref. 3 do not contradict the conclusions of Ref. 2.

<sup>1</sup>J. Chen, Phys. Fluids B 5, 2663 (1993).

<sup>2</sup>G. R. Burkhart, J. F. Drake, P. B. Dusenberry, and T. W. Speiser, J. Geophys. Res. 97, 13, 799 (1992).

<sup>3</sup>D. L. Holland and J. Chen, "Self-consistent current sheet structures in the quiet-time magnetotail," submitted to Geophys. Res. Lett. (1992).

<sup>4</sup>J. Buchner and L. M. Zelenyi, J. Geophys. Res. 94, 11, 821 (1989).

<sup>5</sup>G. R. Burkhart and J. Chen, J. Geophys. Res. 97, 6479 (1992).

<sup>6</sup>J. Chen, J. Geophys. Res. 97, 15011 (1992).

<sup>7</sup>J. W. Eastwood, Planet. Space Sci. 20, 1555 (1972).

<sup>8</sup>T. W. Hill, J. Geophys. Res. 80, 4689 (1975).

<sup>9</sup>P. Francfort and R. Pellat, Geophys. Res. Lett. 3, 433 (1976).



# Reply to "Comment on 'Physics of the magnetotail current sheet' [Phys. Fluids B 5, 2663 (1993)]"

James Chen

Beam Physics Branch, Naval Research Laboratory, Washington, D.C. 20375

Daniel L. Holland

Department of Physics, Illinois State University, Normal, Illinois 61761

(Received 10 November 1993; accepted 12 November 1993)

The comment of Burkhart *et al.* seeks to disagree with a discussion given in Ref. 1 concerning Refs. 2 and 3. Reference 1 gives a brief review of the nonlinear particle dynamics in the magnetotail. Reference 2, hereafter referred to as BDDS, presented Vlasov current sheet solutions in the regime  $v_D/v_i \gtrsim 1$ , with discussions of a number of equilibrium properties in the regime  $v_D/v_i \lesssim 1$ . Here  $v_D \equiv cE_z/B_z$  and  $v_i$  is the ion thermal velocity. In the work of Holland and Chen,<sup>3</sup> hereafter referred to as HC, the explicit emphasis is on the regime  $\hat{v}_D \equiv v_D/v_i \ll 1$  because the quiet-time magnetotail typically has  $\hat{v}_D \ll 1$ . The solutions obtained in the regime  $\hat{v}_D \gtrsim 1$  are in agreement with those of BDDS. The equilibria in the  $\hat{v}_D \ll 1$  regime<sup>3</sup> are in good agreement with observations of quiet-time magnetotail.<sup>4</sup> Various similarities and differences are discussed at length by HC. In particular, HC found no evidence of the catastrophic loss of equilibrium conjectured to occur for  $\hat{v}_D \ll 1$  by BDDS. Burkhart *et al.*, which designation will refer to the comment as distinguished from BDDS, object to the discussion of this difference contained in Sec. III B of Ref. 1. The comment is not well founded, and there is no need for any changes to either the discussion given in the review paper or the original paper of Holland and Chen.

The comment has essentially two components. The first point is that BDDS obtained equilibrium solutions for  $\hat{v}_D$  as low as 0.35, below which no solution could be found. Burkhart *et al.* argue that  $\hat{v}_D = 0.35$  is in the  $\hat{v}_D \ll 1$  regime. Substantively, HC explicitly presented a solution for  $\hat{v}_D = 0.1$ , which is significantly smaller than the smallest critical  $\hat{v}_D$  value (0.35) given by BDDS and which is well within the regime where equilibria could not be found by BDDS. For our purposes here,  $\hat{v}_D \ll 1$  refers to values substantially smaller than those of BDDS. The two studies used similar test-particle simulation algorithms. The key difference is that the model of BDDS constrains the input distribution function to be a drifting Maxwellian parameterized by the drift velocity  $v_D$  while HC allow the input distribution function to have high-energy tail such as kappa function distributions. The observed distribution functions are typically well described by kappa function distributions.<sup>5</sup> This point is discussed explicitly by HC.

The second argument, which occupies the bulk of the comment, is essentially that the conjectured catastrophe is controlled by a parameter  $\kappa_A$  rather than  $v_D$  and that BDDS proposed a physical explanation based on a consideration of forces.<sup>6</sup> The discussion is simply a summary of the original paper with no new information. Neither argument is germane. The  $\kappa_A$  parameter essentially measures

the Larmor radius based on the thermal velocity in the  $B_z$  field in relation to the current sheet thickness. This quantity is determined after a converged solution is obtained. Thus it neither plays a role in the actual iteration procedure nor is it a specifiable control parameter. Each iteration consists of fixing the magnetic field, pushing particles through the fixed field, calculating the current density  $J_y$  on a finite grid, and finally obtaining the new magnetic field given by the current. This updated magnetic field is then used as the input field for the next iteration. The input distribution is parametrized by  $\hat{v}_D$ , which is the actual control parameter used by BDDS. Lack of converged solutions occurs in the iteration scheme when the successive iterations cannot match  $J_y$  and  $B$  field with sufficiently small fluctuations. As for the forces referred to by Burkhart *et al.*, they are not a part of the actual convergence criteria. Note that BDDS did not demonstrate that the lack of convergence can be identified as a catastrophe according to standard theory.<sup>7</sup>

The key issue is why this iteration scheme failed to converge. It was shown in HC (Figs. 2 and 3) that as  $\hat{v}_D$  is reduced with drifting Maxwellian or kappa function distributions, the diamagnetism contributes an increasing amount of current which is in the opposite direction from that given by  $\nabla \times B$ . The high-energy tail contributes mostly transient orbits<sup>8,9</sup> that counter the diamagnetic current, allowing equilibria to be formed in the current sheet geometry. The noise in the calculated current increases in relative magnitude to the total cross-tail current, rendering convergence more difficult or impossible.

It is interesting to note that HC constrained  $b_n \equiv B_z/B_x$ , where  $B_z$  is uniform and  $B_x$  is the asymptotic value while BDDS allowed  $B_x$  to decrease or  $b_n$  to increase as  $v_D$  is decreased. As  $\hat{v}_D$  is reduced, the cross-tail current decreases.<sup>3</sup> Holland and Chen increase this current  $J_y$  by introducing high-energy tails or field-aligned input distributions and determine the density by the self-consistency requirement. In contrast, BDDS allow  $B_x$  to decrease, reducing the required cross-tail current given by  $\nabla \times B$ . As a result, as  $\hat{v}_D$  is reduced, the field tends to the uniform  $B_z$  geometry. This limiting configuration is a possible equilibrium in which there is no net current (except for the source coil current, of course). The algorithms of HC and BDDS are not suited for studying nearly uniform magnetic-field configurations because the basic iteration scheme requires calculation of currents on finite grids, and the noise can overwhelm the weak current to which one attempts to converge.

sh  
ej  
th  
tw  
it  
de  
th  
so  
of  
As an explanation of the catastrophe, BDDS also invoked the conjecture<sup>10</sup> that the degree of chaos increases as  $\kappa \rightarrow 1$  and claimed that this causes the catastrophe. No actual casual relationship between exponential divergence (the defining attribute of chaos), catastrophe, and forces was established. Furthermore, this conjecture<sup>10</sup> is inconsistent with a quantitative calculation of the average exponential divergence rate (Fig. 16, Ref. 9). In contrast, HC related the effects of the high-energy tail and/or more field-aligned pitch-angle distribution in the input particle population to the well-known phase-space topology of the dynamical system.<sup>11</sup> Chaos *per se* plays no causal role.

w  
ol  
tr  
E  
c  
c  
l  
t  
t  
s  
s  
c  
f  
r  
c  
(  
The argument based on Eq. (1) of Burkhart *et al.* is mathematically incorrect: (1) the definition  $\bar{a} = b_n^{-1} \kappa$  (correcting for the erroneous power of  $b_n \neq 0$ ) shows that the  $z$ -dependent term in Eq. (1) vanishes as  $\kappa^2 \propto \bar{a}^2$ , faster than the  $x$ -dependent term, and (2) correcting the erroneous omission of  $\bar{a}^2$  multiplying  $\bar{p}_x^2$  and  $\bar{p}_y^2$ , Eq. (1) yields the manifestly incorrect relation  $l=0$  in the limit  $\kappa \rightarrow 0$  discussed by Burkhart *et al.* It has been shown that  $\kappa \rightarrow 0$  is an ambiguous limit and is not equivalent to the integrable limit  $B_n=0$ .<sup>9,11</sup>

Clearly, if a numerical iteration procedure does not converge, one has to first determine precisely why the actual iteration scheme fails. In summary, HC has given a quantitative and specific explanation for the lack of convergence in the  $\hat{v}_D \ll 1$  regime in terms of the diamagnetic current. If the diamagnetic current were calculated and found to remain small relative to the total current as the

"catastrophe" is approached, then there might be a substantive argument with respect to the published results of HC. Unfortunately, Burkhart *et al.* have not calculated the diamagnetic current, and the comment contains nothing new or substantive in response to this specific challenge. No "correction" of any kind in the discussion of Ref. 1 or HC is warranted.

## ACKNOWLEDGMENTS

We thank Dr. P. J. Cargill and Dr. J. B. Harold for useful discussions.

This work was supported by the National Aeronautics and Space Administration under Grant No. W-16,991 and the Office of Naval Research.

<sup>1</sup>J. Chen, *Phys. Fluids B* 5, 2663 (1993).

<sup>2</sup>G. R. Burkhart, J. F. Drake, P. B. Dusenbery, and T. W. Speiser, *J. Geophys. Res.* 97, 13799 (1992).

<sup>3</sup>D. L. Holland and J. Chen, *Geophys. Res. Lett.* 20, 1775 (1993).

<sup>4</sup>D. J. McComas, C. T. Russell, R. C. Elphic, and S. J. Bame, *J. Geophys. Res.* 91, 4287 (1986).

<sup>5</sup>S. P. Christon, D. J. Williams, D. G. Mitchell, L. A. Frank, and C. Y. Huang, *J. Geophys. Res.* 94, 13409 (1989).

<sup>6</sup>P. Francfort and R. Pellat, *Geophys. Res. Lett.* 3, 433 (1972).

<sup>7</sup>P. T. Saunders, *Catastrophe Theory, An Introduction to Catastrophe Theory* (Cambridge University Press, Cambridge, 1980).

<sup>8</sup>G. R. Burkhart and J. Chen, *J. Geophys. Res.* 96, 14033 (1991).

<sup>9</sup>J. Chen, *J. Geophys. Res.* 97, 15011 (1992).

<sup>10</sup>J. Büchner and L. M. Zelenyi, *J. Geophys. Res.* 94, 11821 (1989).

<sup>11</sup>J. Chen and P. J. Palmadesso, *J. Geophys. Res.* 91, 1499 (1986).

# KINETIC CURRENT SHEET EQUILIBRIA IN THE QUIET-TIME MAGNETOTAIL

Daniel L. Holland

Illinois State University, Normal, IL 61790-4560

James Chen

Naval Research Laboratory, Washington, DC 20375

## ABSTRACT

The structure of the quiet-time magnetotail is studied using a one-dimensional test particle simulation. Vlasov equilibria are obtained in the regime where  $v_D = E_y c / B_z$  is much less than the ion thermal velocity and are self-consistent in that the current and magnetic field satisfy Ampere's law. Ions are assumed to carry the current, and electrons are taken to form a neutralizing background contributing no current. Force balance between the plasma and magnetic field is satisfied everywhere. The source distribution of particles determines the current sheet structure. The particle density, the cross-tail current density, and nondiagonal pressure tensor are computed for different forms of source distribution functions. It is shown that distribution functions with high-energy tails such as the  $\kappa$  function and/or field-aligned anisotropies are essential for establishing equilibria. The previously identified role of diamagnetic current in determining the current sheet structure is quantified in detail.

## I. INTRODUCTION

The structure of the quiet-time magnetotail has been a long standing problem in space physics with the early work focusing on MHD equilibria [e.g., 1]. It is well established, however, that in the vicinity of the field reversal, the thermal ion gyroradius is on the order of the gradient scale length of the magnetic field, and hence MHD becomes an inadequate description of the plasma equilibrium. Thus, the exact ion dynamics must be accounted for properly. A frequently used kinetic model of the magnetotail magnetic field is the quasi-neutral sheet,

$$\mathbf{B} = B_0 F(z/\delta) \hat{\mathbf{x}} + B_z \hat{\mathbf{z}}. \quad (1)$$

Here  $B_0$  is the asymptotic magnetic field strength in the  $x$ -direction,  $B_z$  is a constant magnetic field normal to the current sheet,  $\delta$  is the scale length of the field reversal and  $F(z/\delta)$  is an odd function of  $z$  with  $F(z \rightarrow \pm\infty) = \pm 1$ . A particular example is the modified Harris neutral sheet with  $F(z/\delta) = \tanh(z/\delta)$ . In this model, particles are either trapped near the midplane (integrable orbits) or approach the midplane, interact with the current sheet and then leave (transient and stochastic orbits) [2]. Each of these classes of orbits occupy distinct regions of phase space which have boundaries that are impenetrable in the absence of "noise" (cf Figure 1). It has been suggested that an observable signature of the phase space partitioning would

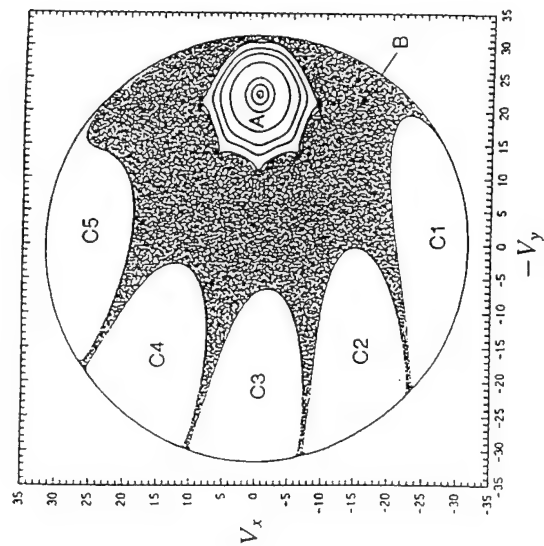


Figure 1. Poincaré surface of section map for  $b_n = 0.1$  and  $H = 500$  (adapted [21]). Region A is integrable, and region B is stochastic. Regions C1-C5 are the transient regions.

be peaks and valleys in the ion distribution function whose separation scales as  $H^{1/4}$  where  $H = (mv^2/2)/(mb_z^2\Omega_z^2\delta^2)$  is the normalized energy,  $b_z = B_z/B_0$ ,  $v$  is the velocity of the particle and  $\Omega_z$  is the cyclotron frequency in the constant  $B_z$  field. Such a signature has been observed in ISEE-1 data [3]. The significance of this result is that we are able to infer information about the global structure of the magnetotail from a single local satellite measurement. This is possible because the local particle distribution contains information about the entire orbital history of each of the individual ions, which in turn depends on the global structure of the magnetotail and the partitioning of phase space.

It is known that the integrable orbits cannot contribute to the total current, although they may modify the local current profile [4]. The transient and stochastic orbits, on the other hand, traverse a distance in the  $y$ -direction given by  $\Delta y \approx 2v/\Omega_z$  while interacting with the current sheet and thus contribute a net current. Here,  $v$  is the velocity of the particle and  $\Omega_z$  is the cyclotron frequency in the constant  $B_z$  field. We note however, that a transient orbit contributes far more to the cross-tail current than does a stochastic orbit since they both travel essentially the same distance across the tail but the transient does the traversal in much less time. For magnetic fields of the form of Eq. (1), a constant dawn to dusk electric field,  $E_y$ , may be removed

from the equations of motion by transforming into the deHoffman-Teller (dH-T) reference frame which moves towards the Earth with a speed  $v_D = E_y c/B_z$ . This transformation is not possible if  $B_z$  or  $E_y$  is spatially varying.

Previous authors [5-8] have calculated self-consistent current sheet profiles in the regime of large  $E_y$ , i.e.,  $v_D \gg v_{th}$ , where  $v_{th}$  is the ion thermal velocity. *Burkhardt et al.* [6] also examined the regime  $v_D \lesssim v_{th}$  and found that if  $v_D$  was made sufficiently small, their code could no longer find converged solutions. Coincident with their decrease of  $v_D$ , they found an increase in the value of  $\kappa = 2H^{-1/4}$  with a maximum value of  $\kappa \approx 0.7$  for their last converged solution. Based on this they invoked the conjecture that  $\kappa \approx 1$  results in maximum chaos of the system and that there is a resulting catastrophic loss of equilibrium. It should be noted that the quantity  $\kappa$  is not a control parameter for the system, but is only calculated after a given initial configuration has converged. In addition, objective measures of chaos (e.g. the exponential divergence rate of nearby orbits) indicate that  $\kappa \approx 1$  does not yield the maximum chaos [10].

*Holland and Chen* [8] found self-consistent equilibria in the regime  $v_D \ll v_{th}$ . They also found that if the input distribution does not have some minimum amount of field aligned anisotropy (e.g. a bulk drift or field aligned beams), the plasma diamagnetism becomes too large and the cross-tail particle current due to the meandering motion of the ions is insufficient to create the required field reversal. In such a case, no self-consistent equilibria may exist. Furthermore, the amount of field aligned anisotropy required was found to depend on  $b_z$ , with larger values of  $b_z$  requiring a larger anisotropy for convergence. (Note that larger values of  $b_z$  result in larger values of  $\kappa$ .) For nearly isotropic distributions, we have found that the increase in the relative importance of the diamagnetic current results in an increase in the numerical noise of the system, making convergence a more difficult process. Since *Burkhardt et al.* [6] failed to find convergence in the regime of large  $b_z$  with a nearly isotropic source distribution of particles, we believe that their failure to find equilibria is due to an increase in the diamagnetic current relative to the cross-tail particle current, rather than any chaotic effect.

A primary difference between the results of *Burkhardt et al.* [6] and those of *Holland and Chen* [8] is that *Burkhardt et al.* constrained the source distribution to be a drifting Maxwellian and fixed the value of the asymptotic density and the value of  $B_z$ . Thus when the drift velocity of the distribution function was decreased, the magnitude of the cross-tail current and hence the magnitude of the asymptotic value of  $B_z$  also decreased. This resulted in larger values of both  $b_z$  and  $\kappa$ . *Holland and Chen* on the other hand fixed the value of  $b_z$  and allowed the magnitude of the particle density to be determined so as to give the required cross-tail current for any given functional form of the source distribution of particles. A more detailed comparison of the results of *Holland and Chen* and those of *Burkhardt et al.* may be found in reference [11].

In this paper, we examine the relationship between the self-consistent current sheet profiles (e.g. plasma density, current density and pressure tensor) and the underlying phase space structures and particles sources.

## II. MODEL

We have developed a one-dimensional (1D) model of the current sheet in the quiet-time magnetotail. The electron contribution to the total cross-tail current is negligible with respect to the ion current and hence the electrons are simply regarded as a neutralizing background. A fully kinetic description of the ions is retained. The first velocity moment of the Vlasov equation gives,

$$\nabla \cdot (\mathbf{P} + m\mathbf{N}\mathbf{U}\mathbf{U} + \frac{B^2}{8\pi}\mathbf{I} - \frac{\mathbf{B}\mathbf{B}}{4\pi}) = 0 \quad (2)$$

where  $\mathbf{P} = m \int d\mathbf{v} (\mathbf{v} - \mathbf{U})(\mathbf{v} - \mathbf{U}) f(\mathbf{r}, \mathbf{v})$ ,  $\mathbf{N}\mathbf{U} = \int d\mathbf{v} \mathbf{v} f(\mathbf{r}, \mathbf{v})$  and  $N = \int d\mathbf{v} f(\mathbf{r}, \mathbf{v})$  are the pressure, flux and particle density,  $f(\mathbf{r}, \mathbf{v})$  is the ion distribution function and  $\mathbf{I}$  is the unit matrix. In 1D with only  $\partial/\partial z \neq 0$ , Eq. (2) becomes

$$P_{xz} - \frac{B_x B_z}{4\pi} = \text{const} \quad (3a)$$

$$P_{yz} - \frac{B_y B_z}{4\pi} = \text{const} \quad (3b)$$

$$P_{zz} + \frac{B_x^2 + B_y^2 - B_z^2}{8\pi} = \text{const.} \quad (3c)$$

Here we have used the continuity equation and the symmetry of the system to deduce that  $\mathbf{N}\mathbf{U}_z = 0$ .

An iterative technique is used to calculate the density, current and pressure profiles. A functional form for the source distribution of particles is chosen (e.g., Maxwellian or kappa distribution) and ion orbits are followed through a prescribed magnetic field of the form (1). The density and current for each particle are calculated by linearly interpolating the particle's position and velocity onto a grid at each time step. The total density, current density and pressure tensor elements are obtained by summing over the single particle contributions subject to appropriate normalizations. Ampere's law is used to obtain the field given by the current which is then used to calculate ion orbits for the next iteration. The process is repeated until the  $z$  integrated difference in the magnetic field energy between two successive iterations is negligible. A complete description of the numerical technique can be found in reference [12]. In practice, we use a relaxation technique in which we mix the old and new calculated magnetic fields. This is particularly important in the regime of  $v_D \ll v_A$  where glitches in the magnetic field are amplified in subsequent iterations by ion diamagnetism. We also include small-amplitude low-frequency pitch-angle scattering using a collision operator [13], which allows orbits to populate the integrable regions of phase space. A practical benefit is that inclusion

of scattering increases the rate of convergence to self-consistent equilibria. The resulting current sheet satisfies  $\nabla \times \mathbf{B} = (4\pi/c)\mathbf{J}$  and is insensitive to the amplitude of the scattering.

The physical particle density, current density and pressure tensor ( $N(z_m)$ ,  $\mathbf{J}(z_m)$ ,  $\mathbf{P}(z_m)$ ) are related to the corresponding calculated quantities ( $n(z_m)$ ,  $\mathbf{j}(z_m)$ ,  $\mathbf{p}(z_m)$ ) by

$$N(z_m) = (\eta/L^3)n(z_m), \quad \mathbf{J}(z_m) = (\eta q \Omega_0/L^2)\mathbf{j}(z_m) \\ \mathbf{P}(z_m) = (\eta m \Omega_0^2/L)\mathbf{p}(z_m)$$

where  $z_m$  is the  $m$ -th grid point,  $\eta$  is a scaling factor,  $L$  is a scale length,  $q$  is the charge of the particle,  $m$  is the particle mass and  $\Omega_0 = qB_0/mc$ .

By requiring the  $z$  integrated current density to produce the asymptotic field strength,  $B_0$ , it can be shown that [9]

$$\sigma = L/R_E = 0.036(\bar{n}/n_0)^{1/2} \quad (4a)$$

$$\frac{\eta q \Omega_0}{L^2} = 0.125(B_0/\sigma) n_A/m^2 \quad (4b)$$

$$\frac{\eta m \Omega_0^2}{L} = 7.97 \times 10^{-12} B_0^2 \text{ dyne/cm}^2 \quad (4c)$$

Here  $\bar{n}$  is the calculated density at the top grid point,  $B_0$  is in nT, and  $n_0$  is in  $\text{cm}^{-3}$ . Thus by selecting a source density, a distribution functional form,  $B_0$  and  $B_z/B_0$ , we self-consistently determine the equilibrium structure throughout the current sheet. In the cases shown below  $n_0 = 0.5 \text{ cm}^{-3}$ ,  $B_0 = 20 \text{ nT}$ , and  $B_z/B_0 = 0.1$ .

To fully understand the relation between the nonlinear particle dynamics and the magnetic field, we have developed a post-processing algorithm to separate the total magnetic field,  $\mathbf{B}$ , in the final converged solution into the part due to the particle currents,  $\mathbf{H}$ , and the part due to the diamagnetism of the plasma,  $4\pi\mathbf{M}$  [9]. The particle current is calculated using the guiding center position and velocity in regions where the guiding center is well defined (i.e., non-midplane crossing segments of the trajectories) and the actual particle position and velocity in regions where the guiding center is not well defined (i.e., midplane crossing segments of the trajectories). It is only this part of the current which contributes to the particle energization,  $\mathbf{J} \cdot \mathbf{E}$ . The magnetic field due to the diamagnetism of the plasma is calculated using the instantaneous magnetic moment of the particles only in the regions where the magnetic moment is well defined. The total magnetic field is simply  $\mathbf{B} = \mathbf{H} + 4\pi\mathbf{M}$ . We have found that for particles with pitch angles near  $\pi/2$  the magnetic field due to the particle's diamagnetism is larger in magnitude than the magnetic field due to the particle current and is in the opposite direction. Obviously, if the source distribution is dominated by such particles the resulting magnetic field will have the opposite sign of the assumed magnetic topology, and the system does not converge to a self-consistent solution.

### III. RESULTS

In this section we present some representative equilibrium current sheet profiles which serve to illustrate the relationships between source distribution function features (e.g., pitch-angle distribution and high energy tails), the phase space structure, and the underlying global topology of the magnetotail. As a general comment, we have found that the distribution functions with a high energy tail tend to converge to self-consistent equilibria much more easily than do Maxwellians. Hence we typically use kappa distributions in our work. Additionally, it should be noted that when we are discussing the nature of the source distribution function we may only specify that part of the distribution which is moving towards the field reversal region. The part which is moving away from the field reversal region is self-consistently determined by particles which have interacted with the current sheet. Thus, if for instance we say that the source distribution is an isotropic Maxwellian, we are only referring to the incoming portion of the distribution and not the whole distribution.

**Case 1.** The incoming source of particles for this case is taken to be a kappa distribution ( $\kappa = 4.5$ ) with a bulk drift in the tailward direction (due to the shift into the dH-T frame) of  $v_D = 0.1 v_{th}$ . (Since  $B_z/B_0 = 0.1$ , the actual  $E \times B$  drift velocity in the Earth's frame is only 1 percent of  $v_{th}$ .) The distribution function is modeled using 80 equally spaced energy shells up to  $3.3T$  with 200 particles per shell. Here  $T$  is the normalized thermal energy of the incoming distribution. In Figure 2 we show the density, current, magnetic field and pressure tensor profiles. Figure 3 shows the degree to which local pressure balance is maintained, i.e., the degree to which the equilibrium conditions, Eqs. (3a)–(3c), are satisfied. Defining the temperature as  $P = nT$ , where  $P$  is the average magnitude of the diagonal elements of  $\mathbf{P}$  in the asymptotic regime, we find a value of  $T \approx 28$  keV. The single temperature is to be regarded as an approximate measure of the internal energy because the perpendicular and parallel temperatures are not equal.

Note that the density and the diagonal elements of  $\mathbf{P}$  only vary by  $\sim 10$  percent across the sheet and that the sheet thickness is on the order of a half of an Earth radius ( $R_E$ ). This is consistent with the observations of *McComas et al.* [14] and is in contrast to the solutions in the regime of large  $v_D$  [5–8]. (Typically the observations of *McComas et al.* [14] have  $b_n > 0.1$  which results in a thicker current sheet. cf case 5)

As an interesting exercise, we have fit a modified Harris magnetic field to the self-consistent calculated field with the result  $B = 20 \tanh(z/0.14R_E)nT$  (Figure 4). We note that the agreement between the two fields is quite good, even though the modified Harris model is not a true equilibrium field except in the limit of  $b_n = 0$ . The primary difference between the fields is a slight increase in the magnetic field energy at the edge of the field reversal regions (Points A and B in Figure 4). Additionally, using the calculated magnetic field data, we have plotted the surface of section for  $H = 500$ . (Figure 5) (For the parameters we are using this corresponds to the 500 eV energy level.) This should be compared with Figure 1 which is the same surface of section calculated using the modified Harris model.

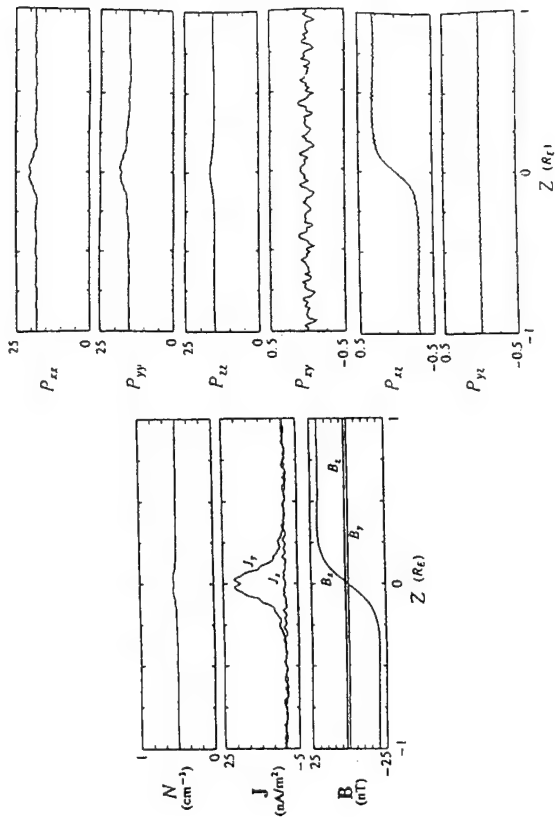


Figure 2. Self-consistent density, current, magnetic field and pressure tensor profiles calculated using a kappa distribution ( $\kappa = 4.5$ ) with a bulk drift in the tailward direction of  $v_D = 0.1 v_{th}$ . The units on the pressure tensor elements are nanodyne/cm<sup>2</sup>.

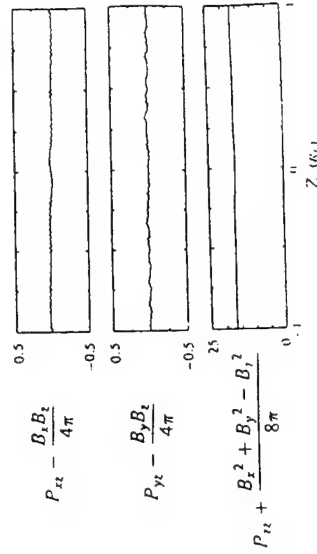


Figure 3. Plot of the left hand side of equations 3 a-c using the results depicted in Figure 2. Since all three curves are essentially flat, we see that pressure balance is maintained to a high degree of accuracy.



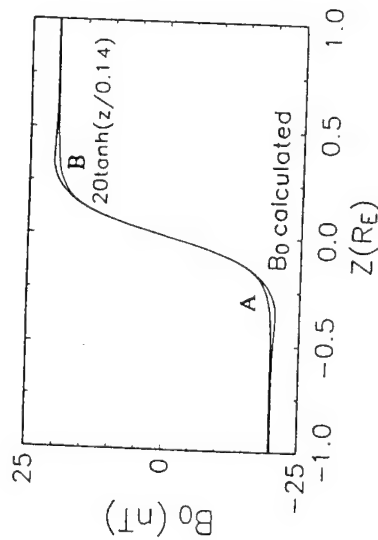


Figure 4. Comparison of the self-consistent field from case 1 with a "best fit" Harris-field.

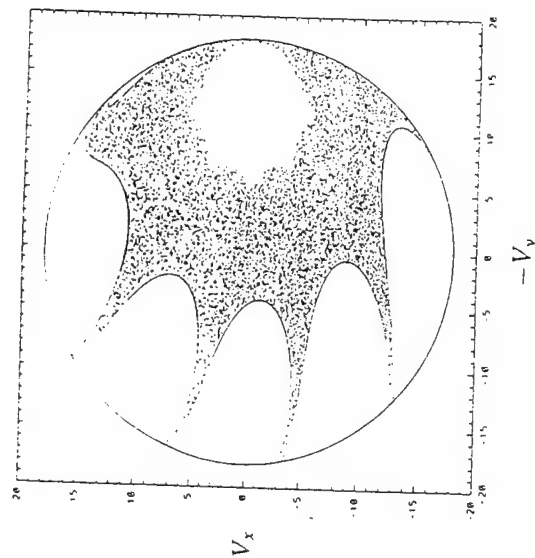


Figure 5. Poincaré surface of section map for  $b_n = 0.1$  and  $H = 500$ , calculated using the self-consistent field for case 1.

The only noticeable difference between Figures 1 and 5 is a slight "tweak" near the end of the "fingers" of the stochastic region. We believe that this is caused by the presence of a small y-component in the self-consistent magnetic field. One should note, however, that in this case the boundary between the stochastic and transient regions does not correspond to orbits with pitch angle  $\pi/2$  in the asymptotic region as it does in the modified Harris model. Rather it correspond to orbits with pitch angle  $\pi/2$  at the field energy maximum (Points A and B in Figure 4).

*Case 2.* Here we use an isotropic ( $v_D = 0$ ) kappa distribution ( $\kappa = 4.5$ ) as the bulk of the source distribution. In addition we have added a high energy beam which comprises five percent of the total density and which is modeled as a drifting  $v_D = 1$ ) kappa distribution ( $\kappa = 4.5$ ) and which has a thermal energy of one half of the bulk distribution. The bulk distribution function is modeled using 80 equally spaced energy shells up to  $3.37$  whereas the beam component is modeled using 20 equally spaced energy shells with thermal energies up to  $3.37T_b$  where  $T_b$  is the thermal energy of the beam. Each energy shell contains 200 particles. In Figure 6, we again show the equilibrium density, current, magnetic field and pressure tensor profiles. Although not shown, the equilibrium again satisfies pressure balance to a high degree of accuracy. Again defining  $P = nT$  we have  $T \approx 36$  keV. The most significant aspect of these results is that there is a broadening of the current sheet to the extent that it is now  $\sim 1R_E$  in thickness. We also note that the negative current at the edge of the current sheet has increased in magnitude and that there are corresponding peaks in the magnetic field energy at these locations. We mention in passing that if the beam density is reduced much below the value used in this particular data set, we are unable to obtain converged solutions due to the large diamagnetic current of the bulk distribution. At the present time it is not clear whether or not one may obtain self-consistent equilibria with completely isotropic source distributions or whether one needs a certain degree of anisotropy (due to either bulk drifts or beams). We have found that converged solutions may be obtained with smaller anisotropies for smaller values of  $b_n$ . This is consistent with the analysis of *Holland and Chen* [12].

*Case 3.* The initial incoming distribution function for this case is taken to be a Maxwellian with a bulk drift in the tailward direction of  $v_D = 0.1 v_{th}$  with a high energy isotropic tail which comprises 10 percent of the total density. The bulk distribution function is modeled using 80 equally spaced energy shells up to  $3.37$  whereas the tail component is modeled using 17 equally spaced and equally weighted energy shells with energies between  $2T$  and  $2.7T$ . Each energy shell contains 200 particles. In Figure 7 we show the density, current and magnetic field profiles. In addition, using the algorithm described above, we have separated the magnetic field into the part due to the plasma diamagnetism, and the part due to the cross-tail "meandering" motion of the ions. Although not shown, the pressure tensor once again satisfies local force balance. The "temperature" in this case is  $T = 9$  keV. The interesting feature of these results is that at this low drift velocity with an isotropic source of particles, the plasma diamagnetism cancels  $\sim 85\%$  of the field created by the cross-tail ion current. If  $v_D$  is made smaller, a larger fraction

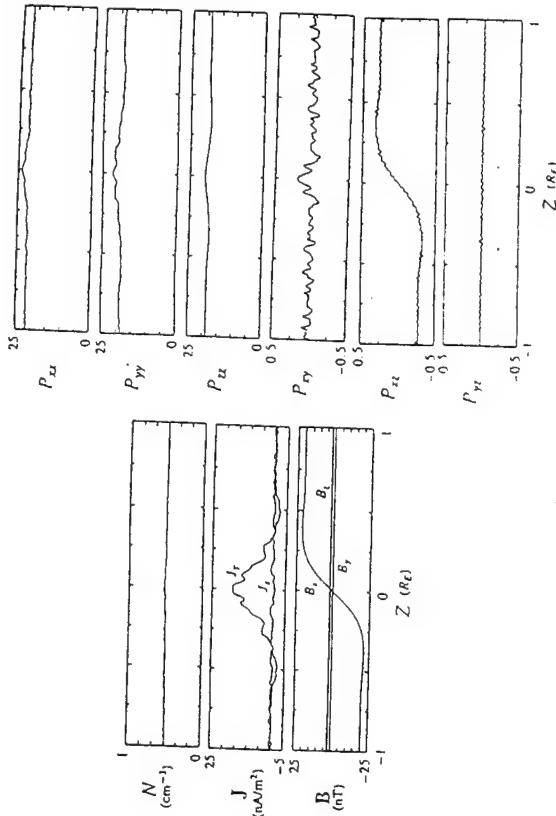


Figure 6. Self-consistent density, current, magnetic field and pressure tensor profiles calculated using an isotropic kappa distribution ( $\kappa = 4.5$ ) with a beam which comprises 5% of the total density. The beam is modeled using a drifting ( $v_D = v_{th}$ ) kappa distribution ( $\kappa = 4.5$ ) with a thermal temperature of one half that of the bulk distribution. The units on the pressure tensor elements are nanodyne/cm<sup>2</sup>.

of the field created by the cross-tail ion current is canceled by the diamagnetism.   
**Case 4.** Here we use a Maxwellian distribution with a tailward bulk drift of  $v_D = 2 v_{th}$ . The distribution function is modeled using 80 equally spaced energy shells up to  $3.3T$  with 200 particles per shell. Figures 8 shows the density, current, magnetic field and the break down of the magnetic field into the diamagnetic and cross-tail current portions of the converged solution (which again satisfies force balance conditions, Eqs.(3a)–(3c)). The most significant aspects of these results are that the current sheet thins down to approximately  $0.1R_E$  and that the particle density near the midplane increases to over three times the asymptotic density. The “temperature” in this case is  $T = 2 \text{ keV}$ .

These results are in agreement with those of *Burkhart et al.* [6] based on drifting Maxwellian source distributions with  $v_D \gg v_{th}$  and differ from the quiet-time structures inferred by *McComas et al.* [14]. Due to the large value of  $v_D$ , the majority of the particles have pitch angles nearly field aligned (anti-field aligned) and hence we would not expect a large diamagnetic field. This is indeed the case

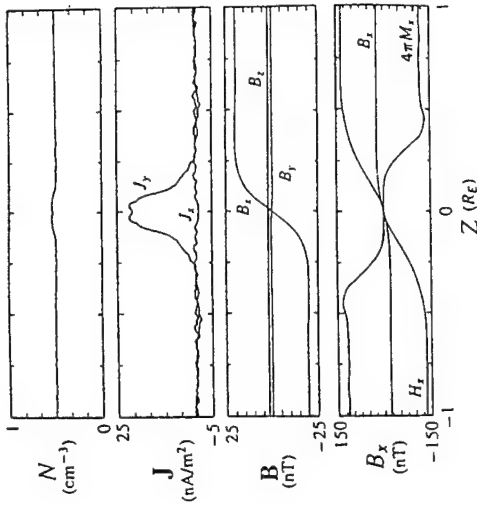


Figure 7. Self-consistent density, current and magnetic field profiles calculated using a Maxwellian with a bulk drift in the tailward direction of  $v_D = 0.1 v_{th}$  and a high energy isotropic tail which comprises 10 percent of the total density.

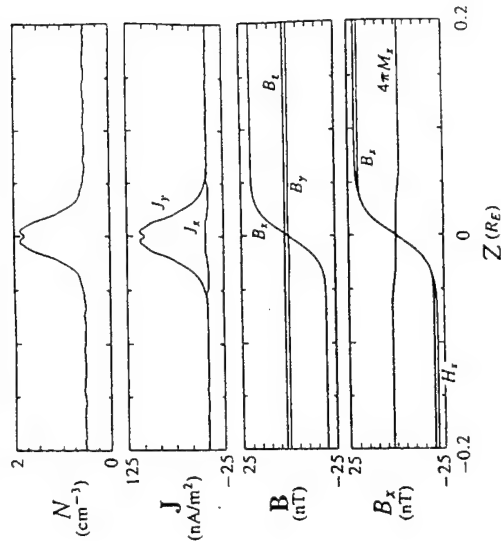


Figure 8. Self-consistent density, current and magnetic field profiles calculated using a Maxwellian source distribution of particles with a bulk drift in the tailward direction of  $v_D = 2 v_{th}$ .



as can be seen in Figure 8d which shows only a small difference between  $B_x$  and  $H_x$ . The current sheet is much thinner because field aligned particles are primarily of the Speiser (transient) type and have small velocities, and hence small amplitude oscillations, in the  $z$  direction near the midplane. This is demonstrated by the surface of section in Figure 9 showing that particles which are nearly asymptotically field aligned intersect the midplane with small  $v_z$ .

Note that for a given value of  $B_0$  a thinner current sheet leads to a greater current density,  $J_y$ . A thin current sheet is more unstable to the collisionless tearing mode [15] and may be more susceptible to other forms of disruption [16].

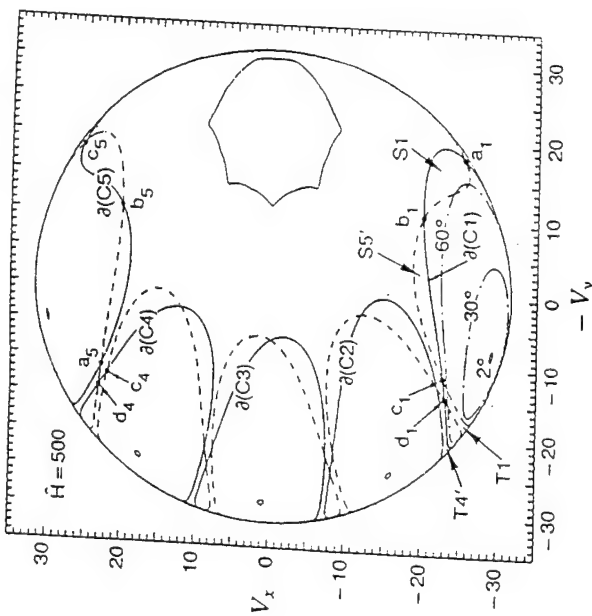


Figure 9. Poincaré surface of section map for the modified Harris model with  $b_n = 0.1$  and  $H = 500$  showing the mapping of particles with asymptotic pitch angles of 2, 30, 60, and 90 degrees.

**Case 5.** In this section we use the same source of particles each time but vary the ratio  $b_n = B_z/B_0$ . The incoming source of particles is taken to be a kappa distribution ( $\kappa = 5.5$ ) with a bulk drift in the tailward direction of  $v_D = 1.3 v_{th}$ , and we again model the distribution function using 80 equally spaced energy shells up to  $3.3T$  with 200 particles per shell. The relatively high drift velocity has been used for these results because we have found that in general, large values of  $b_n$ , require a larger anisotropy in the source distribution to obtain convergence. This is again because particles tend to have a larger diamagnetic currents for larger values of  $b_n$ .

In Figure 10, we plot the density current and magnetic field profiles for  $b_n = 0.1, 0.3$ , and  $0.5$ . Note that larger values of  $b_n$  tend to produce broader and flatter current sheets. In addition, we notice that the current sheet tends to develop a two peak structure. The physical basis for the current sheet broadening can be understood by examining the surfaces of section plotted in Figure 11. Note that for small values of  $b_n$  all of the transient regions of phase space lie near the edge of the circle and consequently have small values of  $v_z$  near the midplane. Again, since the amplitude of the  $z$ -oscillation determines the current sheet thickness, small values of  $b_n$  result in thin current sheets. As  $b_n$  becomes larger, the transient regions extends inward towards the center of the circle, and there is a larger spread in the range of  $v_z$  and a corresponding spread in the current sheet.

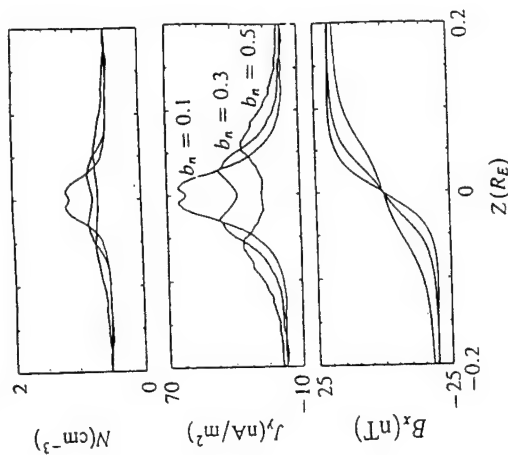


Figure 10. Self-consistent density, current and magnetic field profiles calculated using a kappa distribution ( $\kappa = 5.5$ ) with a bulk drift in the tailward direction of  $v_D = 1.3 v_{th}$  and  $b_n = 0.1, 0.3, 0.5$ .

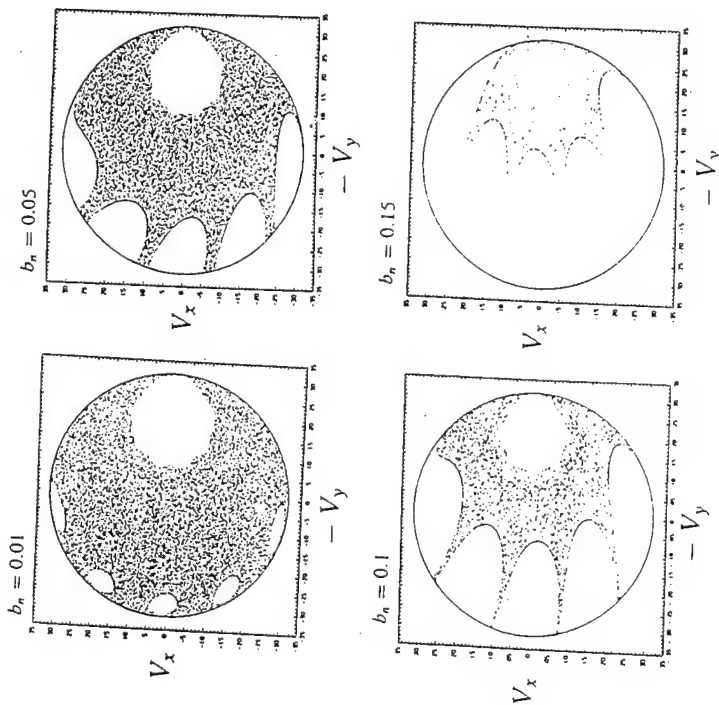


Figure 11. Poincaré surface of section maps for the cases  $\hat{H} = 500$  and  $b_n = 0.01, 0.05, 0.1, 0.15$ .

#### IV. DISCUSSION

We have calculated self-consistent current sheet equilibria to model the quiet-time magnetotail. The principal conclusion is that the distribution of particles entering the current sheet critically determines the equilibrium structure. This is in accord with our previous conclusion that the net cross-tail current is determined by the source distribution rather than by quantities such as chaotic conductivity [17]. The key dynamical property is the partitioning of phase space into distinct regions ("differential memory").

(1) We have demonstrated that many of the attributes of the self-consistent solutions, e.g. thinner current sheets for more field aligned distributions and thicker current sheets for larger values of  $b_n$ , are readily understood in terms of the phase space partitions. In addition, we have found that the self-consistent magnetic field structure for many cases is remarkably "Harris-like" and that the resulting phase

space partitions are nearly identical with those calculated using the modified Harris model. These results combined with our earlier work on the effects of collisions on the nonlinear dynamics of charged particles in the magnetotail [13] go a long way toward understanding the observation of predicted distribution function signatures in ISEE-1 data [3], even though the prediction was based on calculations done in a modified Harris magnetic field with no collisions or noise.

(2) Using nearly isotropic source distributions (cases 1, 2, and 3) and assuming reasonable asymptotic values for the density and magnetic field, we found a current sheet equilibria with thickness  $\sim R_E$  and relatively flat density profile. Both of these properties are in good agreement with observation [14]. In general we have found that high energy tails, which are ubiquitous in space plasmas [18], greatly aid in the convergence to self-consistent solutions.

(3) For a predominantly field aligned distribution (cases 4 and 5), the sheet thickness is much less than an  $R_E$ , and the density profile is sharply peaked, in agreement with previous models in this regime [6,7]. This regime of solution may be relevant to the thin current sheets observed just before substorm onset [16].

(4) The diamagnetism of the plasma is found to play a significant role for Nearly isotropic distributions but is unimportant for nearly field aligned distributions. Note that the diamagnetic current is in the opposite direction from that given by  $\mathbf{J} \times \mathbf{B}/c = \nabla p$ . It is the total current (particle plus diamagnetic) that satisfies Eq. (2). Thus the nonadiabatic particle motion not only needs to produce the desired field reversal, it must also overcome the plasma diamagnetism. This clearly shows that kinetic effects play a critical role in establishing equilibrium.

(5) The inclusion of small to moderate noise levels has little effect on the equilibrium profiles. This is consistent with the results of reference [13] which demonstrated that small to moderate amplitude collisions do not significantly modify the phase space partitions and thus the relative populations of transient and stochastic orbits in a given input distribution. In contrast, in the pure Harris neutral sheet the current sheet tends to spread and decay away in the presence of noise [19]. The difference arises from the fact that the quasi-neutral sheet is driven by external sources, whereas the pure Harris neutral sheet is supported by particles which are trapped near the midplane and which can diffuse away.

An important aspect of our work is that field-aligned source distributions result in thinner current sheets than do isotropic source distributions. This indicates that larger values of the dawn-to-dusk electric field and thus larger values of  $v_D$  can result in a thinning of the current sheet due to the ion dynamics. This is separate from any MHD effects. Since thin current sheets are more unstable, this kinetic thinning of the tail is a potentially important process during the growth phase of a substorm [20]. Some signatures of the kinetic thinning are that the density becomes strongly peaked, the current density becomes larger and more strongly peaked, and the off diagonal elements in the pressure tensor become larger. This kinetic mechanism will be examined in greater detail in a future publication.

# ACKNOWLEDGEMENTS

This work was supported by NASA (W-16,991) and ONR.

## REFERENCES

- [1] Vasyliunas, V. M., *Rev. Geophys. Space Phys.*, **13**, 303, 1975.
- [2] Chen, J., and P. J. Palmadesso, *J. Geophys. Res.*, **91**, 1499, 1986.
- [3] Chen, J., G. R. Burkhardt, and C. Y. Huang, *Geophys. Res. Lett.*, **17**, 2237, 1990a.
- [4] Chen, J., and P. J. Palmadesso, *Magnetotail Physics*, edited by A. T. Y. Lui, p. 321, The Johns Hopkins University Press, Baltimore, MD, 1987.
- [5] Eastwood, J. W., *Planet. Space Sci.*, **20**, 1555, 1972.
- [6] Burkhardt, G. R., J. F. Drake, P. B. Dusenbery, and T. W. Speiser, *J. Geophys. Res.*, **97**, 13799, 1992.
- [7] Pritchett, P. L. and F. V. Coroniti, *J. Geophys. Res.*, **97**, 16773, 1992.
- [8] Holland, D. L., and J. Chen, *Geophys. Res. Lett.*, **20**, 1775, 1993.
- [9] Buchner, J. and L. M. Zelenyi, *J. Geophys. Res.*, **94**, 11821, 1986.
- [10] Chen, J., *J. Geophys. Res.*, **97**, 15011, 1992.
- [11] Chen, J. and D. L. Holland, *Phys Plasmas*, **1**, 803, 1994.
- [12] Holland, D. L., and J. Chen, NRL Memorandum Report # 7168, 1992.
- [13] Holland, D. L., and J. Chen, *Geophys. Res. Lett.*, **18**, 1579, 1991.
- [14] McComas, D. J., C. T. Russel, R. C. Elphic, S. J. Bame, *J. Geophys. Res.*, **91**, 4287, 1986.
- [15] Coppi, B., G. Laval, and R. Pellat, *Phys. Rev. Lett.*, **16**, 1207, 1966.
- [16] Lui, A. T., C.-L. Chang, A. Mankofsky, H.-K. Wong and D. Winske, *J. Geophys. Res.*, **96**, 11,389, 1991.
- [17] Holland, D. L., and J. Chen, *Geophys. Res. Lett.*, **19**, 1231, 1992a.
- [18] Christon S. P., D. J. Williams, D. G. Mitchell, L. A. Frank and C. Y. Huang, *J. Geophys. Res.*, **94**, 13409, 1989.
- [19] Crew, G. B., *EOS Trans. AGU*, **72** supp 418, 1991
- [20] Mitchell, D. G., D. J. Williams, C. Y. Huang, L. A. Frank, and C. T. Russel, *Geophys. Res. Lett.*, **17**, 583, 1990.

NONLINEAR DYNAMICS OF PARTICLES IN THE MAGNETOSPHERE:  
A TUTORIAL REVIEW

James Chen and Daniel L. Holland<sup>+</sup>  
Beam Physics Branch, Plasma Physics Division  
Naval Research Laboratory  
Washington, DC 20375-5000

## ABSTRACT

A tutorial discussion of the nonlinear dynamics of charged particles in the magnetotail is given. Recent research from the dynamics point of view has yielded new insights into decades-old issues, illuminating the relationships between the nonlocal particle motion, global magnetic field geometry, and local plasma properties. Some novel theoretical predictions regarding local distribution functions and equilibrium structure of the current sheet have been made based on the dynamics of charged particles, yielding good agreement with observed data.

## 1. INTRODUCTION

The Earth's magnetosphere consists of many distinct regions but exhibits globally coherent phenomena governed by large-scale fields and collisionless charged particles. Examples of globally coherent processes are geomagnetic storms and substorms, whose terrestrial manifestations include dramatic auroral displays (*borealis* in the northern hemisphere and *australis* in the southern hemisphere) and disruption of satellite systems and electric power stations. As a result, the behavior of the magnetosphere is of scientific as well as practical interest. Figure 1 is a schematic drawing of the Earth's magnetosphere with various regions indicated. The coordinate system is shown. The state of the magnetosphere is determined by the solar wind interacting with the Earth's magnetic field via large-scale momentum, energy and particle input. A region of particular interest is the nightside magnetotail which plays a central role in the storage and release of magnetic energy, thus controlling the dynamics of the entire magnetosphere. In this collisionless system, energy transport and coupling between different regions are critically determined by the nonlocal motion of charged particles.

The magnetotail consists of the lobe and the central plasma sheet (CPS) which contains a thin current sheet at the midplane,  $z = 0$ , where the x-component of the magnetic field reverses sign. The current sheet represents magnetic energy, and its dynamics has been a long-standing topic of research. The properties of the current sheet are determined by the distribution of particles entering the midplane

---

<sup>+</sup> Present address: Physics Department, Illinois State University, Normal, IL.

from elsewhere including the ionosphere and the distant X line. Thus, the current sheet is influenced by "remote" processes affecting the different populations of particles following different paths to the current sheet. In the magnetosphere, the charged-particle motion can be complex because adiabatic invariance is not globally applicable. Numerous studies of the motion of particles in the magnetotail have been carried out [1 - 17]. In the early works, individual orbits were studied [1, 4, 6] focusing on the nonadiabatic motion in the current sheet [3, 10]. More recently, Büchner and Zelenyi [15] have extended the treatment of the action integral  $I \equiv \oint \mathbf{z} d\mathbf{z}$  [3] to calculate the variation  $\Delta I$  due to the nonadiabatic motion.

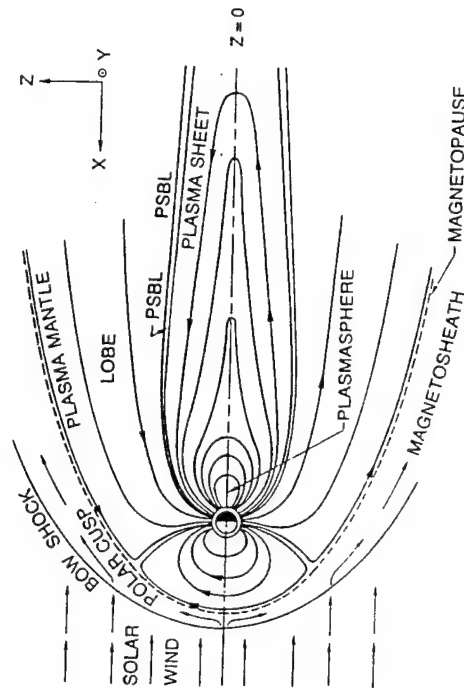


Figure 1. Schematic drawing of the Earth's magnetosphere. Magnetic field lines and various regions are depicted.

A different approach based on modern dynamics point of view is to consider generic properties of families of orbits and phase space topology of the system rather than individual orbits. Chen and Palmadesso [12] first showed that there exist only two global constants of the motion in involution in the magnetotail geometry and that the particle motion is nonintegrable. Using the Poincaré surface of section technique, they found that the phase space is partitioned into disjoint regions occupied by dynamically distinct classes of orbits: unbounded stochastic (chaotic), unbounded transient and bounded integrable (regular) orbits. Based on the partitioning of the phase space, they proposed a process called "differential memory" (section 5) which can significantly influence the time-evolution of

plasma distributions. This process arises from the property that different phase space regions are occupied by orbits with widely separated characteristic orbital time scales so that the respective phase space regions can retain memory of existing population of particles for different lengths of time. The time scales referred to here are the accessibility time, the time for orbits far away from the midplane to reach (i.e., "access") various regions of the phase space. Differential memory has been used to model plasma distribution functions in the magnetotail [17, 18, 19, 20], yielding results in agreement with observations [18]. The underlying partitioning of the phase space proved to be robust in the presence of collisional effects [21]. The same partitioning and differential memory also determine the current sheet equilibria [22]. Thus the nonlinear particle dynamics controls both local and global properties of the central plasma sheet (CPS).

The magnetotail current sheet is a chaotic scattering system in which the outgoing conditions exhibit sensitive dependence on the incoming conditions [23, 24]. The nonlinear dynamical properties of the system are now well established, and the reader is referred to recent reviews for more detail [25, 26]. In another configuration of interest in space and astrophysical environments, Martin [13] studied the nonlinear dynamics of charged particles in an X-type neutral line, using the maximal Lyapunov exponent to quantify the degree of chaos. Possible distribution function signatures [27, 28, 29] and kinetic structure [30] of X-type reconnection regions have been studied. In these studies, isolated X-line geometries were considered. In order to connect an X-line region to the CPS, global electric and magnetic fields must be used. In a recent work, Joyce et al. studied test-particle distributions and energization in an X-line configuration given by a three-dimensional MHD simulation model of the magnetosphere [31]. In this model, test particles are calculated in electric and magnetic fields that are self-consistent within the framework of basic MHD approximations, and the use of a global model allows one to relate the X-line region to the CPS, the overall state of the model magnetosphere, and the condition of the solar wind.

There has been increased interest in the particle dynamics in the magnetotail and the physical implications [17, 18, 19, 20, 27, 28, 29]. Some novel predictions based directly on the topological, i.e., geometrical, properties of the phase space have proved to be in good agreement with observed data [19]. In light of such successes, one can justifiably state that the study of particle motion and plasma properties in the magnetotail within the new framework of nonlinear dynamics has emerged from a *descriptive* stage and entered a *predictive* stage. Here, we provide a brief tutorial review of recent findings relevant to the Earth's magnetotail based on the full-length review paper of [25] with additional new information regarding the exponential divergence of nearby orbits and nonzero  $B_y$  component. The emphasis will be on how the particle dynamics exert controlling influences on physical observables on small- as well as large-scales in the CPS.

## 2. EQUATION OF MOTION

A simple field model for the magnetotail is

$$\mathbf{B}(z) = B_0 f(z) \hat{x} + B_y \hat{y} + B_n \hat{z}, \quad (1)$$

where  $f(z) \rightarrow \pm 1$  as  $z \rightarrow \pm\infty$  so that  $B_0 = B_z(z \rightarrow \infty)$ ,  $B_n$  is the uniform field normal to the midplane ( $z = 0$ ),  $B_y$  is a uniform field across the tail, and  $B_0 f(z)$  is a field-reversed neutral sheet profile. The function  $f(z)$  is often chosen to be antisymmetric about  $z = 0$  with  $f(z = 0) = 0$ . For the earth's magnetotail we typically consider  $b_n \equiv B_n/B_0$  of the order of  $0.05 \sim 0.1$  for the distant magnetotail, but  $b_n$  can be larger near the Earth. The  $B_y$  component is determined by the solar wind conditions, and  $b_y \equiv B_y/B_z$  can have a range of values. In this article, we will use the gauge such that the vector potential is  $\mathbf{A} = A_x(z) \hat{x} + A_y(x, z) \hat{y}$ . Then,

$$A_x(z) = B_y z, \quad (2a)$$

$$A_y(x, z) = -B_0 F(z) + B_n x, \quad (2b)$$

where  $F(z)$  is defined by  $dF(z)/dz \equiv f(z)$ , with the total asymptotic magnetic field  $B = (1 + b_y^2 b_n^2 + b_n^2)^{1/2} B_0$ . The conclusions in this paper, however, are independent of gauge.

Two commonly used forms of  $f(z)$  are the Harris model  $f(z) = \tanh(z/\delta)$  and the parabolic model  $f(z) = z/\delta$  where  $\delta$  is the characteristic half-thickness of the neutral sheet. These two models give  $F(z) = \delta \ln[\cosh(z/\delta)]$  and  $F(z) = (1/2)z^2/\delta$  respectively. In the simplest case,  $B_y = 0$  is used. In the vicinity of the midplane ( $z/\delta \lesssim 1$ ), we have  $\tanh(z/\delta) \sim z/\delta$ , giving  $\ln[\cosh(z/\delta)] \simeq (1/2)(z/\delta)^2$  so that the Harris and parabolic field models are similar for  $z/\delta \lesssim 1$ . For  $z/\delta \gtrsim 1$ , on the other hand, the two model fields diverge significantly. In particular, for the Harris model, if  $|z|$  is greater than some  $z_a \gg \delta$ , we have  $B_x \simeq B_0$ , and the magnetic field is essentially uniform. We will refer to  $|z| > z_a$  as the asymptotic regions. For the parabolic field model the magnitude of  $f(z)$  continues to increase with increasing  $|z|$  and there is no well defined asymptotic region. In reality, the parabolic field should be "truncated" by setting  $f(z) = 1$  for  $|z| \gg \delta$ . In both models, the radius of curvature  $R_c = B_n/(\partial B_x/\partial z)$  at  $z = 0$  is  $R_c = b_n \delta$ . West et al. [5] found that the pitch-angle distributions calculated in a  $B_x$  field with "roll-off" provided by  $\tanh(z/\delta)$  fit the observed data better than the models with power law dependence on  $z$  such as the parabolic field. Dynamically, these two configurations are qualitatively different. With  $B_n \neq 0$ , we will refer to these two models as the "modified Harris" and the "parabolic field" models, respectively. Both will be collectively referred to as quasi-neutral sheets as opposed to pure neutral sheet for which  $B_n, B_y = 0$ .

The single-particle motion can be described by the equation of motion

$$m \frac{d\mathbf{v}}{dt} = \frac{q}{c} \mathbf{v} \times \mathbf{B}. \quad (3)$$

In general, a nonzero  $E_y$ , albeit small during quiet times, exists. If we take  $B_y = 0$  and  $B_n = \text{constant}$ , a uniform  $E_y$  can be simply transformed away by an  $\mathbf{E}_y \times \mathbf{B}_n$  translation. A nonuniform  $\mathbf{E}$  field is more complicated and will not be considered.

There are two important time scales for the quasi-neutral sheet. One is  $\Omega_0 \equiv eB_0/mc$  and the other is  $\Omega_n \equiv eB_n/mc$ . The corresponding Larmor radii are  $\rho_0 \equiv v/\Omega_0$  and  $\rho_n \equiv v/\Omega_n$  where  $v$  is the velocity.

It has long been known that the particle motion in the magnetotail is nonadiabatic. Speiser [1] first identified a class of nonadiabatic orbits in the modified Harris configuration with  $B_y = 0$ , which are sometimes called Speiser orbits. Figure 2 shows such an orbit. This particle executes adiabatic motion far away from the midplane (noncrossing motion), enters the current sheet where it oscillates in the  $z$  direction, traverses the midplane while crossing the midplane at points 1, 2, 3, 4, 5, and is then ejected from the current sheet. The number of midplane crossings depends on the energy and is found to be roughly proportional to  $\hat{H}^{1/4}$  [12], where  $\hat{H}^{1/4}$  is the normalized Hamiltonian (see equation (7) below). While traversing the midplane, the particle motion is a combination of "meandering" (midplane crossing) motion [3] and gyration about the weak  $B_n$  field. For some time, the basic properties of the particle motion were understood in terms of Speiser orbits

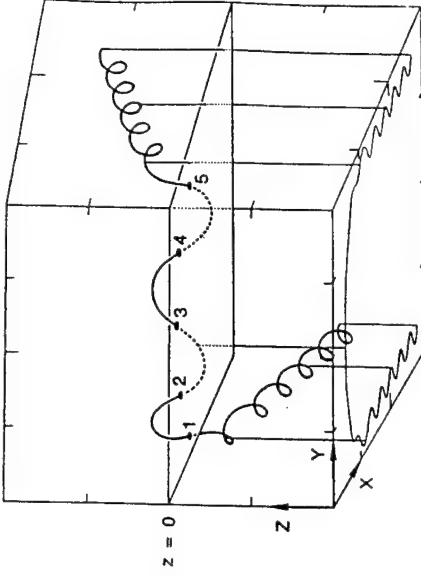


Figure 2. A Speiser orbit. The crossing points at  $Z = 0$  are indicated.  $\hat{H} = 500$  and  $b_n = 0.1$ . The  $Z$  axis is expanded by 1.2. (Adapted from Ref. 12.)



[e.g., 1, 3, 9, 34, 35]. Later, West et al. [4, 5] found orbits whose long-time behaviors are qualitatively different from the Speiser orbits. They studied high-energy electron orbits which make repeated traversals of the midplane before escaping to infinity. By one traversal, we will refer to the motion of entering and leaving the midplane once. One traversal generally has multiple midplane crossings. (Fig. 2 shows one traversal.) Wagner et al. [6] also found similar (ion) orbits and noted that considerable variation in the motion of certain orbits occurs even with nearly identical initial conditions. This is illustrated in Fig. 3, showing two orbits whose initial conditions differ only in the initial phase angle.

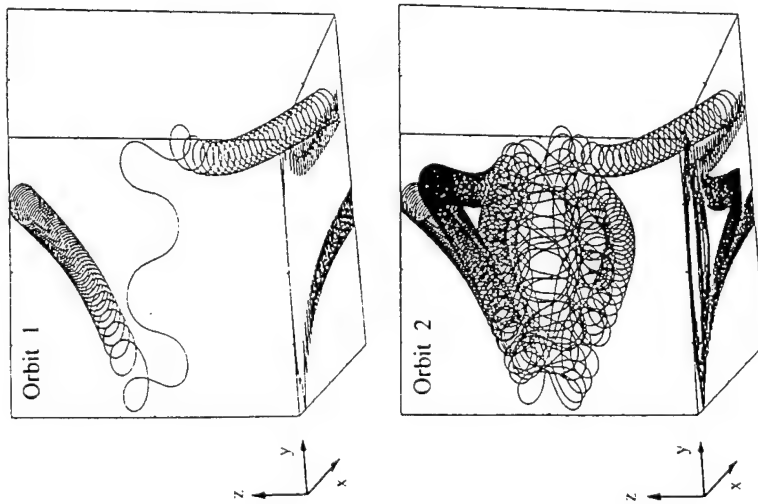


Figure 3. Trajectories of two orbits with initial conditions  $\hat{H} = 500$ ,  $\beta = 100^\circ$ , and  $z = 3.5\delta$ . Orbit 1 has initial phase angle  $\theta = 20^\circ$  and orbit 2 has  $\theta = 50^\circ$ . From Ref. 21.

### 3. NONLINEAR DYNAMICS OF CHARGED PARTICLES

Equation (3) possesses three exact constants of the motion:  $H = mv^2/2$ ,  $P_y = mv_y + (q/c)A_y(x, z)$ , and  $C_x \equiv m(v_x - \Omega_n y + \Omega_n b_n z)$ . However, for  $B_y = 0$ , it was found [12] that these constants are not in involution, having  $[C_x, P_y] = -m\Omega_n \neq 0$ , where we have used  $[y, P_y] = 1$ . This suggests that the system is not integrable. Extensive numerical evidence was given to support this suggestion. Note that the canonical momenta  $P_x$  and  $P_y$  are not simultaneously conserved in this system even though the magnetic field is manifestly invariant under translation in both the  $x$ - and  $y$ -directions. This is because of the fact that magnetic field is given by a vector potential,  $\mathbf{B} = \nabla \times \mathbf{A}$ . This causes the Hamiltonian to depend on  $x$  and  $z$  (or on  $y$  and  $z$  in a different gauge). If an  $N$  dimensional system has  $N$  constants  $\{C_1, \dots, C_N\}$  in involution, i.e.,  $[C_i, C_j] = 0$  for all  $i, j \leq N$ , then the system is completely integrable, and there exists a canonical transformation to a coordinate system with  $N$  cyclic coordinates such that the first integrals  $C_i$  are the new canonical momenta. In the context of Kolmogorov-Arnol'd-Moser (KAM) theory,  $B_n$  is the nonintegrable perturbation. Taking  $b_n \rightarrow 0$ , we have  $[C_x, P_y] = 0$ . For  $B_y \neq 0$ , the above condition,  $[C_x, P_y] = -m\Omega_n$ , remains unchanged. This shows that for any  $B_y(z)$ , the particle motion in the magnetic field  $\mathbf{B}(z) = B_0 f(z)\hat{x} + B_y(z)\hat{y}$  is completely integrable because  $C_x = P_x$ , where  $P_x$  is the  $x$  canonical momentum, and  $[P_x, P_y] = 0$ .

It is convenient to rewrite equation (3) in a dimensionless form [12]:

$$\frac{d^2 X}{d\tau^2} = \frac{dY}{d\tau} - b_y \frac{dZ}{d\tau}, \quad (4)$$

$$\frac{d^2 Y}{d\tau^2} = \frac{d}{d\tau} \left\{ b_n^{-2} \ln [\cosh(b_n Z)] - X \right\}, \quad (5)$$

$$\frac{d^2 Z}{d\tau^2} = b_y \frac{dX}{d\tau} - b_n^{-1} \tanh(b_n Z) \frac{dY}{d\tau}, \quad (6)$$

where the normalization is  $X \equiv (x - P_y/m\Omega_n)/b_n\delta$ ,  $Y \equiv (y + C_x/m\Omega_n)/b_n\delta$ ,  $Z \equiv a/b_n\delta$ ,  $\tau \equiv \Omega_n t$  and  $\dot{X} \equiv dX/d\tau$ . Here, we have assumed the modified Harris model of the magnetic field,  $E_y = 0$ , and  $b_n \equiv B_n/B_0 \neq 0$ . If we set  $b_y = 0$ , we recover equations (5)-(7) of Ref. 12. The normalized Hamiltonian is

$$\hat{H} \equiv H / (mb_n^2 \Omega_n^2 \delta^2). \quad (7)$$

With  $B_y = 0$ , equations (4)-(7) show that the modified Harris model requires two parameters to specify the dynamics:  $b_n$  and  $\hat{H}$ . In the parabolic field model,  $b_n \neq 0$  can be normalized away and only  $\hat{H}$  is needed. If  $B_y \neq 0$ , one additional parameter  $b_y$  need be specified in each case. The integrable limit  $b_n \rightarrow 0$  cannot be

taken directly in either field model. The limit  $\hat{H} \rightarrow \infty$  corresponds to two distinct physical limits:  $b_n \rightarrow 0$  or  $H \rightarrow \infty$  where  $H$  is the unnormalized Hamiltonian. The former leads to the integrable neutral sheet while the latter is not integrable.

For  $B_y = 0$ , equations (4)–(6) are invariant under  $Z \leftrightarrow -Z$  and under the simultaneous replacement  $Y \leftrightarrow -Y$  and  $\tau \leftrightarrow -\tau$ . The latter symmetry operation implies that  $Y$  reversal (not invariant) and  $\tau$  reversal are equivalent. With uniform  $B_y \neq 0$ , the simultaneous replacement of  $Z \leftrightarrow -Z$  and  $b_y \leftrightarrow -b_y$  is an invariant symmetry operation as is the simultaneous replacement of  $Y \leftrightarrow -Y$ ,  $\tau \leftrightarrow -\tau$ , and  $b_y \leftrightarrow -b_y$ . The symmetry properties of the system are important for determining dynamical properties of the entire system.

The previous studies of particle dynamics in the magnetotail have been largely limited to the  $B_y = 0$  case, and we will primarily discuss this case. However, we will briefly describe the generic phase space properties with uniform  $B_y \neq 0$  using Poincaré maps later in this section.

The fundamental dynamics of electrons is identical to that of ions. Aside from the trivial difference in the direction of motion, the main difference is the relevant regimes of  $\hat{H}$ . Using (7), a given value of  $H$  in physical units gives

$$\hat{H}_e = (m_e/m_i) \hat{H}_i, \quad (8)$$

where  $\hat{H}_e$  and  $\hat{H}_i$  are  $H$  normalized for  $m_e$  and  $m_i$ , respectively.

Using normalized quantities, we can write  $\hat{H} = (1/2b_n^4)(\rho_0/\delta)^2$  with  $\rho_n = \rho_0/b_n$ . The normalized Larmor radii are  $\hat{\rho}_0 = b_n(2\hat{H})^{1/2}$  and  $\hat{\rho}_n = (2\hat{H})^{1/2}$ . We will use capital letters for dimensionless coordinates and lower case letters for unnormalized coordinates. Other normalized quantities will be denoted by carets.

Another frequently used parameter is  $\kappa = (R_c/\rho_n)^{1/2} = (2\hat{H})^{-1/4}$ , which has been used to parameterize pitch-angle scattering by the current sheet with  $B_y = 0$  [4, 36]. Büchner and Zelenyi [14] expanded the Hamiltonian for  $\kappa \ll 1$  and proposed to use  $\kappa$  as a measure of chaos.

The dynamical system represented by equations (4)–(7), or equation (3), was first described in detail using the Poincaré surface of section technique [12]. For example, one can consider a plane at  $z = 0$  and record the coordinates  $X$  and  $\dot{X}$  as an orbit crosses the plane. The orbit in Fig. 2 would leave five crossing points,  $(X_1, \dot{X}_1), \dots, (X_5, \dot{X}_5)$ , in the midplane. One can then record these points and construct a constant-energy phase space plot which describes the long-time dynamical properties graphically. Figure 4a shows a surface of section plot constructed at  $Z = 0$  for  $\hat{H} = 500$  and  $b_n = 0.1$  in the modified Harris model. This technique provides a graphic representation of the first return map. For example, in Fig. 2, point 3 is the first return map of point 1, and point 5 is the mapping of point 3. Figures 4a–4b show all the generic phase space properties for this system. The most prominent feature is the sharp division of the phase space. The region denoted by  $A$  is an integrable (regular) region, and it is surrounded by region  $B$  referred to as a stochastic or chaotic region. The regions denoted by  $C$  are referred to as transient regions.

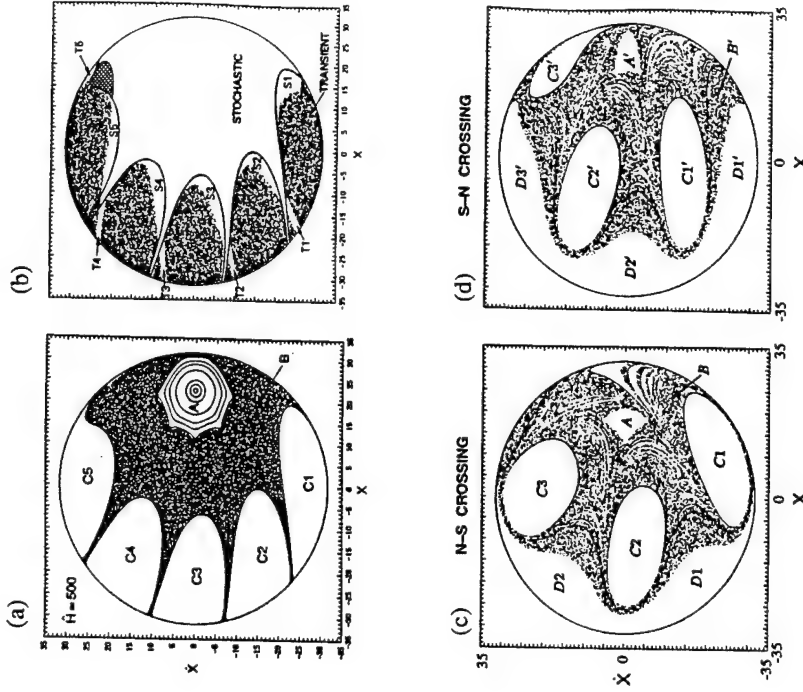


Figure 4. A Poincaré surface of section map.  $b_n = 0.1$ . Adapted from Ref. 12. (a)  $B_y = 0$ . Region  $A$  is integrable and region  $B$  is stochastic. Regions  $C1$ – $C5$  are transient regions. The boundaries  $\partial(C)$  are shown. (b) Internal structure of the transient regions.  $S1$  and  $T1$  are the entry regions for stochastic orbits. The orbits shown are transient orbits. (c)  $B_y = 0.1 B_0$ . Surface of section return map for north-to-south crossings. (d)  $B_y = 0.1 B_0$ . South-to-north crossings.

For  $B_y = 0$ , the equations of motion are symmetric in  $Z$ . As a result, the two directions of crossing at the midplane,  $\dot{Z} > 0$  and  $\dot{Z} < 0$  need not be distinguished. For  $B_y \neq 0$ , however, the  $Z$ -symmetry is lost, and the two directions of midplane crossing must be distinguished by using two phase space surfaces at  $Z = 0$ . For example, if  $B_y \neq 0$ , points 1, 3, 5 and points 2, 4 would be on different surfaces. Figures 4c-4d show the two return maps with  $B_y = B_n = 0.1B_0$  and  $\dot{H} = 500$ . The regions A, B, and C are again occupied by integrable, stochastic, and transient orbits. Regions D are analogous to regions C and exist separately from regions C because of the lack of  $Z$  symmetry. We will return to these figures later.

In the integrable region, a given trajectory is confined to an invariant surface, the so-called KAM surface, whose intersection with the surface  $Z = 0$  is a closed curve. Several representative KAM curves are shown in region A of Fig. 4a. An integrable region consists of infinitely many nested closed curves. In the system given by equations (1) and (3), the  $z$ -extent of the integrable orbits is limited to  $\sim d_j \equiv (2\rho_0\delta)^{1/2}$ . In the absence of noise, integrable orbits remain on the KAM surfaces indefinitely without closing onto themselves (quasi-periodic). There exist integrable orbits which do close onto themselves. They are referred to as periodic or fixed-point orbits. Büchner and Zelenyi [15] proposed that the action  $I$  can serve as the third invariant. The action  $I$  is only an approximate invariant in the current sheet because  $[I, H] \neq 0$ .

In region B of Fig. 4a, nearby orbits which are initially arbitrarily close to each other can diverge exponentially during the time the orbits are in the vicinity of the current sheet [25]. The average exponential divergence rate is calculated in the same way as the standard Lyapunov exponent with the exception that the time used in the calculation is limited to the duration between the first and last crossings of the midplane.

In the modified Harris model, all nonintegrable orbits come from and escape to infinity ( $z \rightarrow \infty$ ), and all orbits from infinity are nonintegrable, making their first midplane crossings in region C1. This is the entry region. All orbits escaping to infinity cross the midplane for the last time in region C1' (not shown in Fig. 2), where C1' denotes the mirror image of C1 about  $\dot{X} = 0$ . The regions C2-C5 are the successive mapping of C1 by equations (4)-(6).

The regions C are shown as "blank" regions only to distinguish them from the surrounding stochastic region. Figure 4b shows the internal structures of the regions C1-C5. The orbits (i.e., points) shown are the transient orbits, making only one traversal of the midplane. For  $\dot{H} = 500$ , they have the appearance of the well-known Speiser orbits shown in Fig. 2. All transient orbits enter the midplane through C1 and the majority of them pass through C2-C5, and escape to infinity. Some escape to infinity after crossing C4 just above T4, which is inside region C1', the exit region. The transient orbits do not enter region B. The number  $N$  of the prominent transient regions is given by

$$N_t \sim (\dot{H}/2)^{1/4} + 1$$

for  $\dot{H} \lesssim (1/2)b_n^{-1/4}$  [12]. (Note that  $N_t$  gives the number  $f$  as in Cf.) This is also the typical number of midplane crossings for an orbit of energy  $\dot{H}$  as it makes one midplane traversal. The scaling dependence is straightforward to obtain and is a consequence of the property  $B_z(z) \simeq B_0 z/\delta$  for  $z/\delta \lesssim 1$  and of the translational invariance in  $y$ . ( $\rho_n \ll L_x$  is assumed.) Several important implications of this scaling dependence have been found recently, and we will discuss them in section 4. The orbits which enter the midplane through S1 or T1 subsequently cross the midplane through S2-S5 or T2-T5, respectively, and then enter region B. These orbits eventually escape through the cross-hatched regions, which are subregions of C1', being the mirror images of S1 and T1. Generally, the entry region C1 consists of subregions corresponding to transient orbits of different midplane crossing numbers (e.g., 4 and 5 for  $\dot{H} = 500$ ), and these subregions are separated by entry regions for stochastic orbits (e.g., T1).

It is instructive to understand the class of orbits comprising the boundaries of the transient regions. These boundaries, which will be denoted by  $\partial(C_j)$ , where  $j = 1, 2, \dots, f$ , are the mapping forward in time of those orbits which have pitch angles  $\beta = \pi/2$  at "infinity" [18]. The boundaries of the transient regions shown in Fig. 4a are constructed by mapping such orbits at  $z = 5\delta$  forward in time. The boundary  $\partial(C1)$  is the first midplane crossing of these orbits, which are subsequently mapped to  $\partial(C2)-\partial(Cf)$  by the equation of motion (3). For more detail regarding the structure and properties of  $\partial(Cf)$ , see section 2.3 of Ref. 25.

In the  $B_y \neq 0$  case the basic partitioning of phase space persists, albeit with some modifications. Figure 4c shows the return map at  $Z = 0$  for north-to-south (N-S) crossings with  $B_y = B_n = 0.1B_0$ , and Fig. 4d shows the return map for south-to-north (S-N) crossings with the same parameters, where north refers to  $Z > 0$  and south to  $Z < 0$ . (Due to the symmetry of the equations of motion under the simultaneous replacement of  $b_y$  with  $-b_y$  and  $Z$  with  $-Z$ , Fig. 4c may also be considered to be the return map for south-to-north crossings and Fig. 4d the return map for north-to-south crossings with  $-B_y = B_n = 0.1B_0$ .) We will give a brief discussion of the phase space structure for this case. The purpose here is not to discuss the detailed properties but to show that the concepts and techniques developed for the simpler  $B_y = 0$  case can be applied to obtain rigorous understanding of the more complicated system.

As in Figs. 4a and 4b, regions A and A' are occupied by integrable (regular) orbits which are confined to KAM surfaces for all time in the absence of noise. All particles approaching the midplane from the north will first cross the midplane in region C1 (N-S crossing). The particles will then cross the midplane again in region C1' (S-N crossing) followed by region C2, C2', C3, and C3'. Some particles then escape to infinity (transient orbits), whereas others will enter the phase space in region B (stochastic orbits). Similarly, those particles approaching the midplane from the south will first enter the surface of section in region D1' (S-N crossing). The particles will then cross the midplane again in region D1 (N-S crossing), D2 and so forth. Subsequently, some particles will escape to

infinity whereas others will reenter the phase space in region  $B$  and make multiple traversals of the midplane (stochastic orbits).

As in the  $B_y = 0$  case, the entry regions ( $C1$  and  $D1'$ ) are the mapping of particles from infinity:  $C1$  is the mapping of particles from  $Z = +\infty$  while  $D1'$  is the mapping from  $Z = -\infty$ . The escape regions are the mirror images of  $C1$  and  $D1'$  about  $V_x = 0$  in the respective surfaces (not shown but see Ref. 25 for the method of constructing phase space regions). Note that the mirror image of a region defined by a set of orbits is equivalent to the time reversed mapping of a same set of orbits. Unlike the  $B_y = 0$  case, however, care must be used to ascertain the surface of exit if  $B_y \neq 0$ . That is, if orbits originating from the north escapes to the south, the escape region and entry region are in the same N-S surface. If the orbits escape to the north, then the entry region is in the N-S surface while the escape region is in the S-N surface.

Analogous to the  $B_y = 0$  case, the entry regions are generally subdivided into regions for entry of transient and stochastic orbits. These subregions are the intersections between the entry region and the time reversed mapping of the regions  $C, C', D$ , and  $D'$ . Then, as mentioned above, the direction of the midplane crossing, i.e., N-S versus S-N, must be taken into account properly. Although this process is much more complicated than the  $B_y = 0$  case, the subregions in the overall entry regions ( $C1$  and  $D1'$ ) can be mapped out geometrically and *exactly*. The details of the phase space structure and their physical significance will be discussed in detail elsewhere.

We have given a brief discussion of the phase space properties with  $B_y \neq 0$ . The emphasis is on the symmetry properties and the existence of the partitioning of the phase space. We have found that the previously identified phase space resonance arising from differential memory [17, 19] persists prominently if  $B_y \lesssim B_n$ . This property and other implications of  $B_y \neq 0$  for physical observables will be discussed in a future publication.

The phase space properties as represented graphically by the surface of section plots, which describe the dynamics of the system completely, are qualitatively similar for  $B_y \neq 0$  and  $B_y = 0$ : the dynamical system consists of integrable, stochastic, and transient trajectories. In the remainder of the paper, we will primarily discuss the case with  $B_y = 0$ .

An important question is how collisions and noise can influence the dynamical properties which have been obtained in the absence of such effects. This is particularly relevant because realistic systems are generally "noisy", and stochastic orbits are sensitively affected by noise. Holland and Chen [21] constructed an *ad hoc* scattering operator which parameterizes a collision by collision frequency  $\nu$ , amplitudes of pitch-angle ( $\Delta\beta$ ) and phase-angle ( $\Delta\phi$ ) scattering, and amplitude of energy change ( $\Delta E$ ). It was found that the KAM surfaces are destroyed with the introduction of collisions while the transient region boundaries  $\partial(C_j)$  are remarkably robust. Figure 5 shows a surface of section plot for  $\tilde{H} = 187.4$ , and  $b_n = 0.1$  with pure pitch-angle scattering of amplitude  $\Delta\phi = \Delta\beta \leq 1^\circ$  and

frequency  $\nu = \Omega_n/2$ . The KAM curves in what would have been an integrable region without collisions are destroyed, showing that orbits can diffuse through the region. In contrast, the boundaries  $\partial(C1)-\partial(C4)$  are essentially intact. This means that the separation between the stochastic and transient orbits remains sharp. Although the KAM surfaces are destroyed, the (former) integrable orbits are nearly trapped for substantially longer periods of time than the stochastic orbits. Thus, the partitioning of the phase space remains. For pure energy scattering, the "collisions" are to have a significant effect on the phase space populations, particles must be transported onto energy surfaces with greatly differing phase space boundaries. If we assume that the "collisions" are due to wave particle interactions, we find that the observed frequencies and amplitudes will not produce a major change in the relative populations of transient and stochastic orbits.

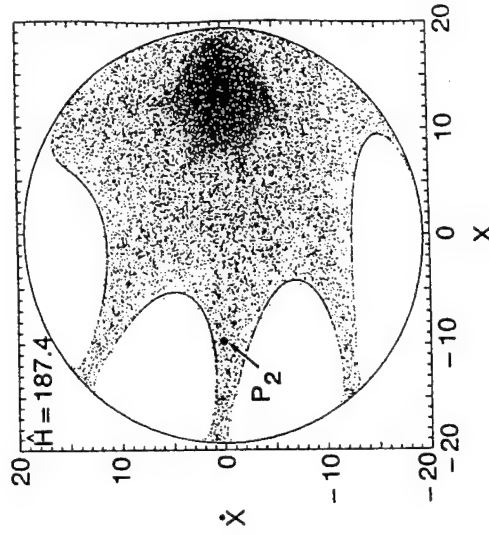


Figure 5. Surface of section for  $\tilde{H} = 187.4$  including pure pitch-angle scattering. The scattering amplitude is  $1^\circ$  in pitch- and phase-angles with a frequency of  $\nu = \Omega_n/2$ . (From Ref. 21.)

The property that nonintegrable orbits are unbounded distinguishes this system from the usual bounded dynamical systems. As Figs. 2 and 3 show, the particle motion in the asymptotic regions is regular. Thus, it is possible to speak of well-defined incoming and outgoing conditions in the asymptotic regions. It was first shown [23] that the entry regions (e.g.,  $S1$  of Fig. 4b) are divided into subregions according to the outgoing states and that such subregions occur on a fractal set. Thus, the outgoing conditions depend sensitively on the incoming

conditions. As an example, the total number of midplane crossings between first and last crossings of the midplane can serve as outgoing conditions. The fractal dimension was found to be  $d \simeq 1.8$  for  $\dot{H} = 500$ , indicating that the outgoing conditions are only poorly predictable from the initial conditions. Similarly the pitch angle is essentially constant for  $|z| \gg \delta$  and can define asymptotic states. This type of system, which has regular asymptotic trajectories but whose outgoing conditions exhibit sensitive dependence on incoming conditions, are often called "chaotic scattering systems". The physical importance of chaotic scattering is that the "external world" can influence and be influenced by the chaotic dynamics in side localized regions. For example, auroral region electric fields can modify the tailward flowing ion distributions which determine the current sheet structure in the tail [22]. In this process, the incoming ions enter the current sheet through C1. The pitch-angle distribution then determines the relative population of transient and stochastic orbits. The term "chaotic scattering" has also been used [e.g., 20] to refer to the variation  $\Delta I$  in the action at the effective potential separatrix [15]. This usage is different from the standard terminology in nonlinear dynamics.

A quantitative measure of the degree of chaos is the Lyapunov exponent, which gives the average rate at which arbitrarily nearby orbits exponentiate away from a reference orbit. Martin [13] computed the Lyapunov exponent for orbits in an X-type magnetic neutral line. For the quasi-neutral sheet configuration, Ref. 25 showed the exponential divergence rate  $\lambda^*$  for individual trajectories and defined a phase space average  $\Lambda$  of  $\lambda^*$ . The usual Lyapunov exponent is defined for infinite time, appropriate for bounded orbits. For chaotic scattering systems such as the quasi-neutral sheet configuration, the infinite time limit is not useful because all nonintegrable orbits are actually regular almost all the time. For individual orbits, a finite-time analogue of the Lyapunov exponent can be defined. Consider an orbit  $\mathbf{x}$  and a nearby orbit  $\mathbf{x} + \delta\mathbf{x}$ . The difference vector  $\delta\mathbf{x}$  lies in the tangent space at  $\mathbf{x}$ . Let its norm be  $w(\mathbf{x}, t) \equiv |\delta\mathbf{x}|$ . Then the exponential divergence rate is

$$\lambda^* = \frac{1}{L\Delta\tau} \sum_{i=1}^L \ln \left( \frac{w_i}{w_0} \right), \quad (9)$$

where  $w_0$  is the norm of the initial tangent vector,  $w_i$  is the norm of the tangent vector after the  $i$ -th time step, and  $\Delta\tau$  is the time step. The number  $L$  is the total number of time steps from the first crossing of the midplane (e.g., in S1 or T1 of Fig. 4b) to the last point of crossing (e.g., in S1' or T1'). The standard Lyapunov exponent corresponds to the limit  $L \rightarrow \infty$ . Recall that the dynamics (but not individual trajectories) in the modified Harris field can be parameterized by two quantities:  $\dot{H}$  and  $b_n$  (plus  $b_y$  if  $B_y \neq 0$ ). For given  $\dot{H}$  and  $b_n$ , however, it is easy to show that the value of  $\lambda^*$  has a wide range, depending on the pitch and phase angles of the orbits. One can average over the pitch and phase angles to characterize the entire stochastic region for each energy surface. We define the average exponential divergence rate by

$$\Lambda(\dot{H}, b_n) \equiv \left( \frac{1}{M} \right) \sum_{m=1}^M \lambda_m^*, \quad (10)$$

where  $\lambda_m^*$  is the divergence rate for the  $m$ -th orbit and  $M$  is the total number of orbits used in the calculation. The individual orbits are distributed uniformly in the stochastic orbit entry regions at  $Z = 0$  (e.g., S1 and T1 of Fig. 4b). The orbits are computed until they enter S1' or T1'. Figure 6a shows the plot of  $\Lambda$  versus  $\dot{H}$  for  $b_n = 0.1$ . We used  $M = 40$ –100 for  $\dot{H} \lesssim 10$  and  $M \simeq 200$ –400 for higher values of  $\dot{H}$ . The rate  $\lambda_m^*$  for each orbit is computed from the first crossing

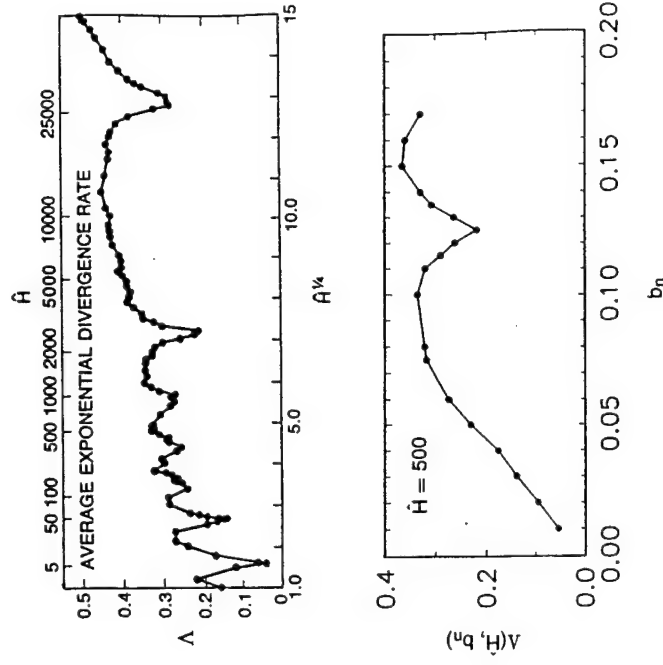


Figure 6. Average exponential divergence rate in the modified Harris model. (a) For fixed  $b_n = 0.1$ . The valleys occur at the resonance energies [equation (15)]. From Ref. 25. (b) For fixed  $\dot{H} = 500$ .

to the last crossing of the midplane. We see that there are certain values of  $\dot{H}$  where  $\Lambda(\dot{H})$  is significantly reduced from the neighboring values. These  $\dot{H}$  values are evenly spaced in  $\dot{H}^{1/4}$ , indicating the existence of resonance, and are related



to the scaling behavior  $N_I \simeq (\dot{H}/2)^{1/4} + 1$  previously mentioned. This resonance effect will be discussed in the next section.

It can be shown that  $\Lambda(\dot{H}, b_n)$  decreases linearly with  $b_n$  for fixed  $\dot{H}$ . Figure 6b shows the actual average exponential divergence rate  $\Lambda(\dot{H}, b_n)$  as a function of  $b_n$  for  $\dot{H} = 500$ . It is clear that  $\Lambda$  is linear in  $b_n$  as  $b_n \rightarrow 0$ . This is important for a mathematically correct understanding of the nature of chaos in this system described the set of equations (4)–(6). This linear scaling behavior is to be expected because  $b_n = 0$  is a completely integrable limit about which the system is perturbed as  $b_n$  increased. The other integrable limit is given by  $B_0 = 0$  which simply gives the motion in a uniform magnetic field  $B_n$ .

It has been conjectured [15] that the degree of chaos increases as  $\kappa \rightarrow 1$ , attaining maximum at  $\kappa = 1$  ( $\dot{H} \rightarrow 0.25$ ) and that it decreases for  $\kappa \rightarrow 0$  ( $\dot{H} \rightarrow \infty$ ). The quantity  $\kappa$  was used as a small expansion parameter, but the conjecture was not based on quantitative relationship between  $\kappa$  and the rate of exponential divergence. Figure 6a shows that the overall tendency of  $\Lambda$  is to increase with increasing  $\dot{H}$ . It has also been found that  $\Lambda$  is small near  $\kappa \simeq 1$ , reaching  $\Lambda = 8 \times 10^{-2}$  as  $\dot{H} \rightarrow 0.25$  (i.e.,  $\kappa \rightarrow 1$ ) (Ref. 25, section 2.6). These properties are contrary to the above conjecture. Another popular notion is that  $\kappa$  can distinguish between different classes of orbits. Actual solutions show that, at any given value of  $\dot{H}$  or equivalently  $\kappa$ , there are integrable, stochastic and transient orbits. Recall that Fig. 3 depicts two orbits whose initial conditions are identical except for the phase angle, i.e., they have exactly the same value of  $\kappa$ . In addition, there are integrable orbits with the same value of  $\kappa$ . The exponential divergence rates  $\lambda^*$  for different individual orbits similarly do not have a single value for given  $\dot{H}$  and  $b_n$ . For  $\dot{H} \rightarrow \infty$ , the integrable regions vanish, and all the orbits are of the transient type [17, 18]. The transient orbits, however, do not exhibit sensitive dependence on initial conditions and are not integrable. Thus, despite its popularity,  $\kappa$  does not constitute an objective measure of chaos.

The quantity  $\kappa$  is a parameter defined by  $\kappa = (2\dot{H})^{-1/4} = b_n(\delta/\rho_0)^{1/2}$ . In the physical system described by equation (3) supplemented by equation (2b), the particle energy ( $\rho_0$ ) can be specified independently in a given magnetic field characterized by  $b_n$  and  $\delta$ . At issue is the nature of the physical system corresponding to  $\kappa \rightarrow 0$ . This limit can be attained either via  $b_n \rightarrow 0$  holding  $\rho_0$  fixed or via  $\rho_0 \rightarrow \infty$  holding  $b_n \neq 0$  fixed. These two limits are physically distinct: the former is the desired integrable limit while the latter is not integrable. In and of itself,  $\kappa \rightarrow 0$  does not imply one or the other limit. In taking the limit in the Hamiltonian or equation of motion, the normalization can dictate what limit is mathematically allowed. For example, Büchner and Zelenyi [14] normalized the equation of motion according to  $\lambda_0 \equiv (\delta/\rho_0)$  and time to  $\tau_0 \equiv (\delta/\rho_0)^{1/2}/\Omega_0$ . In this normalization,  $\kappa \rightarrow 0$  should be taken in the sense of  $b_n \rightarrow 0$  holding  $(\delta/\rho_0)^{1/2}$  fixed because  $(\delta/\rho_0)^{1/2} \rightarrow 0$  would lead to  $\tau_0 = 0$ . Thus, it is equivalent to  $b_n \rightarrow 0$ , which is the integrable neutral sheet. In this normalization, the  $x$  dependence in the Hamiltonian vanishes as  $\kappa \rightarrow 0$  if the parabolic field is used but

not if the modified Harris field is used. In Büchner and Zelenyi [15],  $\kappa$  is defined as above, but the dynamical equations and Hamiltonian are normalized according to  $X \equiv x/(b_n\delta)$  and  $\tau = \Omega_n$  where  $X$  represents normalized spatial coordinates and  $x$  the unnormalized coordinates. This normalization is identical to that of Ref. 12. In this limit,  $b_n \rightarrow 0$  cannot be taken because the spatial coordinates become singular and  $\tau = 0$ . Thus,  $\kappa \rightarrow 0$  can only be taken in the sense of  $(\delta/\rho_0) \rightarrow 0$  with  $b_n \neq 0$  which is equivalent to  $\dot{H} \rightarrow \infty$ . This is patently not the integrable limit while  $b_n \rightarrow 0$  is the integrable current sheet [12]. (No limit was applied in Ref. 12.) The problem with the  $\kappa \rightarrow 0$  limit arises partly because of the desire to fold particle energy into a single parameter to classify the integrability or the degree of chaos according to the particle energy. The particle energy enters  $\kappa$  through  $\rho_0$ . However, integrability depends on  $B_n$  but not on energy. In addition, neither  $\kappa$  nor  $\dot{H}$  is a simple energy or field parameter. Similar care may be needed in characterizing the particle motion in time-dependent models [e.g., Ref. 37].

The model given by equation (1) is independent of  $x$ . The neglect of  $x$ - and  $y$ -dependence within the current sheet is valid if  $\rho_n \ll L_x, L_y$  where  $L_x, L_y$  are the gradient scale lengths in the  $x$ - and  $y$ -directions, respectively. Karimabadi et al. [16] used an  $x$ -dependent model previously used for the magnetotail [38] and found that the dynamics of charged particles can be significantly different from the  $x$ -independent models. In particular, they found a regime in  $\dot{H}$  where the phase space area occupied by integrable orbits is much greater than that in the modified Harris field (the regime of enhanced integrability). They also found that the orbits travel substantially shorter distances in the  $x$ -direction before mirroring than in the  $x$ -independent model. In addition, with an imposed constant  $E_y$ , the particles gained unrealistically high energy. As a result, Karimabadi et al. [16] questioned the applicability of existing  $x$ -dependent field models with uniform  $E_y$ . Burkhart and Chen [24] further clarified the reason for the inapplicability. They showed that the magnetic field as seen by the orbits in the regime of enhanced integrability does not resemble the presumed field geometry of the magnetotail. Specifically, they found that the field lines in this regime are "bulb-shaped" and that the  $x$ -excursion  $\Delta$  of the orbits and the Larmor radius  $\rho_n$  are both comparable to the gradient scale length  $L_x$  in  $x$ . This is not applicable to the earth's magnetotail where  $\Delta, \rho_n \ll L_x \sim 50R_E$  [39]. The apparent agreement between the predictions based on an  $x$ -independent model and observation in the magnetotail [19] indicates that the particle dynamics in the distant magnetotail can be approximated by suitable  $x$ -independent models.

For  $B_y \neq 0$ , we must restrict ourselves to  $E_y = 0$  or make  $\mathbf{E} \perp \mathbf{B}$ . Otherwise the field aligned electric field would accelerate particles to unrealistically high energies. It is found if the  $B_y$  field becomes sufficiently large ( $B_y \gtrsim 2B_z$ ), the majority of the particles directly pass through the sheet and the resonance effects mentioned above and discussed below are negligible. This is a significant result in that it places a limit on the magnitude of the  $y$ -component of the magnetic field if the physical consequences of the resonance effects are observed.



#### 4. PHASE SPACE RESONANCE

We have discussed how the dynamical properties of this system can be graphically described using Poincaré surface of section maps. We now consider how the phase space structures may be related to physical observables. A physically important effect is the phase space resonance referred to above. It was found [17] that, at certain resonance values of  $\hat{H}$  satisfying

$$N \simeq \hat{H}_N^{1/4} - 0.6, \quad (11)$$

where  $N = 1, 2, 3, \dots$ , the entry ( $Ci$ ) and exit ( $Cf$ ) regions become nearly symmetric. The value 0.6 is a numerical scale factor, and  $\hat{H}_N$  denotes the  $N$ -th resonance energy. This equation refines the previously discussed expression  $N_i = (\hat{H}/2)^{1/4} + 1$  with  $N_i = N + 1$ , and the resonance effect incorporates the additional ingredient of symmetry in  $Ci$  and  $Cf$ . The first few resonances occur at  $\hat{H}_1 \simeq 6$ ,  $\hat{H}_2 \simeq 50$ , and  $\hat{H}_3 \simeq 170$ . For  $b_n = 0.1$ , the resonance terminates after  $N = 6$ . It is useful to note that there are  $N_i = N + 1$  prominent transient regions at resonance so that the majority of orbits traversing the current sheet return to the side from which they are incident ("backscattered") at odd- $N$  resonances while the majority of incident orbits exit to the opposite side of the current sheet ("forward scattered") at even- $N$  resonances. (Also see Ref. 25 for a detailed discussion.)

It is easy to infer from Fig. 4b that the entry regions for stochastic orbits (e.g., S1 and T1 for  $\hat{H} = 500$ ) decrease in relative phase space area as the degree of symmetry between  $Ci$  and  $Cf$  increases. By taking the mirror images of the entry regions, we can see that the area of the stochastic orbit exit regions (e.g., the cross-hatched regions in Fig. 4b) decreases as  $Ci$  and  $Cf$  become more symmetric. To see the physical effect of this resonance, consider a population of orbits at a resonance energy, uniformly distributed in phase space in the asymptotic region. Because the relative area of the stochastic orbit entry regions decreases significantly at resonance, the proportion of stochastic orbits also decreases significantly in comparison with neighboring off-resonance energies. One physical consequence is that orbits in asymptotic regions have significantly decreased probability of entering stochastic regions near the midplane. A majority of orbits entering the current sheet are transient orbits at resonance energies. Conversely, stochastic orbits in the vicinity of the current sheet have significantly reduced probabilities of escaping to the asymptotic regions, leading to increased time during which the stochastic orbits are "trapped" in the current sheet. Burkhardt and Chen [17] numerically calculated the time that stochastic orbits spend between the first and the last crossings of the midplane. This time  $\tau_s$ , referred to as the average stochastic orbit trapping time, is a measure of how long stochastic orbits spend in the neutral sheet and is a function of  $\hat{H}$  and  $b_n$ . It was found that, at the values of  $\hat{H}$  given by (11),  $\tau_s(\hat{H})$  is "anomalously" long. Figure 7 shows  $\tau_s(\hat{H})$  for  $b_n = 0.1$ . It is clear that  $\tau_s$  has well-defined peaks evenly spaced in  $\hat{H}^{1/4}$ .

By comparing Figs. 6 and 7, it is easy to see that peaks in  $\tau_s$  coincide with the valleys in  $\Delta$ . Recall that the dynamics of the system depends on two independent parameters  $\hat{H}$  and  $b_n$ ,  $b_n$  is the measure of the nonintegrable perturbation.

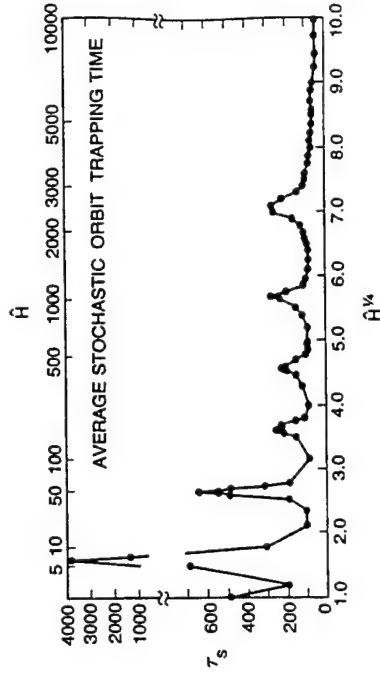


Figure 7. Average stochastic orbit trapping time. (From Ref. 17.)

A physical understanding of the resonance phenomenon can be obtained by carefully considering the phase space structures. Figure 8 shows the boundaries of the transient regions  $\partial(Cf)$  which are the time-forward mapping of orbits with incoming pitch angle  $\beta_1 = \pi/2$  at  $z = 5\delta$  as discussed earlier. These boundaries are shown by solid lines. Here,  $j = 1, \dots, f$  with  $f = 5$  for  $\hat{H} = 500$ . Also shown are the time-reversed mapping of the same asymptotic orbits. They are shown as dashed lines. Because  $y$ - and time-reversals are equivalent, the dashed lines are simply the mirror images of the solid lines. The stochastic orbit entry regions S1 and T1 are identified. (Also see Fig. 4b.) Formally, the stochastic orbit entry regions can be written as  $C1 \cap Cf \cap C(f-1) \cap \dots$ . Here  $\overline{Cj}$  denotes the complement of the region  $Cj$ , and  $\cap$  indicates the intersection of two regions. The exit regions are simply the mirror images of entry regions. Therefore, if  $C1$  and  $Cf$  are completely symmetric, then  $C1$  and  $Cf$  overlap completely and there is no entry or exit region for stochastic orbits. The value  $\hat{H} = 500$  shown in Fig. 8 is near the  $N = 4$  resonance energy. As a result,  $C1$  and  $C5$  have a large overlap. We have also shown several contours (— · —) of constant asymptotic pitch angles  $\beta_1$  which are defined at  $z = 5\delta$ . These contours are the mapping of asymptotic orbits with  $\beta_1 = 2^\circ, 30^\circ$  and  $60^\circ$ . We see that there is a critical value  $\beta_c$  such that all asymptotic orbits with pitch angle  $\beta_1 < \beta_c$  are transient orbits which do not enter the stochastic region. For  $\beta_1 > \beta_c$ , some orbits enter stochastic regions and are scattered chaotically (section 3). For  $\hat{H} = 500$ ,  $\beta_c \simeq 30^\circ$ .

Recall that the dynamics in the modified Harris model can be parameterized by two independent quantities  $\hat{H}$  and  $b_n$ . The quantity  $b_n$  plays an important role in determining the dynamics. We now discuss the dependence of the resonance phenomenon on  $b_n$ . Because of the normalization of  $\hat{H}$  defined by (7), the resonance values  $\hat{H}_N$  do not depend on  $b_n$  for  $b_n \ll 1$  [equation (11)]. However, the termination point of resonance and the number of resonance peaks are determined by  $b_n$ . The dependence of the resonance on  $b_n$  can be understood as follows [17]. There are two critical energies if the current sheet is confined to a finite thickness. The first occurs when  $\rho_0$  is comparable to the radius of curvature  $R_c = b_n \delta$  at  $Z = 0$ . Setting  $\rho_0 = R_c$ , we find

$$\hat{H} \simeq H_1 \equiv \frac{1}{2} b_n^{-2}. \quad (12)$$

This corresponds to  $d_j = (2b_n)^{1/2} \delta < \delta$  so that  $B_x \propto z$ , and the analysis leading to  $N \sim \hat{H}^{1/4}$  is applicable. As  $\hat{H}$  increases, the orbits experience more deviations from  $B_x \propto z$ , and the resonance effect weakens, resulting in a decreased degree of symmetry between C1 and C2. The resonance peaks in  $\tau_s$  and  $\tau_D$  are in fact strongest for  $\hat{H} \lesssim H_1$ , decreasing with increasing  $\hat{H}$  (Figs. 6 and 7). The second critical energy occurs when  $\rho_0 \simeq \delta \gg R_c$ , which is equivalent to  $d_i \simeq \delta$ . This energy is

$$\hat{H} \simeq H_2 \equiv \frac{1}{2} b_n^{-4}. \quad (13)$$

For  $\hat{H} \geq H_2$ , the typical midplane crossing orbits have z-excursions exceeding the current sheet thickness. The magnetic field as seen by such orbits deviates significantly from the linear dependence of  $B_x \propto z/\delta$ , and the resonance effect is no longer operative. Thus, for a given  $b_n$ , there are approximately  $2^{-1/4} b_n^{-1}$  resonance energies. For  $b_n = 0.1$ , Fig. 7 demonstrates these two properties clearly. Here,  $H_1 = 50$  and  $H_2 = 5000$ , corresponding to  $H_1^{1/4} \simeq 2.7$  and  $H_2^{1/4} \simeq 8.4$ .

The ratio  $R_1$  of the area occupied by the entry region C1 to the total area of the energy surface is

$$R_1 \simeq b_n (2\hat{H})^{1/4}. \quad (14)$$

This is applicable to resonance as well as off-resonance  $\hat{H}$  values. At resonance, it can be shown further that the ratio of the total area occupied by the transient regions to the total area of the energy surface is

$$R_T \simeq b_n 2^{1/4} \hat{H}^{1/2}, \quad (15)$$

which is simply  $N/R_1$ . We have numerically verified that the scalings  $R_1 \propto b_n \hat{H}^{1/4}$  is highly accurate (within a few percent) for  $\hat{H} < H_2$ . Physically, the explicit dependence on  $b_n$  is due to the finite thickness of the current sheet.

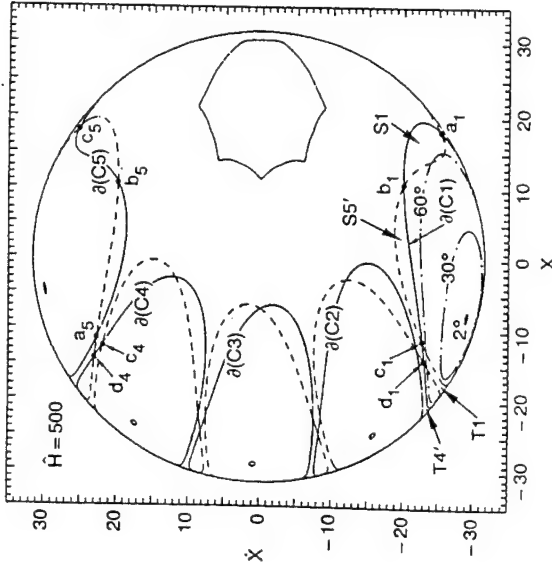


Figure 8. Phase space boundaries for the modified Harris model.  $\hat{H} = 500$  and  $b_n = 0.1$ . Solid lines are the boundaries  $\theta(C1')-\theta(C5)$ . The dashed lines are  $\theta(C1')-\theta(C5')$ . The regions S1, T1, S5' and T4' are shown. The mapping of orbits with the asymptotic pitch angle  $\beta_1$ . The contours (---) of  $\beta_1 = 2^\circ$ ,  $30^\circ$  and  $60^\circ$  are shown. The points  $a_1, b_1$ , and  $c_1$  are mapped onto  $a_5, b_5$ , and  $c_5$ , respectively. The point  $d_1$  is mapped to  $d_4$  and then to  $\infty$ .

As discussed in section 3, the entry regions for stochastic orbits (e.g., S1 of Fig. 4b or Fig. 8) are divided by fractal boundaries corresponding to different outgoing conditions. In terms of pitch angle scattering, the outgoing asymptotic pitch angle  $\beta_2$  depends sensitively on the incoming  $\beta_1$  if an orbit enters the stochastic region. Burkhardt and Chen [24] found that asymptotically field-aligned orbits (i.e.,  $\beta_1 = 0$ ) undergo regular scattering at energies near resonance values, with the outgoing asymptotic pitch angles  $\beta_2$  exhibiting no sensitive dependence on  $\hat{H}$ , while pitch-angle scattering is chaotic at off-resonance energies. This is because, at off-resonance energies, even the asymptotically field-aligned orbits enters stochastic regions so that  $\beta_c \simeq 0$ . Thus, we expect  $\beta_c$  to exhibit peaks at the resonance energies described above and to be small ( $\beta_c \simeq 0$ ) half way between neighboring resonance energies. The critical  $\beta_c(\hat{H})$  has been calculated for fixed  $b_n$  and shows such resonance behavior (see Fig. 14 of Ref. 25).

## 5. PHYSICAL CONSEQUENCES IN THE MAGNETOTAIL

One qualitatively new understanding from the dynamics point of view is the existence of disjoint phase space regions corresponding to distinct classes of orbits. The different regions are characterized by widely separated time scales. An implication is that the different regions are affected by external influences on different time scales in a time-dependent environment. The boundaries between the different regions do not allow uniform propagation of information or particle energy throughout the phase space. Suppose the system contains a population of charged particles initially in thermal equilibrium with external sources. If the conditions of the distant plasma distribution are changed, then the system cannot evolve or relax to conform to the new external conditions uniformly in time throughout the phase space. The dynamically different classes of particles retain the "memory" of the existing particle distribution for different lengths of time. This process was called "differential memory" [12]. It was suggested that differential memory would generate non-Maxwellian distribution functions and associated free-energies. This process has been demonstrated in the trilinear magnetic field [18] and in the modified Harris field [19]. In these studies, the time-evolution of distribution functions following changes in source distributions was calculated using test particles in fixed magnetic fields. It was found that accessibility time scales of the different phase space regions play an important role in the evolution of distribution functions. In our discussion below, we will use the modified Harris model.

It was found that the reduced accessibility of the stochastic regions at resonance can be manifested as peaks and valleys in distribution functions. Applying the resonance condition (11) to the earth's magnetotail and constructing model distribution functions, it was found that observed ion distribution functions do exhibit peaks and valleys occurring at energies given by equation (11) [19]. Figure 9 shows an ion distribution function (the solid line) obtained by ISEE 1. Similar distribution functions were published earlier by Huang et al. [40]. Following the model prediction, one can take the square root of the velocities (i.e.,  $H^{1/4}$ ) at which peaks and valleys occur, and the resulting values should be evenly spaced. In Fig. 10, the circles on Line A are the  $v^{1/2}$  of the peaks and valleys shown in Fig. 9, and Line A is the theoretical prediction based on equation (11). The radius of the circles is roughly the size of error bars. Lines B and C correspond to two additional distribution functions reported by Huang et al. [40]. We see that the agreement is good. The fit is obtained by demanding  $N = -0.6$  at  $v = 0$ . In this figure, it was assumed that the incoming population of orbits from the northern side of the current sheet has a higher density than that of the southern source. Then, the valleys (peaks) correspond to even- $N$  (odd- $N$ ) resonance energies. Thus, the first valley is inferred to be at  $N = 12$ .

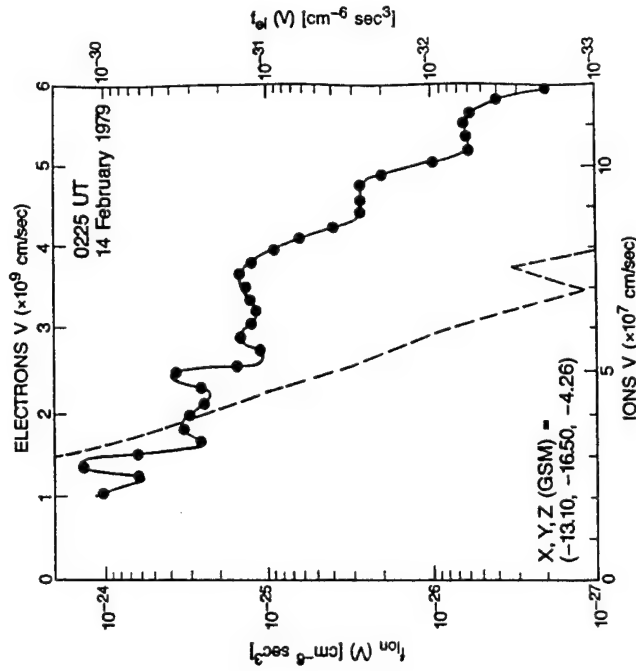


Figure 9. A velocity distribution function in the central plasma sheet ( $v_{\parallel} = 0$ ) measured by ISEE 1. The solid line is for ions (left and bottom axes) and the dashed line is for electrons (right and top axes.)

A second prediction is that electron distributions, corresponding to  $\hat{H} \ll 1$  in the magnetotail [equation (8)], do not exhibit peaks and valleys obeying the  $\hat{H}^{1/4}$  scaling law because the first resonance occurs at  $\hat{H} = 6$ . The dashed line in Fig. 9 is the electron distribution function taken at the same time as the ion distribution. We see that it is essentially structureless.

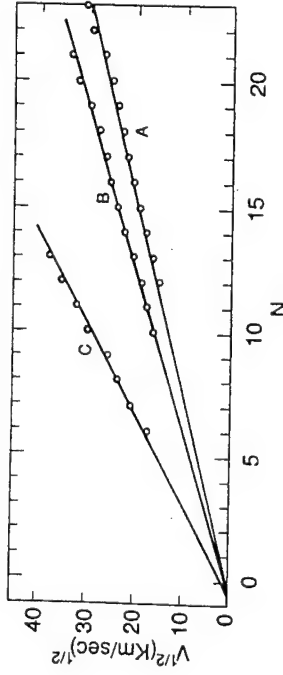


Figure 10. Comparison between theoretical predictions and observations. Circles denote the locations of the valleys and peaks. The straight lines are the theoretical predictions given by equation (15). Line A corresponds to the distribution in Figure 9a. (From Ref. 19.)

Based on the good agreement between the predicted and observed result, it was suggested [19] that the slope of the straight line could be used to infer the thickness of the current sheet using a single spacecraft. This is possible because the equilibrium current sheet thickness  $\delta$  and the Larmor radius of thermal particles are related by

$$\delta = \alpha^{-2} (8/\pi) \Gamma^2 (7/4) \rho_{th} \quad (16)$$

where  $\alpha$  is a factor order unity to be determined,  $\Gamma$  is the gamma function and  $\rho_{th} = v_{th}/\Omega_0$  with  $\Omega_0$  the Larmor frequency in the asymptotic magnetic field  $B_0$ . Using (16), we find that  $b_n \Omega_n \delta = [(8/\pi) \Gamma^2 (7/4)] \alpha^{-2} b_n^2 v_{th}$ , where  $\Omega_0 = qB_0/mc = b_n^{-1} \Omega_n$  has been used. Thus, the slope and the thermal velocity of the distribution gives the quantity  $\alpha/b_n$ . If  $\alpha$  is computed separately, a task we are presently undertaking, then  $b_n$  and hence  $\delta$  may be inferred from the observed distribution functions.

More generally, the phase space topology and the underlying dynamics are determined by global attributes of the system such as the field geometry. Local distribution function signatures which are manifestations of topological properties carry information on large-scale properties. Figure 10 and equation (16) are an example of how one can make use of observed distribution functions as diagnostic tools based on an understanding of the particle dynamics. In this regard, the scaling

exponent  $1/4$  in equation (11) arises from the dependence  $B_x(z) \propto z$  [25]. (Also see section 4.) Thus, the scaling exponent of observed distribution functions can be used to infer the average  $z$ -profile of  $B_x(z)$  as seen by particles during midplane crossing. In numerical simulation studies, the scaling law can indicate the profile of the model field as seen by the simulation particles. The agreement between theory and data shown in Fig. 10 indicates that the charged-particles see  $B_x(z) \propto z$  near the midplane in the Earth's magnetotail.

The relationship between the phase space regions and distribution functions can be illustrated as follows. First, note that the majority of orbits at even- $N$  resonance energies are scattered back toward the source by the current sheet while those at odd- $N$  resonance energies are scattered to the other side of the current sheet. At off-resonance energies, incoming particles are scattered back toward the source and to the other side of the current sheet with nearly equal probability. This process was referred to as "coherent chaotic scattering" [19]. Consider now a distribution of incoming particles in the asymptotic region on one side of the current sheet, say, on the northern ( $z > 0$ ) side. After traversing the current sheet, the particles near the even- $N$  resonance energies are manifested as beams returning to the asymptotic source region while the particles near the odd- $N$  resonances appear as depletions since the particles are coherently scattered to the other (southern) side of the current sheet. At off-resonance energies, backscattering and forward scattering occur with equal probability. A satellite would measure the superposition of particles coming directly from the source, the particles backscattered from the current sheet and the particles forward scattered from the other side of the current sheet, leading to distribution functions of the form given in Fig. 9. (See Ref. 19 for a model distribution function based on this scenario.) The reason for the coherent scattering at resonance is the enhanced degree of symmetry between C1 and C2.

The above scenario applies to  $z \gg \delta$ . In this regime, one possible interpretation of the result is that both peaks and valleys correspond to successive resonance energies. In Ref. 17, the evolution of distribution functions was evaluated at the midplane with sources placed symmetrically about  $z = 0$ . In this case, distribution functions can develop either peaks or valleys at successive resonances depending on whether the source is depleted or enhanced, respectively. These are slightly different manifestations of the same resonance effect. There may be other manifestations. For example, Ashour-Abdalla et al. [20] found beams in their test-particle simulations of the magnetotail, which are also a consequence of the resonance effect discussed above. The main difference is in the different magnetic field model used. We note here that if the magnetic field near the midplane varies as  $(z/\delta)^m$  the separation between adjacent resonances should scale as  $\hat{H}^x$ , where  $x = s/[2(s+1)]$ . For  $s = 1$  this reduces to the standard  $\hat{H}^{1/4}$  scaling. The general scaling  $H \propto \hat{H}^x$  has been verified for field aligned particles with  $s = 3$  and  $s = 5$  [26]. An implication is that the resonance in locally observed distribution functions in the tail can be used as a diagnostic tool for the field profile as seen

by particles. It is interesting to note that the chaotic particle motion in the current sheet leads to more "ordered" (i.e., non-Maxwellian), rather than more random (i.e., Maxwellian) distributions.

The same dynamical properties also play a controlling role in the equilibrium cross-tail current  $J_y(z)$  and particle density  $n(z)$  [22]. A number of one-dimensional (x-independent) self-consistent test-particle equilibrium models have been proposed. In these models, solutions of Vlasov equation satisfying  $\mathbf{J} = (c/4\pi)\nabla \times \mathbf{B}$  and  $(1/c)\mathbf{J} \times \mathbf{B} - \nabla \cdot \mathbf{P} = 0$  are sought. Some authors obtained equilibria in the regime  $v_D \gtrsim v_t$  [34, 41, 42] while others found solutions for  $v_D \ll v_t$  [22]. Here  $v_D = cE_y/B_n$  and  $v_t$  is the thermal velocity. In the Eastwood regime ( $v_D \gg v_t$ ), both current and particle densities are peaked in the current sheet while in the  $v_D \ll v_t$  regime, the particle density is nearly constant across the current sheet while  $J_y(z)$  is peaked. The latter is consistent with quiet-time magnetotail observations [43]. In the simulations described in Ref. 41, no converged equilibria could be found for  $v_D$  smaller than some critical value for given system parameters. In this work, the input distribution function is constrained to be a drifting Maxwellian parameterized by  $v_D$ . The smallest critical value was  $v_D/v_t \simeq 0.35$  with another example giving 1.2. This was interpreted as a catastrophic loss of equilibrium as  $v_D/v_t \rightarrow 0$ . In contrast, Holland and Chen [22] performed similar test-particle simulations in the  $v_D/v_t \ll 1$  regime and obtained good equilibria down to  $v_D/v_t < 0.1$ . In obtaining equilibria in this regime, they allowed the input distribution functions to have high-energy tails. In this regard, a  $\kappa$  function (Maxwellian with a power-law tail), which is prevalent in magnetospheres [44], was found to yield good equilibria at  $v_D/v_t = 0.05$ . Holland and Chen [22] attributed the lack of equilibria to the constraint that the input distribution be drifting Maxwellians. Such distributions in the  $v_D/v_t \ll 1$  regime results in strong diamagnetic currents which flow in the opposite direction to what is required by  $\mathbf{J} = \nabla \times \mathbf{B}$ . The high-energy tail or field-aligned distribution counters the diamagnetic effect. It should be noted that the catastrophe conclusion of Burkhart et al. [41] is given in terms of a parameter  $\kappa_A$ , and a physical explanation in terms of force balance argument of Francfort and Pellat [45]. Careful examination of the catastrophe result shows that (1) actual numerical convergence fails when  $v_D$  becomes small, and (2) neither  $\kappa$  nor forces of Ref. 45 is used in the numerical iteration process. Thus neither point is germane to the actual process of non-convergence. One should show that diamagnetic current is weak near the point of suggested catastrophe for a demonstration for the physical applicability of the catastrophe to the magnetotail current sheet.

The above simulations show that the pressure tensor generally has off-diagonal elements to establish force balance in both x and z directions. As the input distribution function becomes more field-aligned, the current sheet thins. A thin current sheet is more unstable to the collisionless tearing mode [46] and may be more susceptible to other forms of disruption [47]. The anisotropic pressure may also increase the growth rate of the tearing mode [48]. An interesting possi-

bility is that the auroral electric field may produce more field-aligned distribution of ions flowing tailward, resulting in thinner current sheets due to ion dynamics.

A non-Maxwellian distribution function such as the one shown in Fig. 9 also represents free-energy that can drive plasma waves. Huba et al. [49] studied linear stability properties of a model distribution function resembling Fig. 9 and found that a low-amplitude broadband electrostatic noise can be generated in the quiet-time central plasma sheet of the earth's magnetotail. The linear dispersion properties proved to be quite consistent with observed wave spectra.

In a different vein, it has been suggested [13, 32, 33] that the chaotic motion in the current sheet may constitute a form of collisionless "chaotic conductivity". Martin [13] suggested that the Lyapunov exponent may provide the time scale of decorrelation of nearby orbits, taking the place of collision frequency. Using the fluctuation-dissipation theorem and linearized Vlasov theory, Horton and Tajima [32, 33] argued that the zero frequency conductivity of the neutral sheet can be determined using the two-time velocity correlation function:

$$\sigma_{\alpha\beta} = (ne^2)/(Mv_{th}^2) \int dv f(v) \int_0^\infty d\tau C_{\alpha\beta}(\tau) \quad (17)$$

$$C_{\alpha\beta}(\tau) = \lim_{T \rightarrow \infty} \frac{1}{T} \int_0^T dt v_{\alpha}(t) v_{\beta}(t + \tau). \quad (18)$$

Calculation of  $C_{\alpha\beta}(\tau)$  showed a power-law decay in time which is suggestive of a collision-like momentum scattering and dissipation in analogy with the Lorentz gas problem. For the magnetotail,  $\sigma_{yy}$  and  $C_{yy}$  are studied because the cross-tail current is of primary interest. The idea of chaotic conductivity is an appealing one in a collisionless environment. If such a quantity could be defined and calculated for the magnetotail in terms of quantities characterizing the entire system, the electric field  $E_y$  and current density  $J_y$  could be related by a local quantity  $\sigma$  such that  $J_y = \sigma E_y$ ; by calculating how  $\sigma$  depends on the global system parameters, one could reduce global considerations to a local quantity.

Recently, Holland and Chen [50] re-examined the concept of chaotic conductivity in the magnetotail. They found that since the magnetotail is a chaotic scattering system as opposed to a classical chaotic system, the underlying assumptions leading to the use of two-time correlation functions may be inapplicable to zero-frequency conductivity and that the two-time correlation functions do not lead to a unique value of "conductivity". Due to intrinsic ambiguities in determining the initial and final points in the time integrations they showed that the correlation function  $C_{yy}$  of a given orbit can decay differently depending on how  $C_{yy}$  is computed. As an illustration of this effect, they calculated the y component of the correlation function for a typical transient orbit and the associated single particle conductivity,

$$\bar{\sigma}_{yy}(T_0) = \int_0^{T_0} C_{yy}(\tau) d\tau,$$



for several values of the time  $T$  over which the correlation function is evaluated. They focused on transient orbits since these contribute the largest percentage of the current and hence would be expected to have the largest conductivity. The total conductivity is defined by  $\sigma_{yy} = \int f(v) \tilde{\sigma}_{yy} d^3v$ , with  $T, T_0 \rightarrow \infty$ . Using an approximate analytical analysis, they were able to show that as  $T$  goes to infinity (equation (18)), the asymptotic mean value of  $\tilde{\sigma}_{yy}$  approaches zero as  $1/T$ . Thus, in practice  $\sigma_{yy}$  depends critically on the time over which  $C_{yy}$  is computed. In evaluating  $C_{yy}$  and  $\tilde{\sigma}_{yy}$ , the first crossing point was used as the starting point for the integrations since it is only in the vicinity of the midplane that the particles are expected to decorrelate. Additionally, they noted that different orbits with dissimilar correlation functions can have essentially the same energy gain. Recall that the orbits in Fig. 3 have essentially the same initial and final conditions and therefore have essentially the same net energy gain. On the other hand, these two orbits obviously contribute very differently to the cross tail current since they have very different time histories. They gave an alternative expression to calculate the energy gain [35]:

$$\Delta H = mc \left( \frac{E_y}{B_n} \right) \left( \frac{2H}{m} \right)^{1/2} (1 + b_n^2)^{-2} (|\cos \beta_1| + |\cos \beta_2|), \quad (19)$$

where  $\beta_1$  and  $\beta_2$  are the asymptotic incoming and outgoing pitch angles, respectively. The chaotic motion of particles in the vicinity of the current sheet plays no role. Numerical calculations show that this expression gives a complete description of energy gain. They also pointed out that the current density  $J_y(z)$  depends primarily on the source particle distribution and the magnetic field topology and that  $J_y$  and  $E_y$  are not related by simple relationships such as an Ohm's law. In this regard, we note that a nonzero  $E_y$  effectively modifies the source particle distribution functions and hence the current but it is in a nontrivial way. The relationship between  $\beta_1$  and  $\beta_2$  is, of course, complicated as evidenced by the existence of fractals and is determined by global magnetic topology. It is unlikely that the global magnetotail structure can be fully understood using local quantities such as a "collisionless" conductivity.

## 6. DISCUSSIONS

The charged-particle motion in the magnetotail has been extensively studied for more than two decades because of its importance for understanding a wide variety of plasma phenomena in the geospace environment. Traditionally, the emphasis was to study the motion of individual particles. The adiabaticity and nonadiabaticity of particle orbits have received considerable attention. A qualitatively different approach is to treat the particle motion as a dynamical system, and geometrical (phase space) properties are exploited to obtain and explain physical observables. The important dynamical properties are the partitioning of the

phase space and the chaotic scattering of incoming orbits by the current sheet. The underlying symmetry properties of the system are of principal importance. The significant phase space structures are robust in the presence of collisions, in contrast to properties of individual orbits. The basic dynamical properties of the magnetotail-like system have been firmly established from first principles. Moreover, the dynamical approach has yielded novel insights previously unavailable from the study of individual orbits. We emphasize that the geometrical approach yields qualitative but rigorously accurate for families of orbits. In contrast, detailed information regarding individual orbits or segments of orbits is not generic to the dynamical system.

The ability of charged particles to carry information and energy over long distances ( $\gg R_E$ ) in the essentially collisionless magnetotail means that the global particle dynamics can influence the distribution of internal energy and currents on a large scale. In view of its robustness, the partitioning of the phase space may play a significant role in determining such large scale properties. The magnetosphere may act as a self-organized critical system [51]. Unlike the usual example of sandpiles, the magnetosphere is determined by globally coherent interaction of fields and collisionless particles. Thus, the nature of long-distance coupling within the magnetosphere is an essential question. If these conclusions prove to be correct, nonlinear dynamics may indeed provide a new framework for a deeper understanding of global magnetospheric processes. (See section 3.6 of Ref. 25.) Clarification of the relationships between particle dynamics and global properties is an important subject of future research. The importance of this line of inquiry is enhanced by the fact that the magnetotail is an observationally testable paradigm for a class of systems containing current sheets.

## ACKNOWLEDGMENTS

This work was supported by the National Aeronautics and Space Administration (W-16,991) and the Office of Naval Research.

## REFERENCES

- [1] T. W. Speiser, *J. Geophys. Res.* **70**, 4219 (1965).
- [2] I. I. Alekseyev, and A. P. Kropotkin, *Geomagn. Aeron. (Engl. Transl.)* **10**, 615 (1970).
- [3] B. U. Ö. Sonnerup, *J. Geophys. Res.* **76**, 8211 (1971).
- [4] H. I. West, R. M. Buck, and M. G. Kivelson, *J. Geophys. Res.* **83**, 3805, 1978.
- [5] H. I. West, R. M. Buck, and M. G. Kivelson, *J. Geophys. Res.* **83**, 3819 (1978).
- [6] J. S. Wagner, J. R. Kan, and S.-I. Akasofu, *J. Geophys. Res.* **84**, 891 (1979).
- [7] P. Gray, and L. C. Lee, *J. Geophys. Res.* **87**, 7445 (1982).



- [8] N. A. Tsyganenko, *Planet. Space Sci.* **30**, 433 (1982).
- [9] L. R. Lyons, and T. W. Speiser, *J. Geophys. Res.* **87**, 2276 (1982).
- [10] T. J. Birmingham, *J. Geophys. Res.* **89**, 2699 (1984).
- [11] L. R. Lyons, *J. Geophys. Res.* **89**, 5479 (1984).
- [12] J. Chen, and P. J. Palmadesso, *J. Geophys. Res.* **91**, 1499 (1986).
- [13] R. F. Martin, *J. Geophys. Res.* **91**, 11985 (1986).
- [14] J. Büchner, and L. M. Zelenyi, *Phys. Lett. A* **118**, 395 (1986).
- [15] J. Büchner, and L. M. Zelenyi, *J. Geophys. Res.* **94**, 11821, 1989.
- [16] H. Karimabadi, P. L. Pritchett, and F. V. Coroniti, *J. Geophys. Res.* **95**, 17153 (1990).
- [17] G. R. Burkhardt and J. Chen, *J. Geophys. Res.* **96**, 14033 (1991).
- [18] J. Chen, H. G. Mitchell, and P. J. Palmadesso, *J. Geophys. Res.* **95**, 15141 (1990).
- [19] J. Chen, G. R. Burkhardt, and C. Y. Huang, *Geophys. Res. Lett.* **17**, 2237 (1990).
- [20] M. Ashour-Abdalla, J. Berchem, J. Büchner, and L. M. Zelenyi, *Geophys. Res. Lett.* **18**, 1603 (1991).
- [21] D. L. Holland and J. Chen, *Geophys. Res. Lett.* **18**, 1579 (1991).
- [22] D. L. Holland and J. Chen, *Geophys. Res. Lett.* **20**, 1775 (1993).
- [23] J. Chen, J. L. Rexford, and Y. C. Lee, *Geophys. Res. Lett.* **17**, 1049 (1990).
- [24] G. R. Burkhardt and J. Chen, *J. Geophys. Res.* **97**, 6479 (1992).
- [25] J. Chen, *J. Geophys. Res.* **97**, 15011 (1992).
- [26] J. Chen, *Phys. Fluids B* **5**, 2663 (1993).
- [27] D. B. Curran, C. K. Goertz, and T. A. Whelan, *Geophys. Res. Lett.* **14**, 99 (1987).
- [28] D. B. Curran and C. K. Goertz, *J. Geophys. Res.* **94**, 272, (1989).
- [29] R. F. Martin, and T. W. Speiser, *J. Geophys. Res.* **93**, 11521 (1988).
- [30] G. R. Burkhardt, J. F. Drake, and J. Chen, *J. Geophys. Res.* **96**, 11539 (1991).
- [31] G. Joyce, J. Chen, S. Slinker, and D. L. Holland, this volume, 1994.
- [32] W. Horton and T. Tajima, *Geophys. Res. Lett.* **17**, 123, 1990.
- [33] J. W. Horton and T. Tajima, *J. Geophys. Res.* **96**, 15811 (1991).
- [34] J. W. Eastwood, *Planet. Space Sci.* **20**, 1555 (1972).
- [35] S. W. H. Cowley, *Planet. Space Sci.* **26**, 539 (1978).
- [36] V. A. Sergeev and N. A. Tsyganenko, *Planet. Space Sci.* **30**, 999 (1982).
- [37] S. C. Chapman, *J. Geophys. Res.* **99**, 5977 (1994).
- [38] B. Lembège and R. Pellat, *Phys. Fluids* **25**, 1995 (1982).
- [39] K. W. Behannon, *J. Geophys. Res.* **73**, 907 (1968).
- [40] C. Y. Huang, C. K. Goertz, L. A. Frank, and G. Rostoker, *Geophys. Res. Lett.* **16**, 563 (1989).
- [41] G. R. Burkhardt, J. F. Drake, P. B. Dusenbery, and T. W. Speiser, *J. Geophys. Res.* **97**, 13799 (1992).
- [42] P. L. Pritchett and F. V. Coroniti, *J. Geophys. Res.*, **97**, 16773 (1992).
- [43] D. J. McComas, C. T. Russell, R. C. Elphic, and S. J. Bame, *J. Geophys. Res.* **91**, 4287 (1986).
- [44] S. P. Christon, D. J. Williams, D. G. Mitchell, L. A. Frank, and C. Y. Huang, *J. Geophys. Res.* **94**, 13409 (1989).
- [45] Ph. Francfort and R. Pellat, *Geophys. Res. Lett.* **3**, 433 (1976).
- [46] B. Coppi, G. Laval, and R. Pellat, *Phys. Rev. Lett.* **16**, 1207 (1966).
- [47] A. T. Y. Lui, C.-L. Chang, A. Mankofsky, H.-K. Wong, and D. Winske, *J. Geophys. Res.* **96**, 11389 (1991).
- [48] J. Chen and P. J. Palmadesso, *Phys. Fluids* **27**, 1198 (1984).
- [49] J. D. Huba, J. Chen, and R. R. Anderson, *J. Geophys. Res.* **97**, 1533 (1992).
- [50] D. L. Holland and J. Chen, *Geophys. Res. Lett.* **19**, 1231 (1992).
- [51] P. Bak, C. Tang, and K. Wiesenfeld, *Phys. Rev. A* **38**, 364 (1988).

PARTICLE ENERGIZATION NEAR AN X-POINT IN THE  
MAGNETOTAIL BASED ON GLOBAL MHD SIMULATION FIELDS

Glenn Joyce, James Chen, and Steven Slinker,  
Beam Physics Branch, Plasma Physics Division,  
Naval Research Laboratory,  
Washington, DC 20375

Daniel L. Holland<sup>†</sup>  
Physics Department, Illinois State University, Normal, IL

## ABSTRACT

Particle acceleration near an X-point in the magnetotail is studied using two dimensional test particle simulations. The magnetotail electric and magnetic field structures are taken from the NRL three dimensional global magnetohydrodynamic (MHD) simulation model which gives a description of the solar wind-magnetosphere interaction. The solar wind conditions correspond to a southward pointing interplanetary magnetic field (IMF). Test particles are generated from a model ion source distribution function that is consistent with the macroscopic MHD parameters in the lobe region outside the current sheet boundary. The particles are pushed through the system, and particle distribution functions are determined earthward and tailward of the X-point. Two ion energy populations are found. One has a low energy distribution with an energy that is similar to the injection energy. This population corresponds to particles that have not crossed the region of the reversal of the  $B_x$  magnetic field. The other population consists of particles which have crossed that region and have energies on the order of a few kilovolts. The details of the acceleration process are determined from an analysis of the motion of randomly selected particles from the simulation.

## I. INTRODUCTION

The Earth's magnetosphere exists because of the interaction between the solar wind and the Earth's dipole field. The large-scale organization of the magnetosphere is established by magnetic fields and essentially collisionless charged particles. A particularly important region of the magnetosphere is the nightside magnetotail that is believed to store the energy released in substorms, a manifestation of global reconfiguration of the magnetic topology. The

<sup>†</sup>NRC/NRL Postdoctoral Research Associate

magnetotail contains the hot Central Plasma Sheet (CPS) surrounded by the cold lobes. The Earth with its neutral atmosphere is enveloped by the ionosphere which is, in turn, coupled to the magnetosphere. Many important physical processes affecting the ionospheric and terrestrial environments are caused by the dynamics of the entire magnetosphere. Conversely, the global dynamics are strongly influenced by the electrical properties of the ionosphere.

Traditionally, the global properties of the magnetosphere have been modeled using MHD simulations. Two examples of these simulations are those constructed by the NRL and UCLA space physics groups. Kinetic processes have been usually studied using simplified mesoscale magnetic and electric fields. For example, Cowley [1], Lyons and Speiser [2], Doxas et al. [3], Horton and Tajima [4,5], and Holland and Chen [6] modeled particle energization in the magnetotail current sheet while Chen et al. [7,8], Burkhardt and Chen [9], and Ashour-Abdalla et al. [10] have modeled particle distribution functions in the central plasma sheet. Wagner et al. [11], Matthaeus et al. [12], Martin, [13], Curran et al. [14], Curran and Goertz [15], Martin and Speiser [16], Burkhardt et al. [17, 18], Moses et al. [19], MacAulay [20], and Speiser & Martin [21] have investigated particle energization in configurations including magnetic X lines. These studies sought to isolate energization mechanisms in specific regions for detailed investigation. However, the physical conditions affecting these regions are determined by the global magnetosphere whose state is controlled by the incident solar wind momentum flux and the interplanetary magnetic field (IMF).

Some recent studies have started to examine how different regions in the magnetosphere can influence each other. For example, the structure of the plasma sheet boundary layer may be strongly influenced by the reconnection process [22,23]; the polar wind may significantly determine the plasma populations in the CPS [24]; and the auroral region electric field can control the near-Earth current sheet structure [25]. The CPS particle distributions that result from particles originating in the lobes have been studied by Ashour-Abdalla et al. [10]. These studies and others may eventually lead to a better understanding of how the properties of the magnetosphere in a localized region can be related to the global properties.

The magnetospheric fields for these models have been based on simple idealizations [26] or on phenomenological fields such as the Tsyganenko [27] model. In the latter approach, a uniform electric field  $E_z$  is imposed on the Tsyganenko field in the dawn-to-dusk direction. The advantage of this method is that the magnetic field is a statistical composite of the actual system, while the disadvantage is that the field may not correspond to any instantaneous magnetospheric configuration. Another disadvantage of this model is that the imposed uniform electric field is not self-consistent. The latter is potentially a serious shortcoming. For example, the energy and momentum flux (i.e.,  $E \times B$ ) are not consistent with the global magnetosphere and the solar wind conditions.

In this paper, we take a different approach to study kinetic properties of the global magnetosphere. We use the electric and magnetic fields given by a global magnetohydrodynamic (MHD) model. We use test-particle simulations to calculate kinetic properties in the MHD fields. MHD models can only approximate the actual solar wind-magnetosphere system based on large-scale energy and momentum balance. However, the fields are self-consistent within the set of basic MHD approximations. In particular, the global energy and momentum transport are treated self-consistently. Thus, we expect to obtain a kinetic picture implied by the global magnetosphere as described by MHD. The physical process of interest in this paper is particle energization and particle entry from the lobes into the CPS near an X-point. We will use the magnetic and electric fields from the Naval Research Laboratory (NRL) global MHD simulation model [28]. In particular, we will consider the magnetotail under the influence of a southward IMF and will study particle energization and ion distribution functions for these configurations. In these calculations, the magnetic X-line and the CPS form a coupled region. The significant new features of the field model are (1) electric field that is self-consistent within the MHD approximations, (2) presence of self-consistent  $B_x$ ,  $B_y$ , and  $B_z$  components, (3) asymmetric X-line and CPS configurations, and (4) perhaps most important, magnetospheric configurations given in relation to IMF conditions.

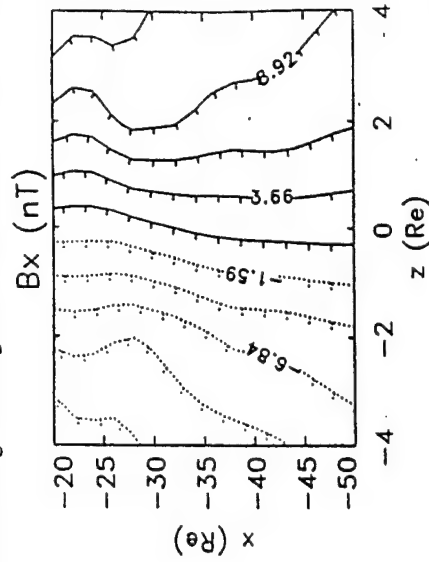


Fig. 1. Contour plot of  $B_x$  taken from the MHD simulation code for a model South IMF.

## II. MHD MODEL OF THE MAGNETOSPHERE

We will first describe the global simulation model developed at NRL, which will constitute the MHD framework to be used in our work. The MHD model will be used as a surrogate global system. We will then discuss the state

of the magnetosphere corresponding to southward IMF. In particular, we will focus on the electric and magnetic fields in the magnetotail and the lobes. We then discuss our model in which test-particle trajectories are calculated using the self-consistent MHD fields. The NRL 3D magnetosphere model uses ideal MHD equations to describe the solar wind and the magnetosphere. The model contains an ionosphere represented as a region inside an inner spherical boundary to the MHD region at 3.5 Earth radii  $R_E$ . The presence of a model of the physics near the earth allows an active interaction between the resistive ionosphere and the rest of the magnetosphere. The model ionosphere has a time varying conductance with a "solar" component to represent photoionization and an auroral conductance that is calculated from the magnetospheric properties.

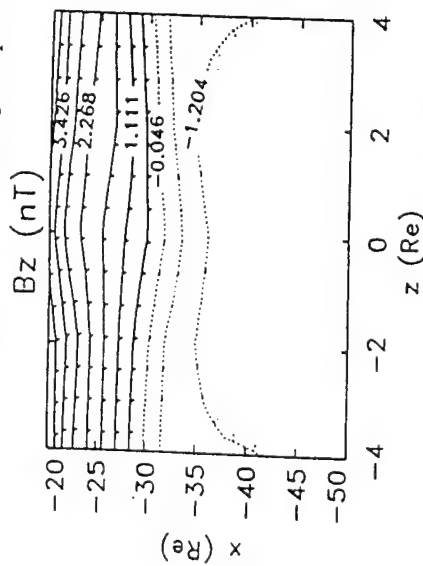


Fig. 2. Contour plot of  $B_z$  taken from the MHD simulation code for a model South IMF. The transition from north to south directed field occurs at about  $x = -30R_\odot$ .

This allows the model to distinguish between the nightside and dayside. The model ionosphere provides a means of relating  $J$  to  $B$  in the near Earth region. The ionospheric currents determine an electrostatic potential that is mapped outward to the magnetospheric boundary. The potential is used to derive an electric field used in the temporal integration of Faraday's Law to update the magnetic field on that boundary. The magnetosphere simulation domain consists of a cylindrical region aligned along the Earth-Sun line with a radius  $60 R_E$ . The ends of the cylinder extend from  $30 R_E$  sunward to up to  $300 R_E$  tailward. Experimental and model solar wind parameters have been used at the outer boundaries of the magnetosphere to complete the model.

The algorithm has been developed to minimize numerical dissipation, but like other models of this class, the representation of current sheet disruption and reconnection are determined, in part by numerical effects. For example, when two oppositely directed magnetic field lines are closer than the grid spacing, the

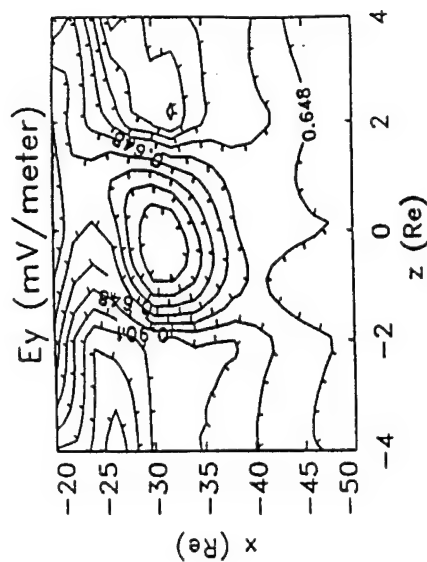


Fig. 3. Contour plot of  $E_y$  field taken from the MHD simulation code for a model South IMF.

code connects the lines. The model reconnection process, then, is determined from a combination of the influence of the model ionosphere and, to a lesser extent, from numerical properties. The reconnection process cannot be described by the ideal MHD formalism. One of the purposes of the kinetic test particle studies is to attempt to provide a realistic estimate of the dissipative processes in disruption regions that can be incorporated into a general MHD model of the magnetosphere. This could, perhaps, have the form of a resistivity. Even with dissipation mechanisms added to a numerical model, the grid resolution will be an important aspect of modeling small scale phenomena such as reconnection. The ionosphere is critically determined by the

The state of the global magnetosphere is critically determined by the solar wind and IMF. For example, severe geomagnetic disturbances are associated with southward turning of the IMF at the dayside magnetopause. The current paradigm is that a southward IMF leads to reconnection at the dayside magnetopause, allowing injection of magnetic flux and solar wind particles into the magnetosphere. This overall picture is qualitatively reproduced by the global MHD model [29]. In our paper, we focus on a particular time period and investigate the kinetic properties of ions. The configuration used throughout this paper was obtained by starting with a steady initial state with a northward IMF and turning the IMF southward. Several interesting properties have been observed in this model system including periods of open and closed magnetospheres, the formation and disruption of neutral points and, at times, the

occurrence of more-or-less steady state reconnection. In particular, there is a case using model data as solar wind input in which after the IMF changes direction from north to south a period of steady state reconnection takes place. The final position of the X-line is at  $x = -32 R_e$  in the usual magnetospheric coordinate system. This appears to be the long time solution from the model. Unless the IMF is turned northward the neutral point will remain here. We have used the model MHD fields and flows from this period to provide a framework for studying the dynamics of charged particles near the neutral point. These fields allow us to study a portion of the magnetosphere that is consistent with the near equilibrium of the global system including the IMF.

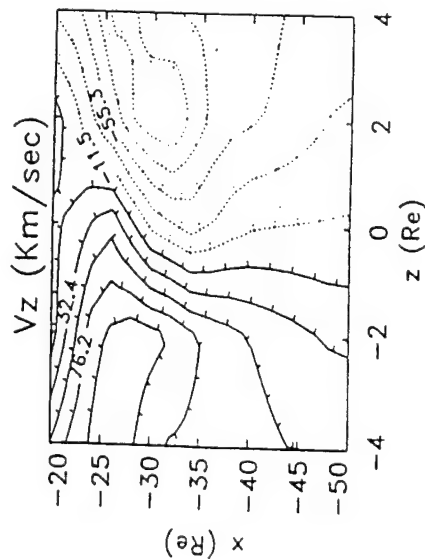


Fig. 4. Contour plot of the flow velocity  $V_z$  from the MHD simulation code. The contours represent a strong flow from the lobes to the central current sheet.

Figs. 1 through 3 show various fields taken from the MHD model for the case of southward IMF. The range of all these figures is from  $-20 < x < -50 R_e$  and  $-4 < z < +4 R_e$  and are shown in the  $y=0$  plane, where  $x$  is the Sun-Earth line pointing sunward,  $y$  is the crosstail direction with  $y=0$  in the noon-midnight plane and  $z$  points north. Figure 1 is a contour plot of the  $x$  component of the magnetic field  $B_x$ . The field varies from  $-12$  to  $12$  nT on the earthward side of the plot and has a scale size of transition from positive to negative of about  $3 R_e$  in the  $z$  direction. This transition region, corresponding to the current sheet, is larger than is generally inferred experimentally. Ideal MHD does not treat the current sheet region accurately and the computational grid is too sparse to resolve the region well. This is one of the weaknesses of this model. In order to accurately describe the magnetotail current sheet, ions must be treated kinetically as described in the introduction. These effects are

neglected in ideal MHD. Figure 2 shows a contour of the  $B_z$  component of the magnetic field. The  $B_z$  field passes through zero at about  $x = -32 R_e$  and defines the position of the X-line. Earthward from the X-line the field begins to be influenced by the Earth's dipole field. Tailward, the field is negative and slowly varying. The value is about  $-2$  nT in this region. Figure 3 shows the  $y$  component of the electric field ( $E_y$ ) which is inferred from MHD through the relation  $E = -V \times B$ . The value of  $E_y$  is typically  $0.5$  to  $1$  mV/meter except in the immediate vicinity of the neutral point where the electric field is smaller because the magnetic field is small there. Figure 4 shows the  $z$  component of the MHD flow velocity ( $V_z$ ), while Figure 5 shows the  $V_x$  flow velocity. From these figures, we expect particles entering the neutral region earthward of the neutral point to be convected earthward while particles entering tailward of the neutral point to be convected tailward. In addition, we see that particles entering from the lobes tend to be drawn into the central region (around  $z=0$ ) as a consequence of the  $E \times B$  drifts. If the IMF is northward, the magnetic flux and particle energy entry into the magnetosphere is significantly reduced from the southward IMF case, and the magnetosphere reaches a quasi-steady configuration.

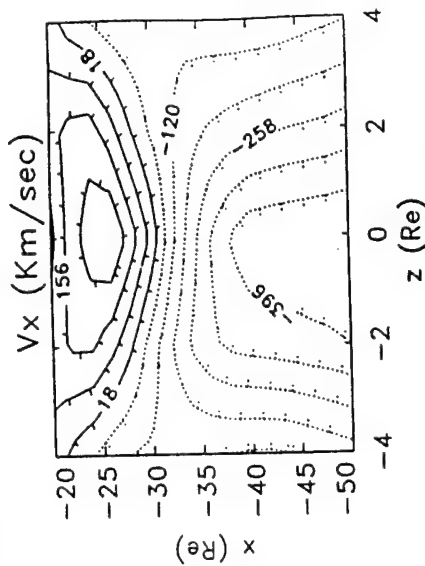


Fig. 5. Contour plot of the flow velocity  $V_x$  from the MHD simulation code. The contours represent an Earthward flow Earthward of the  $x$  point and a tailward flow tailward of the  $x$  point.

### III. TEST PARTICLE SIMULATION MODEL

Our computational model consists of following the orbits of a large number (40,000-50,000) of ions on a two dimensional grid (in  $x$  and  $z$ ) which is selected to be in the  $y=0$  plane. The simulation region for the parameters described above is  $-50 < x < -20 R_e$  and  $-4 < z < +4 R_e$ . This region

contains the neutral point approximately in the center and extends earthward until the Earth's dipole field becomes the dominant field. The magnetic and electric fields are taken from the MHD code interpolated to this grid from the cylindrical grid of the global model, and are frozen in time. We have used the electric fields as inferred from the  $\mathbf{V} \times \mathbf{B}$  relation as discussed above. We investigated the possibility of replacing the  $\mathbf{E}$ , field with a constant field of  $0.5 \text{ mV/m}$ , while requiring that  $\mathbf{E} \cdot \mathbf{B} = 0$ . We found, however, that changing the electric field in an ad hoc manner changes the velocity flow patterns from those of the global model. Using flows inconsistent with the MHD velocities would not be consistent with the pressure balance determined by the global model.

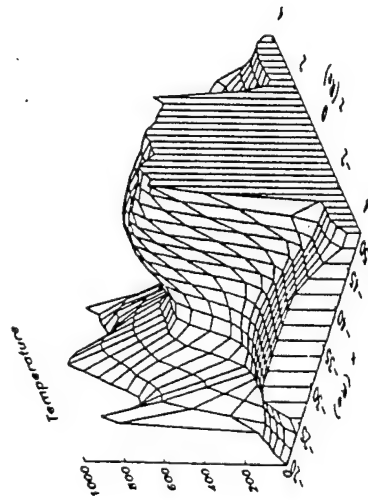


Fig. 6. Surface plot of the kinetic temperature determined from the test particles for the south IMF. The lobe temperature is assumed to be 200 eV. Including directed velocity, the kinetic energy reaches a maximum of 3000 keV in the vicinity of  $x = -50 R_e$ .

The particle pushing algorithm uses a standard method in which the velocities are taken on the half time steps and the positions are on the full time steps. The gyromotion is calculated using the procedure introduced by Boris [30,31]. The particles are injected into the system from the lobe region. For the simulation, this consists of injecting particles at random points along the line  $-45 < x < -25 R_e$  at  $z = \pm 4 R_e$  and  $y = 0$ . The boundaries of the lobe regions, and the injected particles have a relatively low kinetic temperature. The particles are chosen to have an isotropic Maxwellian distribution with  $T = 200 \text{ eV}$  in the lobe region. The boundary at  $x = -50 R_e$  is far enough away from the neutral point to be considered in the far tail in the model. We follow the orbits of the particles until they leave the system. Several averaged particle quantities are

calculated while the particles are in the system. They are the particle density, the three components of the particle velocity,  $V_x, V_y, V_z$ , and six components of the products of the velocity,  $V_x^2, V_y^2, V_z^2, V_x V_y, V_x V_z$ , and  $V_y V_z$ . These quantities are calculated using standard particle laydown techniques. The resulting quantities are the densities, current densities, and terms necessary for the calculation of the kinetic pressure. In addition, we have averaged the kinetic pressure terms to obtain a kinetic temperature for the system.

The positions and velocities of the particles leaving through the end points are recorded and are later analyzed to determine the velocity distributions. Distribution functions are determined for these particles as a function of  $V_{\parallel}$  and  $V_{\perp}$  (where  $\parallel$  and  $\perp$  represent the directions parallel and perpendicular to the local magnetic field) at various regions in  $z$ . Finally, a number of particles are tracked throughout their orbits and the energization process for these particles is investigated. These diagnostics have given us some insight into the formation of energetic particles in the magnetotail.

The kinetic temperature is shown in Figure 6. In the lobe regions, the temperature is about 200 eV which is the assumed input temperature. In the central current sheet region, the temperature is higher ranging from about 600 eV in the vicinity of the X-point to about 1000 eV both Earthward and tailward of the X-point. This represents continual heating of the plasma particles along the central current sheet region.

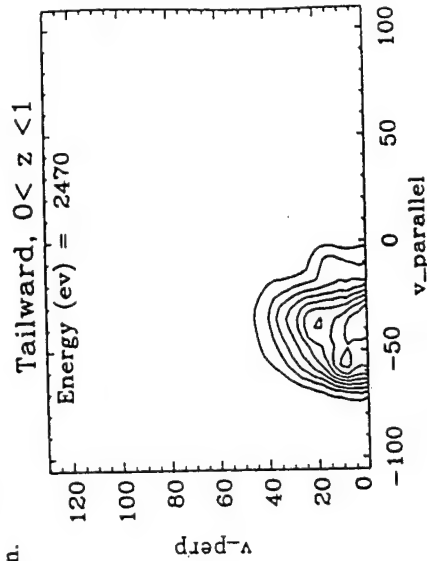


Fig. 7. Distribution function of particles leaving the system at  $x = -50 R_e$  and  $0 < z < 1 R_e$ . There are two distinct populations, a small number of particles which have not crossed the  $z = 0$  plane and have an average energy of 325 eV and a population of particles which have crossed the  $z = 0$  plane at least once and have an average energy of 2500 eV.

We have analyzed the distribution of particles that leave the system



through the ends of the simulation region. Figures 7 through 10 show the velocity distribution functions of particles as they leave the simulation box in the tailward direction. The functions are averages of particles that are broken into fairly large regions, each  $1 R_e$  wide and extending from  $z = 0$  to  $z = 4 R_e$ . We have not included particles leaving in the negative  $z$  direction because the system is relatively symmetric north to south. The particles leaving each segment were formed into distribution functions of  $V_{\parallel}$  and  $V_{\perp}$  where the perpendicular and parallel directions are determined from the magnetic field seen by each particle.

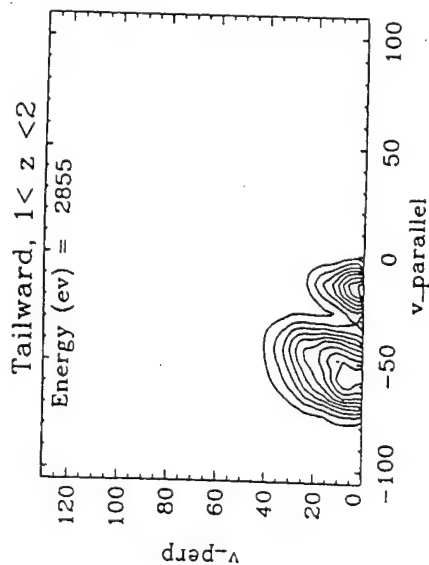


Fig. 8. Distribution function of particles leaving the system at  $x = -50 R_e$  and  $1 < z < 2 R_e$ . There are two distinct populations, those particles which have not crossed the  $z = 0$  plane and have an average energy of 325 eV and those particles which have crossed the  $z = 0$  plane at least once and have an average energy of 3000 eV.

The most notable property of the distribution functions is their binary nature. There is a low energy component which has an energy comparable with the injected energy of the particles, and a high energy component with the energy in the range of a few keV. The particles comprising the low energy distribution are those that have reached the end of the system without ever crossing the  $z = 0$  plane. The particles in the high energy distribution have made at least one crossing of the plane. The nature of the high and low energy portions of the distribution functions do not change significantly in the various  $z$  regions. However, the relative sizes of the two energy portions of the distribution functions are different because of the number of particles that have made crossings of the  $z = 0$  plane. The relative number of accelerated to unaccelerated particles decreases with distance from the axis until at  $z = 4 R_e$  there is no population of accelerated particles. This is especially apparent in

Figures 8 and 9. In these figures both populations are visible with the high energy population dominant in the range  $1 < z < 2$  and the low energy population dominant in the range  $2 < z < 3$ . There is, in fact, some energy gain, but the particles do not gain the keV or so of energy seen in the inner regions.

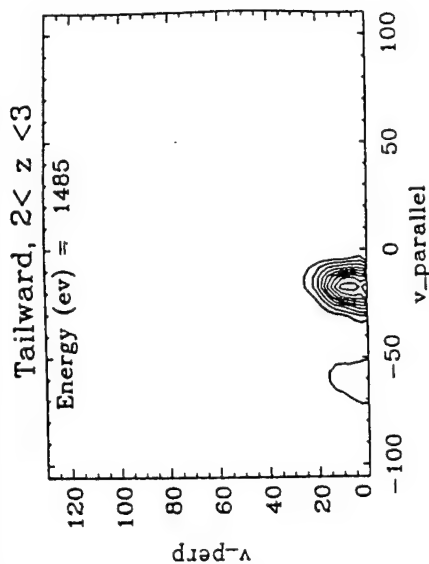


Fig. 9. Distribution function of particles leaving the system at  $x = -50 R_e$  and  $2 < z < 3 R_e$ . There are two distinct populations, those particles which have not crossed the  $z = 0$  plane and have an average energy of 385 eV and those particles which have crossed the  $z = 0$  plane at least once and have an average energy of 4200 eV.

It appears, then, that an observable ion signature tailward of the interaction with an X-line is the simultaneous presence of two energy distributions. Field lines mapping to the lobe regions of the vicinity of the X-line contain distributions made up primarily of particles of low energy typical of the lobe region. Particles on field lines nearer the center of the current sheet are populated with ions in the few keV range. Between these two extremes there will be a mixture of the two energies with the relative population of high energy ions increasing toward the center of the current sheet. The distribution of particles leaving the system on the earthward side differs in many respects from that of the tailward distribution.

The energy gain of the particles is on the order of one kilovolt and the division of particles into two energy groups is less pronounced. In this region, the Earth's dipole field is the dominant magnetic field, so the field-aligned direction has a large  $z$  component unlike that of the tailward region. A larger number of the injected particles travel tailward than earthward although they are introduced symmetrically around the neutral point. This is a departure from the prediction of the MHD model in which the flow direction is away from the neutral point.

This behavior has also been noted by Martin (Private communication 1993). Finally, we note that the  $V_{\perp} - V_{\parallel}$  distributions in Figures 7-10 which are slightly elongated in the  $V_{\perp}$  direction are consistent with observation [32] and with those calculated by Martin and Speiser [16].

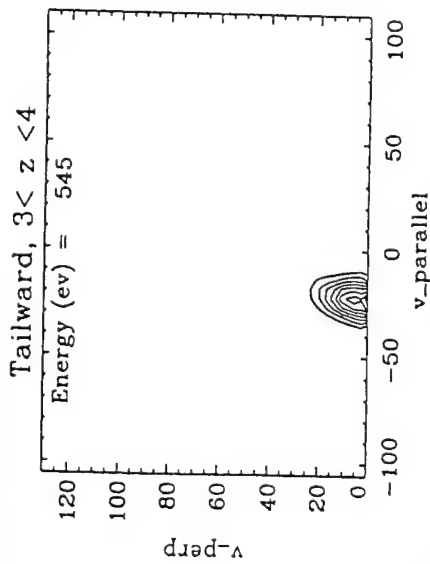


Fig. 10. Distribution function of particles leaving the system at  $x = -50 R_e$  and  $3 < z < 4 R_e$ . In this region, there are no particles which have crossed the  $z = 0$  plane.

In order to demonstrate the energization process, we have studied the orbits of some randomly selected particles. Summaries of a few of these orbits are shown in Figures 11 and 12. Because of the strong  $V_z$  drifts toward the center of the system, in both figures, the initial motion is directed primarily inward. This is the case with all the orbits we have analyzed. When the particles reach the vicinity of  $z = 0$ , they move in the  $x$  direction and eventually reach the simulation system boundary. A majority of the particles leave the system tailward. The particles which cross the  $z$  axis are accelerated to higher energy. This behavior should be contrasted with the general picture of particle motion in a north IMF configuration in which the particles pass the  $z = 0$  plane repeatedly and make large excursions in  $z$ . Many of them eventually leave the system at  $z$  values corresponding to their injection point [25]. Figures 11a-11b show the  $z$  position of the ion orbit as a function of  $x$  and  $y$ . Figures 11c-11d are plots of the kinetic energy of the particle as functions of the coordinates  $z$  and  $y$ . The particle motion near the injection points begins with a general  $\text{ExB}$  drifting toward the  $z = 0$  plane. The motion is a spiraling drift until it reaches the region of weak magnetic field. Near  $z = 0$ , the particle is accelerated in the positive  $y$  (dawn-to-dusk) direction by the  $E_y$  field and its kinetic energy increases with each crossing of  $z = 0$ . In the weak field region, the particle motion changes to relatively large excursions in  $y$  until it leaves the central

region and again is under the influence of a strong magnetic field. A particle generally gains energy when it is moving in the positive  $y$  direction (the direction of the  $E_y$  field component), and is near  $z = 0$ . At other times, the particle gains and loses energy along its gyro-orbit without a significant net gain or loss of energy over the time of a gyroperiod. Figures 12 shows an example of another particle. The general behavior is the same in all the cases we have investigated with the particles making energy gains on each crossing of the axis. Some particles cross many times while some cross only once. We note that the particles need not cross the neutral point itself to gain energy. In fact, in this model, the electric field goes to zero at the point of zero magnetic field. In order to gain energy, however, they must sample the small magnetic field region when there is a significant  $E_y$  field.

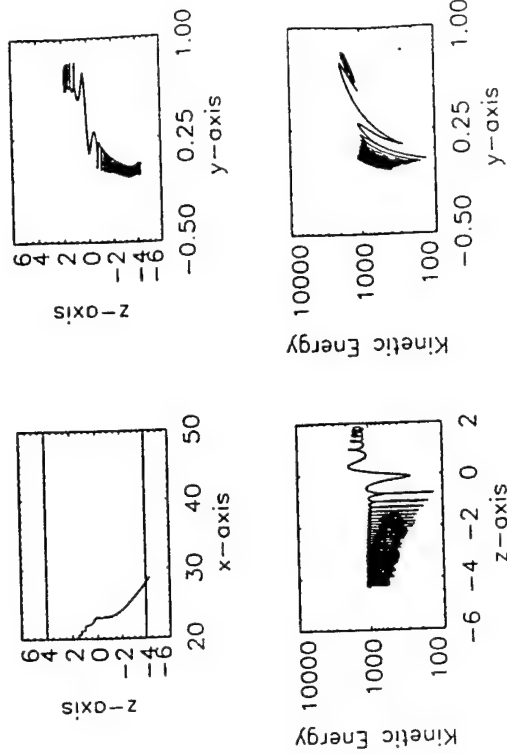


Fig. 11. The orbit and energy of a randomly selected test ion.

- a)  $z$  vs.  $x$  for the particle
- b)  $z$  vs.  $y$  for the particle
- c) kinetic energy vs.  $z$
- d) kinetic energy vs.  $y$

We point out that for all sample orbits, the particles gain energy while they are in the vicinity of  $z = 0$  and that the amount of energy gained (of the order of a few keV) is consistent with the observed temperatures of the CPS. This effect in our test-particle simulation is consistent with the global momentum balance as described by MHD. In contrast, it has been noted earlier [33] that particles can gain unrealistically high energy in two dimensional

magnetic fields with imposed uniform  $E_y$ . This shows the importance of using a self-consistent  $E_y$  based on global momentum balance. It is also interesting to note that separate particle populations (e.g. lower energy vs. higher energy components) are generated during the energization process. The final distribution is not Maxwellian. In the magnetosphere the typical distribution function has the form of a K function with nearly Maxwellian low energy component and a power-law high energy component [34]. In our simulation, inadequate statistics prevent us from making any quantitative conclusions, but the simulated distributions in Figs. 7-9 drop off more slowly than Maxwellian at the higher energies, while Fig. 10 is more nearly Maxwellian.

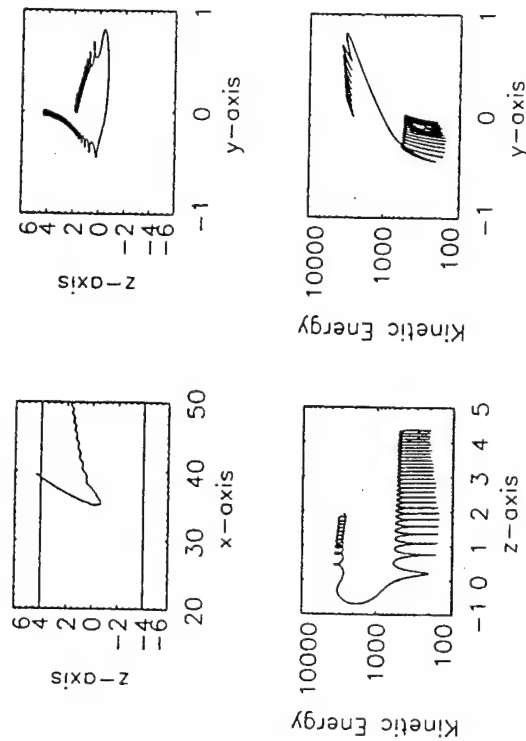


Fig. 12. The orbit and energy of a randomly selected test ion.  
a)  $z$  vs.  $x$  for the particle b)  $z$  vs.  $y$  for the particle  
c) kinetic energy vs.  $z$  d) kinetic energy vs.  $y$

#### IV. SUMMARY

We have used the global framework offered by the NRL MHD simulation code to provide the electric and magnetic fields necessary to investigate charged particle dynamics and energization in the current sheet region of the magnetosphere during steady state reconnection near a neutral point. Although the magnetotail current sheet is not a region where the assumptions of the MHD model are satisfied, the general features generated by

the code are similar to those expected in this part of the magnetosphere. An exception is the scale size of the  $B_z$  transition that should be on the scale of an ion gyroradius, but is several earth radii in the MHD picture. Detailed distribution function information can be obtained from particle tracking using static fields from the MHD code. By analyzing selected orbits, we have determined that the largest energy gain occurs over a small portion of their orbits, namely during crossings of the  $z = 0$  plane. Energy gains tailward of the neutral point are on the order of a few keV while the energy gained by particles in the earthward direction is more modest. In the tailward region, the distribution function divides naturally into two energy components, one for particles that have crossed the  $z = 0$  plane and those that have not.

From our experience, it appears that the three dimensional MHD model can be used to track particles between various regions of the magnetotail, and may provide a basis to extend our knowledge of the role of charged particles in the formation of magnetosphere structure.

#### ACKNOWLEDGMENTS

We would like to thank Joel Fedder and John Lyon for making the results of their study of the south IMF case available to us. This work was supported by the National Aeronautics and Space Administration under Grant No. W-16,991 and the Office of Naval Research.

#### REFERENCES

- [1] S. W. H. Cowley, *Planet. Space Sci.*, **26**, 539, 1978.
- [2] L. R. Lyons and W. Speiser, *J. Geophys. Res.*, **87**, 2276, 1982.
- [3] I. Doxas, W. Horton, K. Sandusky, T. Tajima, and R. Steinolfson, *J. Geophys. Res.*, **95**, 12,033, 1990.
- [4] W. Horton and T. Tajima, *Geophys. Res. Lett.*, **17**, 123, 1990.
- [5] W. Horton, W. and T. Tajima, *J. Geophys. Res.*, **96**, 15,811, 1991.
- [6] D. L. Holland and J. Chen, *Geophys. Res. Lett.*, **19**, 1231, 1992.
- [7] J. Chen, G. R. Burkhardt, and C. Y. Huang, *Geophys. Res. Lett.*, **17**, 2237, 1990a.
- [8] J. Chen, H. G. Mitchell, and P. J. Palmadesso, *J. Geophys. Res.*, **95**, 15,141, 1990b.
- [9] G. R. Burkhardt and J. Chen, *J. Geophys. Res.*, **96**, 14,033, 1991.
- [10] M. Ashour-Abdalla, J. P. Berchem, J. Büchner, and L. M. Zelenyi, *J. Geophys. Res.*, **98**, 5651, 1993.
- [11] J. S. Wagner, P. C. Gray, J. R. Kan, T. Tajima, and S. I. Akasofu, *Planet. Space Sci.*, **29**, 391, 1981.
- [12] W. H. Matthaeus, J. J. Ambrosiano, and M. L. Goldstein, *Phys. Rev. Lett.*, **53**, 1449, 1984.
- [13] R. F. Martin Jr., *J. Geophys. Res.*, **91**, 11985, 1986.

- [14] D. B. Curran, C. K. Goertz, and T. A. Whelan, *Geophys. Res. Lett.*, **14**, 99, 1987.
- [15] D. B. Curran, and C. K. Goertz, *J. Geophys. Res.*, **94**, 272, 1989.
- [16] R. F. Martin and T. W. Speiser, *J. Geophys. Res.*, **93**, 11,521, 1988.
- [17] G. R. Burkhardt, J. F. Drake, and J. Chen, *J. Geophys. Res.*, **95**, 18,833, 1990.
- [18] G. R. Burkhardt, J. F. Drake, and J. Chen, *J. Geophys. Res.*, **96**, 11,539, 1991.
- [19] R. W. Moses, J. M. Finn, and K. M. Ling, *J. Geophys. Res.*, **98**, 4013, 1993.
- [20] A. K. MacAulay, Steady state magnetic reconnection in two finite dimensions: comparison of resistive magnetohydrodynamic and collisionless kinetic results, EOS Supplement, p. 522, October, 1993.
- [21] T. W. Speiser, and R. F. Martin Jr., *J. Geophys. Res.*, **97**, 10775, 1992.
- [22] T. G. Onsager, M. F. Thomsen, J. T. Gosling, and S. J. Bame, *Geophys. Res. Lett.*, **17**, 1837, 1990.
- [23] T. G. Onsager, M. F. Thomsen, R. C. Elphic, and J. T. Gosling, *J. Geophys. Res.*, **96**, 20999, 1991.
- [24] D. C. Delcourt, J. A. Sauvaud, and T. E. Moore, *J. Geophys. Res.*, **98**, 9155, 1993.
- [25] D. L. Holland and J. Chen, *Geophys. Res. Lett.*, **20**, 1775, 1993.
- [26] J. Chen, *J. Geophys. Res.*, **97**, 15,011, 1992.
- [27] N. A. Tsyganenko, *Planet. Space Sci.*, **30**, 5, 1989.
- [28] J. A. Fedder, J. G. Lyon, and C. Mobarry, *Geophys. Res. Lett.*, **18**, 1047, 1991.
- [29] J. A. Fedder, J. G. Lyon, S. P. Slinker, submitted to *J. Geophys. Res.*, 1993.
- [30] J. P. Boris, Relativistic plasma simulation-optimization of a hybrid code, in *Proc. Fourth Conf. Num. Sim. Plasmas*, Naval Res. Lab., Wash., DC 1970.
- [31] C. K. Birdsall and A. B. Langdon, *Plasma Physics via Computer Simulation*, Adam Hilger, New York 1991.
- [32] D. DeCoster, and L. A. Frank, *J. Geophys. Res.*, **84**, 5099, 1979.
- [33] H. Karimabadi, P. L. Pritchett, and F. V. Coroniti, *J. Geophys. Res.*, **95**, 17,153, 1990.
- [34] S. P. Christon, D. J. Williams, D. G. Mitchell, L. A. Frank, and C. Y. Huang, *J. Geophys. Res.*, **94**, 13409, 1989.

# Global Consequences of Nonlinear Particle Dynamics in the Magnetotail

JAMES CHEN AND DANIEL L. HOLLAND<sup>1</sup>

*Beam Physics Branch, Plasma Physics Division, Naval Research Laboratory, Washington, D. C.*

Recent research efforts from the nonlinear dynamics point of view have yielded new insights into the relationships between the particle motion, global magnetic field geometry, and local plasma properties. Some novel theoretical predictions regarding local distribution functions and equilibrium structure of the current sheet have been made based on the dynamics of charged particles, yielding good agreement with observed data. A new framework of understanding kinetic physics of the magnetosphere is emerging. This paper gives a tutorial review of the nonlinear dynamics of charged particles in the magnetotail.

## 1. INTRODUCTION

The motion of charged particles is an essential ingredient for fully understanding plasma properties in a collisionless environment. In a system where the charged particle Larmor radii are much smaller than any spatial length scales, the particle motion can be well approximated by adiabatic theory. Adiabatic invariance may also be applicable if the time variation of the system is sufficiently slow relative to the gyroperiod. If the Larmor radii are much greater than any spatial scale lengths, one may be able to assume unmagnetized particle motion. However, if the Larmor radii and spatial scale lengths are comparable, the particle motion is nonadiabatic and is generally difficult to analyze. If, in addition, particle-particle or wave-particle interactions exist, collectively referred to as "collisions" in this paper, then the complexity of the particle motion is further increased.

The magnetosphere is made up of many distinct regions but exhibits globally coherent behavior governed by large-scale fields and collisionless charged particles. Figure 1 is a schematic drawing of the Earth's magnetosphere with various regions indicated. The coordinate system is shown. A region of particular interest is the nightside magnetotail which plays a central role in the storage and release of magnetic energy, thus controlling the dynamics of the entire magnetosphere. The magnetotail consists of the lobe and the central plasma sheet (CPS) which contains a thin current sheet at the midplane,  $z = 0$ , where the  $x$ -component of the magnetic field reverses sign. The internal structure of the magnetosphere is determined by the solar wind via large-scale momentum balance and energy and par-

ticle input. In this collisionless system, energy transport and coupling between different regions are critically determined by the charged-particle motion in the large-scale fields.

The current sheet represents magnetic energy, and its dynamics have been a long-standing topic of research. Numerous studies of the motion of particles in the magnetotail have been carried out [Speiser, 1965; Alekseyev and Kropotkin, 1970; Sonnerup, 1971; West *et al.*, 1978a, b; Wagner *et al.*, 1979; Gray and Lee, 1982; Tsyganenko, 1982; Lyons and Speiser, 1982; Birmingham, 1984; Lyons, 1984; Chen and Palmadesso, 1986; Martin, 1986; Büchner and Zelenyi, 1986, 1989; Karimabadi *et al.*, 1990; Burkhardt and Chen, 1991]. The box on the right in Figure 1 shows the basic configuration of magnetic field models used in many theoretical studies. In the early works, individual orbits were studied [Speiser, 1965; West *et al.*, 1978a, b; Wagner *et al.*, 1979] using adiabatic invariance and deviations therefrom [Sonnerup, 1971; Birmingham, 1984]. More recently, Büchner and Zelenyi [1989] have extended the treatment of the action integral  $I \equiv \oint \dot{z} dz$  [Sonnerup, 1971] to calculate the variation  $\Delta I$  due to the nonadiabatic motion using an asymptotic matching approximation (the so-called slow separatrix crossing theory [Cary *et al.* [1986]]).

A different approach is to consider families of orbits and phase space topology of the system rather than individual orbits. Chen and Palmadesso [1986] first showed that there exist only two global constants of the motion in involution in the magnetotail topology and that the particle motion is nonintegrable. Using the Poincaré surface of section technique, they found that the phase space is partitioned into disjoint regions occupied by dynamically distinct classes of orbits: unbounded stochastic (chaotic), unbounded transient and bounded integrable (regular) orbits. Based on the partitioning of the phase space, they proposed a process called "differential memory" (section 5) which can significantly influence the time-evolution of plasma

Space Plasmas: Coupling Between Small  
and Medium Scale Processes  
Geophysical Monograph 86  
Copyright 1995 by the American Geophysical Union

distributions. This process arises from the property that different phase space regions are occupied by orbits with widely separated orbital time scales so that the respective phase space regions can retain memory of existing population of particles for different lengths of time. The time scales referred to here are the accessibility time, the time for orbits far away from the midplane to reach (i.e., "access") various regions of the phase space. Differential memory has been used to model plasma distribution functions in the magnetotail [Chen *et al.*, 1990a, b; Burkhardt and Chen, 1991; Ashour-Abdalla *et al.*, 1991], yielding results in agreement with observations [Chen *et al.*, 1990a]. The underlying partitioning of the phase space proved to be robust in the presence of collisional effects [Holland and Chen, 1991]. The same partitioning and differential memory also determine the current sheet equilibria [Holland and Chen, 1993]. Thus the nonlinear particle dynamics controls both local and global properties of the central plasma sheet (CPS).

Büchner and Zelenyi [1986] proposed a mapping to model the chaos in this system. The mapping is based on discrete jumps in the action, which were evaluated later using the separatrix crossing technique [Büchner and Zelenyi 1989]. In this approach, one divides a given trajectory into a sequence of segments and maps the action of one segment to that of the next using the variations in the action. Full solutions have not been generated for the modified Harris or parabolic field models using this mapping theory to date. A fully solved mapping has been applied to a model field in which different segments of a trajectory are calculated analytically and then matched [Chen *et al.*, 1990b]. The field is idealized but has the quasi-neutral sheet topology, and the basic dynamical properties are common to the more realistic models.

The magnetotail current sheet is a chaotic scattering system in which the outgoing conditions exhibit sensitive dependence on the incoming conditions [Chen *et al.*, 1990c; Burkhardt and Chen, 1991]. The basic nonlinear dynamical properties of the system are now well established, and the reader is referred to recent reviews for more detail [Chen, 1992, 1993]. In another configuration of interest, Martin [1986] studied the nonlinear dynamics of charged particles in an X-type neutral line, using the maximal Lyapunov exponent to quantify the degree of chaos. Possible distribution function signatures [Curran *et al.*, 1987; Curran and Goertz, 1989; Martin and Speiser, 1988] and the kinetic structure of X-type reconnection regions [Burkhardt *et al.*, 1990, 1991; Moses *et al.*, 1993] have been studied.

Much work has been done to explore the physical implications of nonlinear particle dynamics [e.g., Curran *et al.*, 1987; Martin and Speiser, 1988; Curran and Goertz, 1989; Chen *et al.*, 1990a, b; Karimabadi *et al.*, 1990; Horton and Tajima, 1990, 1991; Burkhardt and Chen, 1991; Ashour-Abdalla *et al.*, 1990, 1991]. Some novel predictions based directly on the topological, i.e., geometrical, properties of the phase space have proved to be in good agreement with observed data [Chen *et al.*, 1990a; Burkhardt and Chen, 1991]. In light of such successes, one can justifiably state that the study of particle motion and

plasma properties in the magnetotail within the new framework of nonlinear dynamics has emerged from a *descriptive* stage and entered a *predictive* stage. This in turn has provided an impetus for further development of this subject. For example, attempts are being made to include time dependence in the understanding of particle dynamics [Chapman and Watkins, 1993; Chapman, 1994]. The present paper is intended to give an introductory overview of recent findings relevant to the Earth's magnetotail. It is based on the full-length review paper of Chen [1992] with additional information on the dynamics with  $B_y \neq 0$  and chaotic conductivity. We will illustrate how the global field topology determines the locally measurable distribution functions, and how the current sheet is critically influenced by conditions in other regions such as the ionosphere. Because the charged particles are collisionless in the magnetosphere, processes occurring on micro- to macro-scales are coupled through the particle motion governed by the large-scale fields.

## 2. THE DYNAMICAL SYSTEM

A simple field model for the magnetotail is

$$\mathbf{B}(z) = B_0 f(z) \hat{x} + B_y \hat{y} + B_n \hat{z}, \quad (1)$$

where  $f(z) \rightarrow \pm 1$  as  $z \rightarrow \pm\infty$  so that  $B_0 = B_x(z \rightarrow \infty)$ .  $B_n$  is the uniform field normal to the midplane ( $z = 0$ ),  $B_y$  is a uniform field across the tail, and  $B_0 f(z)$  is a field-reversed neutral sheet profile. (See Figure 1 for the coordinate system.) The function  $f(z)$  is often chosen to be antisymmetric about  $z = 0$  with  $f(z = 0) = 0$ . For the earth's magnetotail we typically consider  $b_n \equiv B_n/B_0$  of the order of 0.05 ~ 0.1 for the distant magnetotail, but  $b_n$  can be larger near the Earth. The  $B_x$  component is determined by the solar wind conditions, and  $b_y \equiv B_y/B_0$  can have a range of values. In this article, we will use the gauge such that the vector potential is  $\mathbf{A} = A_x(z) \hat{x} + A_y(x, z) \hat{y}$ . Then,

$$A_x(z) = B_y z, \quad (2a)$$

$$A_y(x, z) = -B_0 F(z) + B_n x, \quad (2b)$$

where  $F(z)$  is defined by  $dF(z)/dz \equiv f(z)$ , with the total asymptotic magnetic field  $B = (1 + b_y^2 b_n^2 + b_n^2)^{1/2} B_0$ . The conclusions in this paper, however, are independent of gauge.

Two commonly used forms of  $f(z)$  are the Harris model  $f(z) = \tanh(z/\delta)$  and the parabolic model  $f(z) = z/\delta$  where  $\delta$  is the characteristic half-thickness of the neutral sheet. These two models give, respectively,

$$F(z) = \delta \ln[\cosh(z/\delta)], \quad F(z) = (1/2)z^2/\delta.$$

In the simplest case,  $B_y = 0$  is used. In the vicinity of the midplane ( $z/\delta \lesssim 1$ ), we have  $\tanh(z/\delta) \sim z/\delta$ , giving



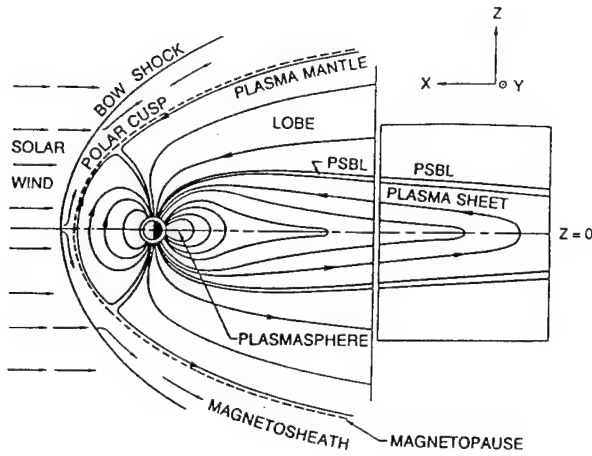


Fig. 1. Schematic drawing of the earth's magnetosphere. Magnetic field lines and various regions are depicted. The coordinate system is shown. (From Chen [1992].)

$\ln[\cosh(z/\delta)] \simeq (1/2)(z/\delta)^2$  so that the Harris and parabolic field models are similar for  $z/\delta \lesssim 1$ . If  $z/\delta \gtrsim 1$ , on the other hand, the two model fields diverge significantly. In particular, for the Harris model, if  $|z|$  is greater than some  $z_0 \gg \delta$ , we have  $B_x \simeq B_0$ , and the magnetic field is essentially uniform. We will refer to  $|z| > z_0$  as the asymptotic regions. For the parabolic field model the magnitude of  $f(z)$  continues to increase with increasing  $|z|$ , the current density is everywhere uniform, and there is no well defined asymptotic region. The essence of the asymptotic regions is the physical property that the current sheet is surrounded by regions with significantly less current, where the particle motion is qualitatively different from that inside the current sheet. Dynamically, this is manifested in the chaotic scattering nature of the system. From a modelling point of view, the dynamics in the asymptotic (or external) regions can be considered separately. Thus, the parabolic field should be "truncated" for application to any realistic system, for example, by setting  $f(z) = 1$  for  $|z| \gg \delta$ . The system then becomes topologically equivalent to the modified Harris model. Thus, Büchner and Zelenyi [1990] heuristically incorporated separatrix crossing into a truncated parabolic field model. In both field models, the radius of curvature  $R_c = B_n/(\partial B_x/\partial z)$  at  $z = 0$  is  $R_c = b_n \delta$ . West *et al.* [1978b] found that the pitch-angle distributions calculated in a  $B_x$  field with "roll-off" provided by  $\tanh(z/\delta)$  fit the observed data better than the models with power law dependence on  $z$  such as the parabolic field. Dynamically, these two configurations are qualitatively different. We will refer to these two models as the "modified Harris" and the "parabolic field" models, respectively. Both will be collectively referred to as quasi-neutral sheets as opposed to pure neutral sheet for which  $B_n = 0$ .

The single-particle motion can be described by the equation of motion

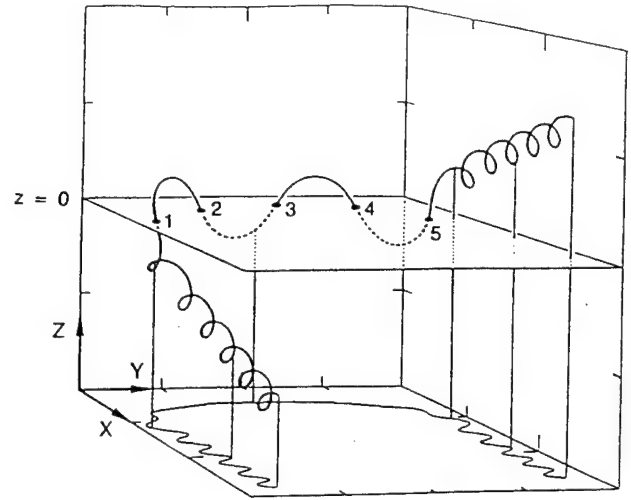


Fig. 2. A Speiser orbit. The crossing points at  $Z = 0$  are indicated.  $\tilde{H} = 500$  and  $b_n = 0.1$ . The  $Z$  axis is expanded by 1.2. (Adapted from Chen and Palmadesso [1986].)

$$m \frac{dv}{dt} = \frac{q}{c} \mathbf{v} \times \mathbf{B}. \quad (3)$$

In general, a nonzero  $E_y$ , albeit small during quiet times, exists. If we take  $B_y = 0$  and  $B_n = \text{constant}$ , a uniform  $E_y$  can be simply transformed away by an  $\mathbf{E}_y \times \mathbf{B}_n$  translation. A nonuniform  $\mathbf{E}$  field is more complicated and will not be considered.

There are two important time scales for the quasi-neutral sheet. One is  $\Omega_0 \equiv eB_0/mc$  and the other is  $\Omega_n \equiv eB_n/mc$ . The corresponding Larmor radii are  $\rho_0 \equiv v/\Omega_0$  and  $\rho_n \equiv v/\Omega_n$  where  $v$  is the velocity.

It has been known that the particle motion in the magnetotail is nonadiabatic. Speiser [1965] first identified a class of orbits in the modified Harris configuration with  $B_y = 0$ , which are sometimes called Speiser orbits. Figure 2 shows such an orbit. This particle executes adiabatic motion far away from the midplane (noncrossing motion), enters the current sheet where it oscillates in the  $z$  direction, traverses the midplane while crossing the midplane at points 1, 2, 3, 4, 5, and is then ejected from the current sheet. The number of midplane crossings depends on the energy and is found to be roughly proportional to  $\tilde{H}^{1/4}$  [Chen and Palmadesso, 1986], where  $\tilde{H}^{1/4}$  is the normalized Hamiltonian (see equation (7) below). While traversing the midplane, the particle motion is a combination of "meandering" (midplane crossing) motion [Sonnerup, 1971] and gyration about the weak  $B_n$  field. For some time, the basic properties of the particle motion were understood in terms of the Speiser orbits and within the framework of adiabatic invariance and deviations therefrom [e.g., Speiser, 1965; Sonnerup, 1971; Eastwood, 1972; Cowley, 1978; Lyons and Speiser, 1982, 1985; Speiser and Lyons, 1984]. However, West *et al.* [1978a, b] found orbits whose

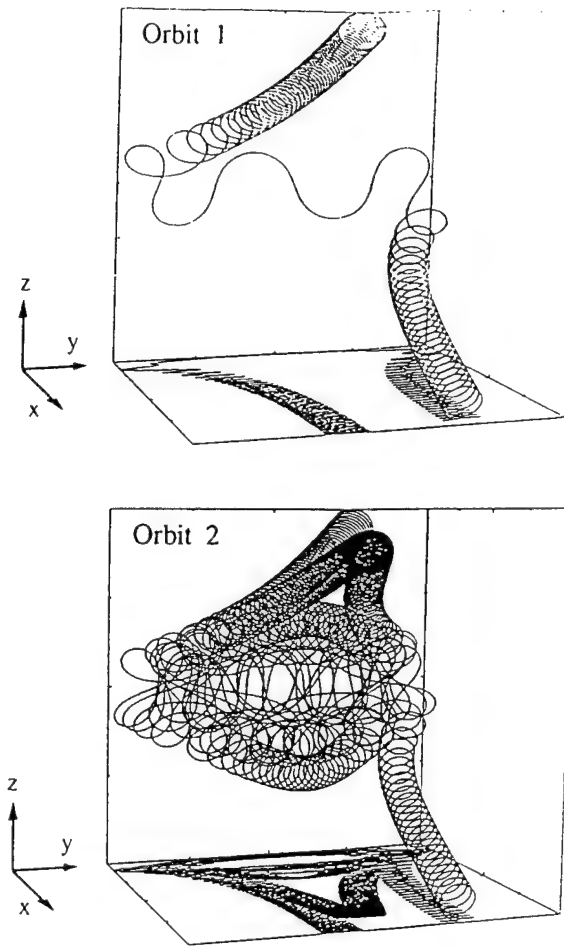


Fig. 3. Trajectories of two orbits with initial conditions  $\tilde{H} = 500$ ,  $\beta = 100^\circ$ , and  $z = 3.5\delta$ . Orbit 1 has  $\theta = 20^\circ$  and orbit 2 has  $\theta = 50^\circ$ . From Holland and Chen [1991]

behaviors are qualitatively different from those of the Speiser orbits. They studied high-energy electron orbits which make repeated traversals of the midplane before finally escaping to infinity. By one traversal, we will refer to the motion of entering and leaving the midplane once. One traversal generally has multiple midplane crossings. Figure 2 shows one traversal with five crossings. Wagner *et al.* [1979] also found similar ion orbits and noted that considerable variation in the motion of certain orbits occurs even with nearly identical initial conditions. This property is illustrated in Figure 3 which shows two orbits whose initial conditions differ only in the phase angle

### 3. NONLINEAR DYNAMICS OF CHARGED PARTICLES

Equation (3) possesses three exact constants of the motion:  $H = mv^2/2$ ,  $P_y = mv_y + (q/c)A_y(x, z)$ , and  $C_x \equiv$

$m(v_x - \Omega_n y + \Omega_n b_y z)$ . However, it was found that these constants are not in involution, having  $[C_x, P_y] = -m\Omega_n \neq 0$ , where use was made of  $[y, P_y] = 1$  [Chen and Palmadesso, 1986]. This suggests that the system is not integrable. Extensive numerical evidence was given to support this suggestion. Note that the canonical momenta  $P_x$  and  $P_y$  are not simultaneously conserved in this system even though the magnetic field is manifestly invariant under translation in both the  $x$ - and  $y$ -directions. This is because of the fact that magnetic field is given by a vector potential,  $\mathbf{B} = \nabla \times \mathbf{A}$ . This causes the Hamiltonian to depend on  $x$  and  $z$  (or on  $y$  and  $z$  in a different gauge). If an  $N$ -dimensional system has  $N$  constants  $\{C_1, \dots, C_N\}$  in involution, i.e.,  $[C_i, C_j] = 0$  for all  $i, j \leq N$ , then the system is completely integrable, and there exists a canonical transformation to a coordinate system with  $N$  cyclic coordinates such that the first integrals  $C_i$  are the new canonical momenta. For  $B_y \neq 0$ , the above condition,  $[C_x, P_y] = -m\Omega_n$ , remains unchanged. Note that particle motion in the magnetic field  $\mathbf{B}(z) = B_0 f(z)\hat{x} + B_y(z)\hat{y}$  is completely integrable because  $C_x = P_x$ , where  $P_x$  is the  $x$  canonical momentum, and  $[P_x, P_y] = 0$ .

It is convenient to rewrite equation (3) in a dimensionless component form [Chen and Palmadesso, 1986]:

$$\frac{d^2 X}{d\tau^2} = \frac{dY}{d\tau} - b_y \frac{dZ}{d\tau}, \quad (4)$$

$$\frac{d^2 Y}{d\tau^2} = \frac{d}{d\tau} \{b_n^{-2} \ln [\cosh(b_n Z)] - X\}, \quad (5)$$

$$\frac{d^2 Z}{d\tau^2} = b_y \frac{dX}{d\tau} - b_n^{-1} \tanh(b_n Z) \frac{dY}{d\tau}, \quad (6)$$

where the normalization is  $X \equiv (x - P_y/m\Omega_n)/b_n\delta$ ,  $Y \equiv (y + C_x/m\Omega_n)b_n\delta$ ,  $Z \equiv a/b_n\delta$ ,  $\tau \equiv \Omega_n t$  and  $\dot{X} \equiv dX/d\tau$ . Here, we have assumed the modified Harris model of the magnetic field,  $E_y = 0$ , and  $b_n \equiv B_n/B_0 \neq 0$ . The normalized Hamiltonian is

$$\tilde{H} \equiv H / (mb_n^2 \Omega_n^2 \delta^2). \quad (7)$$

With  $B_y = 0$ , equations (4)–(7) show that the modified Harris model requires two parameters to specify the dynamics:  $b_n$  and  $\tilde{H}$ . In the parabolic field model,  $b_n \neq 0$  can be normalized away and only  $\tilde{H}$  is needed. If  $B_y \neq 0$ , one additional parameter  $b_y$  need be specified in each case. The integrable limit  $b_n \rightarrow 0$  cannot be taken directly in either field model. The limit  $\tilde{H} \rightarrow \infty$  corresponds to two distinct physical limits:  $b_n \rightarrow 0$  or  $H \rightarrow \infty$  where  $H$  is the unnormalized Hamiltonian. The former leads to the integrable neutral sheet while the latter is not integrable.

For  $B_y = 0$ , equations (4)–(6) are invariant under  $Z \mapsto -Z$  and under the simultaneous replacement  $Y \mapsto -Y$  and  $\tau \mapsto -\tau$ . The latter symmetry operation implies that  $Y$  reversal (not invariant) and  $\tau$  reversal are equivalent. With  $B_y \neq 0$ , the simultaneous replacement of  $Z \mapsto -Z$  and  $b_y \mapsto -b_y$  is an invariant symmetry operation as is the simultaneous replacement of

$Y \leftrightarrow -Y$ ,  $\tau \leftrightarrow -\tau$ , and  $b_y \leftrightarrow -b_y$ . The symmetry properties of the system are important for determining dynamical properties of the entire system.

The previous studies of particle dynamics in the magnetotail have been largely limited to the  $B_y = 0$  case, and we will primarily discuss this case. However, we will briefly describe the generic phase space properties with  $B_y \neq 0$  using the surface of section technique later in this section.

The fundamental dynamics of electrons is identical to that of ions. Aside from the trivial difference in the direction of motion, the main difference is the applicable regimes of  $\hat{H}$ . Using the normalization (7), a given value of  $H$  in physical units gives

$$\hat{H}_e = (m_e/m_i) \hat{H}_i, \quad (8)$$

where  $\hat{H}_e$  and  $\hat{H}_i$  are  $H$  normalized for  $m_e$  and  $m_i$ , respectively.

In terms of the normalized quantities, we can write  $\hat{H} = (1/2b_n^4)(\rho_0/\delta)^2$  with  $\rho_n = \rho_0/b_n$ . The normalized Larmor radii are  $\hat{\rho}_0 = b_n(2\hat{H})^{1/2}$  and  $\hat{\rho}_n = (2\hat{H})^{1/2}$ . In this paper, we will use capital letters for dimensionless coordinates and lower case letters for unnormalized coordinates. Other normalized quantities will be denoted by carets.

Another frequently used parameter is  $\kappa = (R_c/\rho_n)^{1/2} = (2\hat{H})^{-1/4}$ , which has been used to parameterize pitch-angle scattering by the current sheet with  $B_y = 0$  [West et al., 1978b; Sergeev and Tsyganenko, 1982; Sergeev et al., 1983]. Büchner and Zelenyi [1989] expanded the Hamiltonian for  $\kappa \ll 1$  and proposed to use  $\kappa$  as a measure of chaos. This, however, proved to be inconsistent with the actual solutions (section 3).

The dynamical system represented by equations (4)–(7), or equation (3), was first described in detail using the Poincaré surface of section technique for  $B_y = 0$  [Chen and Palmadesso, 1986]. For example, one can consider a plane at  $z = 0$  and record the coordinates  $X$  and  $\dot{X}$  as an orbit crosses the plane. The orbit in Figure 2 would leave five crossing points,  $(X_1, \dot{X}_1), \dots, (X_5, \dot{X}_5)$ , in the midplane. One can then record these points and construct a constant-energy phase space plot which describes the long-time dynamical properties graphically. Figure 4a shows a surface of section plot constructed at  $Z = 0$  for  $\hat{H} = 500$  and  $b_n = 0.1$  in the modified Harris model. This technique provides a graphic representation of the first return map. For example, in Figure 2, point 3 is the first return map of point 1, and point 5 is the mapping of point 3. Figures 4a–4b show all the generic phase space properties for this system. The most prominent feature is the sharp division of the phase space. The region denoted by  $A$  is an integrable (regular) region, and it is surrounded by region  $B$  referred to as a stochastic or chaotic region. The regions denoted by  $C$  are referred to as transient regions.

For  $B_y = 0$ , the equations of motion are symmetric in  $Z$ . As a result, the two directions of crossing at the midplane,  $\dot{Z} > 0$  and  $\dot{Z} < 0$ , need not be distinguished. For  $B_y \neq 0$ , however, the  $Z$ -symmetry is lost, and the two directions of midplane crossing must be distinguished by using two phase space surfaces at

$Z = 0$ . For example, if  $B_y \neq 0$ , points 1, 3, 5 and points 2, 4 would be on different surfaces. Figures 4c–4d show the two return maps with  $B_y = B_n = 0.1B_0$  and  $\hat{H} = 500$ . The regions  $A$ ,  $B$ , and  $C$  are again occupied by integrable, stochastic, and transient orbits. Regions  $D$  are analogous to regions  $C$  and exist separately from regions  $C$  because of the lack of  $Z$  symmetry. These figures will be discussed in more detail later.

In the integrable region, a given trajectory is confined to an invariant surface, the so-called Kolmogorov-Arnol'd-Moser (KAM) surface, whose intersection with the surface  $Z = 0$  is a closed curve. Several representative KAM curves are shown in region  $A$  of Fig. 4a. An integrable region consists of infinitely many nested closed curves. In the system given by equations (1) and (3), the  $z$ -extent of the integrable orbits is limited to  $\sim d_j \equiv (2\rho_0\delta)^{1/2}$ . In the absence of noise, integrable orbits remain on the KAM surfaces indefinitely without closing onto themselves (quasi-periodic). There exist integrable orbits which do close onto themselves. They are referred to as periodic or fixed-point orbits. Büchner and Zelenyi [1986, 1989] proposed that the action  $I$  can serve as the third invariant. Although  $I$  is approximately conserved in the current sheet [Sonnerup, 1971], it is easy to see that  $[I, H] \neq 0$  so that  $I$  is not an invariant.

In region  $B$  of Figure 4a, nearby orbits which are initially arbitrarily close to each other can diverge exponentially during the time the orbits are in the vicinity of the current sheet [Chen, 1992]. The average exponential divergence rate is calculated in the same way as the standard Lyapunov exponent with the exception that the time used in the calculation is limited to the duration between the first and last crossings of the midplane.

In the modified Harris model, all nonintegrable orbits come from and escape to infinity ( $z \rightarrow \infty$ ), and all orbits from infinity are nonintegrable, making their first midplane crossings in region  $C1$ . This is the entry region. All orbits escaping to infinity cross the midplane for the last time in region  $C1'$  (not shown in Figure 2), where  $C1'$  denotes the mirror image of  $C1$  about  $\dot{X} = 0$ . The regions  $C2$ – $C5$  are the successive mapping of  $C1$  by the equation of motion (3), or equivalently equations (4)–(7).

The regions  $C$  are shown as "blank" regions only to distinguish them from the surrounding stochastic region. Figure 4b shows the internal structures of the regions  $C1$ – $C5$ . The orbits (i.e., points) shown are the transient orbits, making only one traversal of the midplane. For  $\hat{H} = 500$ , they have the appearance of the well-known Speiser orbits shown in Figure 2. All transient orbits enter the midplane through  $C1$  and the majority of them pass through  $C2$ – $C5$ , and escape to infinity. Some escape to infinity after crossing  $C4$  just above  $T4$ , which is inside region  $C1'$ , the exit region. The transient orbits do not enter region  $B$ . The number  $N$  of the prominent transient regions is given by

$$N_t \sim (\hat{H}/2)^{1/4} + 1$$

for  $\hat{H} \lesssim (1/2)b_n^{-1/4}$  [Chen and Palmadesso, 1986]. (Note that  $N_t$  gives the number  $f$  as in Cf.) This is also the typical number of midplane crossings for an orbit of energy  $\hat{H}$  as it makes one

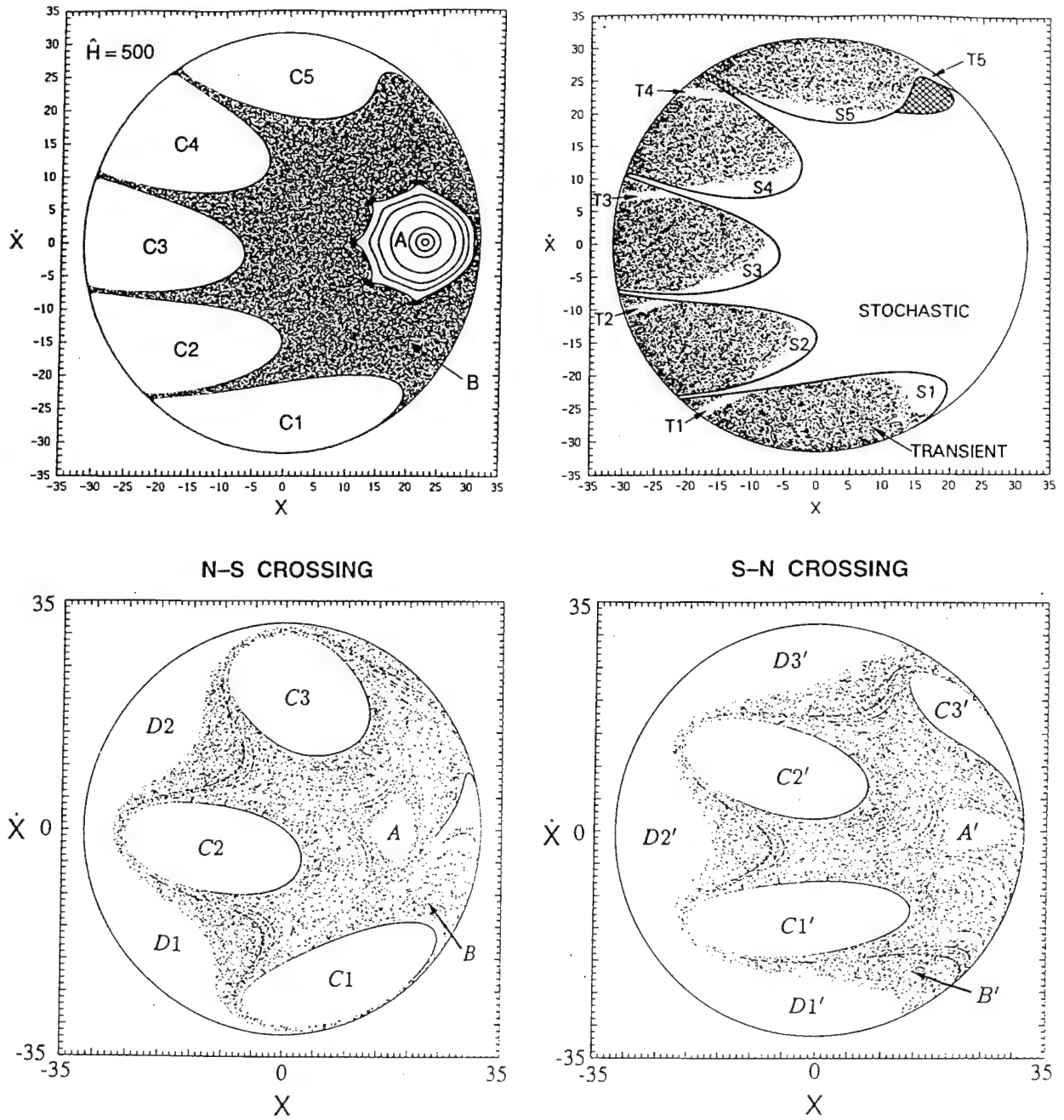


Fig. 4. A Poincaré surface of section map.  $b_n = 0.1$ . Adapted from Chen and Palmadesso [1986]. (a)  $B_y = 0$ . Region A is integrable and region B is stochastic. Regions C1–C5 are transient regions. The boundaries  $\partial(C_j)$  are shown. (b) Internal structure of the transient regions. S1 and T1 are the entry regions for stochastic orbits. The orbits shown are transient orbits. (c)  $B_y = 0.1 B_0$ . Surface of section return map for north-to-south crossings. (d)  $B_y = 0.1 B_0$ . South-to-north crossings.

midplane traversal. The scaling dependence is straightforward to obtain and is a consequence of the property  $B_x(z) \simeq B_0 z / \delta$  for  $z/\delta \lesssim 1$  and of the translational invariance in  $y$ . ( $\rho_n \ll L_x$  is assumed.) Several important implications of this scaling dependence have been found recently, and we will discuss them in section 4. The orbits which enter the midplane through  $S1$  or  $T1$  subsequently cross the midplane through  $S2$ – $S5$  or  $T2$ – $T5$ , respectively, and then enter region  $B$ . These orbits eventually escape through the cross-hatched regions, which are subregions of  $C1'$ , being the mirror images of  $S1$  and  $T1$ . Generally, the entry region  $C1$  consists of subregions corresponding to transient orbits of different midplane crossing numbers (e.g., 4 and 5 for  $\dot{H} = 500$ ), and these subregions are separated by entry regions for stochastic orbits (e.g.,  $T1$ ).

It is instructive to understand the class of orbits comprising the boundaries of the transient regions. These boundaries, which will be denoted by  $\partial(C_j)$ , where  $j = 1, 2, \dots, f$ , are the mapping forward in time of those orbits which have pitch angle  $\beta = \pi/2$  at "infinity" [Chen et al., 1990b]. The boundaries of the transient regions shown in Figure 4a are constructed by mapping such orbits at  $z = 5\delta$  forward in time. The boundary  $\partial(C1)$  is the first midplane crossing of these orbits, which are subsequently mapped to  $\partial(C2)$ – $\partial(Cf)$  by the equation of motion (3). For more detail regarding the structure and properties of  $\partial(C_j)$ , see Chen [1992, section 2.3].

In the  $B_y \neq 0$  case the basic partitioning of phase space persists, albeit with some modifications. Figure 4c shows the return map at  $Z = 0$  for north-to-south (N–S) crossings with  $B_y = B_n = 0.1B_0$ , and Figure 4d shows the return map for south-to-north (S–N) crossings with the same parameters, where north refers to  $Z > 0$  and south to  $Z < 0$ . (Due to the symmetry of the equations of motion under the simultaneous replacement of  $b_y$  with  $-b_y$  and  $Z$  with  $-Z$ , Figure 4c may also be considered to be the return map for south-to-north crossings and Figure 4d the return map for north-to-south crossings with  $-B_y = B_n = 0.1B_0$ .) Below we will give a brief discussion of the phase space structure for this case. The purpose here is not to discuss the detailed properties but to show that the concepts developed for the simpler  $B_y = 0$  case can be similarly applied to obtain rigorous understanding of the more complicated system.

As in Figures 4a and 4b, regions  $A$  and  $A'$  are occupied by integrable (regular) orbits which are confined to KAM surfaces for all time in the absence of noise. All particles approaching the midplane from the north will first cross the midplane in region  $C1$  (N–S crossing). The particles will then cross the midplane again in region  $C1'$  (S–N crossing) followed successively by region  $C2$ ,  $C2'$ ,  $C3$ , and  $C3'$ . Some particles then escape to infinity (transient orbits), while others will reenter the phase space in region  $B$  (stochastic orbits). Similarly, those particles approaching the midplane from the south will first enter the surface of section in region  $D1'$  (S–N crossing). The particles will then cross the midplane again in region  $D1$  (N–S crossing),  $D2$  and so forth. Subsequently, some particles will escape to infinity whereas others will reenter the phase space in region  $B$  and make multiple traversals of the midplane (stochastic orbits).

As in the  $B_y = 0$  case, the entry regions ( $C1$  and  $D1'$ ) are the mapping of particles from infinity:  $C1$  is the mapping of particles from  $Z = +\infty$  while  $D1'$  is the mapping from  $Z = -\infty$ . The escape regions are the mirror images of  $C1$  and  $D1'$  about  $\dot{X} = 0$  in the respective surfaces (not shown but see Chen [1992] for the method of constructing phase space regions). Note that the mirror image of a region defined by a set of orbits is equivalent to the time reversed mapping of the same set of orbits. Unlike the  $B_y = 0$  case, however, care must be used to ascertain the surface of exit if  $B_y \neq 0$ . That is, if orbits originating from the north escapes to the south, the escape region and entry region are in the same N–S surface. If the orbits escape to the north, then the entry region is in the N–S surface while the escape region is in the S–N surface.

Analogous to the  $B_y = 0$  case, the entry regions are generally subdivided into subregions for transient and stochastic orbits. These subregions are the intersections between the entry region and the time reversed mapping of the regions  $C$ ,  $C'$ ,  $D$ , and  $D'$ . Then, as mentioned above, the direction of the midplane crossing, i.e., N–S versus S–N, must be taken into account properly. Although this process is much more complicated than the  $B_y = 0$  case, the subregions in the overall entry regions ( $C1$  and  $D1'$ ) can be mapped out geometrically and exactly.

The  $D$  regions have internal subdivisions just as in the standard transient regions (Figure 4b). The details of the phase space structure and their physical significance will be discussed in detail elsewhere.

The phase space properties as represented graphically by the surface of section plots, which describe the dynamics of the system completely, are qualitatively similar for  $B_y \neq 0$  and  $B_y = 0$ : the dynamical system consists of integrable, stochastic, and transient trajectories. In the remainder of the paper, we will primarily discuss the case with  $B_y = 0$ .

An important question is how collisions and noise can influence the dynamical properties which have been obtained in the absence of such effects. This is particularly relevant because realistic systems are generally "noisy", and stochastic orbits are sensitively affected by noise. Holland and Chen [1991] constructed an *ad hoc* scattering operator which parameterizes a collision by collision frequency  $\nu$ , amplitudes of pitch-angle ( $\Delta\beta$ ) and phase-angle ( $\Delta\phi$ ) scattering, and amplitude of energy change ( $\Delta E$ ). It was found that the KAM surfaces are destroyed with the introduction of collisions while the transient region boundaries  $\partial(C_j)$  are remarkably robust. Figure 5 shows a surface of section plot for  $\dot{H} = 187.4$ , and  $b_n = 0.1$  with pure pitch-angle scattering of amplitude  $\Delta\phi = \Delta\beta \leq 1^\circ$  and frequency  $\nu = \Omega_n/2$ . The KAM curves in what would have been an integrable region without collisions are destroyed, showing that orbits can diffuse through the region. In contrast, the boundaries  $\partial(C1)$ – $\partial(C4)$  are essentially intact. This means that the separation between the stochastic and transient orbits remains sharp. Although the KAM surfaces are destroyed, the (former) integrable orbits are nearly trapped for substantially longer periods of time than the stochastic orbits. Thus, the partitioning of the phase space remains between all regions. For

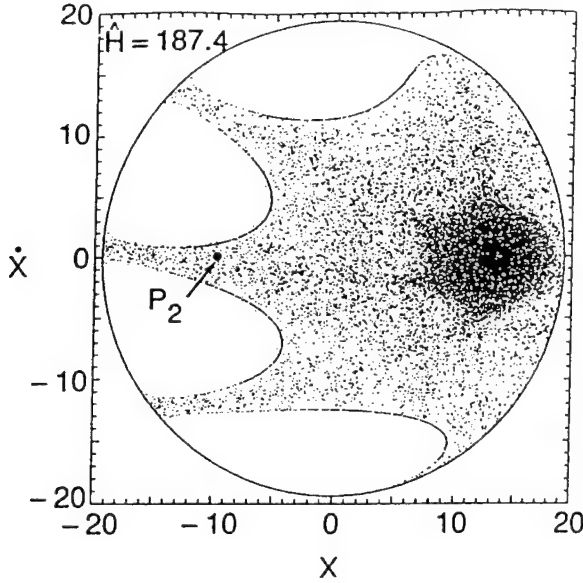


Fig. 5. Surface of section for  $\tilde{H} = 187.4$  including pure pitch-angle scattering. The scattering amplitude is  $1^\circ$  in pitch- and phase-angles with a frequency of  $\nu = \Omega_n/2$ . (From *Holland and Chen*, [1991].)

pure energy scattering, if the "collisions" are to have a significant effect on the phase space populations, particles must be transported onto energy surfaces with greatly differing phase space boundaries. If we assume that the "collisions" are due to wave particle interactions, we find that the observed frequencies and amplitudes will not produce a major change in the relative populations of transient and stochastic orbits.

The property that nonintegrable (stochastic and transient) orbits are unbounded distinguishes this system from the usual bounded dynamical systems. As Figures 2 and 3 show, the particle motion in the asymptotic regions is regular. Thus, it is possible to speak of well-defined incoming and outgoing conditions in the asymptotic regions. It was first shown [*Chen et al.*, 1990c] that the stochastic orbit entry regions (e.g., S1 of Figure 4b) are divided into subregions according to the outgoing states and that such subregions occur on a fractal set. Therefore the outgoing conditions of stochastic orbits depend sensitively on the incoming conditions while transient orbits exhibit no such sensitivity. As an example, the total number of midplane crossings between first and last crossings of the midplane can serve as an outgoing condition. The fractal dimension was found to be  $d \approx 1.8$  for  $\tilde{H} = 500$ , indicating that the outgoing conditions are only poorly predictable from the initial conditions. Similarly the pitch angle is essentially constant for  $|z| \gg \ell$  and can define asymptotic states. This type of system, which has regular asymptotic trajectories but whose outgoing conditions exhibit sensitive dependence on incoming conditions, are often called chaotic scattering systems. The physical importance

of chaotic scattering is that the "external world" can influence and be influenced by the chaotic dynamics inside localized regions. For example, auroral region electric fields can modify the tailward flowing ion distributions which then determine the current sheet structure in the tail [*Holland and Chen*, 1993]. In this process, the incoming ions enter the current sheet through C1. The entry (C1) and exit (C1') regions constitute the conduit between the current sheet and the "external" regions. As a result, the pitch-angle distribution of incoming particles and the internal structure of C1 determine the relative population of transient and stochastic orbits. Such structure of C1 and how the transient and stochastic orbits determine the current sheet structure will be discussed later (section 5). The term "chaotic scattering" has also been used [*Ashour-Abdalla et al.*, 1990, 1991; *Brittnacher and Whipple*, 1991] to refer to the variation  $\Delta I$  in the action at the effective potential separatrix [*Büchner and Zelenyi*, 1989]. This usage is different from the standard terminology in nonlinear dynamics.

A quantitative measure of the degree of chaos is the Lyapunov exponent, which gives the average rate at which arbitrarily nearby orbits exponentiate away from a reference orbit. *Martin* [1986] computed the Lyapunov exponent for orbits in an X-type magnetic neutral line. For the quasi-neutral sheet configuration, *Chen* [1992] showed the exponential divergence rate  $\lambda^*$  for individual trajectories and defined a phase space average  $\Lambda$  of  $\lambda^*$ . The usual Lyapunov exponent is defined for infinite time, appropriate for bounded orbits. For chaotic scattering systems such as the quasi-neutral sheet configuration, the infinite time limit is not useful because all nonintegrable orbits are actually regular almost all the time. For individual orbits, a finite-time analogue of the Lyapunov exponent can be defined. Consider an orbit  $\mathbf{x}$  and a nearby orbit  $\mathbf{x} + \delta\mathbf{x}$ . The difference vector  $\delta\mathbf{x}$  lies in the tangent space at  $\mathbf{x}$ . Let its norm be  $w(\mathbf{x}, t) \equiv \|\delta\mathbf{x}\|$ . Then the exponential divergence rate for a given orbit is

$$\lambda^* = \frac{1}{L\Delta\tau} \sum_{i=1}^L \ln \left( \frac{w_i}{w_0} \right), \quad (9)$$

where  $w_0$  is the norm of the initial tangent vector,  $w_i$  is the norm of the tangent vector after the  $i$ -th time step, and  $\Delta\tau$  is the time step. The number  $L$  is the total number of time steps from the first crossing of the midplane (e.g., in S1 or T1 of Figure 4b) to the last point of crossing (e.g., in S1' or T1'). The standard Lyapunov exponent corresponds to the limit  $L \rightarrow \infty$ . Recall that the dynamics (but not individual trajectories) in the modified Harris field can be parameterized by two quantities:  $\tilde{H}$  and  $b_n$  (plus  $b_y$  if  $B_y \neq 0$ ). For given  $\tilde{H}$  and  $b_n$ , however, it is easy to show that the value of  $\lambda^*$  has a wide range, depending on the pitch and phase angles of the orbits. One can average over the pitch and phase angles to characterize the entire stochastic region for each energy surface. We define the average exponential divergence rate by

$$\Lambda(\tilde{H}, b_n) \equiv \left( \frac{1}{M} \right) \sum_{m=1}^M \lambda_m^*, \quad (10)$$



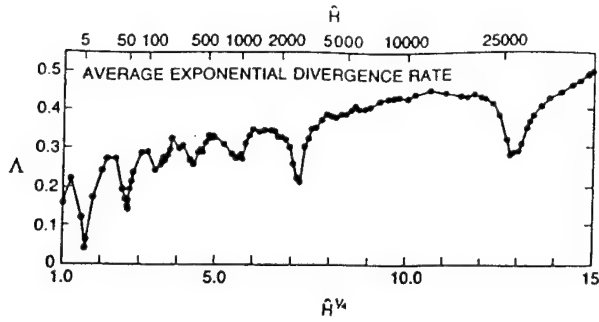


Fig. 6. Exponential divergence rate averaged over the phase space in the modified Harris model. The valleys occur at the resonance energies given by equation (15). (From Chen [1992].)

where  $\lambda_m^*$  is the divergence rate for the  $m$ -th orbit and  $M$  is the total number of orbits used in the calculation. The individual orbits are distributed uniformly in the stochastic orbit entry regions at  $Z = 0$  (e.g., S1 and T1 of Figure 4b or Figure 8). The orbits are computed until they enter S1' or T1'. Figure 6 shows the plot of  $\Lambda$  versus  $\hat{H}$  for  $b_n = 0.1$ . We used  $M = 40$ –100 for  $\hat{H} \lesssim 10$  and  $M \simeq 200$ –400 for higher values of  $\hat{H}$ . The rate  $\lambda_m^*$  for each orbit is computed from the first crossing to the last crossing of the midplane. We see that there are certain values of  $\hat{H}$  where  $\Lambda(\hat{H})$  is significantly reduced from the neighboring values. These  $\hat{H}$  values are evenly spaced in  $\hat{H}^{1/4}$ , indicating the existence of resonance, and are related to the scaling behavior  $N_i \simeq (\hat{H}/2)^{1/4} + 1$  previously mentioned. This resonance effect will be discussed in the next section. It can be shown that  $\Lambda(\hat{H}, b_n)$  decreases linearly with  $b_n$  for fixed  $\hat{H}$ . This is to be expected because  $b_n \rightarrow 0$  is a completely integrable limit.

It has been conjectured [Büchner and Zelenyi, 1987, 1989] that the degree of chaos increases as  $\kappa \rightarrow 1$ , attaining maximum at  $\kappa = 1$  ( $\hat{H} \rightarrow 0.25$ ) and that it decreases for  $\kappa \rightarrow 0$  ( $\hat{H} \rightarrow \infty$ ). The quantity  $\kappa$  was used as a small expansion parameter, but the conjecture was not based on quantitative relationship between  $\kappa$  and the rate of exponential divergence. Figure 6 shows that  $\Lambda(\hat{H}, b_n)$  has no monotonic dependence on  $\hat{H}$  (and for fixed  $b_n$  in the modified Harris model) and that the overall tendency of  $\Lambda$  is to increase with increasing  $\hat{H}$ . It has also been found that  $\Lambda$  is small near  $\kappa \simeq 1$ , reaching  $\Lambda = 8 \times 10^{-2}$  as  $\hat{H} \rightarrow 0.25$  (i.e.,  $\kappa \rightarrow 1$ ) [Chen, 1992, section 2.6]. These properties are contrary to the above conjecture. Another popular notion is that  $\kappa$  can distinguish between different classes of orbits. Actual solutions show that, at any given value of  $\hat{H}$  or equivalently  $\kappa$ , there are integrable, stochastic and transient orbits. Recall that Figure 3 depicts two orbits whose initial conditions are identical except for the phase angle, i.e. they have exactly the same value of  $\kappa$ . When the particles leave the current sheet they have similar properties. Yet, one orbit is stochastic and the other is transient. In addition, there are integrable orbits with the same value of

$\kappa$  as shown in Figure 4a of Chen and Palmadesso [1986]. The exponential divergence rates  $\lambda^*$  for different individual orbits similarly do not have a single value for given  $\hat{H}$  and  $b_n$ . For  $\hat{H} \rightarrow \infty$ , the integrable regions vanish, and all the orbits are of the transient type [Chen et al., 1990b; Burkhardt and Chen, 1991]. The transient orbits, however, do not exhibit sensitive dependence on initial conditions and are not integrable. Thus, the system does not become more integrable as  $\kappa \rightarrow 0$ . Despite its popularity,  $\kappa$  does not constitute an objective measure of chaos. Note that there is an ambiguity in the limit  $\kappa \rightarrow 0$  since this limit can be taken by either  $\hat{H} \rightarrow \infty$  holding  $b_n$  fixed or  $b_n \rightarrow 0$  holding  $\hat{H}$  fixed. The latter corresponds to an integrable limit while the former does not. The mathematical difficulty arises from the fact that the normalization of equations leading to  $\kappa$  and equivalently to  $\hat{H}$  diverges in the integrable limit  $b_n \rightarrow 0$ , as was pointed out earlier [Chen and Palmadesso, 1986]. The expansion based on  $\kappa \ll 1$  is not meaningfully extendable to  $\kappa \sim 1$ . In contrast, it can be shown readily that  $\Lambda$  decreases linearly with  $b_n \rightarrow 0$  for fixed  $\hat{H}$ . Similar ambiguities have also been noted in characterizing the particle motion in time-dependent models [Chapman, 1994].

The model given by equation (1) is independent of  $x$ . The neglect of  $x$ - and  $y$ -dependence within the current sheet is valid if  $\rho_n \ll L_x, L_y$  where  $L_x, L_y$  are the gradient scale lengths in the  $x$ - and  $y$ -directions, respectively. Karimabadi et al. [1990] used an  $x$ -dependent model and found that the dynamics of charged particles can be significantly different from the  $x$ -independent models. In particular, they found a regime in  $\hat{H}$  where the phase space area occupied by integrable orbits is much greater than that in the modified Harris field (the regime of enhanced integrability). They also found that the orbits travel substantially shorter distances in the  $x$ -direction before mirroring than in the  $x$ -independent model. In addition, with an imposed constant  $E_y$ , the particles gained unrealistically high energy. As a result, Karimabadi et al. [1990] questioned the applicability of existing  $x$ -dependent field models with uniform  $E_y$ . Burkhardt and Chen [1992] further investigated the reason for the inapplicability. They found that the magnetic field as seen by the orbits in the regime of enhanced integrability does not resemble the presumed field geometry of the magnetotail. Specifically, they found that the field lines in this regime are "bulb-shaped" and that the  $x$ -excursion  $\Delta$  of the orbits and the Larmor radius  $\rho_n$  are both comparable to the scale length  $L_x$ . This is different from the Earth's magnetotail where  $\Delta, \rho_n \ll L_x \sim 50R_E$  [Behannon, 1968]. The apparent agreement between the predictions based on an  $x$ -independent model and observation in the magnetotail reported by Chen et al. [1990a] indicates that the particle dynamics in the distant magnetotail can be approximated by suitable  $x$ -independent models.

For  $B_y \neq 0$ , we must restrict ourselves to  $E_x = 0$  or make  $\mathbf{E} \perp \mathbf{B}$ . Otherwise the field aligned electric field would accelerate particles to unrealistically high energies. It is found if the  $B_y$  field becomes sufficiently large ( $B_y \gtrsim 2B_z$ ), the majority of the particles directly pass through the sheet and the resonance

effects mentioned above and discussed below are negligible. This is a significant result in that it places a limit on the magnitude of the  $y$ -component of the magnetic field if the physical consequences of the resonance effects are observed.

#### 4. PHASE SPACE RESONANCE

We have discussed how the dynamical properties of this system can be graphically described using Poincaré surface of section maps. We now consider how the phase space structures may be related to physical observables. A physically important effect is the phase space resonance referred to above. It was found [Burkhart and Chen, 1991] that, at certain resonance values of  $\hat{H}$  satisfying

$$N \simeq \hat{H}_N^{1/4} - 0.6, \quad (11)$$

where  $N = 1, 2, 3, \dots$ , the entry ( $Ci$ ) and exit ( $Cf$ ) regions become nearly symmetric. The value 0.6 is a numerical scale factor, and  $\hat{H}_N$  denotes the  $N$ -th resonance energy. This equation refines the previously discussed expression  $N_i = (\hat{H}/2)^{1/4} + 1$  with  $N_i = N + 1$ , and the resonance effect incorporates the additional ingredient of symmetry in  $Ci$  and  $Cf$ . The first few resonances occur at  $\hat{H}_1 \simeq 6$ ,  $\hat{H}_2 \simeq 50$ , and  $\hat{H}_3 \simeq 170$ . For  $b_n = 0.1$ , the resonance terminates after  $N = 6$ . It is useful to note that there are  $N_i = N + 1$  prominent transient regions at resonance so that the majority of orbits traversing the current sheet return to the side from which they are incident ("backscattered") at odd- $N$  resonances while the majority of incident orbits exit to the opposite side of the current sheet ("forward scattered") at even- $N$  resonances. (Also see Chen [1992] for a detailed discussion.)

It is easy to infer from Figure 4b that the entry regions for stochastic orbits (e.g.,  $S1$  and  $T1$  for  $\hat{H} = 500$ ) decrease in relative phase space area as the degree of symmetry between  $Ci$  and  $Cf$  increases. By taking the mirror images of the entry regions, we can see that the area of the stochastic orbit exit regions (e.g., the cross-hatched regions in Figure 4b) decreases as  $Ci$  and  $Cf$  become more symmetric. To see the physical effect of this resonance, consider a population of orbits at a resonance energy, uniformly distributed in phase space in the asymptotic region. Because the relative area of the stochastic orbit entry regions decreases significantly at resonance, the proportion of stochastic orbits also decreases significantly in comparison with neighboring off-resonance energies. One physical consequence is that orbits in asymptotic regions have significantly decreased probability of entering stochastic regions near the midplane. A majority of orbits entering the current sheet are transient orbits at resonance energies. Conversely, stochastic orbits in the vicinity of the current sheet have significantly reduced probabilities of escaping to the asymptotic regions, leading to increased time during which the stochastic orbits are effectively "trapped" in the current sheet. Burkhart and Chen [1991] numerically calculated the time that stochastic orbits spend between the first

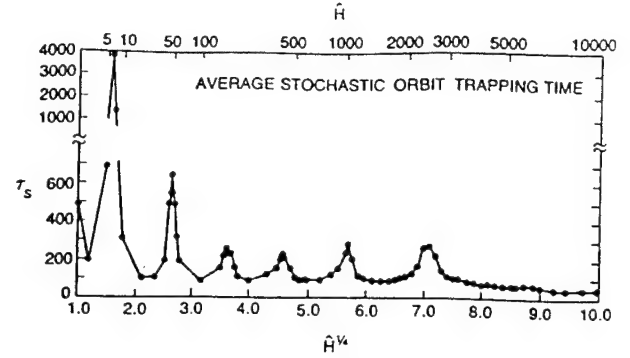


Fig. 7. Average stochastic orbit trapping time. (From Burkhart and Chen [1991].)

and the last crossings of the midplane. This time  $\tau_s$ , referred to as the average stochastic orbit trapping time, is a measure of how long stochastic orbits spend in the neutral sheet and is a function of  $\hat{H}$  and  $b_n$ . It was found that, at the values of  $\hat{H}$  given by (11),  $\tau_s(\hat{H})$  is "anomalously" long. Figure 7 shows  $\tau_s(\hat{H})$  for  $b_n = 0.1$ . It is clear that  $\tau_s$  has well-defined peaks evenly spaced in  $\hat{H}^{1/4}$ . By comparing Figures 6 and 7, it is easy to see that peaks in  $\tau_s$  coincide with the valleys in  $\Lambda$ . Recall that the dynamics of the system depends on two independent parameters  $\hat{H}$  and  $b_n$ . The quantity  $b_n$  is important because it is the measure of the nonintegrable perturbation.

A physical understanding of the resonance phenomenon can be obtained by carefully considering the phase space structures. Figure 8 shows the boundaries of the transient regions  $\partial(Cj)$  which are the mapping of orbits with incoming pitch angle  $\beta_1 = \pi/2$  at  $z = 5\delta$  forward in time, as discussed earlier. These boundaries are shown by solid lines. Here,  $j = 1, \dots, f$  with  $f = 5$  for  $\hat{H} = 500$ . Also shown are the time-reversed mapping of the same asymptotic orbits. They are shown as dashed lines. Because  $y$ - and time-reversals are equivalent, the dashed lines are simply the mirror images of the solid lines. The stochastic orbit entry regions  $S1$  and  $T1$  are identified. (Also see Figure 4b.) Formally, the stochastic orbit entry regions can be written as  $C1 \cap \overline{Cf} \cap C(f-1) \cap \dots$ . Here  $\overline{Cj}$  denotes the complement of the region  $Cj$ , and  $\cap$  indicates the intersection of two regions. The exit regions are simply the mirror images of entry regions. Therefore, if  $C1$  and  $Cf$  are completely symmetric, then  $C1$  and  $Cf$  overlap completely and there is no entry or exit region for stochastic orbits. The value  $\hat{H} = 500$  shown in Figure 8 is near the  $N = 4$  resonance energy. As a result,  $C1$  and  $C5'$  have a large overlap. We have also shown several contours (— · —) of constant asymptotic pitch angles  $\beta_1$  which are defined at  $z = 5\delta$ . These contours are the mapping of asymptotic orbits with  $\beta_1 = 2^\circ, 30^\circ$  and  $60^\circ$ . We see that there is a critical value  $\beta_c$  such that all asymptotic orbits with pitch angle  $\beta_1 < \beta_c$  are transient orbits which do not enter the stochastic region. For  $\beta_1 > \beta_c$ , some orbits enter stochastic regions and are scattered chaotically (section 3). For  $\hat{H} = 500$ ,  $\beta_c \simeq 30^\circ$ .

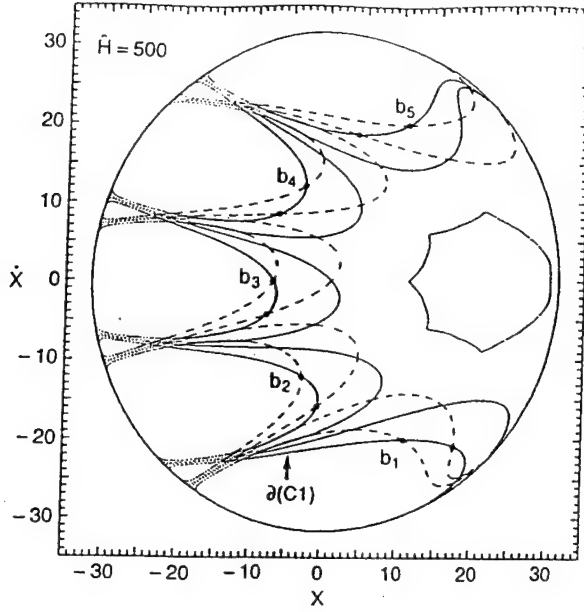


Fig. 8. Phase space boundaries for the modified Harris model.  $\hat{H} = 500$  and  $b_n = 0.1$ . Solid lines are the boundaries  $\partial(C1) - \partial(C5)$ . The dashed lines are  $\partial(C1') - \partial(C5')$ . The regions  $S1$ ,  $T1$ ,  $S5'$  and  $T4'$  are shown. The mapping of orbits with the asymptotic pitch angle  $\beta_1$ . The contours (---) of  $\beta_1 = 2^\circ$ ,  $30^\circ$  and  $60^\circ$  are shown. The points  $a_1$ ,  $b_1$ , and  $c_1$  are mapped onto  $a_5$ ,  $b_5$ , and  $c_5$ , respectively. The point  $d_1$  is mapped to  $d_4$  and then to  $\infty$ .

As discussed in section 3, the entry regions for stochastic orbits (e.g.,  $S1$  of Figure 4b or Figure 8) are divided by fractal boundaries corresponding to different outgoing conditions. In terms of pitch angle scattering, the outgoing asymptotic pitch angle  $\beta_2$  depends sensitively on the incoming  $\beta_1$  if an orbit enters the stochastic region. Burkhardt and Chen [1992] found that asymptotically field-aligned orbits (i.e.,  $\beta_1 = 0$ ) undergo regular scattering at energies near resonance values, with the outgoing asymptotic pitch angles  $\beta_2$  exhibiting no sensitive dependence on  $\hat{H}$ , while pitch-angle scattering is chaotic at off-resonance energies. This is because, at off-resonance energies, even the asymptotically field-aligned orbits enters stochastic regions so that  $\beta_c \approx 0$ . The quantity  $\beta_c$  can be calculated numerically and is shown in Figure 9. We see that the peaks in  $\beta_c$  occur at nearly the same energies as the peaks in  $\tau_x$  (Figure 7), which in turn are essentially the same as the valleys in the average exponential divergence rate  $\Lambda$  (Figure 6) and that  $\beta_c \approx 0$  approximately half way between neighboring resonance peaks. The numerical data points are simply connected by straight lines. Each point has been computed with 500 orbits, uniformly distributed over the phase space and initially located at  $z = 5\delta$ . We have compared a number of representative points of this figure with the corresponding surface of section plots and found that the results are consistent. This figure complements Figure 4 of Burkhardt and Chen [1992].

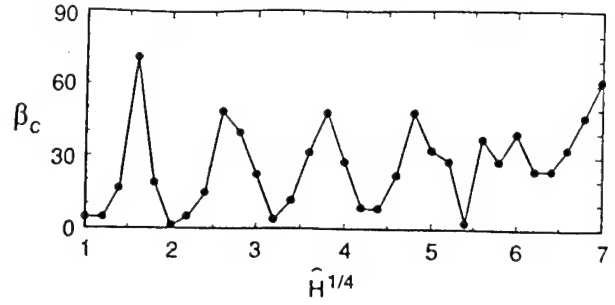


Fig. 9.  $\beta_c$  versus  $\hat{H}^{1/4}$ . Asymptotic incoming pitch angle  $\beta_1 < \beta_c$  corresponds to regular scattering.

Recall that the dynamics in the modified Harris model can be parameterized by two independent quantities  $\hat{H}$  and  $b_n$ . The quantity  $b_n$  plays an important role in determining the dynamics because it describes the nonintegrable perturbation. We now discuss the dependence of the resonance phenomenon on  $b_n$ . Because of the normalization of  $\hat{H}$  defined by (7), the resonance values  $\hat{H}_N$  do not depend on  $b_n$  for  $b_n \ll 1$  [equation (11)]. However, the termination point of the resonance effect and the number of resonance peaks are determined by  $b_n$ . The dependence of the resonance on  $b_n$  can be understood as follows [Burkhardt and Chen, 1991]. There are two critical energies if the current sheet is confined to a finite thickness. The first occurs when  $\rho_0$  is comparable to the radius of curvature  $R_c = b_n \delta$  at  $Z = 0$ . Setting  $\rho_0 = R_c$ , we find

$$\hat{H} \approx H_1 \equiv \frac{1}{2} b_n^{-2}. \quad (12)$$

This corresponds to  $d_i = (2b_n)^{1/2} \delta < \delta$  so that  $B_x \propto z$ , and the analysis leading to  $N \sim \hat{H}^{1/4}$  is applicable. As  $\hat{H}$  increases, the orbits experience more deviations from  $B_x \propto z$ , and the resonance effect weakens, resulting in a decreased degree of symmetry between  $C1$  and  $Cf$ . The resonance peaks in  $\tau_x$  and  $\tau_D$  are in fact strongest for  $\hat{H} \lesssim H_1$ , decreasing with increasing  $\hat{H}$  (Figures 6 and 7). The second critical energy occurs when  $\rho_0 \approx \delta \gg R_c$ , which is equivalent to  $d_i \approx \delta$ . This energy is

$$\hat{H} \approx H_2 \equiv \frac{1}{2} b_n^{-4}. \quad (13)$$

For  $\hat{H} \geq H_2$ , the typical midplane crossing orbits have  $z$ -excursions exceeding the current sheet thickness. The magnetic field as seen by such orbits deviates significantly from the linear dependence of  $B_x \propto z/\delta$ , and the resonance effect is no longer operative in general (but see the discussion in the next paragraph). Thus, for a given  $b_n$ , there are approximately  $2^{-1/2} b_n^{-1}$  resonance energies. For  $b_n = 0.1$ , Figure 7 demonstrates these two properties clearly. Here,  $H_1 = 50$  and  $H_2 = 5000$ , corresponding to  $H_1^{1/4} \approx 2.7$  and  $H_2^{1/4} \approx 8.4$ .

In obtaining  $H_1$  and  $H_2$ , we have used  $\rho_0$  based on the total kinetic energy with no reference to the pitch angle of a tra-

jectory. As a result, we expect that an ensemble of particles with a range of pitch-angle and energy distribution to show the expected cutoff in the resonance indicated by (13). However, asymptotically field-aligned particles cross the midplane with small  $v_z$ , as can be seen from the 2° contours in Figure 8, so that their  $z$ -excursions remain small. It can be shown that such trajectories continue to exhibit the resonance effect beyond  $H_2$ . This means that a field-aligned beam of particles can exhibit resonance beyond  $H_2$ .

The ratio  $R_1$  of the area occupied by the entry region C1 to the total area of the energy surface is

$$R_1 \simeq b_n (2\hat{H})^{1/4}. \quad (14)$$

This is applicable to resonance as well as off-resonance  $\hat{H}$  values. At resonance, it can be shown further that the ratio of the total area occupied by the transient regions to the total area of the energy surface is

$$R_T \simeq b_n 2^{1/4} \hat{H}^{1/2}, \quad (15)$$

which is simply  $N_1 R_1$ . We have numerically verified that the scalings  $R_1 \propto b_n \hat{H}^{1/4}$  is highly accurate (within a few percent) for  $\hat{H} < H_2$ . Physically, the explicit dependence on  $b_n$  is due to the finite thickness of the current sheet.

## 5. PHYSICAL CONSEQUENCES IN THE MAGNETOTAIL

One qualitatively new understanding from the dynamics point of view is the existence of disjoint phase space regions corresponding to distinct classes of orbits. The different regions are characterized by widely separated time scales. An implication is that the different regions are affected by external influences on different time scales in a time-dependent environment. The boundaries between the different regions do not allow uniform propagation of information or particle energy throughout the phase space. Suppose the system contains a population of charged particles initially in thermal equilibrium with external sources. If the conditions of the distant plasma distribution are changed, then the system cannot evolve or relax to conform to the new external conditions uniformly in time throughout the phase space. The dynamically different classes of particles retain the "memory" of the existing particle distribution for different lengths of time. This process was called "differential memory" [Chen and Palmadesso, 1986]. It was suggested that differential memory would generate non-Maxwellian distribution functions and associated free-energies. This process has been demonstrated in the trilinear magnetic field [Chen *et al.*, 1990b] and in the modified Harris field [Chen *et al.*, 1990a; Burkhart and Chen, 1991]. In these studies, the time-evolution of distribution functions following changes in source distributions was calculated using test particles in fixed magnetic fields. It was found that accessibility time scales of the different phase space regions play an important role in the evolution of dis-

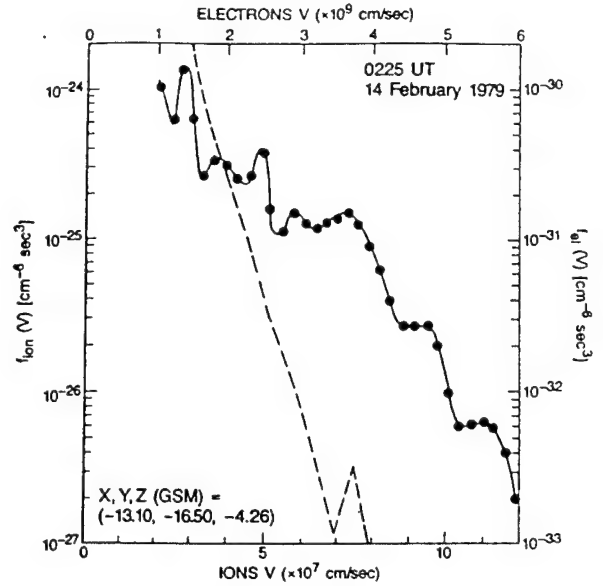


Fig. 10. A velocity distribution function in the central plasma sheet ( $v_{\parallel} = 0$ ) measured by ISEE 1. The solid line is for ions (left and bottom axes) and the dashed line is for electrons (right and top axes.)

tribution functions. In our discussion below, we will use the modified Harris model.

It was found that the reduced accessibility of the stochastic regions at resonance can be manifested as peaks and valleys in distribution functions. Applying the resonance condition (11) to the earth's magnetotail and constructing model distribution functions, it was found that observed ion distribution functions do exhibit peaks and valleys occurring at energies given by equation (11) [Chen *et al.*, 1990a]. Figure 10 shows an ion distribution function (the solid line) obtained by ISEE 1. Similar distribution functions were published earlier by Huang *et al.* [1989]. Following the model prediction, one can take the square root of the velocities (i.e.,  $H^{1/4}$ ) at which peaks and valleys occur, and the resulting values should be evenly spaced. In Figure 11, the circles on Line A are the  $v^{1/2}$  of the peaks and valleys shown in Figure 10, and Line A is the theoretical prediction based on equation (11). The radius of the circles is roughly the size of error bars. Lines B and C correspond to two additional distribution functions reported by Huang *et al.* [1989]. We see that the agreement is good. The fit is obtained by demanding  $N = -0.6$  at  $v = 0$ . In this figure, it was assumed that the incoming population of orbits from the northern side of the current sheet has a higher density than that of the southern source. Then, the valleys (peaks) correspond to even- $N$  (odd- $N$ ) resonance energies with the first valley inferred to be at  $N = 12$ .

A second prediction is that electron distributions, corresponding to  $\hat{H} \ll 1$  in the magnetotail [equation (8)], do not exhibit peaks and valleys obeying the  $\hat{H}^{1/4}$  scaling law because the first resonance occurs at  $\hat{H} = 6$ . The dashed line in Figure 10 is the

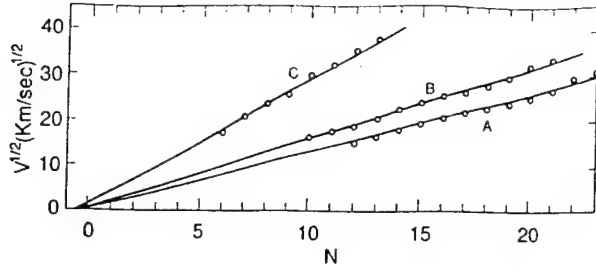


Fig. 11. Comparison between theoretical predictions and observations. Circles denote the locations of the valleys and peaks. The straight lines are the theoretical predictions given by equation (15). Line A corresponds to the distribution in Figure 9a. (From Chen *et al.* [1990a].)

electron distribution function taken at the same time as the ion distribution. We see that it is essentially structureless.

Based on the good agreement between the predicted and observed result, Chen *et al.* [1990a] suggested that the slope of the straight line could be used to infer the thickness of the current sheet using a single space craft. This is possible because the equilibrium current sheet thickness  $\delta$  and the Larmor radius of thermal particles are related by

$$\delta = \alpha^{-2} (8/\pi) \Gamma^2 (7/4) \rho_{th} \quad (16)$$

where  $\alpha$  is a factor order unity to be determined,  $\Gamma$  is the gamma function and  $\rho_{th} = v_{th}/\Omega_0$  with  $\Omega_0$  the Larmor frequency in the asymptotic magnetic field  $B_0$ . Using (16), we find that  $b_n \Omega_n \delta = [(8/\pi) \Gamma^2 (7/4)] \alpha^{-2} b_n^2 v_{th}$ , where  $\Omega_0 = qB_0/mc = b_n^{-1} \Omega_n$  has been used. Thus, the slope and the thermal velocity of the distribution gives the quantity  $\alpha/b_n$ . If  $\alpha$  is computed separately, a task we are presently undertaking, then  $b_n$  and hence  $\delta$  may be inferred from the observed distribution functions.

More generally, the phase space topology and the underlying dynamics are determined by global attributes of the system such as the field geometry. Local distribution function signatures which are manifestations of topological properties carry information on large-scale properties. Figure 11 and equation (16) are an example of how one can make use of observed distribution functions as diagnostic tools based on an understanding of the particle dynamics. In this regard, the scaling exponent  $1/4$  in equation (11) arises from the dependence  $B_x(z) \propto z$  [Chen, 1992]. (Also see section 4.) Thus, the scaling exponent of observed distribution functions can be used to infer the average  $z$ -profile of  $B_x(z)$  as seen by particles during midplane crossing. In numerical simulation studies, the scaling law can indicate the profile of the model field as seen by the simulation particles. The agreement between theory and data shown in Figure 11 indicates that the charged-particles see  $B_x(z) \propto z$  near the midplane in the Earth's magnetotail.

The relationship between the phase space regions and distribution functions can be illustrated as follows. First, note that

the majority of orbits at even- $N$  resonance energies are scattered back toward the source by the current sheet while those at odd- $N$  resonance energies are scattered to the other side of the current sheet. At off-resonance energies, incoming particles are scattered back toward the source and to the other side of the current sheet with nearly equal probability. This process was referred to as "coherent chaotic scattering" [Chen *et al.*, 1990a]. Consider now a distribution of incoming particles in the asymptotic region on one side of the current sheet, say, on the northern ( $z > 0$ ) side. After traversing the current sheet, the particles near the even- $N$  resonance energies are manifested as beams returning to the asymptotic source region while the particles near the odd- $N$  resonances appear as depletions since the particles are coherently scattered to the other (southern) side of the current sheet. At off-resonance energies, backscattering and forward scattering occur with equal probability. A satellite would measure the superposition of particles coming directly from the source, the particles backscattered from the current sheet and the particles forward scattered from the other side of the current sheet, leading to distribution functions of the form given in Figure 10. (See Chen *et al.* [1990a] for a model distribution function based on this scenario.) The reason for the coherent scattering at resonance is the enhanced degree of symmetry between C1 and Cf.

The above scenario applies to  $z \gg \delta$ . In this regime, one possible interpretation of the result is that both peaks and valleys correspond to successive resonance energies. In the study of Burkhardt and Chen [1991], the evolution of distribution functions was evaluated at the midplane with sources placed symmetrically about  $z = 0$ . In this case, distribution functions can develop either peaks or valleys at successive resonances depending on whether the source is depleted or enhanced, respectively. These are slightly different manifestations of the same resonance effect. There may be other manifestations. For example, Ashour-Abdalla *et al.* [1991] found beams in their test-particle simulations of the magnetotail, which are also a consequence of the resonance effect discussed above. The main difference is in the different magnetic field model used. We note here that if the magnetic field near the midplane varies as  $(z/\delta)^m$  the separation between adjacent resonances should scale as  $\tilde{H}^\chi$ , where  $\chi = s/[2(s+1)]$ . For  $s = 1$  this reduces to the standard  $\tilde{H}^{1/4}$  scaling. The general scaling  $H \propto \tilde{H}^\chi$  has been verified for field aligned particles with  $s = 3$  and  $s = 5$  [Chen, 1993]. An implication is that the resonance in locally observed distribution functions in the tail can be used as a diagnostic tool for the field profile as seen by particles. Figure 9 suggests that pitch-angle resolved distributions would also show beams at resonance energies. It is interesting to note that the chaotic particle motion in the current sheet leads to more "ordered" (i.e., non-Maxwellian), rather than more random (i.e., Maxwellian) distributions.

The same dynamical properties also play a controlling role in the equilibrium cross-tail current  $J_y(z)$  and particle density  $n(z)$  [Holland and Chen, 1993]. A number of one-dimensional

( $x$ -independent) self-consistent test-particle equilibrium models have been proposed [Burkhat *et al.*, 1992; Pritchett and Coroniti, 1992; Holland and Chen, 1993]. In these models, solutions of Vlasov equation satisfying  $\mathbf{J} = (c/4\pi)\nabla \times \mathbf{B}$  and  $(1/c)\mathbf{J} \times \mathbf{B} - \nabla \cdot \mathbf{P} = 0$  are sought. Some authors obtained equilibria in the regime  $v_D \gtrsim v_i$  [Eastwood, 1972; Burkhat *et al.*, 1992; Pritchett and Coroniti, 1992] while others found solutions for  $v_D \ll v_i$  [Holland and Chen, 1993]. Here  $v_D = cE_y/B_n$  and  $v_i$  is the thermal velocity. In the Eastwood regime ( $v_D \gg v_i$ ), both current and particle densities are peaked in the current sheet while in the  $v_D \ll v_i$  regime, the particle density is nearly constant across the current sheet while  $J_y(z)$  is peaked. The latter is consistent with quiet-time magnetotail observations [McComas *et al.*, 1986]. In the simulations of Burkhat *et al.* [1992], they could not find converged equilibria for  $v_D$  smaller than some critical value for given system parameters. In this work, the input distribution function is constrained to be a drifting Maxwellian parameterized by  $v_D$ . The smallest critical value was  $v_D/v_i \simeq 0.35$  with another example giving 1.2. This was interpreted as a catastrophic loss of equilibrium as  $v_D/v_i \rightarrow 0$ . In contrast, Holland and Chen [1993] performed similar test-particle simulations in the  $v_D/v_i \ll 1$  regime and obtained good equilibria down to  $v_D/v_i < 0.1$ . In obtaining equilibria in this regime, they allowed the input distribution functions to have high-energy tails. In this regard, a  $\kappa$  function (Maxwellian with a power-law tail), which is prevalent in magnetospheres [Christon *et al.*, 1989], was found to yield good equilibria at  $v_D/v_i = 0.05$ . Holland and Chen [1993] attributed the lack of equilibria to the constraint that the input distribution be drifting Maxwellians. Such distributions in the  $v_D/v_i \ll 1$  regime results in strong diamagnetic currents which flow in the opposite direction to what is required by  $\mathbf{J} = (c/4\pi)\nabla \times \mathbf{B}$ . The high-energy tail or field-aligned distribution counters the diamagnetic effect. It should be noted that the catastrophe conclusion of Burkhat *et al.* [1992] is given in terms of a parameter  $\kappa_A$ , and a physical explanation in terms of force balance argument of Francfort and Pellat [1976]. Careful examination of the catastrophe result shows that (1) actual numerical convergence fails when  $v_D$  becomes small, and (2) neither  $\kappa$  nor forces of Francfort and Pellat [1976] is used in the numerical iteration process. Thus neither point is germane to the actual process of nonconvergence. One should show that diamagnetic current is weak near the point of suggested catastrophe for a demonstration for the physical applicability of the catastrophe to the magnetotail current sheet.

The above simulations show that the pressure tensor generally has off-diagonal elements to establish force balance in both  $x$  and  $z$  directions. As the input distribution function becomes more field-aligned, the current sheet thins. A thin current sheet is more unstable to the collisionless tearing mode [Coppi *et al.*, 1966] and may be more susceptible to other forms of disruption [e.g., Lui *et al.*, 1991]. The anisotropic pressure may also significantly increase the growth rate of the tearing mode [Chen and Palmadesso, 1984; Burkhat and Chen, 1989]. An interesting

possibility is that the auroral region electric field may produce more field-aligned distribution of ions flowing tailward, resulting in thinner current sheets due to ion dynamics.

A non-Maxwellian distribution function such as the one shown in Figure 10 also represents free-energy that can drive plasma waves. Huba *et al.* [1992] studied linear stability properties of a model distribution function resembling Figure 10 and found that a low-amplitude broadband electrostatic noise can be generated in the quiet-time central plasma sheet of the earth's magnetotail. The linear dispersion properties proved to be quite consistent with observed wave spectra.

In a different vein, it has been suggested [Martin, 1986; Horton and Tajima, 1990, 1991; Horton *et al.*, 1991a,b] that the chaotic motion in the current sheet may constitute a form of collisionless "chaotic conductivity". Martin [1986] suggested that the Lyapunov exponent may provide the time scale of decorrelation of nearby orbits, taking the place of collision frequency. Using the fluctuation-dissipation theorem [Horton *et al.*, 1990b] and linearized Vlasov theory, [Horton and Tajima, 1990, 1991; Horton *et al.*, 1990a] argued that the zero frequency conductivity of the neutral sheet can be determined using the two-time velocity correlation function:

$$\sigma_{\alpha\beta} = (ne^2)/(Mv_{th}^2) \int dv f(v) \int_0^\infty d\tau C_{\alpha\beta}(\tau) \quad (17)$$

$$C_{\alpha\beta}(\tau) = \lim_{T \rightarrow \infty} \frac{1}{T} \int_0^T dt v_\alpha(t) v_\beta(t + \tau). \quad (18)$$

Calculation of  $C_{\alpha\beta}(\tau)$  showed a power-law decay in time which is suggestive of a collision-like momentum scattering and dissipation in analogy with the Lorentz gas problem. For the magnetotail,  $\sigma_{yy}$  and  $C_{yy}$  are studied because the cross-tail current is of primary interest. The idea of chaotic conductivity is an appealing one in a collisionless environment. If such a quantity could be defined and calculated for the magnetotail in terms of quantities characterizing the entire system, the electric field  $E_y$  and current density  $J_y$  could be related by a local quantity  $\sigma$  such that  $J_y = \sigma E_y$ . In addition, by calculating how  $\sigma$  depends on the global system parameters, one could reduce global considerations to a local quantity.

Recently, Holland and Chen [1992] re-examined the concept of chaotic conductivity in the magnetotail. They found that since the magnetotail is a chaotic scattering system as opposed to a classical chaotic system, the underlying assumptions leading to the use of two-time correlation functions may be inapplicable to zero-frequency conductivity and that the two-time correlation functions do not lead to a unique value of "conductivity". Due to intrinsic ambiguities in determining the initial and final points in the time integrations they showed that the correlation function  $C_{yy}$  of a given orbit can decay differently depending on how  $C_{yy}$  is computed. As an illustration of this effect, they calculated the  $yy$  component of the correlation func-



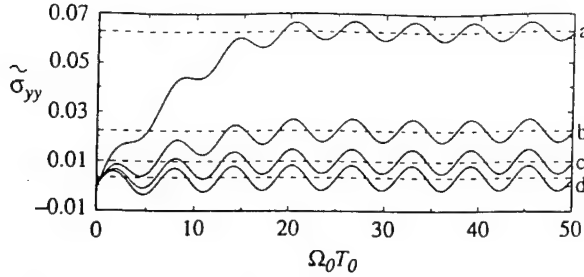


Fig. 12.  $\tilde{\sigma}_{yy}$  versus  $\Omega_0 T_0$ : (the asymptotic mean value of  $\tilde{\sigma}_{yy}$  is given in parentheses) (a)  $\Omega_0 T = 274$ , (0.0625); (b)  $\Omega_0 T = 774$ , (0.0224); (c)  $\Omega_0 T = 1774$ , (0.0099); and (d)  $\Omega_0 T = 5774$ , (0.00325).

tion for a typical transient orbit and the associated single particle conductivity,

$$\tilde{\sigma}_{yy}(T_0) = \int_0^{T_0} C_{yy}(\tau) d\tau$$

for several values of the time  $T$  over which the correlation function is evaluated. They focused on transient orbits since these contribute the largest percentage of the current and hence would be expected to have the largest conductivity. The total conductivity is defined by  $\sigma_{yy} = \int f(v) \tilde{\sigma}_{yy} d^3v$ , with  $T, T_0 \rightarrow \infty$ . Figure 12 shows the calculated  $\tilde{\sigma}_{yy}(T_0)$  for several values of  $T$ . For fixed  $T$  and large  $T_0$ , the conductivity oscillates with a constant amplitude about some mean value. As  $T$  goes to infinity (equation(18)), the asymptotic mean value of  $\tilde{\sigma}_{yy}$  approaches zero as  $1/T$ . Using an approximate analytical analysis, they were able to show that this is the expected behavior for a chaotic scattering system of this type. Thus, in practice  $\sigma_{yy}$  depends critically on the time over which  $C_{yy}$  is computed. In evaluating  $C_{yy}$  and  $\tilde{\sigma}_{yy}$ , the first crossing point was used as the starting point for the integrations since it is only in the vicinity of the midplane that the particles are expected to decorrelate. Additionally, they noted that different orbits with dissimilar correlation functions can have essentially the same energy gain. Recall that the orbits in Figure 3 have essentially the same initial and final conditions and therefore have essentially the same net energy gain. On the other hand, these two orbits obviously contribute very differently to the cross tail current since they have very different time histories. They gave an alternative expression to calculate the energy gain [Cowley, 1978]:

$$\Delta H = mc \left( \frac{E_y}{B_n} \right) \left( \frac{2H}{m} \right)^{1/2} (1 + b_n^2)^{-2} (|\cos \beta_1| + |\cos \beta_2|), \quad (19)$$

where  $\beta_1$  and  $\beta_2$  are the asymptotic incoming and outgoing pitch angles, respectively. The chaotic motion of particles in the vicinity of the current sheet plays no role. Numerical calculations show that this expression gives a complete description of energy gain. They also pointed out that the current density  $J_z(z)$  depends primarily on the source particle distribution and

the magnetic field topology and that  $J_y$  and  $E_y$  are not related by simple relationships such as an Ohm's law. In this regard, we note that a nonzero  $E_y$  effectively modifies the source particle distribution functions and hence the current but it is in a non-trivial way. The relationship between  $\beta_1$  and  $\beta_2$  is, of course, complicated as evidenced by the existence of fractals and is determined by global magnetic topology. It is unlikely that the global magnetotail structure can be fully understood using local quantities such as a "collisionless" conductivity.

## 6. DISCUSSIONS

The charged-particle motion in the magnetotail has been extensively studied for more than two decades because of its importance for understanding a wide variety of plasma phenomena in the geospace environment. Traditionally, the emphasis was to study the motion of individual particles. The adiabaticity and nonadiabaticity of particle orbits have received considerable attention. A qualitatively different approach is to treat the particle motion as a dynamical system, and geometrical (phase space) properties are exploited to obtain and explain physical observables. The important dynamical properties are the partitioning of the phase space and the chaotic scattering of incoming orbits by the current sheet. The underlying symmetry properties of the system are of principal importance. The significant phase space structures are robust in the presence of collisions, in contrast to properties of individual orbits. The basic dynamical properties of the magnetotail-like system have been firmly established from first principles. Moreover, the dynamical approach has yielded novel insights previously unavailable from the study of individual orbits. We emphasize that the geometrical approach yields qualitative but rigorously accurate for families of orbits. In contrast, detailed information regarding individual orbits or segments of orbits is not generic to the dynamical system.

The ability of charged particles to carry information and energy over long distances ( $\gg R_E$ ) in the essentially collisionless magnetotail means that the global particle dynamics can influence the distribution of internal energy and currents on a large scale. In view of its robustness, the partitioning of the phase space may play a significant role in determining such large scale properties. The magnetosphere may act as a self-organized critical system [Bak *et al.*, 1988]. Unlike the usual example of sandpiles, the magnetosphere is determined by globally coherent interaction of fields and collisionless particles. Thus, the nature of long-distance coupling within the magnetosphere is an essential question. If these conclusions prove to be correct, nonlinear dynamics may indeed provide a new framework for a deeper understanding of global magnetospheric processes. (See section 3.6 of Chen [1992].) Clarification of the relationships between particle dynamics and global properties is an important subject of future research. The importance of this line of inquiry is enhanced by the fact that the magnetotail is an observationally testable paradigm for a class of systems containing current sheets.

**Acknowledgments.** This work was supported by the National Aeronautics and Space Administration (W-16,991) and the Office of Naval Research.

## REFERENCES

- Alekseyev, I. I., and A. P. Kropotkin, Interaction of energetic particles with the neutral sheet in the tail of the magnetosphere, *Geomagn. Aeron., Engl. Transl.*, 10, 615, 1970.
- Ashour-Abdalla, M., J. Berchem, J. Büchner, and L. M. Zelenyi, Chaotic scattering and acceleration of ions in the Earth's magnetotail, *Geophys. Res. Lett.*, 17, 2317, 1990.
- Ashour-Abdalla, M., J. Berchem, J. Büchner, and L. M. Zelenyi, Large and small scale structures in the plasma sheet: A signature of chaotic motion and resonance effects, *Geophys. Res. Lett.*, 18, 1603, 1991.
- Bak, P., C. Tang, and K. Wiesenfeld, Self-organized criticality, *Phys. Rev. A*, 38, 364, 1988.
- Behannon, K. W., Mapping of the Earth's bow shock and magnetic tail by Explorer 33, *J. Geophys. Res.*, 73, 907, 1968.
- Birmingham, T. J., Pitch angle diffusion in the Jovian magnetodisc, *J. Geophys. Res.*, 89, 2699, 1984.
- Brittnacher, M. J. and E. C. Whipple, Chaotic jumps in the generalized first adiabatic invariant in current sheets, *Geophys. Res. Lett.*, 18, 1599, 1991.
- Büchner, J., and L. M. Zelenyi, Deterministic chaos in the dynamics of charged particles near a magnetic field reversal, *Phys. Lett. A*, 118, 395, 1986.
- Büchner, J., and L. M. Zelenyi, Chaotization of the electron motion as the cause of an internal magnetotail instability and substorm onset, *J. Geophys. Res.*, 92, 13,456, 1987.
- Büchner, J., and L. M. Zelenyi, Regular and chaotic charged particle motion in magnetotail-like field reversals, I, Basic theory of trapped motion, *J. Geophys. Res.*, 94, 11,821, 1989.
- Büchner, J., and L. M. Zelenyi, The separatrix tentacle effect of ion acceleration to the plasma sheet boundary, *Geophys. Res. Lett.*, 17, 127, 1990.
- Burkhart, G. R. and J. Chen, Linear, collisionless, bi-Maxwellian neutral-sheet tearing instability, *Phys. Rev. Lett.*, 63, 159, 1989.
- Burkhart, G. R., and J. Chen, Differential memory in the Earth's magnetotail, *J. Geophys. Res.*, 96, 14,033, 1991.
- Burkhart, G. R., and J. Chen, Chaotic scattering of pitch angles in the current sheet of the magnetotail, *J. Geophys. Res.*, 97, 6479, 1992a.
- Burkhart, G. R., and J. Chen, Particle motion in  $x$ -dependent Harrislike Magnetotail models, in press, *J. Geophys. Res.*, 1992b.
- Burkhart, G. R., J. F. Drake, P. B. Dusenbery, and T. W. Speiser, *J. Geophys. Res.*, 97, 13,799, 1992.
- Cary, J. R., E. F. Escande, and J. L. Tennyson, Adiabatic-invariant change due to separatrix crossing, *Phys. Rev. A*, 34, 4256, 1986.
- Chapman, S. C., Properties of single particle dynamics in a parabolic magnetic reversal with general time dependence, *J. Geophys. Res.*, 99, 5977, 1994.
- Chapman, S. C. and N. W. Watkins, Parameterization of chaotic particle dynamics in a simple time-dependent field reversal, *J. Geophys. Res.*, 98, 165, 1993.
- Chen, J., Nonlinear particle dynamics in the magnetotail, *J. Geophys. Res.*, 97, 15,011, 1992.
- Chen, J., Kinetic physics of the magnetotail, *Phys. Fluids B* 5, 2663, 1992.
- Chen, J. and P. J. Palmadesso, Tearing instability in an anisotropic neutral sheet, *Phys. Fluids*, 27, 1198, 1984.
- Chen, J., and P. J. Palmadesso, Chaos and nonlinear dynamics of single-particle orbits in a magnetotail-like magnetic field, *J. Geophys. Res.*, 91, 1499, 1986.
- Chen, J., G. R. Burkhart, and C. Y. Huang, Observational signatures of nonlinear magnetotail particle dynamics, *Geophys. Res. Lett.*, 17, 2237, 1990a.
- Chen, J., H. G. Mitchell, and P. J. Palmadesso, Differential memory in the trilinear model magnetotail, *J. Geophys. Res.*, 95, 15,141, 1990b.
- Chen, J., J. L. Rexford, and Y. C. Lee, Fractal boundaries in magnetotail particle dynamics, *Geophys. Res. Lett.*, 17, 1049, 1990c.
- Christon, S. P., D. J. Williams, D. G. Mitchell, L. A. Frank, and C. Y. Huang, Spectral characteristics of plasma sheet ion and electron populations during undisturbed geomagnetic conditions, *J. Geophys. Res.*, 94, 13,409, 1989.
- Coppi, B., G. Laval, and R. Pellat, Dynamics of the geomagnetic tail, *Phys. Rev. Lett.*, 16, 1207, 1966.
- Cowley, S. W. H., A note on the motion of charged particles in one-dimensional magnetic current sheet, *Planet. Space Sci.*, 26, 539, 1978.
- Curran, D. B., and C. K. Goertz, Particle distributions in a two-dimensional reconnection field geometry, *J. Geophys. Res.*, 94, 11,521, 1989.
- Curran, D. B., C. K. Goertz, and T. A. Whelan, Ion distributions in a two-dimensional reconnection field geometry, *Geophys. Res. Lett.*, 14, 99, 1987.
- Eastwood, J. W., Consistency of fields and particle motion in 'Speiser' model of the current sheet, *Planet. Space Sci.*, 20, 1555, 1972.
- Francfort, Ph. and R. Pellat, Magnetic merging in collisionless plasmas, *Geophys. Res. Lett.*, 3, 433, 1976.
- Gray, P., and L. C. Lee, Particle pitch angle diffusion due to non-adiabatic effects in the plasma sheet, *J. Geophys. Res.*, 87, 7445, 1982.
- Holland, D. L., and J. Chen, Effects of collisions on the nonlinear particle dynamics in the magnetotail, *Geophys. Res. Lett.*, 18, 1579, 1991.
- Holland, D. L., and J. Chen, On chaotic conductivity in the magnetotail, *Geophys. Res. Lett.*, 19, 1231, 1992.
- Holland, D. L. and J. Chen, Self-consistent current sheet structures in the quiet-time magnetotail, *Geophys. Res. Lett.*, 20, 1775, 1993.
- Horton, W., and T. Tajima, Decay of correlations and the collisionless conductivity in the geomagnetic tail, *Geophys. Res. Lett.*, 17, 123, 1990.
- Horton, W., and T. Tajima, Collisionless conductivity and stochastic heating of the plasma sheet in the geomagnetic tail, *J. Geophys. Res.*, 96, 15,811, 1991.
- Horton, W., C. Liu, B. Burns, and T. Tajima, Collisionless plasma transport across loop magnetic fields, *Phys. Fluids B*, 3, 2192, 1991.
- Horton, W., C. Liu, J. Hernandez, and T. Tajima, *Geophys. Res. Lett.*, 18, 1575, 1991b.
- Huang, C. Y., C. K. Goertz, L. A. Frank, and G. Rostoker, Observational determination of the adiabatic index in the quiet time plasma sheet, *Geophys. Res. Lett.*, 16, 563, 1989.
- Huba, J. D., J. Chen, and R. R. Anderson, Electrostatic turbulence in the Earth's central plasma sheet produced by multiple-ring ion distributions, *J. Geophys. Res.*, 97, 1533, 1992.
- Karimabadi, H., P. L. Pritchett, and F. V. Coroniti, Particle orbits in two-dimensional equilibrium models for the magnetotail, *J. Geophys. Res.*, 95, 17,153, 1990.
- Lembège, B. and R. Pellat, Stability of a thick two-dimensional quasineutral sheet, *Phys. Fluids*, 25, 1995, 1982.
- Lui, A. T., C.-L. Chang, A. Mankofsky, H.-K. Wong, and D. Winske, A cross-tail current instability for substorm expansion, *J. Geophys. Res.*, 96, 11,389, 1991.
- Lyons, L. R., Electron energization in the geomagnetic tail current sheet, *J. Geophys. Res.*, 89, 5479, 1984.

- Lyons, L. R., and T. W. Speiser, Evidence of current sheet acceleration in the geomagnetic tail, *J. Geophys. Res.*, **87**, 2276, 1982.
- Lyons, L. R., and T. W. Speiser, Ohm's law for a current sheet, *J. Geophys. Res.*, **90**, 8543, 1985.
- Martin, R. F., Chaotic particle dynamics near a two-dimensional magnetic neutral point with application to the geomagnetic tail, *J. Geophys. Res.*, **91**, 11,985, 1986.
- Martin, R. F., and T. W. Speiser, A predicted energetic ion signature of a neutral line in the geomagnetic tail, *J. Geophys. Res.*, **93**, 11,521, 1988.
- McComas, D. J., C. T. Russell, R. C. Elphic, and S. J. Bame, The near-earth cross-tail current sheet: Detailed ISEE 1 and 2 case studies, *J. Geophys. Res.*, **91**, 4287, 1986.
- Moses, R. W., J. M. Finn, and K. M. Ling, Plasma heating by collisionless magnetic reconnection: Analysis and computation, *J. Geophys. Res.*, **98**, 4013, 1993.
- Neishtadt, A. I., Variation of adiabatic invariant accompanying transition through separatrix, *Sov. J. Plasma Phys.*, Engl. Transl., **12**, 568, 1986.
- Pritchett, P. L., and F. V. Coroniti, Formulation and stability of the self-consistent one-dimensional tail current sheet, *J. Geophys. Res.*, **97**, 16,773, 1992.
- Rogers, S. H., and E. C. Whipple, Generalized adiabatic theory applied to the magnetotail current sheet, *Astrophys. Space Sci.*, **144**, 231, 1988.
- Sergeev, V. A., and N. A. Tsyganenko, Energetic particle losses and trapping boundaries as deduced from calculations with a realistic magnetic field model, *Planet. Space Sci.*, **30**, 999, 1982.
- Sergeev, V. A., E. M. Sazhina, N. A. Tsyganenko, J. Å. Lundblad, and F. Sorras, Pitch-angle scattering of energetic protons in the magnetotail current sheet as the dominant source of their isotropic precipitation into the nightside ionosphere, *Planet. Space Sci.*, **31**, 1147, 1983.
- Sonnerup, B. U. Ö., Adiabatic particle orbits in a magnetic null sheet, *J. Geophys. Res.*, **76**, 8211, 1971.
- Speiser, T. W., Particle trajectories in model current sheets. I, Analytical solutions, *J. Geophys. Res.*, **70**, 4219, 1965.
- Speiser, T. W., Conductivity without collisions or noise, *Planet. Space Sci.*, **18**, 613, 1970.
- Speiser, T. W., and L. R. Lyons, Comparison of an analytical approximation for particle motion in a current sheet with precise numerical calculations, *J. Geophys. Res.*, **89**, 147, 1984.
- Swift, D., The effect of the neutral sheet on magnetospheric plasma, *J. Geophys. Res.*, **82**, 1288, 1977.
- Timofeev, A. V., On the problem of constancy of the adiabatic invariant when the nature of the motion changes, *Sov. Phys. JETP*, **48**, 656, 1978.
- Tsyganenko, N. A., Pitch-angle scattering of energetic particles in the current sheet of the magnetospheric tail and stationary distribution functions, *Planet. Space Sci.*, **30**, 433, 1982.
- Wagner, J. S., J. R. Kan, and S.-I. Akasofu, Particle dynamics in the plasma sheet, *J. Geophys. Res.*, **84**, 891, 1979.
- West, H. I., R. M. Buck, and M. G. Kivelson, On the configuration of the magnetotail near midnight during quiet and weakly disturbed periods: State of the magnetosphere, *J. Geophys. Res.*, **83**, 3805, 1978a.
- West, H. I., R. M. Buck, and M. G. Kivelson, On the configuration of the magnetotail near midnight during quiet and weakly disturbed periods: Magnetic field modeling, *J. Geophys. Res.*, **83**, 3819, 1978b.
- Whipple, E., M. Rosenberg, and M. Brittner, Magnetotail acceleration using generalized drift theory: A kinetic merging scenario, *Geophys. Res. Lett.*, **17**, 1045, 1990.
- Zwingmann, W., Self-consistent magnetotail theory: Equilibrium structures including arbitrary variation along the tail axis, *J. Geophys. Res.*, **88**, 9101, 1983.



NRL/MR/6794--96-7789

# Test Particle Calculation of Electric Currents In Magnetic Field-Reversed Regions

J. CHEN

*Beam Physics Branch  
Plasma Physics Division*

D.L. HOLLAND

*Department of Physics, Illinois State University  
Normal, IL*

April 3, 1996

Approved for public release; distribution unlimited.

REPORT DOCUMENTATION PAGE			Form Approved OMB No. 0704-0188	
Public reporting burden for this collection of information is estimated to average 1 hour per response, including the time for reviewing instructions, searching existing data sources, gathering and maintaining the data needed, and completing and reviewing the collection of information. Send comments regarding this burden estimate or any other aspect of this collection of information, including suggestions for reducing this burden, to Washington Headquarters Services, Directorate for Information Operations and Reports, 1215 Jefferson Davis Highway, Suite 1204, Arlington, VA 22202-4302, and to the Office of Management and Budget, Paperwork Reduction Project (0704-0188), Washington, DC 20503.				
1. AGENCY USE ONLY (Leave Blank)	2. REPORT DATE  April 3, 1996	3. REPORT TYPE AND DATES COVERED  Interim		
4. TITLE AND SUBTITLE  Test Particle Calculation of Electric Currents In Magnetic Field-Reversed Regions			5. FUNDING NUMBERS  PE - 67-3788-05	
6. AUTHOR(S)  D.L. Holland,* and J. Chen				
7. PERFORMING ORGANIZATION NAME(S) AND ADDRESS(ES)  Naval Research Laboratory Washington, DC 20375-5320			8. PERFORMING ORGANIZATION REPORT NUMBER  NRL/MR/6794-96-7789	
9. SPONSORING/MONITORING AGENCY NAME(S) AND ADDRESS(ES)  Office of Naval Research      NASA 800 North Quincy Street      Washington, DC 20546 Arlington, VA 22217-5660			10. SPONSORING/MONITORING AGENCY REPORT NUMBER	
11. SUPPLEMENTARY NOTES  *Illinois State University, Normal, IL 61790-4560				
12a. DISTRIBUTION/AVAILABILITY STATEMENT  Approved for public release; distribution unlimited.			12b. DISTRIBUTION CODE	
13. ABSTRACT (Maximum 200 words)  A wide range of important plasma phenomena can take place in boundary layers between regions of oppositely directed magnetic fields where collisionless particles can execute magnetized and unmagnetized motion sequentially. Much work has been done recently to study such phenomena in space physics settings using test particle simulations. An important quantity in such systems is the electric current carried by charged particles, since it is this current which must produce the field reversal. Additionally one must calculate the particle density and pressure tensor in order to verify the existence of self-consistent equilibria. We present in this paper an algorithm for evaluating self-consistent Vlasov equilibria in magnetic field-reversed regions. In addition, we describe a technique to separate the magnetic field into the contribution due to the plasma diamagnetism, $4\pi M$ , and the part due to the actual particle current, $H$ .				
14. SUBJECT TERMS  Nonlinear particle dynamics      Simulations Magnetosphere Test particle			15. NUMBER OF PAGES  29	
			16. PRICE CODE	
17. SECURITY CLASSIFICATION OF REPORT  UNCLASSIFIED	18. SECURITY CLASSIFICATION OF THIS PAGE  UNCLASSIFIED	19. SECURITY CLASSIFICATION OF ABSTRACT  UNCLASSIFIED	20. LIMITATION OF ABSTRACT  UL	

## CONTENTS

I.	INTRODUCTION .....	1
II.	SINGLE PARTICLES .....	2
III.	PARTICLE DISTRIBUTIONS .....	5
IV.	APPLICATION TO THE MAGNETOTAIL .....	6
V.	EFFECTS OF DIAMAGNETISM .....	9
VI.	NUMERICAL ALGORITHM .....	13
VII.	CONCLUSIONS .....	14
	ACKNOWLEDGMENTS .....	15
	REFERENCES .....	16
	APPENDIX A .....	17
	APPENDIX B .....	20
	APPENDIX C .....	20



# TEST PARTICLE CALCULATION OF ELECTRIC CURRENTS IN MAGNETIC FIELD-REVERSED REGIONS

## I. INTRODUCTION

Many naturally occurring systems can be thought of as boundary regions between oppositely directed magnetic fields, where the dominant magnetic component of the magnetic field reverses sign and where "current sheets" are formed. Such field reversal regions occur in laboratory as well as astrophysical plasmas, and important physical phenomena such as reconnection can take place.

In space and astrophysical plasmas, the charged particles are usually collisionless. A simple example of a field reversal which models the Earth's magnetotail is the quasi-neutral sheet shown in Figure 1. The  $x$ -component of the magnetic field,  $B_x(z)$ , reverses sign at  $z = 0$ . The particle motion in this system is nonadiabatic [1] and has been shown to undergo chaotic scattering [2,3]. Another example of a field reversed geometry is given in Figure 2. Here there is an  $X$ -type neutral line at  $x = 0$  and  $z = 0$ , where the magnetic field vanishes. The particle motion near an  $X$ -line is also chaotic [4,5].

Because of the chaotic particle motion, the properties of plasmas in regions containing current sheets are nontrivial to study. An approach that has been fruitful is to use test particle simulations in which the charged particle motion is integrated in prescribed fields [6-13]. Although such simulations do not contain complete physical interactions, the results have often been successful in explaining observed satellite data [7,10].

A key property of magnetic field reversals is the electric current profile which determines the magnetic field, the magnetic energy distribution, and particle distribution function, the last representing the internal and free energy distribution of the plasma. Issues concerning current distributions have been investigated using test-particle simulations [13-19, 25]. For example, *Burkhart et al.* [14] modeled the structure of the "dissipation" region in collisionless reconnection. In this work, the current was calculated by following a distribution of particles through a prescribed field. Using the calculated current, a new magnetic field is calculated. The process was iterated until Ampere's law is satisfied. In some recent papers, self-consistent equilibrium current sheets have been computed in the magnetotail geometry [15,17,18]. In these works, the cross-tail current density is again constructed by binning the contributions from each test particle using a rectangular (Cartesian) grid and is iterated until self-consistency is achieved. The particle orbits are computed directly from the equation of motion.

An important feature of the particle motion in and near field reversals is that a given particle orbit consists of alternating segments of magnetized and unmagnetized motion [1]. A field reversal thus can be divided into spatial regions according to the type of particle motion. Consider a particle of energy  $H = mv^2/2$ . It is nearly unmagnetized while in the region  $|z| \lesssim d_j \equiv (\rho_z L)^{1/2}$ , where  $\rho_z$  is the particle's gyroradius in the  $z$ -component of the magnetic field and  $L$  is the scale length of the reversal region in the  $x$ -component of the magnetic field, and it is magnetized for  $|z| \gtrsim d_j$  [17].

In this report, we examine in detail the process of numerically computing electric currents in systems in which the particle motion alternately undergoes magnetized and unmagnetized motion. In addition, we describe an algorithm for approximately separating the magnetic field

into the part due to the plasmas diamagnetism,  $4\pi\mathbf{M}$ , and the part due to the actual particle current,  $\mathbf{H}$ .

## II. SINGLE PARTICLES

In test particle simulations, particle motion is computed in prescribed fields. The resulting equilibrium profiles (i.e., electric currents, particle density, and pressure tensor) can then be used to calculate the fields, which in turn may be used as a new prescribed field in the test particle simulation. This process may be iterated to self-consistency. Hence, a fundamental step is to compute the contribution of each particle to the equilibrium profiles in a given field. At any given time the distribution which represents a single particle is formally given by

$$f_{sp}(\mathbf{r}, \mathbf{v}, t) = \frac{1}{L^3 \Omega_0^3} \delta\left(\frac{\mathbf{r} - \mathbf{r}(t)}{L}\right) \delta\left(\frac{\mathbf{v} - \mathbf{v}(t)}{\Omega_0 L}\right). \quad (1)$$

Here  $L$  is a characteristic scale length for the system and  $\Omega_0$  is a characteristic frequency. Typically, computation of physical quantities is carried out using Cartesian coordinates where we have

$$\delta\left(\frac{\mathbf{r} - \mathbf{r}(t)}{L}\right) = \delta\left(\frac{x - x(t)}{L}\right) \delta\left(\frac{y - y(t)}{L}\right) \delta\left(\frac{z - z(t)}{L}\right) \quad (2a)$$

and

$$\delta\left(\frac{\mathbf{v} - \mathbf{v}(t)}{\Omega_0 L}\right) = \delta\left(\frac{v_x - v_x(t)}{\Omega_0 L}\right) \delta\left(\frac{v_y - v_y(t)}{\Omega_0 L}\right) \delta\left(\frac{v_z - v_z(t)}{\Omega_0 L}\right). \quad (2b)$$

The instantaneous particle and current densities are found by evaluating the zeroth and first velocity moments of  $f_{sp}$ , i.e.  $n(\mathbf{r}, t) = \int d\mathbf{v} f(\mathbf{r}, \mathbf{v}, t)$  and  $\mathbf{j}(\mathbf{r}, t) = qn(\mathbf{r}, t)\mathbf{U}(\mathbf{r}, t) = q \int d\mathbf{v} \mathbf{v} f(\mathbf{r}, \mathbf{v}, t)$ . Defining the normalized variables  $\hat{\mathbf{r}} = \mathbf{r}/L$  and  $\hat{\mathbf{v}} = \mathbf{v}/(\Omega_0 L)$ , these become

$$n(\hat{\mathbf{r}}, t) = \frac{1}{L^3} \delta[\hat{\mathbf{r}} - \hat{\mathbf{r}}(t)] \quad (3a)$$

and

$$\mathbf{j}(\hat{\mathbf{r}}, t) = \frac{q\Omega_0}{L^2} \hat{\mathbf{v}}(t) \delta[\hat{\mathbf{r}} - \hat{\mathbf{r}}(t)]. \quad (3b)$$

Instead of evaluating the pressure tensor  $\mathbf{p}(\mathbf{r}, t) = m \int d\mathbf{v} (\mathbf{v} - \mathbf{U})(\mathbf{v} - \mathbf{U}) f(\mathbf{r}, \mathbf{v}, t)$ , we calculate the second velocity moment of  $f_{sp}$ , i.e.  $\mathbf{q}(\mathbf{r}, t) = m \int d\mathbf{v} \mathbf{v} \mathbf{v} f(\mathbf{r}, \mathbf{v}, t)$ , since this does not require *a priori* knowledge of the average flow velocity  $\mathbf{U}$ . Evaluating this integral, we find

$$\mathbf{q}(\hat{\mathbf{r}}, t) = \frac{m\Omega_0^2}{L} \hat{\mathbf{v}}(t) \hat{\mathbf{v}}(t) \delta[\hat{\mathbf{r}} - \hat{\mathbf{r}}(t)]. \quad (3c)$$

It is trivial to show that  $\mathbf{q}$  may be written in terms of  $\mathbf{p}$ ,  $\mathbf{j}$ , and  $n$  as,

$$\mathbf{q} = \mathbf{p} + (m/q^2 n) \mathbf{j} \mathbf{j}.$$

(With this relation in mind, we shall henceforth simply refer to  $q$  as the pressure unless otherwise stated.)

In a standard particle in cell code it is the instantaneous density and current which is distributed onto a grid for each particle at every time step [20]. The resulting total density and current is then used to calculate updated fields which are used to "push" the particles for the next time step. In self-consistent test particle simulations, on the other hand, a particle is "pushed" through the system in a prescribed field from its point of injection to its point of escape. After "pushing" all of the particles in a source distribution through the system, the average currents and densities each particle contributes while in the system are added together to determine the total current and density which are then used to update the fields. Thus, the test particle code is very well suited for determining time stationary solutions with very good spatial resolution using a relatively small number of particles. By its very nature, however, it can only yield information regarding time evolution in the sense of a series of quasistatic equilibria.

The contribution of a single particle to the equilibrium quantities is obtained by averaging the values of those quantities along the trajectory for the time  $T$  the particle is in the system *i.e.*

$$\bar{n}(\hat{\mathbf{r}}) = \frac{1}{T} \int_0^T n(\hat{\mathbf{r}}, t) dt \quad (4a)$$

$$\bar{\mathbf{j}}(\hat{\mathbf{r}}) = \frac{1}{T} \int_0^T \mathbf{j}(\hat{\mathbf{r}}, t) dt. \quad (4b)$$

$$\bar{q}(\hat{\mathbf{r}}) = \frac{1}{T} \int_0^T q(\hat{\mathbf{r}}, t) dt. \quad (4c)$$

(Note that the value of  $T$  will in general be different for each particle.) If we assume that the particle phase space information (*i.e.* position and velocity) are known at the evenly spaced time intervals,  $t_n = n\Delta t$ , where  $0 < n < N$  and  $N\Delta t = T$ , we may approximate the integral in (4a) as a finite sum. Hence the average single particle density becomes

$$\bar{n}(\hat{\mathbf{r}}) = \frac{1}{L^3} \mathbf{D}(\hat{\mathbf{r}}) = \frac{1}{L^3} \left[ \frac{1}{N} \sum_{n=0}^N \delta_{\hat{\mathbf{r}}, \hat{\mathbf{r}}_n} \right]. \quad (5a)$$

Here  $\delta_{\hat{\mathbf{r}}, \hat{\mathbf{r}}_n}$  is the Kroneker delta function,  $\hat{\mathbf{r}}_n = \hat{\mathbf{r}}(n\Delta t)$  and  $\mathbf{D}(\hat{\mathbf{r}})$  is the normalized single particle density. In a similar manner, the average current density and pressure which may be attributed to a single particle may be written as

$$\bar{\mathbf{j}}(\hat{\mathbf{r}}) = \frac{q\Omega_0}{L^2} \mathbf{J}(\hat{\mathbf{r}}) = \frac{q\Omega_0}{L^2} \left[ \frac{1}{N} \sum_{n=0}^N \hat{\mathbf{v}}(n\Delta t) \delta_{\hat{\mathbf{r}}, \hat{\mathbf{r}}_n} \right]. \quad (5b)$$

$$\bar{q}(\hat{\mathbf{r}}) = \frac{m\Omega_0^2}{L} \mathbf{Q}(\hat{\mathbf{r}}) = \frac{q\Omega_0^2}{L} \left[ \frac{1}{N} \sum_{n=0}^N \hat{\mathbf{v}}(n\Delta t) \hat{\mathbf{v}}(n\Delta t) \delta_{\hat{\mathbf{r}}, \hat{\mathbf{r}}_n} \right]. \quad (5c)$$

Where  $\mathbf{J}(\hat{\mathbf{r}})$ , and  $\mathbf{Q}(\hat{\mathbf{r}})$  are the normalized single particle current density and pressure tensor profiles respectively. Using (5) it is a trivial matter to distribute the single particle density and current onto a grid. In essence, by using the above technique, we are relating average residence times of particles in a region to equilibrium profiles.

As a concrete example, we consider particle motion in the modified Harris model of the Earth's magnetotail  $\mathbf{B} = B_0 \tanh(z/L) \hat{\mathbf{x}} + B_z \hat{\mathbf{z}}$  (Fig. 1). Here  $B_0$  is the asymptotic value of the field due to the current sheet,  $L$  is the characteristic scale length of the field reversal,  $B_z$  is a constant magnetic field normal to the current sheet, and  $\hat{\mathbf{x}}$  is in the sunward direction. The particle motion in this geometry is well documented. (A review can be found in reference [17].) Since the fields in the modified Harris model are translationally invariant in the  $x$  and  $y$  directions, we need only consider variations in the  $z$ -direction when calculating the current and density profiles. Similar techniques may be used for  $X$ -line geometries (Figure 2), however, in that case we must use a two-dimensional grid since there is variation in both the  $x$  and  $z$  directions.

Assume that we wish to distribute the current and density profiles onto a one dimensional grid in the  $z$  direction with  $M + 1$  equally spaced points between  $\pm \hat{z}_{max}$ . If on the  $n^{th}$  time step, the particle falls between the  $m^{th}$  and  $(m + 1)^{th}$  grid points, we use a linear interpolation scheme to distribute the Kronecker delta weight function onto the grid, i.e. we add to the density and current at each of these points the amounts

$$\Delta n(\hat{z}_m) = \frac{|\hat{z}_m - \hat{z}|}{\Delta \hat{z}} \quad (6a)$$

$$\Delta n(\hat{z}_{m+1}) = \frac{|\hat{z}_{m+1} - \hat{z}|}{\Delta \hat{z}} \quad (6b)$$

$$\Delta j(\hat{z}_m) = \hat{v}(n\Delta t) \frac{|\hat{z}_m - \hat{z}|}{\Delta \hat{z}} \quad (6c)$$

$$\Delta j(\hat{z}_{m+1}) = \hat{v}(n\Delta t) \frac{|\hat{z}_{m+1} - \hat{z}|}{\Delta \hat{z}} \quad (6d)$$

$$\Delta q(\hat{z}_m) = \hat{v}(n\Delta t) \hat{v}(n\Delta t) \frac{|\hat{z}_m - \hat{z}|}{\Delta \hat{z}} \quad (6e)$$

$$\Delta q(\hat{z}_{m+1}) = \hat{v}(n\Delta t) \hat{v}(n\Delta t) \frac{|\hat{z}_{m+1} - \hat{z}|}{\Delta \hat{z}} \quad (6f)$$

Here we have defined  $\Delta \hat{z} = 2\hat{z}_{max}/M$ . This procedure is followed so long as the particle position falls between  $\pm \hat{z}_{max}$ . Of course, if we are to use the top (bottom) grid point, we must use a guard cell, i.e., if the particle lies between  $\hat{z}_{max}$  and  $\hat{z}_{max} + \Delta \hat{z}$ , ( $-\hat{z}_{max}$  and  $-\hat{z}_{max} - \Delta \hat{z}$ ) we must add to the density, current and pressure at the top (bottom) point amounts equal to (6a), (6c) and (6e) ((6b), (6d) and (6f)) where now  $\hat{z}_m = \hat{z}_M$  ( $\hat{z}_{m+1} = \hat{z}_1$ ). Finally, in order to insure unit probability of finding the particle in the system, all quantities are normalized such that the height integrated density (i.e. the sum over the  $\mathbf{D}(\hat{z})$  contributions at each grid point) is equal to one.

### III. PARTICLE DISTRIBUTIONS

Having found the equilibrium profiles due to a single particle moving through the field reversal region, we now wish to weight these single particles in such a fashion as to model a source distribution of particles. In this context there is some ambiguity as to how to perform the reconstruction based on what is assumed to be known. Here we shall discuss two possible normalization options. In both cases, we assume that each particle represents a unit volume of phase space and we launch shells of constant energy and reconstruct the source distribution by properly weighting the shells. The difference between the two normalization schemes arise in how we weight the particles on a given energy shell.

In the first scenario, (which is the more general of the two) we assume that we know the density of the incoming distribution and that the density of the outgoing distribution is determined by the particle dynamics. In this case, we calculate the density a given particle gives to the top grid cell when it is initially approaching the midplane (assuming the particle is launched from above the field reversal region) and normalize the density for that particle such that this contribution is unity. Note that this normalization implies that if a particle leaves from the bottom of the current calculation region, the density of the top cell will be unity. If the particle leaves from the top, however, the density of the top cell will be greater than unity. Once we have calculated the density and current for each of the particles on a given energy shell, all of the single particle densities and currents are added together and divided by the total number of particles that enter into the density calculation region for that shell. Note that in this scenario, we may either symmetrize the current sheet by assuming equal particle sources above and below the midplane, or we may launch separate distributions from each source region.

In the second technique, we assume *a priori* that the particle sources are symmetric and that we only know the total density which a particle contributes to the top grid cell is equal to unity. In this case we symmetrize the single particle density and current before normalizing them. The single particle equilibrium profiles are then normalized such that the density in the top grid cell is unity. (Note that this now includes particles that are entering and leaving the system in the normalization.) The single particles profiles for a given energy shell are added together and divided by the total number of particles which enter the current calculation region for that shell.

In general the first technique is preferable since it reduces the number of assumptions made in the analysis. Computationally it is much more difficult, however, since we must keep track of the particle while it is initially approaching the midplane and make a determination as to when to cut off the calculation of the normalization factor (*i.e.* how many counts the particle contributes to the top grid cell.)

For either technique, once we have calculated the current contribution for each shell, we normalize the profiles by their relative phase space volumes. This is done so that we do not need to space the shells equally in velocity. For example, suppose we have  $P$  energy levels between  $\hat{H} = \hat{H}_{min}$  and  $\hat{H} = \hat{H}_{max}$ . The  $p^{th}$  shell is then taken to represent the phase space volume  $(v_p - v_{p-1})/v_{max}$ , where  $\hat{H} = \frac{1}{2}mv^2$  and  $p = 1, 2, \dots, P$ . The phase space volume

represented by the first shell is simply  $v_1/v_{max}$ . Note that in this weighting scheme the sum of all of the shells has unit weight. Finally the shells are weighed by the desired model velocity distribution function, (e.g. Maxwellian, Kappa, etc.) and summed together to produce the total density and current for the assumed particles sources.

#### IV. APPLICATION TO THE MAGNETOTAIL

In the case of the magnetotail, we are primarily interested in the y-component of the current, since this is the component which produces the x-component of the magnetic field, i.e. the field reversal. Using the calculated current, we compute an updated magnetic field which we then use as the input field. For the one-dimensional case discussed here, the magnetic field is calculated by numerically integrating the calculated y-current profile in the z-direction with the numerical constant found by requiring the magnetic field to vanish at the midplane. (For a two-dimensional case such as the X-line geometry, it is simpler to solve for the vector potential using a two-dimensional Poisson solver.) In updating the magnetic field, we have employed an overall weighting factor on the current and density so as to insure that the amplitude of the asymptotic magnetic field remains unchanged. The process is iterated until the input and calculated field profiles have converged.

Recently it has been found that if all three components of the current are kept, an antisymmetric y-component of the magnetic field grows until its peak value is on the order of the x-component [21-23]. This field is believed to be the test particle code (time independent) analog of a wave which has been shown to develop in the current sheet using time dependent hybrid simulations [23]. For the purpose of our discussion here, it suffices to note that if the source distribution of particles is highly field aligned, this wave has a fast growth rate and saturates, with  $B_y$  on the order of  $B_x$ . For more isotropic source distributions, it was found that the growth rate is much slower (on the order of half an hour for magnetotail parameters) and saturated with a much smaller amplitude [23]. Thus, it only makes sense to use the test particle formulation for calculating equilibria for the cases in which we have a nearly isotropic source of particles. (It is also important to note that in order to successfully run the hybrid simulation, one needs to input the self-consistent magnetic field structure calculated using the test particle code. If this is not done, the hybrid simulation starts too far from equilibrium which results in too much free energy for wave growth and a resulting disruption of the equilibrium.) Henceforth, we will suppress the y-component of the magnetic field and use only source distributions that produce small  $B_y$ .

To compare our results with observed quantities, we must convert our simulation results into physically meaningful units. Using equations (5a-c), we see that the total particle density, current density and pressure may be written as

$$\bar{n}_{tot}(\hat{z}) = \frac{\eta}{L^3} \sum_{i=1}^{N_p} C_i D_i(\hat{z}) = \frac{\eta}{L^3} D_{tot}(\hat{z}), \quad (7a)$$



$$\bar{\mathbf{J}}_{tot}(\hat{z}) = \frac{\eta q \Omega_0}{L^2} \sum_{i=1}^{N_p} C_i \mathbf{J}_i(\hat{z}) = \frac{\eta q \Omega_0}{L^2} \mathbf{J}_{tot}(\hat{z}) \quad (7b)$$

$$\bar{\mathbf{P}}_{tot}(\hat{z}) = \frac{\eta m \Omega_0^2}{L} \sum_{i=1}^{N_p} C_i \mathbf{P}_i(\hat{z}) = \frac{\eta m \Omega_0^2}{L} \mathbf{P}_{tot}(\hat{z}) \quad (7c)$$

where  $C_i$  is the weighting applied to the  $i^{th}$  particle density,  $N_p$  is the number of particles used and  $\eta$  is an overall weighting factor used to ensure a constant asymptotic magnetic field strength. We now need to relate  $\eta$ ,  $L$  and our dimensionless density, current, and pressure to measured values of the asymptotic magnetic field and density.

From Ampere's law, the asymptotic value of the magnetic field may be related to the height integrated current through the relation

$$2B_0 = \mu_0 \frac{\eta q \Omega_0}{L} \int_{-\infty}^{+\infty} \mathbf{J}_{tot}(\hat{z})(dz/L) \quad (8)$$

In our computational algorithm, we wish to we maintain a constant magnitude for the asymptotic magnetic field (*i.e.*,  $B(-\infty)/B_0 = -1$  and  $B(+\infty)/B_0 = +1$ ). and hence we require

$$\int_{-\infty}^{+\infty} \mathbf{J}_{tot}(\hat{z})(dz/L) = 2 \quad (9)$$

Substituting (9) into (8) we find that the amplitude of the magnetic is given by

$$B_0 = 4\pi \times 10^2 \frac{\eta q \Omega_0}{L} \text{ nT} \quad (10)$$

or equivalently, since  $\Omega_0$  is proportional to  $B_0$  we find that

$$\eta/L = 5.19 \times 10^{16} \frac{\mu}{Z^2} \text{ m}^{-1} \quad (11)$$

where  $\mu$  is the ratio of the ion to the proton mass and  $Z$  is the charge state of the ion. Thus we have a relationship between the simulation quantities  $\eta/L$  and physically determined quantities. (Typically we assume that the ions are protons so that  $\mu = Z = 1$ .)

From equation (7a) we know that the asymptotic density (or alternatively the density in the top cell) is given by

$$\bar{n}_{tot}(\hat{z}_{max}) = \frac{\eta}{L^3} \mathbf{D}_{tot}(\hat{z}_{max})$$

where  $z_{max}$  is the maximum value of the normalized position. If we require that  $\bar{n}_{tot}(\hat{z}_{max}) = n_0$  where  $n_0$  is the physical particle density given in particles per cubic centimeter, we find that

$$\frac{\eta}{L^3} = \frac{n_0}{\mathbf{D}_{tot}(\hat{z}_{max})} \quad (12)$$

where  $D_{tot}(\hat{z}_{max})$  is the computed density in the top grid cell (output from the code). Hence we have a relationship between the physically measured particle density and the ratio of the simulation quantities  $\eta/L^3$  and  $D_{tot}(\hat{z}_{max})$ . From equations (11) and (12) it is now possible to uniquely determine the values of  $\eta$  and  $L$  separately for any given physical situation.

In space physics it is often useful to give distances in terms of earths radii ( $R_E = 6.37 \times 10^6$  m). To do this we write  $L = \sigma R_E$ , and hence from (11) we have

$$\eta/\sigma = 3.307 \times 10^{23} \frac{\mu}{Z^2}$$

and from (12) we have that

$$\frac{\eta}{\sigma^3} = \frac{n_0}{D_{tot}(\hat{z}_{max})} R_E^3$$

These equation may be solved for  $\sigma$  to obtain

$$\sigma = 0.036 \sqrt{\frac{\mu n_0}{Z^2 D_{tot}(\hat{z}_{max})}} \quad (13)$$

In essence, equation (13) gives us the scale factor for changing from our simulation dimensions to the physical dimensions for a given particle density and ion species.

Using the above results it is now a trivial process to determine the numerical coefficients to convert our simulation density, current and pressure profiles into physically meaningful data, *i.e.*

$$\frac{\eta q \Omega_0}{L^2} = 0.125 (B_0/\sigma) \text{ nA/m}^2. \quad (14)$$

and

$$\frac{\eta m \Omega_0^2}{L} = 7.97 \times 10^{-12} (B_0^2) \text{ dyne/cm}^2. \quad (15)$$

In equations (13)-(15)  $B_0$  is measured in nT and  $n_0$  is measured in  $\text{cm}^{-3}$ ,

An additional quantity of interest is the normalized temperature,  $\hat{T}$ , of the distribution which is input to the code. This is related to the physical temperature,  $T$ , through the relation

$$\hat{T} = 2T/m\Omega_0^2 L^2. \quad (16)$$

Solving for the physical temperature in keV, we find

$$T = 3.88 B_0^2 \sigma^2 \hat{T} (Z^2/\mu) \text{ keV}. \quad (17)$$

In Figure 3 we give an example the self-consistent density, current, magnetic field and pressure profiles calculated using the above algorithm where we have assumed that the particle source is a kappa distribution ( $\kappa = 4.5$ ) with a bulk drift in the tailward direction of 10% of the thermal velocity and a density of  $0.5 \text{ cm}^{-3}$ , the asymptotic magnetic field is 20nT, and  $B_z/B_0 = 0.1$ .

To verify the existence of a self-consistent equilibrium, the density, current and pressure profiles must satisfy global pressure balance. In general this requirement is given by the first moment of the Vlasov equation which yields

$$\nabla \cdot (\mathbf{P} + mN\mathbf{U}\mathbf{U} + \frac{B^2}{8\pi}\mathbf{I} - \frac{\mathbf{B}\mathbf{B}}{4\pi}) = 0 \quad (18)$$

where we are using the actual pressure  $\mathbf{P} = m \int d\mathbf{v} (\mathbf{v} - \mathbf{U})(\mathbf{v} - \mathbf{U}) f(\mathbf{r}, \mathbf{v})$ , and as usual  $N\mathbf{U} = \int d\mathbf{v} \mathbf{v} f(\mathbf{r}, \mathbf{v})$  and  $N = \int d\mathbf{v} f(\mathbf{r}, \mathbf{v})$  are the particle flux and particle density and  $\mathbf{I}$  is the unit matrix. In 1D with only  $\partial/\partial z \neq 0$ , Eq. (18) becomes

$$P_x - \frac{B_x B_z}{4\pi} = \text{const} \quad (19a)$$

$$P_y - \frac{B_y B_z}{4\pi} = \text{const} \quad (19b)$$

$$P_z + \frac{B_x^2 + B_y^2 - B_z^2}{8\pi} = \text{const.} \quad (19c)$$

We have also used the continuity equation and the symmetry of the system to deduce that  $N\mathbf{U}_z = 0$ . In Figure 4 we plot equations (19 a-c) for the case depicted in Figure 3. Note that all three equations are well satisfied.

## V. EFFECTS OF DIAMAGNETISM

An interesting aspect of the field reversed geometry is the effects of diamagnetism. Even though the density in the current sheet typically only varies by a few percent in the cases that produce small  $B_y$ , we find that it is in these cases that the plasma diamagnetism becomes a significant effect. This is because the particle executes magnetized motion for  $|z| \gtrsim (\rho_z L)^{1/2}$ , and unmagnetized motion for  $|z| \lesssim (\rho_z L)^{1/2}$ . When the particle motion changes character, it contributes a diamagnetic current in that region. As we will show, this diamagnetic current depends on the asymptotic pitch angle of the particles with larger pitch angles producing larger diamagnetic currents. In this section we will discuss the diamagnetic current due to an individual particle and then discuss the ramifications on distributions of particles.

Regardless of the intervening motion (*i.e.* chaotic or not), the shift in the y-component of the guiding center is given by

$$\Delta y_{gc} = \sqrt{\frac{2b_z^2 \hat{H}}{1 + b_n^2}} [|\cos \beta_2| + |\cos \beta_1|] \quad (20)$$

where  $b_z = B_z/B_0$  is the ratio of the z and x magnetic fields in the asymptotic region,  $\hat{H} = H/m\Omega_0^2 L^2$  is the normalized energy of the particle,  $\Omega_0 = qB_0/mc$  is the cyclotron frequency in the x-component of the magnetic field, and  $\beta_1$  ( $\beta_2$ ) is the initial (final) pitch angle

of the particle as it enters (leaves) the system. From (20), we may calculate the average current density supplied by a particle to be

$$\langle j \rangle = q\Delta y_{gc}/\Delta t \quad (21)$$

where  $\Delta t$  is the time required for the particle to enter and leave the current calculation region [24].

In Figure 5a we show the trajectory of a typical orbit and in Figure 5b we show the associated current profile in the  $y$ -direction between  $\hat{z} = \pm 5$  as calculated using (6a)-(6d). A positive charge moves in the direction indicated by the arrow. The particle is launched from  $\hat{z}_0 = 6$  with the energy  $H = 0.24m\Omega_0^2 L^2$ , and an initial pitch angle of  $100^\circ$  (using the field conventions of Figure 1). In its interaction with the neutral sheet, here taken to be the time the particle is in the current calculation region ( $|z| \leq 5$ ), the  $y$ -component of the particle guiding center in the asymptotic regions is shifted by an amount  $\Delta y_{gc} = 3.03L$  in a time  $482\Omega_0^{-1}$ . This implies an average  $y$ -current density between  $\hat{z} = \pm 5$  of  $\langle j \rangle = 6.28 \times 10^{-3} qL\Omega_0$ . If we average the numerically calculated current density profile between  $\hat{z} = \pm 5$ , however, we obtain a net negative total current of  $-5.5 \times 10^{-2} qL\Omega_0$ . This somewhat surprising result of a net negative current density is caused by the plasma's diamagnetism and as we shall see is strongly dependent on the asymptotic pitch angle of the particle.

To understand the difference between the numerically computed average current density and the value given by  $q\Delta y_{gc}/\Delta t$  the size of the current calculation region is increased to  $\hat{z} \leq \pm 8$  so that the particle is in the calculation region through out its entire orbit. We have calculated the  $J_y$  profile using equations (6a)-(6d) at several times to see how the current is deposited onto the grid. Figure 6 shows the result at three times: (a)  $T = 200\Omega_0^{-1}$ , (b)  $T = 400\Omega_0^{-1}$ , and (c)  $T = 600\Omega_0^{-1}$ . The important feature to note in these figures is the development of current peaks in regions associated not with any shift in the  $y$ -component of the guiding center, but rather with the injection and exit points of the particles. If these peaks are included in the numerically calculated average current, the net magnitude of the current density is positive and in agreement with the value calculated from  $\langle j \rangle = q\Delta y_{gc}/\Delta t$ . Since the total average current (including the peaks at the entry and exit points) is in agreement with the expected value, this implies we have deposited a net negative current in the midplane which exactly cancels the positive current at the entry and exit points. This negative current in the field reversal region is in addition to the positive current due to the meandering motion of the ion.

The formation of the positive current peaks at the entry and exit points and the deposition of negative currents near the midplane may be intuitively understood if we examine a plot of  $\hat{v}_y$  vs.  $\hat{z}$  (Figure 7a). If we suppose that we are putting the current into bins of width  $L$ , then it is clear that the finite gyroradius effects in the regions where the guiding center is well defined (*i.e.* from points a to b and from points c to d) produce a net positive current in the top and bottom grid cells but tend to leave net negative current near the midplane.

Another way of understanding the development of the current peaks at the entry and exit sites is to examine the case where  $B_z$  goes to zero. Here the magnetic field is purely in the

x-direction but we are still gridding the current as a function of  $z$  (Figure 8). Examining Figure 8, we see that for grid cells above the particle guiding center there are only positive contributions to the y-current density, whereas below the guiding center there are only negative contributions to the y-current density. Thus, we would expect to develop a positive current peak above the guiding center position and a negative current peak of equal magnitude below the guiding center position. If the two peaks are added together, we obtain the physically reasonable result of no net current in the y-direction. The same difficulties do not apply to the x-current density since it has equal positive and negative contributions both above and below the particle guiding center. (This formation of equal and opposite current peaks above and below the guiding center is nothing more than the one-dimensional manifestation of the particles diamagnetism.) If we now allow for finite  $B_z$ , the same general effects will occur in the asymptotic regions (*i.e.* far from the midplane), but now the peaks will tend to separate as we let  $T$  increase since the particles are now moving down the field line. This effect is illustrated in Figure 6a where we have two equal and opposite current peaks separated by a region of zero current. At the time depicted in the Figure 6a, the particle was always in the asymptotic region where the magnetic field is essentially constant.

In appendix A, we show that the net positive y-velocity deposited around the entry and exit point (or conversely the net negative y-velocity deposited near the midplane) for a particle may be approximated by

$$\langle \hat{v}_y \rangle_p \approx 4 \sqrt{\frac{2\hat{H}}{1+b_z^2}} \sin \beta \sum_{k=0}^K \sqrt{1 - \left( \frac{2\pi k b_n \cot \beta}{\sqrt{1+b_z^2}} \right)^2} \quad (22a)$$

where

$$K = \text{Int} \left[ \frac{\sqrt{1+b_z^2}}{2\pi b_z} \tan \beta \right] \quad (22b)$$

The quantity  $\langle \hat{v}_y \rangle_p$  is related to the current density in the peak through the relation  $\langle \hat{v}_y \rangle_p = T \langle j_y \rangle_p$  where  $T$  is the total time between when the particle is injected into, and when it leaves the current calculation region. Figures 9a–9c are plots of the approximate analytic expression (solid line) for  $\langle \hat{v}_y \rangle_p$  as a function of the pitch angle for  $\hat{H} = 1.0$  and (a)  $b_n = 0.1$ , (b)  $b_n = 0.2$  and (c)  $b_n = 0.4$ . The points ( $\bullet$ ) are numerically evaluated by “pushing” the particle through the assumed field and keeping track of the y-velocity deposited around the entry point of the particle. We note that for nearly field aligned particles the value of  $\langle \hat{v}_y \rangle_p$  is small thus indicating that there is only a small diamagnetic current. For pitch angles near  $90^\circ$ , however, there is substantial diamagnetic current in all cases. The agreement between the analytical and the numerical results is in good agreement throughout the parameter space. Note the breaks in both the theoretical and numerical curves. Except for a phase shift which is easily understood in terms of the approximations made in the derivation of the theoretical expression, the locations and number of breaks are in good agreement with the numerical results (*cf.* Appendix A).

It is interesting to estimate the critical pitch angle,  $\beta_c$ , at which the negative diamagnetic current deposited in the vicinity of the midplane is equal to the positive current due to the meandering motion of the particle in the field reversal region (i.e. the pitch-angle at which the net current supplied by the ion is in the wrong direction to aid in the production of the field reversal). As a lowest order approximation, we assume that as the particle crosses the midplane all of its energy is in the y-direction and that it remains in the vicinity of the midplane for one half of a cyclotron orbit in the z-component of the magnetic field [24]. (Note that this is actually an over estimate of the meandering motion current since not all of the energy will be in y-direction.) This implies that the net y-velocity deposited near the midplane due to the meandering motion may be approximated as

$$\langle \hat{v}_y \rangle_m \approx \pi \sqrt{2\hat{H}/b_n} \quad (23)$$

Equation (23) is shown as the horizontal dashed lines in Figures 9a–9c. Furthermore, we assume that the incoming and outgoing pitch-angles are equal, a condition which has been shown to be nearly the case for Speiser-type orbits [18]. Equating (23) with two times (22) (to account for both the incoming and outgoing diamagnetic contributions), it is easily shown that  $\beta_c$  is a solution to the equation

$$\frac{8 b_z \sin \beta_c}{\pi \sqrt{1 + b_z^2}} \sum_{k=0}^K \sqrt{1 - \left( \frac{2\pi k b_z \cot \beta_c}{\sqrt{1 + b_z^2}} \right)^2} = 1 \quad (24)$$

In Figure 10, we show a plot of  $\beta_c$  as a function of  $b_z$  (•) as given by (24). We also show on the same figure the value of  $\beta_c$  found by using the actual value of  $\langle \hat{v}_y \rangle_p$  (i.e., the solid dots in Figures 9a–9c) instead of the approximate value (i.e., the solid lines in Figures 9a–9c). There are two important facets to this figure: the first is that for small values of  $b_z$ , the theoretical and numerical values of  $\beta_c$  are in good agreement, the second is that for larger  $b_z$ ,  $\beta_c$  becomes smaller. This indicates that for an ensemble of particles with random pitch angles the ratio of the meandering motion current to the diamagnetic will be closer to unity for larger values of  $b_z$ .

An important conclusion which may be reached from the above discussion is that if the average pitch angle of a source of particles is greater than  $\beta_c$  the diamagnetic current will be larger than the current due to the meandering motion. In such cases, since the net current is in the wrong direction to create the assumed magnetic field reversal, *no self-consistent solutions exist*. In essence the assumption of the self-consistent solution to the magnetic field and the chosen distribution function are mutually exclusive. If on the other hand the average distribution function has a large drift velocity along the field ( $v_D > v_{th}$ ), the average pitch angle is much less the  $\beta_c$  and the diamagnetic contribution to the current is negligible. In this case it is a simple matter to iterate to self-consistent solutions provided that  $B_y$  is negligible. [15,18,19,25]. As mentioned above, one must be careful in this regime since  $B_y$  is typically non-negligible and grows on a short time scale. In the regime reminiscent of the quiet-time

magnetotail where the field aligned drift is small and the source distribution is nearly isotropic, the average pitch-angle may be close to the critical pitch-angle. Here the diamagnetic current and the meandering motion current are of the same order magnitude and small changes in the distribution function can result in large changes in the self-consistent solutions. Previous attempts to calculate the current sheet structure in the low drift velocity regime [15] found that if the drift velocity is made lower than some critical velocity, then no equilibrium exist. It was also found that larger values of  $b_z$  resulted in a larger value of the critical drift velocity. This loss of equilibrium was referred to as the current sheet catastrophe. We believe that what the authors were actually observing was the transition from the regime in which the meandering current is larger than the diamagnetic current to the regime in which the opposite is true.

## VI. NUMERICAL ALGORITHM

In this section we describe the numerical algorithm used to separate the magnetic field into the part due to the plasma diamagnetism and the part due to the actual particle current. The simplest possible technique is to follow the particle guiding center and to evaluate the guiding center drift and the instantaneous value of the magnetic moment of the particle,  $\mu = mv_{\perp}^2/2B$ . Here  $v_{\perp}$  refers to the component of the velocity which is perpendicular to the magnetic field,  $B$  is the local magnitude of the magnetic field and the direction of  $\mu$  is antiparallel to the local magnetic field. These quantities are then used to calculate the particle current and the magnetization vector  $\mathbf{M}$  of the plasma respectively. (Note that the magnetization vector  $\mathbf{M}$  is calculated in same way as our other equilibrium quantities, i.e. we distribute the instantaneous magnetic moment of each particle on a grid and then add them together with the appropriate weightings.) This technique works well in the asymptotic regions where the guiding center is well defined but fails near the midplane where the guiding center is only poorly defined. We therefore use a hybrid model for calculating the equilibrium profiles. In the regions where the guiding center is well defined, we transform to the guiding center coordinates (position and velocity) for distributing the current density, density and magnetic moment onto the grid whereas in regions where the guiding center is not well defined we use the actual particle position and velocity for distributing the current and density onto the grid. (See appendix B for the calculation of the guiding center location.) This method requires that we follow the actual particle motion in both regions, so that proper phase information is retained for the particle in changing from the magnetized to the unmagnetized regions and *vice versa*. For the case of the magnetotail, the separation between the "magnetized" and "unmagnetized" regions occurs at the separatrix where the particle changes from non-midplane crossing to midplane crossing. In appendix C, we show that the phase space location of the separatrix is approximated by

$$v_z^2 \leq [P_y/M - (q/Mc)A_y(x, z)]^2 - [P_y/M - (q/Mc)A_y(x, z=0)]^2. \quad (25)$$

where  $A_y$  is the vector potential for the magnetic field and  $P_y$  is the y component of canonical momentum for the particle. The condition given by (24) is simply a statement that for a particle



to be classified as a midplane crossing, the energy in the  $z$ -component of the velocity must be larger than the effective potential for the  $z$ -motion evaluated at the midplane.

In Figure 11, we show the density, current and magnetic field profiles calculated using the algorithms described in this paper for the case of a Maxwellian with a bulk drift in the tailward direction of 10% of the ion thermal velocity and a high energy isotropic tail; which comprises 10% of the total density. Note that in this case, (which has a nearly isotropic source distribution) the diamagnetization accounts is approximately 80% of the magnetic field due to the particle currents. In Figure 12 we show the same plots but using a Maxwellian source distribution which has a tailward drift of twice the ion thermal velocity (*i.e.*, a highly field aligned distribution). Note that in this case the plasma diamagnetism is only a small correction to the total magnetic field. One must be careful in interpreting the results in this case; however, since we would expect there to be a rapidly growing  $B_y$  field associated with the highly field aligned distribution.

## VII. CONCLUSIONS

In this report we have described a technique for calculating density, electric current and pressure in a magnetic field reversed region using a test particle simulation. The essence of the technique is to push a distribution of particles through a model magnetic field which is fixed in both time and space. For each particle the density current and pressure are laid down on a grid. After all of the particle trajectories have been calculated we then calculate the total density, current, pressure and magnetic field profiles that the assumed distribution would produce. We then compare the assumed and the calculated magnetic fields. If the difference between the fields is sufficiently small the simulation is stopped and we check to make sure that global pressure balance is obtained [Eq. (19)]. Otherwise, we mix the assumed and the calculated fields and use the combined field in a new iteration of the test particle code. This technique has proven to be very effective for calculating self-consistent equilibrium structures in complex systems such as the magnetotail because it gives very good spatial resolution using a relatively small number of particles. As discussed above, however, it can only yield information regarding time evolution in the sense of a series of quasistatic equilibria.

Using this method we have calculated self-consistent solutions for the equilibrium structure of the Earth's magnetotail during quiet-times which are in good agreement with structures observed in satellite data. An interesting aspect of the solutions is the effect of the plasma diamagnetism. Using a post-processing algorithm (Sections V and VI), we have separated the magnetic field into the components due to the plasma diamagnetism,  $4\pi\mathbf{M}$ , and the part due to the actual particle current,  $\mathbf{H}$ . We find that if the average pitch-angle of the source distribution is too large, the magnitude of the diamagnetic current is large than the magnitude of the particle current and in the wrong direction to produce the assumed field reversal. Obviously, in such cases the two assumptions, *i.e.*, the assumed form of the distribution function and the assumed magnetic field structure, are mutually exclusive and no self-consistent solutions exist. We

further showed that for larger values of  $b_z$  the average pitch angle required for the existence of self-consistent solutions becomes smaller, *i.e.* we require a more field aligned distribution function. We believe that these results explain the reported "current sheet catastrophe" in Reference [15].

#### ACKNOWLEDGEMENTS

The authors gratefully acknowledge many helpful discussions with Dr. Glenn Joyce, Dr. Peter Cargill and Dr. James Harold. This work was supported by NASA (W-16,991) and ONR. A portion of this work was done while D. L. Holland was a National Research Council Research Associate.

## REFERENCES

1. T. W. Speiser, *J. Geophys. Res.*, **70**, 4219, (1965).
2. J. Chen, and P. J. Palmadesso, *J. Geophys. Res.*, **91**, 1499, (1986). (Correction, *J. Geophys. Res.*, **91**, 9025, (1986).)
3. J. Chen, J. L. Rexford, and Y. C. Lee, *Geophys. Res. Lett.*, **17**, 1049, (1990c).
4. R. F. Martin, *J. Geophys. Res.*, **91**, 11,985, (1986).
5. D. B. Curran, C. K. Goertz, and T. A. Whelan, *Geophys. Res. Lett.*, **14**, 99, (1987).
6. T. W. Speiser, D. J. Williams, and H. A. Garcia, *J. Geophys. Res.*, **86**, 723, (1981).
7. L. R. Lyons, and T. W. Speiser, *J. Geophys. Res.*, **87**, 2276, (1982).
8. D. B. Curran, and C. K. Goertz, *J. Geophys. Res.*, **94**, 11,521, (1989).
9. R. F. Martin, and T. W. Speiser, *J. Geophys. Res.*, **93**, 11,521, (1988).
10. J. Chen, G. R. Burkhart, and C. Y. Huang, *Geophys. Res. Lett.*, **17**, 2237, (1990a).
11. J. Chen, H. G. Mitchell, and P. J. Palmadesso, *J. Geophys. Res.*, **95**, 15,141, (1990b).
12. G. R. Burkhart, and J. Chen, *J. Geophys. Res.*, **96**, 14,033, (1991).
13. G. R. Burkhart, G. R., J. F. Drake, and J. Chen, *J. Geophys. Res.*, **95**, 18,833, (1990).
14. G. R. Burkhart, J. F. Drake, and J. Chen, *J. Geophys. Res.*, **96**, 11,539, (1991).
15. G. R. Burkhart, J. F. Drake, P. B. Dusenbery and T. W. Speiser, *J. Geophys. Res.*, **97**, 13,799, 1992.
16. B. U. O. Sonnerup, *J. Geophys. Res.*, **76**, 8211, (1971).
17. J. Chen, *J. Geophys. Res.*, **97**, 15,011, (1992).
18. P. L. Pritchett and F. V. Coroniti, *J. Geophys. Res.*, **97**, 16,773, (1992).
19. Holland, D. L., and J. Chen, *Geophys. Res. Lett.*, **20**, 1775, 1993.
20. J. Dawson, *Rev. Mod. Phys.*, **55**, 403, (1983).
21. Pritchett, P. L., and F. V. Coroniti, *J. Geophys. Res.*, **98**, 15355, 1993.
22. Burkhart, G. R., P. B. Dusenbery, T. W. Speiser, and R. E. Lopez, *J. Geophys. Res.*, **98**, 21373, 1993.
23. Cargill, P. J., J. Chen and J. B. Harold, *Geophys. Res. Lett.*, **21**, 2251, 1994.
24. D. L. Holland and J. Chen, *Geophys. Res. Lett.*, **19**, 1231, (1992).
25. J. W. Eastwood, *Planet. Space Sci.*, **30**, 1641, (1974).

## APPENDIX A

An interesting feature of the results presented in this paper is that as the particle distribution function becomes more isotropic (less field aligned), the diamagnetic contribution to the total cross-tail current becomes larger and that in extreme cases it is large enough to cancel the cross-tail current due to the "meandering motion" of the ions as they cross the midplane. Obviously, in these extreme cases, the assumption of a magnetic field reversed topology and the assumed distribution function are mutually exclusive, since the calculated current is either zero or in the wrong direction to produce the desired field reversal. It is also observed that a larger field aligned anisotropy is required for convergence for larger values of  $b_z$  than for smaller values of  $b_z$ . It is the aim of this appendix to give a theoretical estimate of the effects of pitch angle and  $b_z$  on the diamagnetic current.

Since the net diamagnetic current of a particle in a closed system must be zero, we may calculate the net diamagnetic current that any given particle deposits in the vicinity of the midplane by examining the diamagnetic current that a particle deposits as it enters and leaves the system. In practice, rather than calculating the actual cross-tail current density, we calculate the net  $y$ -velocity an ion deposits as it passes through the calculation region. Whereas these only differ by a normalization factor, it greatly simplifies the analysis.

To determine the net positive  $y$ -velocity,  $\langle \hat{v}_y \rangle$ , a particle deposits around the point where it is launched into the system and the point where it escapes from the system we need to calculate the  $z$ -position, the  $z$ -velocity and the  $y$ -velocity as a function of time. In terms of our normalized units,  $\hat{z} = z/L$ ,  $\hat{v}_z = v_z/(\Omega_0 L)$ , and  $\hat{v}_y = v_y/(\Omega_0 L)$  these are given by

$$\hat{z} = \hat{z}_0 + \sqrt{\frac{2\hat{H}}{1+b_z^2}} \left[ b_z \tau \cos \beta + \frac{1}{\sqrt{1+b_z^2}} \sin \beta \sin(\sqrt{1+b_z^2} \tau) \right] \quad (A1)$$

$$\hat{v}_z = \sqrt{\frac{2\hat{H}}{1+b_z^2}} \left[ b_z \cos \beta + \sin \beta \cos(\sqrt{1+b_z^2} \tau) \right] \quad (A2)$$

$$\hat{v}_y = \sqrt{2\hat{H}} \sin \beta \sin(\sqrt{1+b_z^2} \tau) \quad (A3)$$

where  $\hat{H} = (mv^2/2)/(m\Omega_0^2 L^2)$  is the normalized energy,  $\hat{r} = r/L$  is the normalized position,  $\beta$  is the pitch angle of the particle, and  $b_z = B_n/B_0$  is the ratio of the constant  $z$ -component of the magnetic field with the asymptotic value of the  $x$ -component of the magnetic field.

During a single excursion of the particle above the  $\hat{z} = \hat{z}_0$  plane, we add to the net  $y$ -velocity in this region,  $\langle \hat{v}_y \rangle_p$ , an amount

$$\langle \hat{v}_{yk} \rangle = \int_{\tau_{2k}}^{\tau_{2k+1}} \sqrt{2\hat{H}} \sin \beta \sin(\sqrt{1+b_z^2} \tau) d\tau \quad (A4)$$

where  $\tau_{2k}$ , and  $\tau_{2k+1}$ , are the times at which the particle cross into and out of the region  $\hat{z} \geq \hat{z}_0$  respectively. In actuality, this implies that  $\tau_{2k}$  and  $\tau_{2k+1}$  should be two consecutive solutions to the nonlinear equation

$$b_z \tau \cos \beta + \frac{1}{\sqrt{1+b_z^2}} \sin \beta \sin(\sqrt{1+b_z^2} \tau) = 0 \quad (A5)$$

Rather than solve (A5) for each excursion of the particle above the  $\hat{z} = \hat{z}_0$  plane, we hold the position of the guiding center constant in performing the integration. We then shift the location of the guiding center down by an amount,  $\Delta \hat{z}$ , equal to what it would drift in a complete cyclotron period. This allows us to obtain approximate analytic values for the time limits in the integration. The shift in the  $\hat{z}$  location between two successive integration is given by

$$\Delta \hat{z} = \frac{2\pi b_z}{1+b_z^2} \sqrt{2\hat{H}} \cos \beta \quad (A6)$$

Note that if  $K\Delta \hat{z} > \hat{R}_g$ , where  $K$  is an integer and  $\hat{R}_g$  is the normalized gyroradius of the particle, the particle will not go above the  $\hat{z} = \hat{z}_0$  plane and will thus no longer contribute to the net  $y$ -velocity deposited in that region. Referring to Figure (13), we see that in a given excursion above the  $\hat{z} = \hat{z}_0$ , the particles phase angle goes from  $\theta_k$  to  $\pi - \theta_k$  and hence the time integration runs from

$$\tau_{2k} = (1+b_z^2)^{-1/2} (2\pi k + \theta_k) \quad (A7a)$$

to

$$\tau_{2k+1} = (1+b_z^2)^{-1/2} (2\pi(k+1/2) - \theta_k) \quad (A7b)$$

where

$$\theta_k = \sin^{-1} \left[ \frac{2\pi k b_z}{\sqrt{1+b_z^2}} \cot \beta \right] \quad (A8)$$

Carrying out the integration with the approximate limits, we obtain

$$\langle \hat{v}_{yk} \rangle = \sqrt{\frac{8\hat{H}}{1+b_z^2}} \sin \beta \cos \theta_k \quad (A9)$$

or

$$\langle \hat{v}_{yk} \rangle = \sqrt{\frac{8\hat{H}}{1+b_z^2}} \sin \beta \sqrt{1 - \left( \frac{2\pi k b_z}{\sqrt{1+b_z^2}} \cot \beta \right)^2} \quad (A10)$$

The total  $y$ -velocity deposited above the  $\hat{z} = \hat{z}_0$  plane is found by summing the  $y$ -velocity deposited in that region during the individual excursions, i.e.,

$$\langle \hat{v}_y \rangle_{\text{tot}} = \sum_{k=1}^K \langle \hat{v}_{yk} \rangle. \quad (A11)$$

Here  $K$  is the number of excursions that the particle makes above the  $\hat{z} = \hat{z}_0$  plane and is given by

$$K = \text{Int} \left[ \frac{\sqrt{1 + b_z^2}}{2\pi b_z} \tan \beta \right]. \quad (\text{A12})$$

Combining equations (A10), (A11), and (A12) yields an expression for the net positive y-velocity deposited above the  $\hat{z} = \hat{z}_0$  plane. In addition, we have an equal amount of positive y-velocity deposited symmetrically below the  $\hat{z} = \hat{z}_0$  plane. This is because until a particle has drifted at least one gyroradius in the z-direction the negative and positive contributions to the y-current cannot average to zero. Thus, we see that the total y-velocity in the peaks located around the entry and exit points of the particle is given by

$$\langle \hat{v}_y \rangle_p = 2 \langle \hat{v}_y \rangle_{tot}. \quad (\text{A13})$$

In Figure 9 we show the total y-velocity in the current peaks as a function of the pitch angle as given by (A13) (solid line) and as determined by numerically “pushing the particle” through the field ( $\bullet$ ). As can be seen, the agreement is quite good. One notes, however, that the location of the “breaks” in the curves, which occur whenever the particle is able to add an additional excursion above the  $\hat{z} = \hat{z}_0$  plane, fall in slightly different locations for the theoretical and numerically determined results. For the theoretical curves, the breaks in the curves occur at those pitch-angles for which the particle is able to make an additional excursion above the  $\hat{z} = \hat{z}_0$  plane, i.e. when

$$\beta_k = \tan^{-1} \left[ \frac{2\pi k b_z}{\sqrt{1 + b_z^2}} \right]. \quad (\text{A14})$$

In actuality, the breaks in the curve occur at those pitch angles for which (A5) picks up two additional roots. This happens whenever the amplitude of the sinusoidal variation in  $\tau$  becomes sufficiently large that an additional peak intersects the linear term in (A5). Again, the actual values require a solution to the full nonlinear equation. For  $k = 0$ , this is easily done yielding

$$\beta_0 = \tan^{-1}(b_z). \quad (\text{A15})$$

It is important to note that for predominantly field aligned orbits, i.e., those with pitch angles less than  $\beta_0$  as given by (A15) there are no solutions to (A5) thus indicating that there is no net y-velocity deposited above the  $\hat{z} = \hat{z}_0$  plane. Note that for pitch-angles less than  $\beta_0$  as given by (A15) the numerically determined points in Figures 9a–9c are all zero. For the other roots the solution is not as simple. As a lowest order approximation to the actual solutions we may approximate the roots as occurring whenever the amplitude of the sinusoidal term in (A5) is equal to the value of the linear term at the points  $\sqrt{1 + b_z^2} \tau = (4k + 1)\pi/2$ . This yields the values of  $\beta_k$  given by

$$\beta_k = \tan^{-1} \left[ \left( 2k + \frac{1}{2} \right) \pi b_z \right]. \quad (\text{A16})$$

In actuality, the solutions occur for values of  $\tau$  less than this and thus the values of  $\beta_k$  are slightly off. Referring to Figure 14, however, where we have plotted the linear term in (A5) along with three examples of the sinusoidal term with amplitudes given by (a)  $\beta_0$  as given by (A15) and (b)  $\beta_1$  and (c)  $\beta_2$  as given by (A16) we see that (A16) gives an excellent approximation to the actual value of  $\beta_k$ . Comparing equations (A14) and (A16) we see that there is a small positive shift in the actual location of the  $\beta_k$  over the approximate location.

## APPENDIX B

In this appendix we explicitly write out the transformation between the actual particle position and the guiding center position for magnetic fields of the form  $\mathbf{B} = B_0 f(z) \hat{x} + B_z \hat{z}$ . In general, the transformation is given by

$$\mathbf{R}_{gc} = \mathbf{r} + \frac{\mathbf{v} \times \mathbf{B}}{(q/Mc)B^2}, \quad (\text{B1})$$

where  $B = [B_0 f(z)]^2 + B_z^2$ . Using (B1), it is trivial to show that the guiding center coordinates  $X_{gc}$ ,  $Y_{gc}$ , and  $Z_{gc}$  are given by

$$X_{gc} = x + \frac{b_z v_y}{\Omega_0 [f(z)^2 + b_z^2]} \quad (\text{B2a})$$

$$Y_{gc} = y + \frac{f(z) v_z + b_z v_x}{\Omega_0 [f(z)^2 + b_z^2]} \quad (\text{B2b})$$

$$Z_{gc} = z + \frac{f(z) v_y}{\Omega_0 [f(z)^2 + b_z^2]} \quad (\text{B2c})$$

Thus, we see that given the local value of the magnetic field and the instantaneous velocity, it is a simple matter to calculate the instantaneous guiding center position. For unmagnetized motion in the field reversal region, the instantaneous guiding center has little physical significance or practical utility.

## APPENDIX C

In sections V and VI, we showed that in order to determine the effects of plasma diamagnetism on the equilibrium structure of the magnetotail we needed to separate the orbit into segments which are midplane crossing and segments which are non-midplane crossing. In the former, when calculating equilibrium profiles we distribute the actual particle positions and velocities onto a grid, whereas in the latter we distribute the guiding center positions and



velocities onto a grid. In this appendix we present an approximate expression for the phase space location where the particle changes its behavior from crossing to non-crossing.

We begin by considering the Hamiltonian of a particle in the modified Harris magnetic field

$$H(x, z, v_x, v_z, P_y) = \frac{1}{2} M v_z^2 + U(x, z, v_x, P_y) \quad (C1)$$

where

$$U(x, z, v_x, P_y) = \frac{1}{2} M v_x^2 + \frac{1}{2} M [P_y/M - (q/Mc)A_y(x, z)]^2. \quad (C2)$$

is the effective potential for the  $z$ -motion,  $P_y$  is the  $y$ -component of the canonical momentum and  $A_y$  is the vector potential. For the modified Harris magnetic field,  $A_y$  may be written as

$$A_y(x, z) = -B_0 L \ln[\cosh(z/L)] + B_z x \quad (C3)$$

If  $b_z \ll 1$  the oscillations in the  $z$ -direction are much faster than the oscillations in the  $x$ -direction. As a first approximation, we therefore assume that during a single  $z$ -oscillation the values of both  $v_x$  and  $x$  are constant. This approximation is not strictly valid. Rather, if we take  $v_x$  to be a constant we should approximate  $x = x_0 + v_x t$ . For our purposes, however, we find that the simple approximation is sufficient. This is because the orbits which incur significant error using the standard current calculation technique have large pitch angles and thus small  $v_x$ . Setting  $v_x$  and  $x$  constant, the condition that a particle is non axis crossing is given by

$$H(x, z, v_x, v_z, P_y) \leq U(x, z = 0, v_x, P_y) \quad (C4)$$

i.e., the energy of the particle must be greater than the effective potential at the midplane. This criterion is graphically depicted in Figure 15 where we have drawn the effective potential for  $(P_y/M - \Omega_n x)/(\Omega_0 L) = (a) 1, (b) 0, \text{ and } (c) -1$ , and we have defined  $\Omega_n = qB_z/Mc$ . We have neglected the  $Mv_x^2/2$  contribution to the effective potential, since it only provides a constant offset. The dashed lines correspond to orbits of different energies as compared to effective potential (c). Particle A violates the inequality in (C4) and is midplane crossing. Thus we use actual particle coordinates for calculating the equilibrium profiles. Particle C represents a solution to the inequality (C4) and is non-midplane crossing. Thus we would use guiding center coordinates for calculating the equilibrium profiles. Particle B represents the equality condition in (C4) and is at the transition point between crossing and non-crossing motion. Solving (C4) for  $v_z^2$  we find that the condition a particle with given  $x, z$ , and  $v_x$  is given by

$$v_z^2 \leq [P_y/M - (q/Mc)A_y(x, z)]^2 - [P_y/M - (q/Mc)A_y(x, z = 0)]^2. \quad (C5)$$

We note that since we have written C5 without making explicit use of the Harris model of the magnetic field, we may use other field reversal models by simply using the relevant model for  $A_y$  provided that the approximations regarding  $x$  and  $v_x$  are still valid.

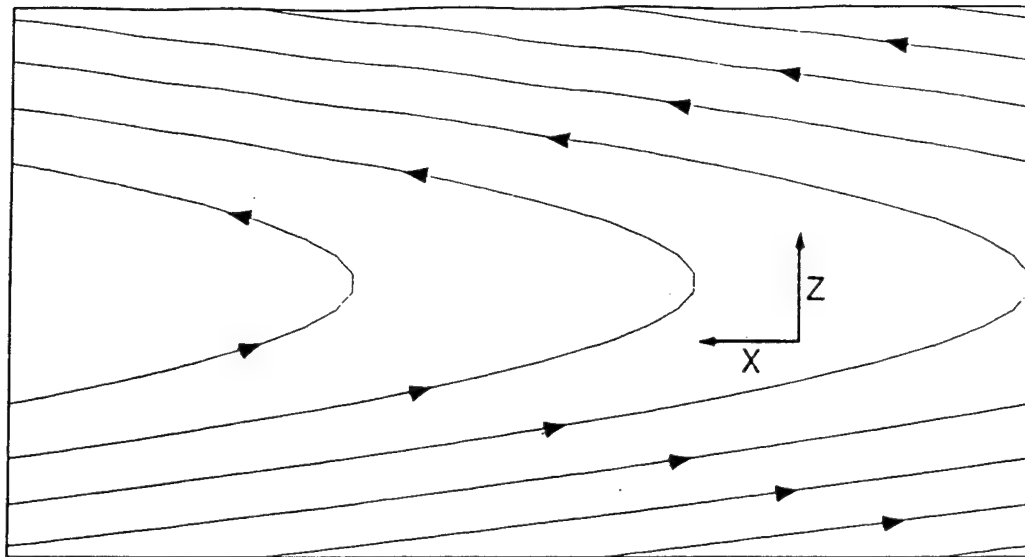


Figure 1: Modified Harris magnetic field geometry

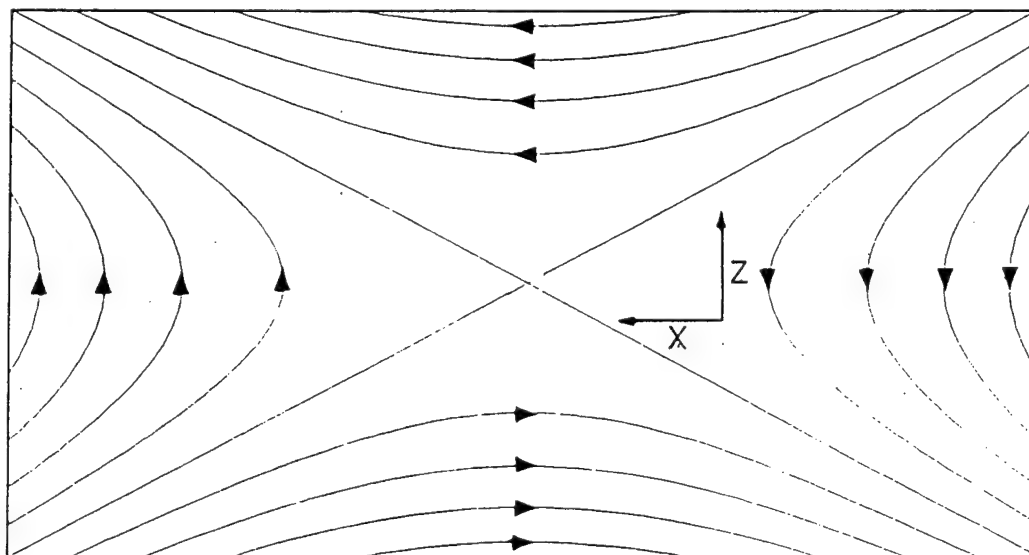


Figure 2: X-line magnetic field geometry

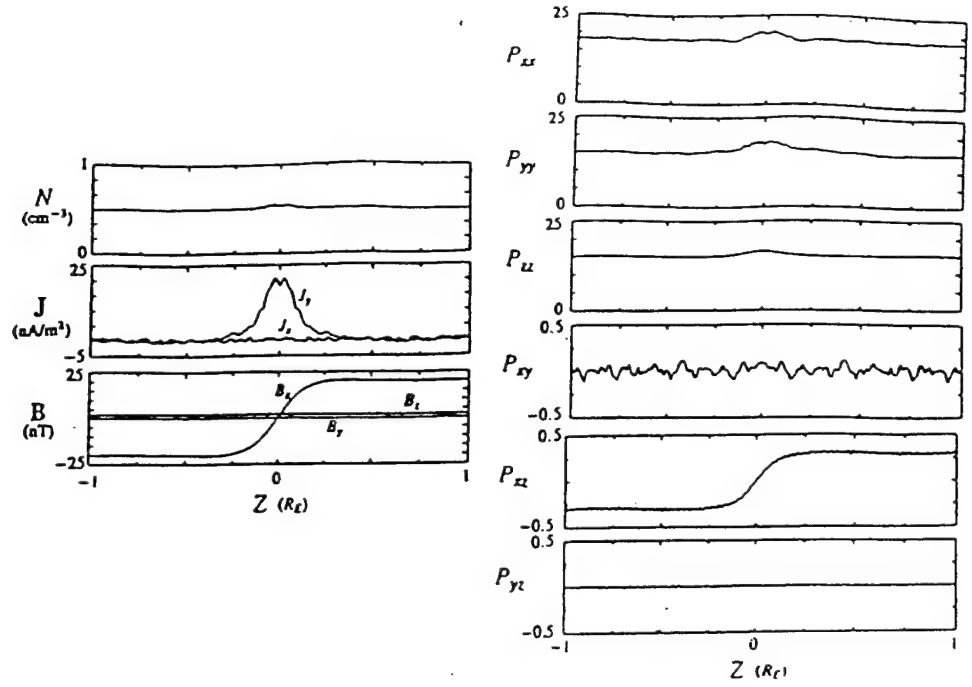


Figure 3. Self-consistent density, current, magnetic field and pressure tensor profiles calculated using a kappa distribution ( $\kappa = 4.5$ ) with a bulk drift in the tailward direction of  $v_D = 0.1 v_{th}$ . The units on the pressure tensor elements are nanodyne/cm<sup>2</sup>.

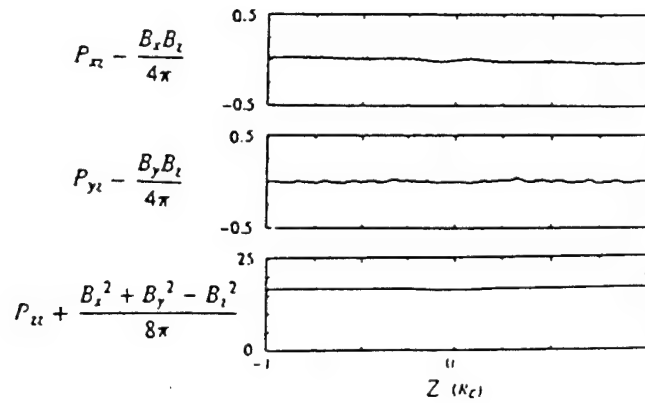


Figure 4. Plot of the left hand side of equations 19 a-c using the results depicted in Figure 3. Since all three curves are essentially flat, we see that pressure balance is maintained to a high degree of accuracy.

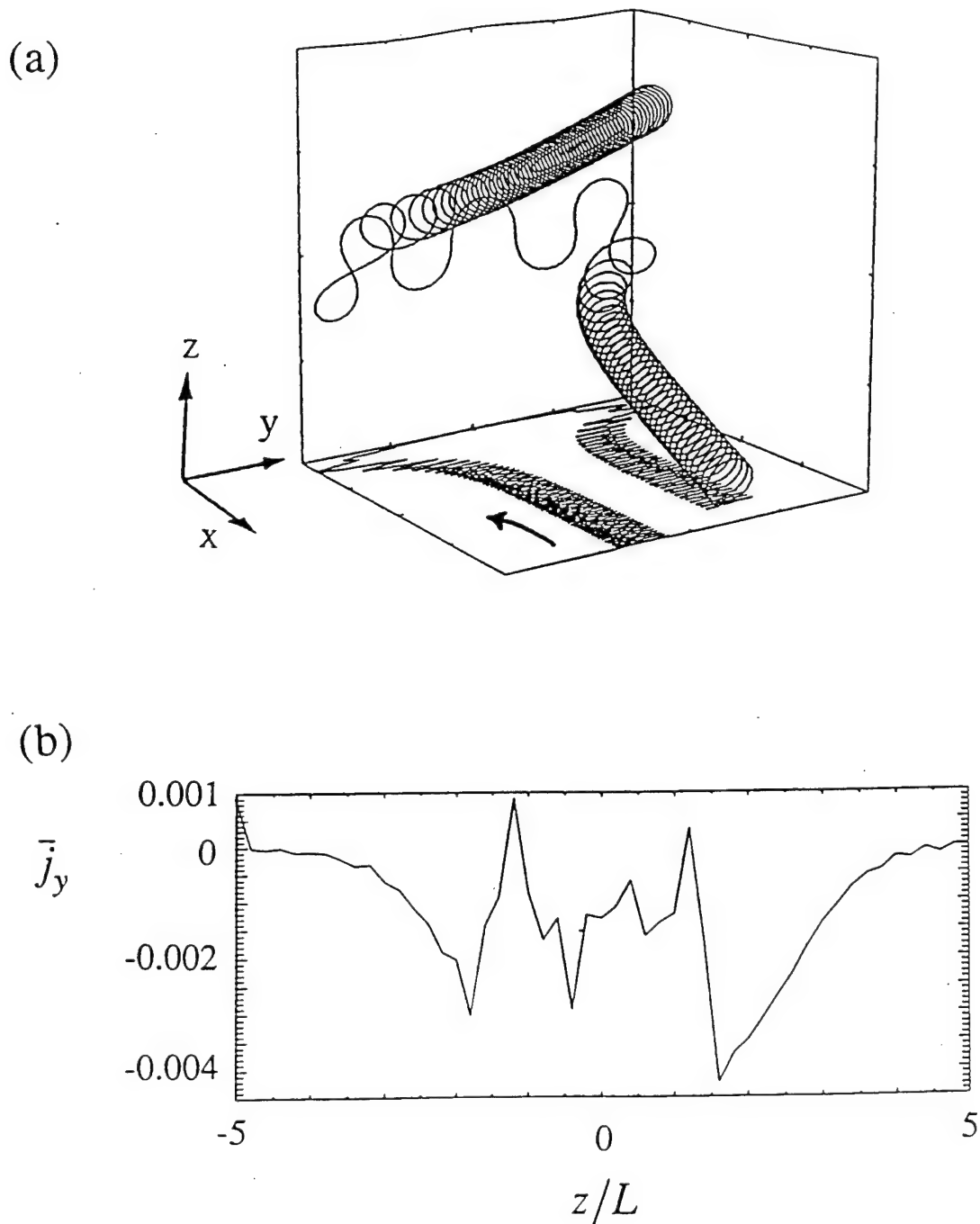


Figure 5: a) Trajectory of an ion with energy  $H = 0.24 L^2 \Omega_0^2$ , initial pitch angle  $\beta = 100^\circ$ , initial phase angle  $\phi = 0^\circ$  and initial starting position  $z/L = 6$ . b) Current profile of the particle in Fig. 3.a as calculated from the standard ridding algorithm with the top grid cell located at  $z/L = 5$ .

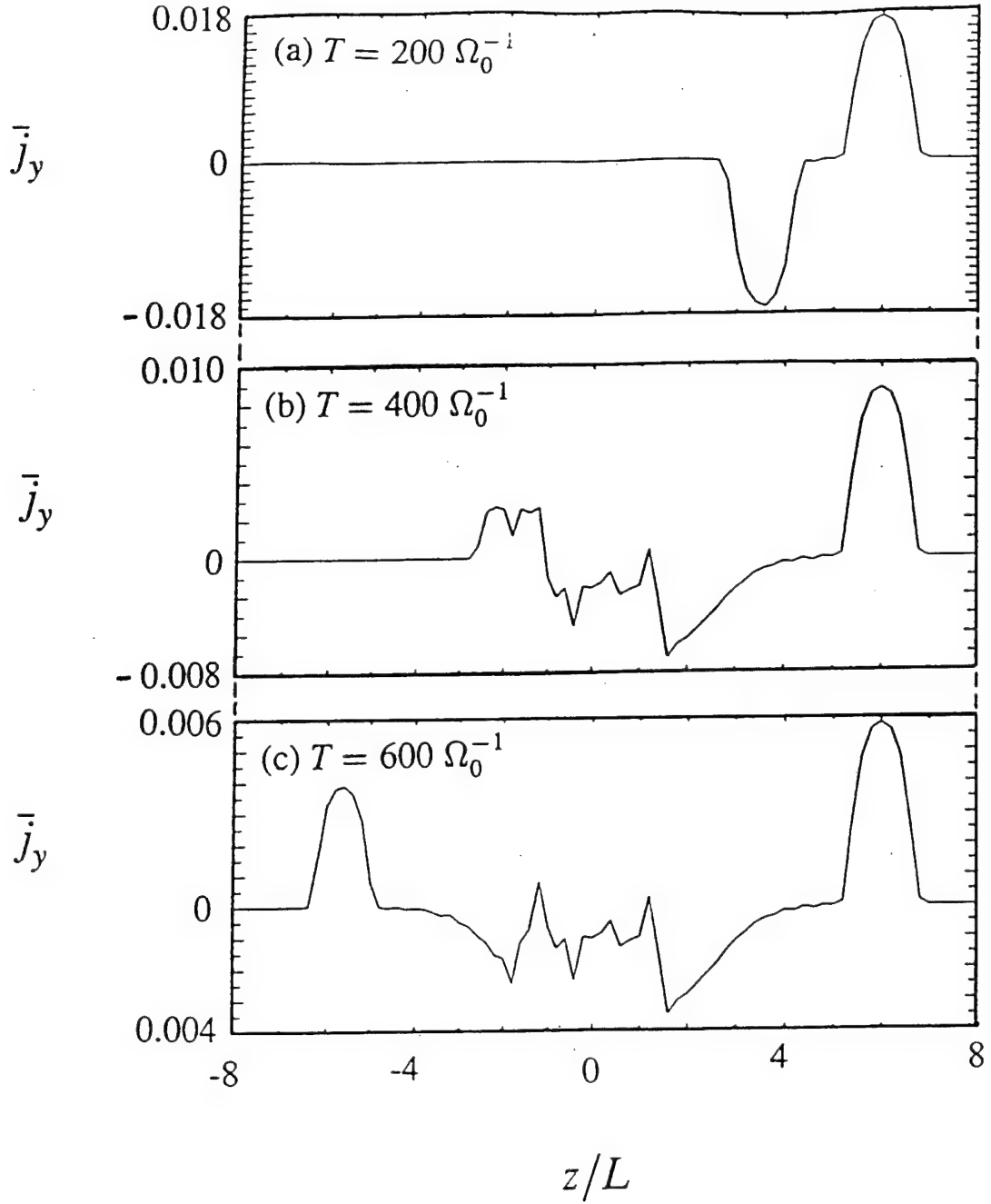


Figure 6: Current profile for the particle in Fig. 5a at the three times: a)  $T = 200 \Omega_0^{-1}$ , b)  $T = 400 \Omega_0^{-1}$ , and c)  $T = 600 \Omega_0^{-1}$ . The top grid cell is taken to be  $z/L = 8$ .

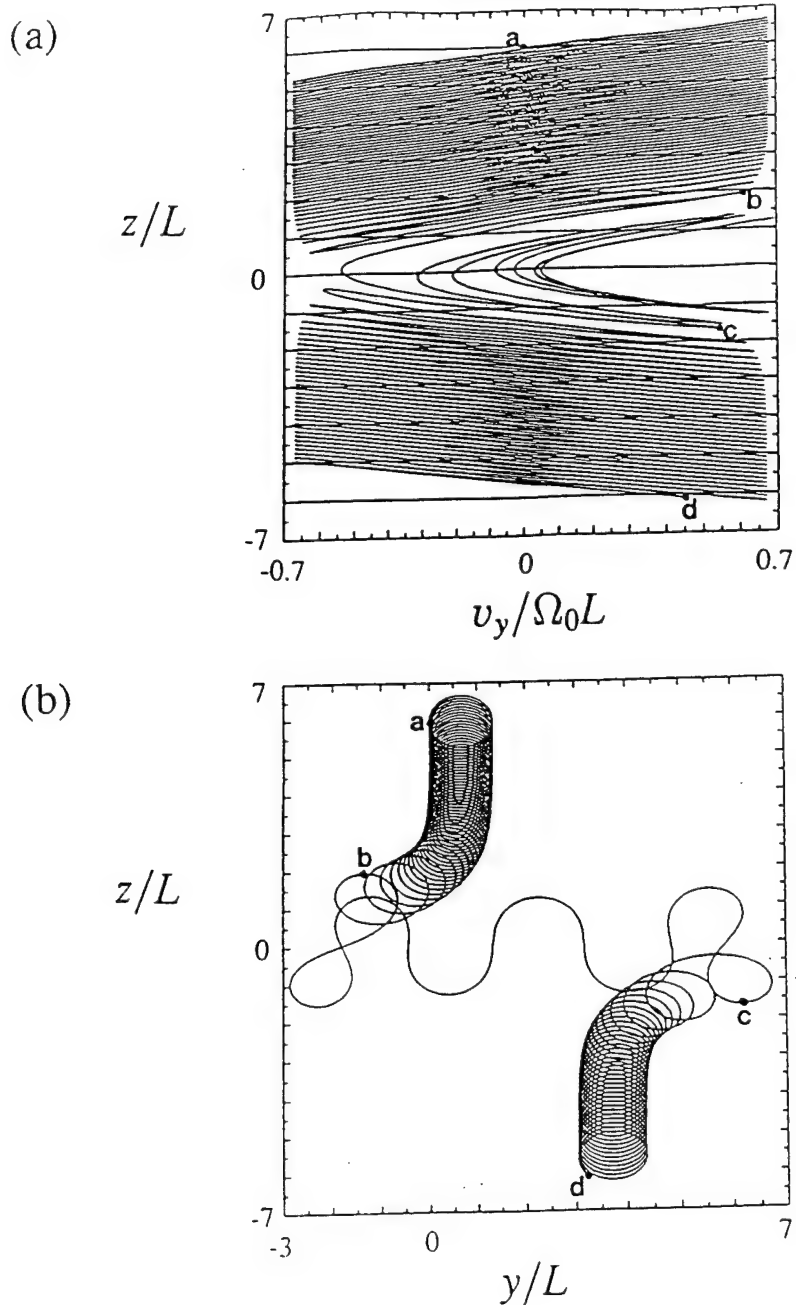


Figure 7: a)  $v_y/\Omega_0 L$  as a function of  $z/L$  for the particle in Fig. 5a. The particle is non midplane crossing on the segments a-b and c-d, and we use guiding center coordinates. The particle is midplane crossing on the segment b-c and we use true particle coordinates. Notes that if actual particle coordinates are used on the segments a-b and c-d, there is an excess of positive y-velocity in the regions  $5.3 \leq z/L \leq 6.7$  and  $-6.3 \leq z/L \leq -5$  and an excess of negative y-current in the regions  $0.5 \leq z/L \leq 1.9$  and  $-2 \leq z/L \leq -0.3$ . b)  $y/L$  as a function of  $z/L$  for the same particle. Note the  $\nabla B$  drift in the regions around  $|z/L| = 2$  and the large y-velocity at  $|z/L| = 1$ .

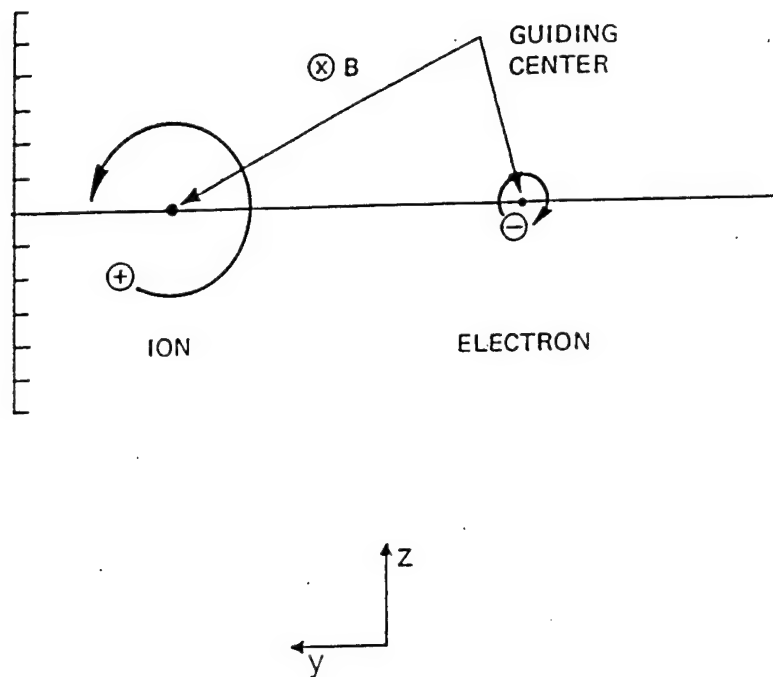


Figure 8: Schematic diagram of ion and electron gyro orbits in a constant magnetic field  $\mathbf{B} = B_0 \hat{x}$ . Note that above the guiding center the particles have only positive  $y$ -current, whereas below the guiding center the particles have only negative  $y$ -current



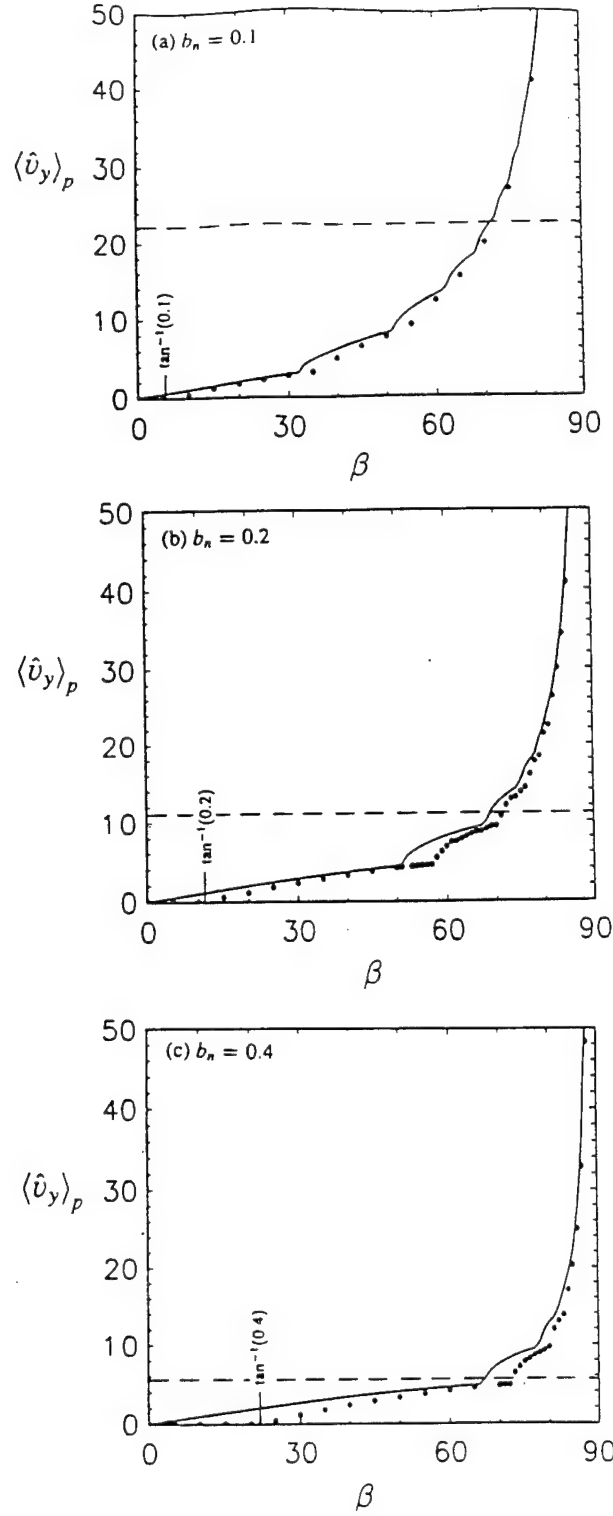


Figure 9: Magnitude of the positive y-velocity deposited near the launching point of the particle as a function of the pitch-angle and for (a)  $b_z = 0.1$ , (b)  $b_z = 0.2$  and (c)  $b_z = 0.4$ . The solid line is the approximate expression given by (22a) and (22b). The dots are found by pushing the particles through the magnetic field. The dashed vertical lines indicate the pitch-angle that below which there is no net positive velocity left at the launching point.

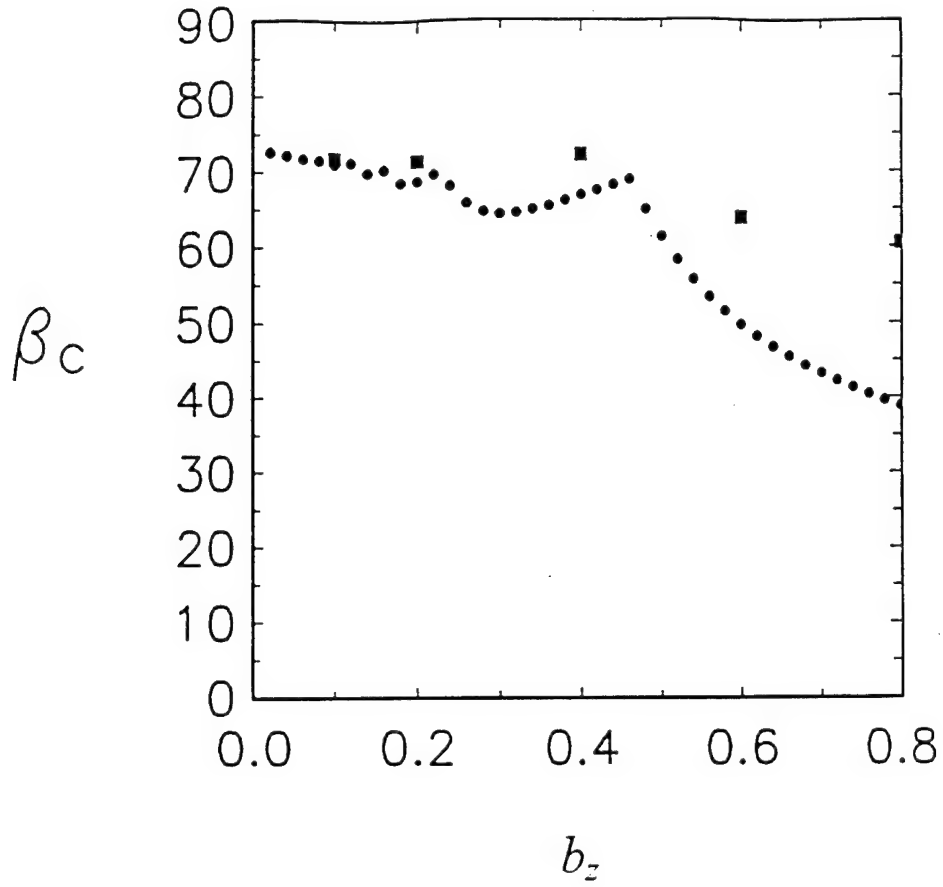


Figure 10: Plot of the critical pitch-angle  $\beta_c$  for which the error current at the midplane equals the meandering current at the midplane as a function of  $b_z$  as calculated from Eq. 24 (•). The other points (■) are calculated using the numerically determined values of  $\langle \hat{v}_y \rangle_p$ .

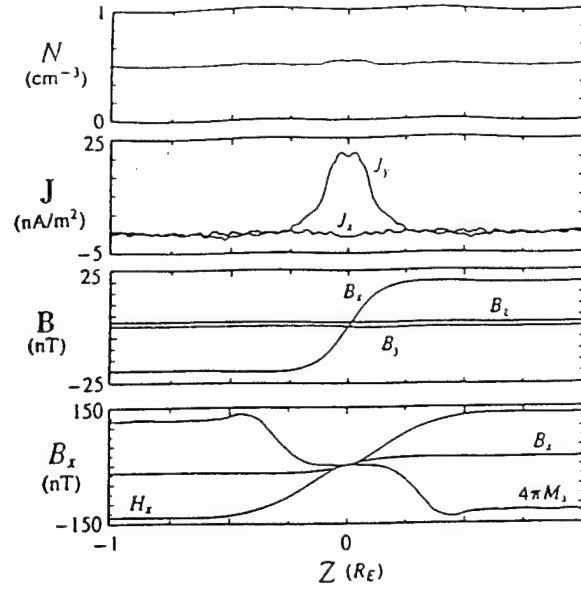


Figure 11. Self-consistent density, current and magnetic field profiles calculated using a Maxwellian with a bulk drift in the tailward direction of  $v_D = 0.1 v_{th}$  and a high energy isotropic tail which comprises 10 percent of the total density.

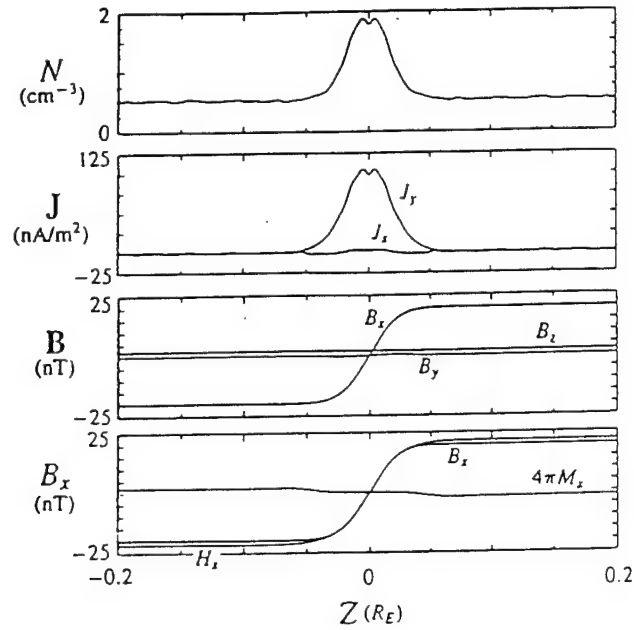


Figure 12. Self-consistent density, current and magnetic field profiles calculated using a Maxwellian source distribution of particles with a bulk drift in the tailward direction of  $v_D = 2 v_{th}$ .

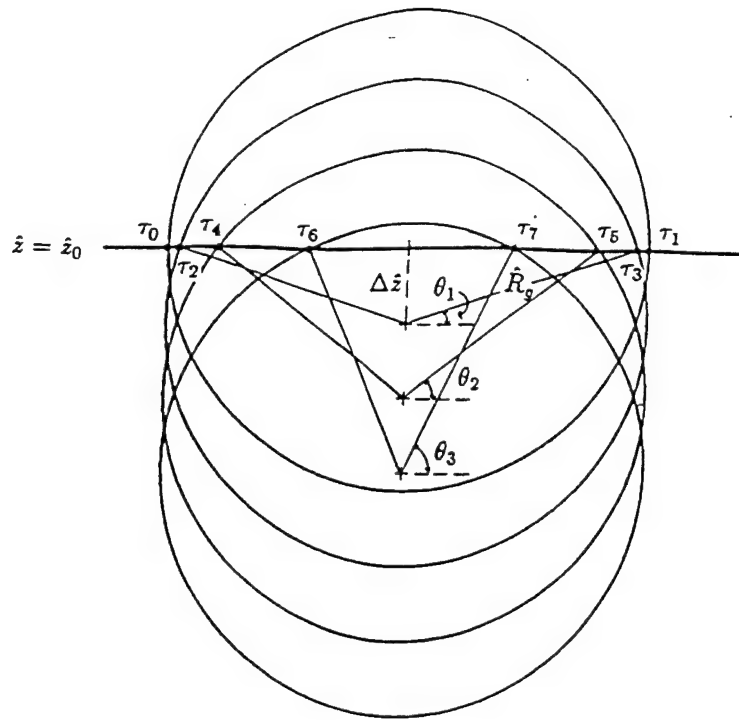


Figure 13: Approximate particle orbits used in deriving Eq. (A.9-A.11)

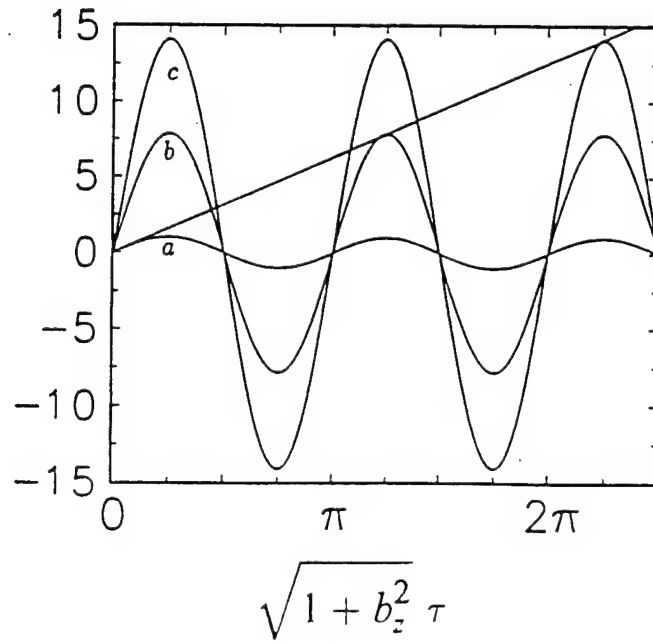


Figure 14: Plot showing graphical solution to equation (A.5). Two new roots to the equation occur when the amplitude of the sinusoidal oscillation  $b_z^{-1} \tan(\beta_k) \sin(\sqrt{1 + b_z^2} \tau)$  increases sufficiently to cross the line  $\sqrt{1 + b_z^2} \tau$ . The curve depicted are for (a)  $\beta_k = \tan^{-1}(b_z)$ , (b)  $\beta_k = \tan^{-1}(5\pi b_z/2)$ , and (c)  $\beta_k = \tan^{-1}(9\pi b_z/2)$ .

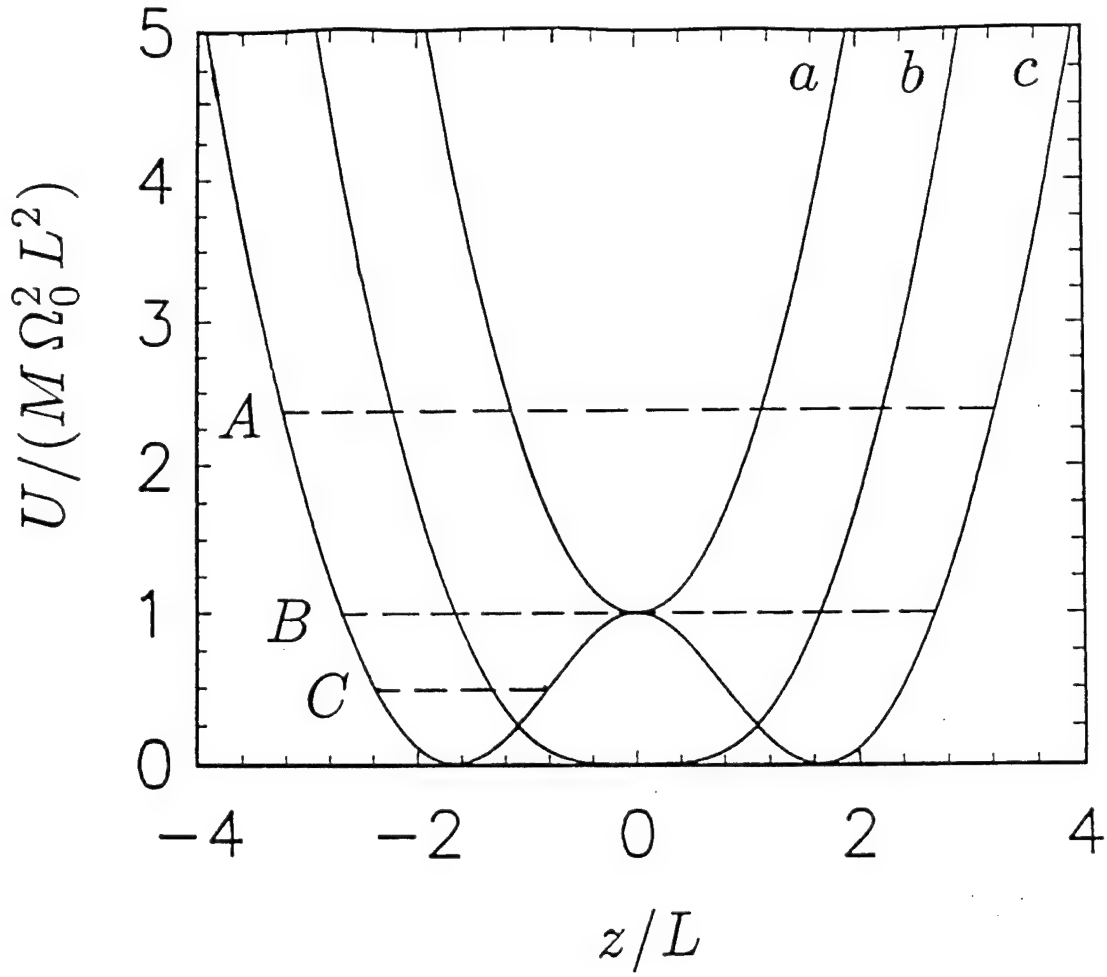


Figure 15: Effective potential for the  $z$ -motion for  $(P_y/M - \Omega_n x)/(\Omega_0 L) = (a) 1, (b) 0,$  and  $(c) -1$ . The dashed lines correspond to orbits of different energies as compared to effective potential (c). Particle A violates the inequality in (C4) and is midplane crossing. Particle C represents a solution to the inequality (C4) and is non-midplane. Particle B represents the equality condition in (C4) and is at the transition point between crossing and non-crossing motion.



NRL/MR/6756--95-7734

# **Nonlinear Particle Dynamics in the Magnetotail: A Laboratory Study**

## **1. The Experimental Configuration and Numerical Simulation**

D. WALKER  
J. CHEN  
C. SIEFRING  
D. DUNCAN  
J. STRACKA  
J. ANTONIADES

*Charged Particle Physics Branch  
Plasma Physics Division*

J. BOWLES

*SFA, Inc.  
Landover, MD*

D. HOLLAND

*Physics Department  
Illinois State University*

September 25, 1995

Approved for public release; distribution unlimited.

REPORT DOCUMENTATION PAGE			Form Approved OMB No. 0704-0188	
Public reporting burden for this collection of information is estimated to average 1 hour per response, including the time for reviewing instructions, searching existing data sources, gathering and maintaining the data needed, and completing and reviewing the collection of information. Send comments regarding this burden estimate or any other aspect of the collection of information, including suggestions for reducing this burden, to Washington Headquarters Services, Directorate for Information Operations and Reports, 1215 Jefferson Davis Highway, Suite 1204, Arlington, VA 22202-4302, and to the Office of Management and Budget, Paperwork Reduction Project (0704-0188), Washington, DC 20503.				
1. AGENCY USE ONLY (Leave Blank)	2. REPORT DATE September 25, 1995	3. REPORT TYPE AND DATES COVERED Interim		
4. TITLE AND SUBTITLE Nonlinear Particle Dynamics in the Magnetotail: A Laboratory Study 1. The Experimental Configuration and Numerical Simulation			5. FUNDING NUMBERS	
6. AUTHOR(S) D. Walker, J. Bowles,* D. Holland,** J. Chen, C. Siefring, D. Duncan, J. Stracka, and J. Antoniadis				
7. PERFORMING ORGANIZATION NAME(S) AND ADDRESS(ES) Naval Research Laboratory Washington, DC 20375-5320			8. PERFORMING ORGANIZATION REPORT NUMBER NRL/MR/6756-95-7734	
9. SPONSORING/MONITORING AGENCY NAME(S) AND ADDRESS(ES) Office of Naval Research 800 North Quincy Street Arlington, VA 22217-5660			10. SPONSORING/MONITORING AGENCY REPORT NUMBER	
11. SUPPLEMENTARY NOTES *SFA, Inc., Landover, MD **Physics Department, Illinois State University				
12a. DISTRIBUTION/AVAILABILITY STATEMENT Approved for public release; distribution unlimited.			12b. DISTRIBUTION CODE	
13. ABSTRACT (Maximum 200 words)  We have performed the initial stages of an experiment designed to investigate particle dynamics in the magnetotail. The experiment was developed for and performed in the large Space Physics Simulation Chamber (SPSC) at the Naval Research Laboratory. The results of this experiment lend support to the idea that particle scattering from the magnetotail neutral sheet is not random but that there exist resonances in the number and direction of scattered particles as a function of energy. The effort began with construction and testing of the magnetic field configuration necessary to simulate the quiet-time magnetotail field: a neutral sheet magnetic field profile $B_0(z)x$ with a superimposed normal field $B_z$ . Once complete, electrons of variable energy were injected into the field region created and the scattered current collected by back-scattered and forward-scattered collection plates was analyzed as a function of electron energy. The experiment was used to test the hypothesis that single particle scattering from a neutral sheet profile as described can be "coherent" and can at times demonstrate resonance effects as a function of energy.				
14. SUBJECT TERMS Magnetotail Particle Experiment			15. NUMBER OF PAGES 70	
			16. PRICE CODE	
17. SECURITY CLASSIFICATION OF REPORT UNCLASSIFIED	18. SECURITY CLASSIFICATION OF THIS PAGE UNCLASSIFIED	19. SECURITY CLASSIFICATION OF ABSTRACT UNCLASSIFIED	20. LIMITATION OF ABSTRACT UL	



## TABLE OF CONTENTS

Section	Page
ABSTRACT.....	1
I     Introduction.....	1
I.1    Theory.....	2
I.2    Experiment.....	4
II    Approach.....	4
II.1   Experimental Design.....	4
II.2   Description of Particle Code.....	5
II.3   Finite Wire Effects.....	7
II.4   Effects of Finite Grid Size.....	7
III   Overall Objectives.....	10
IV    Experimental Configuration.....	10
IV.1   Experimental Chamber Description.....	10
IV.2   Mechanical Design Considerations.....	11
IV.2.1   Grid Design.....	11
IV.2.2   B(dot) Loop Probe.....	12
IV.2.3   Current Collector Plates.....	12
IV.2.4   Pulse Forming Network.....	13
IV.2.5   Electron Beam.....	13
V     Experimental Results.....	13
V.1    Current Collection during Pulsing.....	13
V.2    Magnetic Field.....	14
VI    Comparison of Results to Theory.....	15
VI.1   Theoretical Resonance Dependence of $b_n$ .....	15
VI.2   Simple Theory.....	16
VI.3   Results from Numerical Work.....	18
VI.4   Experimental Results.....	18
VI.4.1   Resonances.....	19
VI.4.2   Collected Current as a function of $y$ .....	20
VII   Scaling Considerations and Future Work.....	20
VIII  References.....	22

Nonlinear Particle Dynamics in the Magnetotail: A Laboratory Study  
1. The Experimental Configuration and Numerical Simulation

DN Walker, J. Bowles<sup>a</sup>, D. Holland<sup>b</sup>, J. Chen, C. Sieftring, D. Duncan<sup>a</sup>, J. Stracka  
and J. Antoniadis

<sup>a</sup>Sachs Freeman Assoc., Landover MD, <sup>b</sup>Physics Dept., Illinois State University

ABSTRACT

We have performed the initial stages of an experiment designed to investigate particle dynamics in the magnetotail. The experiment was developed for and performed in the large Space Physics Simulation Chamber (SPSC) at the Naval Research Laboratory. The results of this experiment lend support to the idea that particle scattering from the magnetotail neutral sheet is not random but that there exist resonances in the number and direction of scattered particles as a function of energy. The effort began with construction and testing of the magnetic field configuration necessary to simulate the quiet-time magnetotail field: a neutral sheet magnetic field profile  $B_0(z)$  with a superimposed normal field  $B_z$ . Once complete, electrons of variable energy were injected into the field region created and the scattered current collected by back-scattered and forward-scattered collection plates was analyzed as a function of electron energy. The design of the particle detector plates for back- and forward-scattered collection, along with noise shielding, secondary emission suppression and testing to insure that the electron beam represented single particle behaviour were key elements in the experimental buildup phase. In addition theoretical modelling of the experimental configuration was a primary contributor to the basic feasibility study and ultimate design of the effort. The experiment was used to test the hypothesis that single particle scattering from a neutral sheet type profile as described can be "coherent" and can at times demonstrate resonance effects as a function of energy. The final experimental configuration was not a perfect realization of the idealized Harris magnetic field form but retained important features necessary for resonance structures as predicted by the design software. This paper, which is concerned with a description of the design and ultimate experimental build-up for the effort, is the first of two papers. The second paper concentrates primarily on the initial results of the experimentation and will follow shortly as a companion paper.

I Introduction

This paper documents the design and buildup of an unusual laboratory experiment designed to examine recent theoretical predictions of nonlinear particle dynamics in a magnetic field which is designed to simulate the earth's magnetotail, the modified Harris field. As the magnetotail is believed to be important for energy storage and release, the structure of the tail, including the current sheet, is a key element necessary for understanding large scale changes in the magnetic field, particle acceleration and other physical effects associated with geomagnetic substorms. The global structure, however, is difficult to ascertain as there is as yet no "snapshot" of the magnetosphere available. On the other hand, particle distribution functions are directly accessible via in-situ measurements and there have been attempts to deduce global attributes of the magnetosphere from point measurements of plasmas. Also, since charged particle motion is governed by the large-scale magnetic and electric fields, information related to global

thorough analysis of the particle dynamics. As a result, the nonlinear dynamics of charged particles moving in these fields continues as an integral part of a complete characterization of the magnetosphere.

The laboratory experiment is designed to provide a surrogate global system which has the topological properties of the magnetotail. Because distribution functions and current sheet structure are related to the phase space structure of the magnetic configuration, we have numerically investigated particle motion in experimentally realizable fields. Initially we have investigated coherence scattering properties in the different fields and ultimately we intend to construct pitch-angle resolved distribution functions in the field to accompany those predicted by the numerical simulations. These efforts have led to the experimental configuration of four current carrying meshes described below. Finally, we have related the computed distribution functions to the scale length of the mesh-generated field. In these numerical calculations, various important realistic experimental constraints have been included. For example, the finite mesh wire thickness and the attendant field inhomogeneities, in addition to the deviation of the field from the Harris form have been included explicitly as outlined below.

### 1.1 Theory

There has been considerable effort over the years in understanding magnetotail charged particle motion in the attempt to explain various properties of this near earth region. The quiet time magnetotail magnetic field may be modelled by a neutral sheet profile  $B_0(z)\hat{x}$  with a superimposed normal field  $B_z\hat{z}$  where  $\hat{x}$  and  $\hat{z}$  are unit vectors: the so-called "quasi-neutral sheet" geometry. Figure (1) is a model magnetic field which has the general topology of the magnetotail field depicted in Figure (2). The coordinate system is also shown in Figure (1). The sunward direction is along the positive x-axis. A considerable volume of early work already exists which deals with a number of specialized aspects of the particle motion. The methods used include approximate analytical methods [Speiser, 1965; Alekseyev and Kropotkin, 1970; Sonnerup, 1971; Stern and Palmadesso, 1975; Pellat and Schmidt, 1979] and numerical methods [Speiser, 1967; Cowley, 1971; Eastwood, 1972; Swift, 1977; Speiser and Lyons, 1984]. West et al. [1978a,b] and Wagner et al. [1979] studied orbits that are now known as stochastic orbits.

In all of the works cited above the underlying implicit concept is that particle motion in a quasi-neutral sheet is ultimately regular and integrable. Chen and Palmadesso, [1986] were able to show that particle motion in the quasi-neutral sheet (modified Harris magnetic field form) is nonintegrable with only two constants of the motion, and that the phase space is partitioned into disjoint regions occupied by dynamically distinct classes of orbits which they characterize as stochastic, integrable (regular) and transient. Examples of these phase space plots are shown in Figure (3). There are visible in the plots, discrete regions or distinct boundaries which have been shown to isolate incoming particles (entry) from outgoing ones (exit). The two constants of the motion which are sufficient to parameterize the particle motion are a normalized Hamiltonian,  $\hat{H}$  and a parameter related to the magnetic field topology,  $b_0 = B_{z0}/B_{x0}$ . Considerable attention has been given also by other authors to understanding the nature of the nonintegrable motion in the magnetotail [Buechner and Zelenyi, 1986, 1989; Kaufmann et al., 1993(a), 1993(b); Kaufmann and Lu, 1993]. For example, Buechner and Zelenyi [1989] have similarly derived a parameter  $\kappa$  related to the normalized Hamiltonian ( $\kappa = (2\hat{H})^{-1/4}$ ) which they use as a measure of chaos: for  $\kappa \sim 1$  chaos is greatest and is reduced for  $\kappa \ll 1$  and for  $\kappa \gg 1$ . For purposes here, chaotic behaviour really means that the final states, after interaction with a scattering center, have a sensitive dependence on the initial states, i.e., if all orbits were truly only stochastic there would be no relationship between these two asymptotic states whatsoever. The physical implications of particle orbits in the magnetotail including stochastic orbits have been treated by numerous authors [Chen et al., 1990a,b; Doxas et al., 1990; Horton and Tajima, 1990; Burkhardt and Chen, 1991; Ashour-Abdalla et al., 1990].

The entry and exit subregion boundaries defined above are important because these regions define the measureable states of particle trajectories and are connected to the asymptotic regions via these trajectories. A satellite measurement of particles, for example, samples asymptotic, or final state, properties of the particles. Also, initial and final pitch angles are characterized as incoming and outgoing. The stochastic, transient and integrable particle orbits occupy different and distinct regions of phase space delineated by the boundaries discussed above and the classes of orbits allowed are characterized by widely different time scales. It was suggested that the phase space partition and the separation of time scales can lead to non-Maxwellian features in the distribution functions in response to changes in boundary conditions, i.e., in the asymptotic distribution. It was shown that at certain energies given approximately by  $\hat{H}^{1/4} = N + 0.6$ , particles approaching the midplane from the asymptotic region have limited access to the stochastic regions; conversely, particles that are in the stochastic regions at the resonance energies are trapped near the midplane for long periods of time. Put another way, at these energies the particles have transient characteristics and therefore after being injected can be measured as they emerge on more or less the same time scale. These ideas lead to the concepts of differential memory and "coherent" scattering. Using the model field of Figure (1), Burkhardt and Chen, [1991] modelled the CPS distributions and in particular introduced a density change in the initial distribution at  $t=0$ . The subsequent time evolution of the distribution function  $f(v,t)$  is calculated for  $t > 0$ . The results show that, following such a change, the distribution function  $f(v)$  develops measurable peaks and valleys whose locations obey the characteristic scaling law of  $\hat{H}^{1/4}$ . Here  $\hat{H}$  is the normalized Hamiltonian for each species and is defined by  $\hat{H} = (mv^2/2)/(mb_n \Omega_n^2 \delta^2)$  where  $b_n = B_{z0}/B_{x0}$  and  $\Omega_n = eB_{z0}/mc$ . The resonance scaling then is given by  $N + 0.6 \sim \hat{H}^{1/4}$  where  $N$  represents integers. A plot of the model steady state distribution function at  $z = +3\delta$  is shown in Figure (5) as an illustration of the resonance effect found above. We explore this figure and its relationship to Figure (4) in more detail below.

The effects of collisions on the phase space orbits are of interest because the physical properties above have been deduced from these orbits in the absence of particle scattering. For example, the scaling law above, which has been predicted for the location of peaks and valleys in ion distribution functions in the central plasma sheet [Burkhardt and Chen, 1991] should be re-examined in the presence of collisions for possible important effects on physical properties. This has been investigated in numerical simulations in relation to pitch-angle scattering and energy exchange [Holland and Chen, 1991], but as yet no laboratory work has been undertaken. Moreover, the non-Maxwellian distribution function with a resonance scaling  $N \sim \hat{H}^{1/4}$  shows very good agreement with observations [Chen et al., 1990a] and has been shown to be unstable to electrostatic waves [Huba et al., 1991].

An important conclusion from above is that analysis of particle motion predicts that the phase space particle orbits are separable into the distinct stochastic, transient and integrable regions. Each class of orbit is dynamically distinct and, as seen in Figure (3), even the regions are disjoint from one another. The time scales associated with each of these regions can be used to define separate classes of particles. For example, the resonance scaling given above was originally derived in connection with the "transient regions" in the phase space and, as is pointed out by [Burkhardt and Chen, 1991], the "stochastic regions" seen in Figure (3) constitute an altogether separate class of particles and do not overlap the resonant energy regions. At the  $N$ -th such resonance, the majority of the transient particles crosses the equator  $N + 1$  times. If  $N + 1$  is even (odd), such orbits originating from  $z = \infty$  will enter the equatorial plane and escape to  $z = +\infty$  ( $-\infty$ ). Viewed as a chaotic scattering system, therefore, the current sheet scatters the transient particle class "coherently" at resonance. In Figure (4), we have plotted  $C_r = 1 - R$  versus  $\hat{H}^{1/4}$  for a particular choice of  $b_n$ . Here  $R = n/s$  ( $n < s$ ) or  $R = s/n$  ( $s < n$ ) where  $n$  and  $s$  are the fraction of north ( $z > 0$ )- or south-bound scattered orbits, respectively, relative to the incoming orbits from  $z = +\infty$  with normalization  $n + s = 1$ .

As an illustration, we show in Figure (5) a model distribution function  $f(v)$  using  $C_r$  of Figure (4)

based on the above model. The observer is assumed to be at  $z = +3\delta$ . Maxwellians  $f_j = \exp(-\hat{r}T_j)$  ( $j = 1, 2$ ) are used for the source distributions with  $f_2(0) = \beta f_1(0)$ . For this figure, we have used  $T_1 = 20000$  °K,  $T_2 = 16000$  °K,  $\beta = .5$  and  $b_n = 0.05$ .  $f_1$  represents particles scattered toward the current sheet from the North and  $f_2$  from the South. No attempt to fit a specific data set is made.

## I.2 Experiment

It has been pointed out a number of times that space-related laboratory experimentation can be divided into at least two separate categories (e.g., Faelthammar, 1974): (i) experiments intended to investigate basic physical processes which play a role in space plasma dynamics, and (ii) experiments designed to literally simulate geophysical structures. When considering experimentation related to the second category, scaling considerations become paramount and can be so stringent as to put into question the applicability of the results to space physics [Block, 1967; Fahleson, 1967]. Laboratory work of this nature, for example the early terella series of experiments, has met with limited, but at times, impressive success [Block, 1955, 1956; Alfven et. al., 1963, 1964; Kawashima, et al., 1965]. A compilation of the early experiments has been given by Schindler [1969]. A number of other more recent experiments belonging largely to the first category have yielded significant new insight into areas such as magnetic reconnection [Stenzel and Gekelman, 1981] and double layer simulation [Alport et al., 1986; Hairapetian and Stenzel, 1990] and velocity shear instabilities related to the space plasma environment [Koepke and Amatucci, 1994] and parameter regime.

The phenomenon which we investigate here belongs to the class of basic physics of particle dynamics in a magnetosphere-earth magnetic field region. To do this the essential features of the quiet-time magnetotail magnetic field region have been constructed. Our initial purpose is to determine if resonances predicted by the theory can be measured experimentally. The experimental arrangement in the SPSC is shown in schematic form in Figure (6). After constructing an approximation to the magnetotail magnetic field topology using a pulsed grid network, we injected electrons into the "neutral sheet" taking care that the electron beam was sufficiently single particle-like. To investigate whether "coherent" particle scattering occurs at neutral sheet crossings for particular "resonant" particles, we placed detectors (sectorized current collection sheets) as shown in Figure (6), varied the energy of the incoming beam, and tracked the number of forward and backscattered particles for a given initial energy; by varying the energy of the injected particles over a wider range we will eventually be able to determine the distribution.

## II Approach

The theoretical basis of this study is sketched in the Introduction and the major references are given therein. This Section focusses on the experimental method and its relationship to the particle code which was used to define parameter ranges and which also was essential in predicting which of the physical models under consideration would provide the basic resonance structures discussed above.

### II.1 Experimental Design and Configuration

In developing the experimental field model and configuration we have used a test particle simulation as described in the following Section II.2. This simulation allowed us to vary the value of  $b_n$ , the number and

simulation as described in the following Section II.2. This simulation allowed us to vary the value of  $b_n$ , the number and location of the current sheets, as well as the current carried by each sheet. In addition, the model includes both the discrete nature of the wires and their finite radius. With these inclusions, we were able to determine the amount of scattering as particles cross the sheet and the percentage of particles which are lost.

In preparing the laboratory experiments we chose to model the distributed neutral sheet using a number of equally spaced thin current sheet sections. Such a series of distributed transmissive current sheets approximates the Harris magnetic field form. The thin current sheets were constructed using highly transparent arrays of wires as shown schematically in Figure (7). In theory, by using an arbitrarily large number of properly weighted thin sheets, we could reproduce the true Harris current distribution. In practice, however, it is desirable to use the minimum number of sheets possible since for each crossing of a sheet there is a finite probability of losing the particle. In addition, the discrete nature of the grid wires causes a small amount of scattering. Computer simulations, as covered in Section II.2 below, using varying numbers of grids have shown that the optimum representation consists of four grids as pictured (the "quadgrid" model). Also simulations show that finite wire effects are negligible for wire sizes selected.

The choice of 1m x 1m grids is a compromise between the desire to maintain field constancy and size constraints imposed by the chamber environment. Because of the finite size along the y-direction, the desire for field constancy requires a relatively small separation between adjacent sheets. This allows a measurement of the most number of resonant peaks for a given  $b_n$ . In addition, it is necessary to separate the wires as much as possible without disturbing field constancy around a particular wire to reduce scattering and particle losses. From an experimental viewpoint, however, it is desirable to have the wires as large as possible (to carry more current). In the simulations we have used wires ranging from 40 to 80 microns and in the laboratory we have tested the current carrying capability of tungsten and other materials from 10 to 70 microns. We have used wire separations ranging from 1mm to 2mm, sheet separations from 1 to 5 cm and  $b_n$  ranging from 0.1 to 0.4 in the test particle simulations. We found that the experimental configuration which best met the conflicting requirements was a four sheet configuration of 1.8 cm separation between planes, an inter-wire spacing of 1.59 mm, a wire radius of 60 microns and a normalized magnetic field ratio,  $b_n$ , of 0.2. In this arrangement, 60% of the current is carried by the two inner sheets with the remaining 40% carried by the two outer sheets. Also there are current carrying field shaping bars pictured in Figure (8) which carry currents of the same order of magnitude as the entire sheet (see below).

For the configuration defined above we find that at the very low energies particle loss is 50% of electrons in traversing the structure, whereas at the higher energies this figure is 10%. Our experimentation only used particle energies greater than about 200 eV with most experimentation in the 100's of eV to keV range. As described below, in many cases of interest low entry particle pitch angles were maintained thus allowing higher energies in examining the resonance effects. We did not expect any significant effects on the scattering amplitudes due to particle interaction with the wires and this is confirmed by experimentation results. Very low energy particles (in the eV to 10's of eV range) experience unacceptable levels of scattering in addition to being affected much more by noise levels apparent in any pulsed environment such as the one described here. Also, for wire radii which are larger, we began to lose an unacceptably large percentage of the particles and therefore the resonance structures lose resolution. We describe the effects of finite wire sizes below.

## II.2 Description of particle code

The theoretical modeling of the experiment was performed using a test particle code in which a source distribution of particles is selected and pushed through a prescribed magnetic field. The numerical algorithm used is the standard leap frog method with the step size chosen small enough to resolve the highest frequency (shortest scale length) in the system.

We have written the code so that we may use a number of model input distribution functions. In particular, for any given energy (or multiple energies) we launch  $N$  particles with a random spread in pitch and phase angle  $(\delta, \phi)$  about a given pitch angle  $\beta$  and phase angle  $\theta$ . Note that by choosing  $\beta$ ,  $\theta$  and  $\delta\phi$  we may model anything from beams to completely isotropic distributions.

The models used for magnetic field went through a number of iterations listed below. In order to construct a magnetic field with the same general topology as the Earth's magnetotail, (i.e. a long scale length in both the  $x$  and  $y$  directions and a short scale length in  $z$ , where  $x$  is the direction of the primary component of the field above the current sheet,  $y$  is the direction of the current, and  $z$  is normal to the current sheet) we need to have a current sheet which is very broad in both  $x$  and  $y$  and has a finite thickness in  $z$ . Ideally, we would have an infinite current sheet with a current density given by

$$J(z) = J_0 \text{sech}^2(z) \hat{y} \quad (1)$$

(Note that we are using dimensionless variables so the  $z$  is normalized to some scale length,  $L$ , typically the half-width of the current sheet.) Since this is not possible in a laboratory environment we need to design a surrogate system which has the same general topology as the actual system. We have chosen to use a set of thin current sheets evenly spaced in  $z$  with the currents in each grid weighted to mimic the actual distributed current sheet. As a lowest order approximation, we neglect any finite wire effects and take the current sheets to have an infinite extent in both  $x$  and  $y$ , i.e. we take the current density to be

$$J(z) = J_0 \sum_i \alpha_i \delta(\text{abs}[z - z_i]) \hat{y} \quad (2)$$

where  $\alpha_i$  is the fraction of the total current in the  $i^{\text{th}}$  wire and  $z_i$  is its location. Obviously if we use an infinite number of such current sheets we may reconstruct the current density profile of Equation (1) to arbitrary accuracy. In practice, this current distribution must be constructed in the lab using a set of wire grids, and even though these grids are highly transparent, each time a particle passes through one there is a small probability the particle will be absorbed and also a small amount of scattering. Thus, it is desirable to use as small a number of grids as is possible to obtain the desirable results. We have found the minimum number of grids required to obtain the resonance scaling in the forward (backward) scattering probability is four, and that even numbers of grids in general given better results than odd numbers. In particular, we have found that a reasonable model uses four grids with 30% of the total current carried on each of the inner two grids and 20% carried on each of the outer two grids. The inner grids are located at  $z = \pm 0.33$  and the outer grids at  $z = \pm 1$ . This configuration mimics the topology of the magnetotail current sheet quite well for high energy particles which traverse a large fraction of the current sheet thickness in their meandering and therefore tend to integrate over the discrete nature of the grid structure. For low energy particles, on the other hand the quantized nature of the field is quite apparent and the  $\tilde{H}^{1/4}$  scaling in the forward (backward) scattering probability is lost.

### IL3 Finite Wire Effects



The current sheets in an experimental configuration are not infinitely thin and uniform but are instead constructed from discrete wires which may both scatter and absorb particles. Far from a given current sheet we may neglect the discrete nature of the wires and use the uniform thin sheet approximation. Within a certain distance of a current sheet, however, a particle will "see" the current sheet as being constructed from individual wires. To model this effect, when a particle is within a distance of two wire spacings from a current sheet we model that particular grid as fifty individual wire ( $\pm 25$  wires in either direction from the location of the particle). The other grids are still modeled as uniform thin sheets, since the particle is far from them. No significant differences were found when a larger number of wires were used. In addition, to account for particles being lost to the grid, if a particle comes within a wire radius of the location of a wire we remove the particle from the simulation. A particularly interesting aspect of the results of this portion of the theoretical modeling is that three grids have a higher transparency (absorbed fewer particles) than would be expected from purely geometrical arguments. This is because the magnetic field near a wire increases as  $1/r$  and tends to keep particles from reaching the wire.

#### II.4 Effects of Finite Grid Size

The next major complication to the ideal case of four infinite, uniform thin grids to be examined is the fact that the grids are not infinite in extent but rather are finite in both  $x$  and  $y$ . As long as we are within grids, the effects of truncating in the  $y$ -direction is not important, however, we find that the truncation in the  $x$ -direction results in a significant deviation from a simple field reversal topology. We again neglect the finite wire effects and model each of the grids shown in Figure (8) as a thin current sheet that has a width  $2a$ . The magnetic field for a current sheet of this form is given by

$$B_x = \frac{\mu_0 I}{4\pi a} [\tan^{-1}(a - \frac{x}{z}) + \tan^{-1}(a + \frac{x}{z})] \quad (3)$$

and,

$$B_z = \frac{\mu_0 I}{8\pi a} \ln \left[ \frac{(a-x)^2 + z^2}{(a+x)^2 + z^2} \right] \quad (4)$$

The total magnetic field from all four grids is found by adding magnetic fields of this form with the appropriate shift in the  $z$  for each grid. A vector plot of this field combined with a constant  $z$ -component (due to the Helmholtz coils) is plotted in Figure (9). Note that instead of the magnetotail like geometry that we are attempting to reproduce, we have created closed field lines which are much more reminiscent of a O-type geometry.

To rectify this problem we have added shaping bars modeled as current filaments in  $x$ -direction of length  $2a$  located at either edge of the grids seen in Figure (8). The current being fed into the wire at one end and being bled off is a linear function of  $x$ . The feeder bar for the inner two grids is modeled as a single filament located at  $z = 0$  and  $y = a$ , whereas the bar feeding the outer two grids is modeled as two current filaments located at  $z = \pm c$  and  $y = b$ . The currents are fed into the inner and outer grids from opposite ends of the grid. We have calculated the total magnetic field (4 finite grids + shaping bars

+ feeding bars) in this case to be given by

$$B_x = \frac{\mu_0 I}{4\pi a} \left[ \frac{\epsilon_0}{2} [Q(a, 1, x, z) + Q(a, -1, x, z)] + \frac{\epsilon_i}{2} [Q(a, 1/3, x, z) + Q(a, -1/3, x, z)] \right. \\ \left. + 2\epsilon_R R(a, a_R, x, z) + 2\epsilon_L R(a, -a_L, x, z) \right] \quad (5)$$

$$B_y = \frac{\mu_0 I}{4\pi a} \left[ \frac{\epsilon_i}{2} [G(a, a, 0, x, y, z) - G(a, -a, 0, x, y, z)] - \frac{\epsilon_0}{2} [G(a, b, c, -x, y, z) \right. \\ \left. + G(a, b, -c, -x, y, z) - G(a, -b, c, -x, y, z) - G(a, -b, -c, -x, y, z)] \right] \quad (6)$$

and,

$$B_z = \left[ \left[ \frac{\epsilon_i}{2} [P(a, 1/3, x, z) + P(a, -1/3, x, z) - H(a, a, 0, x, y, z) + H(a, -a, 0, x, y, z)] \right. \right. \\ \left. + [P(a, 1, x, z) + P(a, -1, x, z) + \frac{1}{2} H(a, b, c, -x, y, z) + \frac{1}{2} H(a, b, -c, -x, y, z) \right. \\ \left. - \frac{1}{2} H(a, -b, c, -x, y, z) + \frac{1}{2} H(a, b, -c, -x, y, z)] \right. \\ \left. - 2\epsilon_R S(a, a_R, x, z) - 2\epsilon_L S(a, -a_L, x, z) \right] + B_H \quad (7)$$

where the functions G, H, P, Q, R and S are defined as,

$$G(a, b, c, x, y, z) = \frac{z-c}{(z-c)^2 + (y-b)^2} \left[ \frac{(x^2 - a^2) + (y-b)^2 + (z-c)^2}{\sqrt{(a+x)^2 + (y-b)^2 + (z-c)^2}} - \sqrt{(a-x)^2 + (y-b)^2 + (z-c)^2} \right] \quad (8)$$

$$H(a, b, c, x, y, z) = \frac{-(y-b)}{(z-c)^2 + (y-b)^2} \left[ \frac{(x^2 - a^2) + (y-b)^2 + (z-c)^2}{\sqrt{(a+x)^2 + (y-b)^2 + (z-c)^2}} - \sqrt{(a-x)^2 + (y-b)^2 + (z-c)^2} \right] \quad (9)$$

$$P(a, b, x, z) = \frac{1}{2} \ln \left[ \frac{(a-x)^2 + (z-b)^2}{(a+x)^2 + (z-b)^2} \right] \quad (10)$$

$$Q(a, b, x, z) = \tan^{-1} \left( \frac{a-x}{z-b} \right) + \tan^{-1} \left( \frac{a+x}{z-b} \right) \quad (11)$$

$$R(a,b,x,z) = \frac{az}{(x-b)^2 + z^2}, \quad S(a,b,x,z) = \frac{a(x-b)}{(x-b)^2 + z^2} \quad (12)$$

This field is plotted in Figure (10) and it shows similarity to the Harris type model configuration shape to a greater degree than the O-type geometry seen in Figure (9).

We have plotted in Figures (11) through (15) the results of test particle simulations using the final model covered above. We use here and in the majority of the remaining plots the convention that the normalized energy is plotted as  $\hat{H}_D^{1/4} = b_n \hat{H}^{1/4}$  as in, for example, Holland and Chen, [1993]. The usefulness of this is evident, as the plots are now not restricted to a particular value of  $b_n$ . The conventional values of  $\hat{H}^{1/4}$  are then easily recovered simply by dividing abscissa values by  $b_n$ . Figure (11) is a plot of the correlation function,  $C_r$ , for the case in which  $B_0 = 20$  gauss and  $\delta = 10$  cm. The resonant peak structures at particular normalized energies are evident in this plot. Figures (12) and (13) are plots of the percentage of particles forward and backward scattered from the four grid region for these parameters. Figures (14) and (15) plotted for this simulated case show a contour plot of scattering amplitudes versus pitch angle with the right hand limit corresponding to forward scattered particles. The resonance peaks are clearly visible in Figure (14) and even more dramatically in the three dimensional view of Figure (15). The source particle distribution for these results represents particles injected within 10 degrees of field alignment. Based on these results we can prepare Table I, for example, which gives electron energy and drift in the y direction for each individual peak. The energies used in the table are beam energies in eV required to resolve the Nth peak for the scale length  $\delta$  and the given  $B_x, b_n$ . The energies are calculated from their normalized values,  $\hat{H}$ , by

$$H = \hat{H}(m\Omega_e^2 \delta^2 b_n^2), \quad \hat{H} = (N+0.6)^4 \quad (13)$$

We might note that the magnitude of  $B_x$ , the x-component of the field, is chosen here as 20 gauss whereas the z-magnitude is 2 gauss. Also, the resonance peaks are strongest for  $\rho_0 < R_c$  and the peaks vanish for  $\rho_0 > R_c$ , where  $R_c$  is the radius of curvature of field lines in the current sheet.

TABLE 1

Energies to resolve the N th Peak in the distribution function and the distance moved along y (dy)

$B_x = 20$  gauss,  $B_z = 2$  gauss,  $\delta = 10$  cm

N	E(eV)	dy(cm)
2	32	8
3	120	16
4	340	27
5	800	40
6	1700	62
7	3360	81

The value of  $\delta$ , which is the half width of the field, is taken here as 10 cm in order to account for the nonlinearity in the region of the wires. It defines the magnetic field and adjustments which must be made to reproduce a given configuration i.e., the shaping of the field and the placement of current carrying conductors is determined by this parameter.

### III Overall Objectives

As described previously, we have performed a number of simulation studies of various types of neutral sheet configurations. These results along with earlier models have been used to design the current experimental arrangement. The overall general objectives of the investigation are summarized as follows:

(i) To test the hypothesis that particles injected from the asymptotic regions as described above follow an energy scaling law related to the location of peaks and valleys in the absence of scattering for a vacuum field as shown in Figure (5), (ii) To test the theoretical results that produce the different classes of phase space orbits as seen in Figure (3) i.e., to verify that quiet-time magnetotail distributions can be grouped according to transient, stochastic and integrable regions, (iii) To verify and give a diagnostic for measurement of current sheet thickness based on the energy scaling considerations above and finally, (iv) To introduce noise (i.e., in the form of a variable plasma density) in order to determine the effect on the phase space orbits and the results of the above investigations.

Specific primary experimental questions which we have addressed to date are:

(i) What percentage of injected particles are forward-scattered and back-scattered? (ii) How far across the "neutral sheet" do the particles move? (Our test particle simulations have also predicted these results.) and, (iii) How many crossings are observed at a given energy? i.e., what is N?

### IV. Experimental Configuration

#### IV.1 Experimental Chamber Description

The experimental work was performed in the large Space Physics Simulation Chamber (SPSC) at the Naval Research Laboratory as shown schematically in Figure (6). The axial magnetic field provided by the five coil Helmholtz arrangement is variable to near 80 gauss continuously or to .5 kgauss in the pulsed mode. Base chamber pressures are near  $10^{-7}$  torr and there is a microwave plasma source [Walker, et. al., 1994] located at the far right hand side endcap as shown in the Figure. Plasma densities are variable through this source in a range of  $10^3 - 10^9 \text{ cm}^{-3}$  for various gases and electron temperatures range from a few tenths of an eV to 1 eV. The ions are typically near room temperature. The pulsed field which is effectively steady state on the time scale of the experiment has a lower range pulse width of 100  $\mu\text{sec}$ . The chamber has been configured with multiple ports to allow easy access during experimentation. Figure (6) shows the primary experimental arrangement. The essential data acquisition and waveform analysis schemes are based on waveform analysers in portable CAMAC crates, digitizing oscilloscopes, and Macintosh-based LABVIEW II software.

To provide the x-component of the Harris field where,

$$\vec{B}(x,z) = B_0 \tanh\left(\frac{z}{\delta}\right) \hat{i} + B_0 \hat{k} \quad (14)$$

the grid is pulsed and the field component produced by the pulsed grids adds to the constant z-component produced by the external Helmholtz coils. A typical voltage pulse applied to the inner two grid planes is shown in Figure (16) in an early raw form. The pulse was subsequently flattened by shaping circuits and remained constant over a period of time near 120  $\mu\text{sec}$ . The period within the voltage pulse during

which the data was sampled is indicated by the 50  $\mu$ sec window shown on the pulse.

Experiment diagnostics used in the first phase of experimentation consisted primarily of a 3-axis DC Bell gaussmeter, a 3-axis B (dot) loop probe and the forward and backward scattered collector plates seen on either side of the current carrying grid in Figure (6). These instruments are described below.

## IV.2 Mechanical Design Considerations

### Overview

The experimental operation scenario for this work is shown schematically in the 2D view of Figure (17). Electrons of specified energy are injected in vacuum toward the current carrying mesh. The mesh has dimensions of 1m x 1m and consists of 4 separate planes of tungsten wire carrying equal currents in the same direction. The planes are separated by 1.8 cm. The wires in the meshes are separated by 1.59 mm. The particles are injected into the magnetic field with pitch angle resolution of below 5 degrees. The magnetic field is produced by a combination of the field produced by the mesh and that produced by the external Helmholtz coils of the chamber configuration. The grid structure is referred to as the "quadgrid" model primarily because of the structure of the mesh configuration which contains 4 separate planes as described above. The two large detectors consist of 16 quadrant-sectored current sensor boards each and measure forward and back-scattered electron current.

The experimental scenario requires pulsing for a number of reasons related to the magnitude of currents carried in the wires (near 1 kAmp/wire). By digital sampling of the diagnostic instruments we were able to reconstruct both the field and the scattered particles, e.g., once a steady state magnetic field configuration is reached at the end of the current pulse rise time, the electron gun is operated at different accelerating potentials. This is the basic scenario required to experimentally investigate current collection vs electron energy. By pulsing the current, we avoid problems associated with heating and emission at higher current levels and we can also take averages of particle fluxes over many pulsing cycles. In this way it is possible to reconstruct the distribution function from the individual spectra. For definition of the phase space maps the configuration will change with particles being injected in the equatorial plane. When plasma is introduced as a perturbation further problems associated with the self-consistent interaction between plasma and pulsed grids must be considered and the topology restudied in detail. The initial results are vacuum results. This section addresses mechanical design concerns related to the components outlined above.

### IV.2.1 Grid Design

The current-carrying grids are shown in multiple schematic views in Figure (7) and (8). Figures (18) and (19) show engineering drawings. The grids were designed using 3/8" - 16 threaded brass rod welded to a T-shaped machined brass support which functions as a current carrying feeder bar. Figure (18) shows dimensions and configuration while Figure (19) shows an end-on view of the brass rods and copper bar. The wire spacing is automatically provided by the threads in the brass rods and this affords a measure of protection as the threaded wire sinks into the grooves and is therefore below the contact level of the rod when placed on a horizontal surface. The wires passing over the machined brass support are further soldered to the support to insure contact integrity.

As seen from the end-on view to the left in Figure (18), the entire grid structure is designed such that the inner pair of grids slides on insulating supports between the two outer grid planes. With this

arrangement, separate voltages can be applied to inner and outer grids as is in fact the case and covered in Section II above, i.e., the design calls for differing currents in each separate two-grid set. The outer grid structure, which is responsible for the structural support of the entire unit, is supported by 1/2" round fiberglass rods which are bolted to the sides of the structure.

In addition to the grid wires there are magnetic field shaping bars shown in Figure (8) and discussed in Section III. The bars run parallel to the wires at each end as shown and carry varying currents. These bars add primarily a z-component to the field at the position of beam injection and are used to insure that the beam is guided to the grid area for interaction. The magnitude of these currents as discussed above is of the same order as those carried by the grids themselves.

The choice of tungsten wire over copper for the grid windings was governed primarily by the higher tensile strength of tungsten since neither material heats significantly to cause concerns of electron emission in pulse lengths of the order of 50-100  $\mu$ sec at current levels near 1 kAmp. It was feared, however, that repeated inadvertent contact with the grids could cause stretching and warping of the copper whose Young's Modulus is about a factor of 4 less than tungsten.

Figure (20) is a photograph which shows the grids mounted in the SPSC. Pictured also is the electron gun to the right of the figure. The injection position was later changed to the left of the grids.

#### IV.2.2 B (dot) Loop Probe

Because of the nature of the pulsed experiment it was necessary to construct a measurement of the magnetic field which would detect the first time derivative of B and integrate it (Hutchinson, 1987). The simplest and most common method of making this measurement at a point in space is to use a loop of wire and exploit the integral form of Faraday's law. To measure 3 components of B we have constructed three orthogonal loops mounted on a common block as shown in Figure (21). Typical current levels of the grids produced magnetic fields are of the order of 10 gauss with rise times between 20 and 50  $\mu$ sec. The loops are 1 cm in diameter and consist of three turns of copper wire. A low number of turns is used to limit the inductance for the necessary time response. There is a separate Burr Brown opa 620 differential operational amplifier for each axis as seen in the figure and the emf produced is amplified by a gain 100. Since each axis is independent it is possible to measure simultaneously the rate of change of each component of B. The output of the amplifier is fed to a Tektronix digitizing oscilloscope (TDS 460) and the traces stored and read by Labview\* software. To produce the final field strength, DC offsets are removed and the signal integrated with respect to time. Measurement of the steady fields and calibration of the B(dot) loops were performed with a Bell gaussmeter (also 3-axis) Hall probe. As described in Section V below, measurements of the magnetic field during pulsing were made with a resolution of 10 cm across the entire face of the grid structure.

#### IV.2.3 Current Collector Plates

The photograph of Figure (22) shows the current collectors before installation in the experimental configuration. In this view the 16 sectored collection areas of each plate are easily seen. As mentioned above one primary collection mode in this experiment consisted of ganging together four of the plates horizontally to form 4 rows; current is then sensed to each row independently of which plate collects the current. There was an amplifier attached to each active row of the boards inside the vacuum. The plates

as installed can be seen in perspective with respect to the chamber dimensions in Figure (23). What is shown is the backscattered plate only as the forward plate, being directly behind the grid, is obscured from view. The electron beam accelerator in the lower right hand corner was moved to the left side of the grid during experimentation. All vacuum penetrations to the grid and the collector plate structure were made through a single flange and all penetrations were isolated. We initially encountered noise problems with the bare detector plates and were only able to solve this by covering each plate in a Faraday cage screen and grounding the screen to chamber ground. In fact the wire hanging from the center of the picture is attached to this shield. In addition the plates were biased negatively by 9 volts in order to avoid secondary emission from incident beam electrons. Once these precautions were in place the noise level during pulsing was actually quite low as can be seen in Figures (24) and (25) below; less than perhaps a few mv above background noise levels.

Figures (24) and (25) show back-and forward- scattered current collection as a function of electron beam energy. The data display is taken from a Tektronix TDS 460 digital oscilloscope screen. These figures are displayed to give an overall view of the scattered current collection by the sensor plates. We analyze these Figures in more detail in the following section on Experimental Results.

#### IV.2.4 Pulsing Forming Network (PFN)

The PFN used to provide the current pulse to the grid is shown in Figure (26). The basic design follows that of Guillemin, [1935]. An example of the applied voltage pulse waveform is shown in Figure (16).

#### IV.2.5 Electron Beam

The electron beam was provided by the Kimball Physics EMG-14 (50 eV - 10 keV) electron gun and programmable power supply. Current at the injection position varied from 10 to 100  $\mu$ a. At these current levels beam spreading at the distances required for injection is negligible. The beam was steerable and approximated to a high degree single particle orbits. It is shown in Figure (27) focussed on a phosphor screen at the approximate beam injection point into the grid area. As mentioned, spreading is quite small over this distance as can be seen in the Figure.

### V Experimental Results

#### V.1 Current collection during pulsing

In Figures (24) and (25) we have plotted the output of the amplifier circuits on each of the backscattered and forward scattered plates using the Tektronix TDS 420 digital display oscilloscope traces. These plots are for the purpose of demonstrating variable levels of current collection as a function of differing electron energy and the shift in enhanced levels of collection with energy and with  $b_n$ . Each separate signal represents total current collected by either the forward- or the backward-scattered plate, i.e., there is no sectoring for separate signals as a function of collection position on the plates as is done in a later section. In this following section we compare the energy levels of enhanced collections with those of theoretical predictions at given magnetic field ratios,  $b_n$ .

Current collected by both plates is displayed at two different values of  $B_z$  in Figures (24) and (25); back-scattered current is the upper trace of the two and forward-scattered is the lower one. In plate 1 of Figure (24) we have indicated the electron beam pulse width; the rise time of the electron beam signal



is on the order of 10's of nanoseconds and throughout the experimental series the beam on-time was adjusted between 20 and 100  $\mu\text{sec}$ . The beam on-time logic pulse of 100  $\mu\text{sec}$  is at the top of each plate. In addition the first trace in the upper lefthand corner of Figure (24) is taken with no electron emission (i.e., the current filament of the electron gun is turned off) in order to see the noise background. Major divisions along the ordinate are 20 mv. The conversion between voltage scales on the oscilloscope face and current collected by the sensor plates is a factor of  $10^5$ , or 1 volt corresponds to 10  $\mu\text{a}$  of collected plate current. It should be noted that pulsing of the grid is taking place during the beam on-time whether the beam is emitted or not; the logic signal is used to pulse both the grids with current and, after a small delay the electron accelerator. The three remaining plates of Figure (24) show various levels of collected currents associated with differing levels of electron beam emission energy.

In Figure (24) the gradual emergence of the backward-scattered signal from noise levels begins to occur as beam energy increases to 400 eV. At 550 eV this level is maximum and then begins to recede as the energy increases further. The forward-scattered signal shows a slight increase during this time but it is clearly the backward-scattered contribution which is dominant.

At lower energy and different field strength it is the forward scattered signal which is dominant as inspection of Figure (25) shows. This signal gradually emerges and recedes in the transition from beam energy of 150 eV to 450 eV.

Each of the figures above is consistent with the general idea of resonance in scattered particle collection as a function of particle energy; in addition, this is also evidence of shifting enhancements in back-and forward- current collection as a function of energy. This will be investigated in more detail below and compared to numerical simulations of particles with different injection distributions.

## V.2 Magnetic Field

A complete set of 600 measurements characterizes the entire field region, i.e., the measurement set consists of three separate xy planes on each side of the outer grids separated by  $z = \delta$ .

Pictured in Figure (28) are the x, y and z components of the pulsed field as measured by the  $B(\dot{\phantom{a}})$  loops in the area at  $z=2\delta$  from the backscattered grid during pulsing at one particular current level. This figure does not include the constant Helmholtz coil field along z. The units of the figures are multiples of  $\delta$ , the half width of the magnetic field. The point (0,0) corresponds to the center of the grid, the y-axis is along the direction of current flow in the wire meshes and the x-axis represents distance across the grid perpendicular to the direction of current flow. What is clear from this figure is the relatively constant value of  $B_x$  and  $B_y$  in the central region of the grid where most of the experiment is performed; on the other hand, the value of  $B_z$  varies from a relatively large positive value at the extreme right hand side of the grid ( $x=-60$ ) to a negative value near the left hand side. This variation is largely the undesirable result of the current carrying feeder bars which supply current to the grid wires; there is also some contribution to this result from the current carrying cabling which is attached to the bars although these effects have been largely minimized by favorable geometrical placement and by placing cables carrying current in opposite directions alongside one another. This value of  $B_z$  is reversed in sign on the opposite side (forward-scattered) of the grid. The constant value of the Helmholtz coil-produced magnetic field along the z-axis must be added to these values to produce the required modified Harris field configuration of Equation (14).

Although the plots of magnetic field surfaces as shown in Figure (28) are helpful in understanding the magnitudes of the field components they provide little insight into magnetic field direction. Therefore

in an alternate view of the grid produced magnetic field, we show in Figures (29) through (31) vector plots at constant  $y$  for better comparison to the modified Harris field form shape. These figures which are the primary interaction region of the beam with the grid show cross sections at  $y=68, 78$  and  $88$  cm from the bottom of the grid. Each of the figures shows the field produced with no Helmholtz external field,  $B_{zH} = 0$ , and with  $B_{zH} = 4$  gauss. The  $z=0$  position corresponds to the center of the grid and  $x=0$  corresponds to the left side of the grid in these figures. There is variable linear scaling used on the vector lengths and the grid sizes are symmetric so that the direction of the field vector inferred from the plots is a true indication of the direction in space. The magnetic field along  $x$ ,  $B_x$ , is near 10 gauss for the measurements closest to the grid on the backscattered side but is somewhat reduced from these levels on the forward grid planes. Accompanying these plots is Figure (32) which shows the magnetic field streamlines as derived from graphics software using linear interpolation and 10 cm square resolution. The streamline plots are shown for comparison to the vector routines and were taken only at the  $y=78$  cm location. They also do not include as many points as the corresponding vector plot and therefore do not match the structure exactly. It is clear from all of these plots, however, that there is not perfect symmetry in the field produced on either side of the grids; although this would be expected to complicate a comparison of the results to theory the fundamental resonant structure is expected to remain intact.

## VI Comparison of Results to theory

### VI.1 Theoretical resonance dependence on $b_n$

The positions of resonance peaks as a function of energy are provided by the relation,

$$(N+0.6) \sim \hat{H}^{1/4} \quad (15)$$

where  $\hat{H}$  is the normalized Hamiltonian with normalization factor given by ,

$$mb_n^2 \Omega_n^2 \delta^2 = mb_n^4 \Omega_0^2 \delta^2 \quad (16)$$

where  $m$  is the electron mass,  $b_n = (B_z/B_x)$ ,  $\Omega_n = eB_z/mc$ ,  $\Omega_0 = eB_x/mc$  and  $\delta$  is the half-width of the neutral sheet. For given consecutive peaks  $N_i, N_{i+1}$ ,

$$(N_{i+1}+0.6)^4 - (N_i+0.6)^4 = \frac{H_{i+1} - H_i}{mb_n^2 \Omega_n^2 \delta^2} \quad (17)$$

Consecutive peak separation in energy is therefore predicted to be,

$$mb_n^2 \Omega_n^2 \delta^2 [(N_{i+1}+0.6)^4 - (N_i+0.6)^4] \quad (18)$$

with the peak position in eV given as,

$$H = (mb_n^2 \Omega_n^2 \delta^2)(N+0.6)^4 \quad (19)$$

The resonant peak separations and positions as a function of energy derived above are based on results of the Harris magnetic field configuration and therefore some differences are expected in terms of the positions of the peaks as a function of energy for the grid field models used in the present work. This is covered in an earlier section and below. Also it should be noted that for large  $N$ , the factor of 0.6 can be ignored. However, most of the experimental results presented are for small  $N$  number and therefore this form is retained.

## VI.2 Simple Theory

In order to evaluate the experimental results it is useful to first consider some simplified physical pictures associated with particle motion in the field. Figure (33) is such a simplified schematic of particle injection into the simulated neutral sheet region (or the plane forming our current grids) at the  $z=0$  position. The basic drawing is taken from Chen and Palmadesso, [1986] and shows a transient orbit executing five  $z=0$  current sheet crossings, i.e.,  $N=4$ . The original figure has been modified to show the current grids position. The particle scattering collection plates described above are parallel to the  $z=0$  plane and spaced a few  $\delta$  on either side of the grids. The plates themselves along with the magnetic field lines are omitted from this drawing for clarity but recall that the magnetic field has only an  $x,z$  component in the modified Harris form.

### Turnaround points in $Z$

If  $B_z$  is taken near zero (or if  $b_n$  is small) particle motion within the current sheet can be considered as nearly motion in a pure neutral sheet [Sonnerup, 1971] so that the problem can be viewed at fixed  $x$  as in Figure (34) and motion is considered only in the  $yz$  plane. There is a pure oscillation in this plane with the position of the turn-around point in  $z$ , only a function of the injection angle at the edge of the sheet and the Larmor radius in the field,  $B_x$ . This is equivalent to considering only the component of the injection velocity which is perpendicular to  $B_x$  at injection, i.e., since we assume small  $b_n$  [Kaufmann and Lu, 1993; Chen and Palmadesso, 1986]. This case, which is simpler to analyze than the three dimensional case, can provide insight into particle motion and turn-around conditions in the current sheet field.

It is easy to show under the assumptions above that the positions of the turning points for the planar single particle motion described are given by [Chen and Palmadesso, 1986; Sonnerup, 1971],

$$z_t = \pm \sqrt{2\rho_0\delta(1-\cos\alpha)} \quad (20)$$

where  $\rho_0 = V_{\perp}/\Omega_0$  is the particle Larmor radius at the  $z=0$  plane,  $\Omega_0$  is the cyclotron frequency in the field  $B_x$  and  $\alpha$  is the angle between  $V_{\perp}$  and the  $y$ -axis. Since, in order to turn around, the particle must be within one Larmor radius of the neutral sheet edge where  $B_x$  is maximum this implies that  $z_t \max \approx \delta$  or  $\rho_0 = \delta/2$  or from Equation (20),

$$\sqrt{2\rho_0\delta} \leq \delta \quad (21)$$

Equation (20) may also be re-expressed as,

$$z_t = \pm (2mE_{\perp})^{1/4} \sqrt{\frac{2\delta(1-\cos\alpha)}{eB_x}} \quad (22)$$

or,

$$z_t = \pm \sqrt{\frac{2\delta p_{\perp}(1-\cos\alpha)}{eB_x}} = \pm \sqrt{\frac{2\delta(p_{\perp}-p_y)}{eB_x}} \quad (23)$$

where  $p_{\perp}$  is the perpendicular component of particle momentum. From Equations (22) and (23) it is apparent that the turnaround positions in  $z$  are a function of both total energy and the angle  $\alpha$ . In the general case there is a contribution both perpendicular and parallel to  $B$  due to the  $x$ - component of the injection velocity.

#### Dependence of resonant peaks on perpendicular energy

As seen from the above the particle turning points in  $z$  are a function of particle momentum along  $z$ , the half width of the current sheet ( $\delta$ ) and the magnetic field along  $x$ . It might be noted also that the smaller the ratio  $b_n (=B_x/B_{x0})$  the more closely the approximation here resembles the actual injection scenario. However, the resonance condition does not have an explicit dependence on this ratio as is seen in Equation (21). It should be noted at this point that the definition of the Larmor radius,  $\rho_L = p_{\perp}/eB$ , as traced through Equations (21) through (23) above, allows relatively higher injection energies depending on the single particle injection angle with respect to the magnetic field, i.e., the criterion of Equation (21) can be satisfied for higher total energies than at first would appear. This can be seen from the following simple argument based on the resonance condition of Equation (15). We note that the normalization factor of Equation (16) can be expressed as,

$$mb_n^4 \Omega_0^2 \delta^2 = mb_n^4 \left(\frac{v_{\perp}}{\rho_0}\right)^2 \delta^2 \quad (24)$$

where  $v_{\perp}$  is the component of injection velocity perpendicular to  $B_x$ . Expressing this in terms of a perpendicular energy we can re-express  $\hat{H}$  as,

$$\hat{H} = \frac{H}{2E_{\perp} b_n^4 \left(\frac{\delta}{\rho_0}\right)^2} \quad (25)$$

Using the turn-around condition expressed in Equation (21) to define the minimum value of the normalization constant, we have,

$$N_{\max} = \hat{H}_{\max}^{\frac{1}{4}} = \left(\frac{H}{8E_{\perp} b_n^4}\right)^{\frac{1}{4}} \quad (26)$$

or the maximum number of resonances observable depends upon the energy component perpendicular to  $x$  and is therefore also a function of the injection pitch angle.

There is, however, a complicated dependence of the injection pitch angle with respect to the initial field at the injection position and the field at the turnaround position. For example, in the limit that  $B_x \ll B_z$  essentially all of the particle energy for nearly field aligned injection would be injected perpendicular to the small  $B_x$  value; as injection energies increase therefore, one would expect to encounter the limit of Equation (21) fairly quickly. However, in the opposite limit when  $B_x \gg B_z$  (small

$b_n$ ) nearly field aligned injection would be essentially along  $B_x$  with a small component perpendicular to  $x$ . In this case and generally for relatively small values of  $b_n$  one can inject high particle energies and observe resonances predicted due to the small component of  $E_\perp$  and thus the satisfaction of the boundary condition of Equation (21). This is the case for most of the experimental work performed and described here. Indeed, it is the intermediate case which we observe to produce the resonant structures for our injection scenarios which include a 10-15 degree cone about the field direction..

### VL3 Results from the numerical work

Our primary injection pitch angle was near field aligned (or 180 degrees from field alignment) for most of the experimental work presented here. The numerical simulations described above were performed for 3 different injection distributions at fixed values of  $b_n$ . The results presented in this section are based on injection of a ring distribution into either the modified Harris field or the quad-grid field. The cone angle of this injection is in all cases less than 10 degrees from field alignment (or anti-parallel to field alignment)

Figures (35) and (36) show the coherence factor,  $C_r$ , defined earlier, versus the normalized Hamiltonian values of Chen and Palmadesso. Each of the plots is performed for the ring distribution at injection and for different values of  $b_n$ . Each figure is for two values of  $b_n$  and includes both the modified Harris distribution in addition to the experimental configuration as simulated numerically and described earlier. Figures (35a,c) and (36a,c) are for the Harris case and Figures (35b,d) and (36b,d) are for the quad-grid model. A conclusion which arises from these plots is that there appear resonant structures extending to higher and higher values of  $\hat{H}^{1/4}$  for decreasing values of the ratio  $b_n$  in the near field aligned injections in the numerical program, i.e., there are more peaks extending to higher values of the normalized energy as one traces the figures from Figure (35) through Figure (36) in which  $b_n$  changes from .3 to .6. This is consistent with the arguments above which, through Equation (21), show that the maximum number of neutral plane crossings is inversely proportional to both the ratio  $b_n$  and the perpendicular component of injection energy. When the injection angle is varied much above the approximately 10 degree cone angle about field alignment, the resonant structures seen in these figures begin to disappear both in the case of the Harris field and for the case of the experimental scenario. This behaviour is seen for the Harris field distributions in Figure (37) in which injection pitch angles of 20,30 and 50 degrees are shown in increasing order from bottom to top of the page. Energy ranges in these figures are not as broad as in earlier Figures 35 and 36 but they may nevertheless be compared for peak structure to Figure (35a). (Note that the abscissa scale in the plots of Figure (37) are in units of  $b_n \hat{H}^{1/4}$  so that to compare the peak positions with Figures (35) and (36) one divides the abscissa values of Figure (37) by  $b_n$  ).

It should be noted that, with the normalization scheme of Chen and Palmadesso, [1986] as described in Equation (15) a value of  $B_x$  and  $b_n$  must be specified in order to calculate the actual energy in eV as can be seen through Equation (19). As an example of this calculation, an  $N=2$  (i.e.,  $\hat{H}^{1/4}=.6$ ) resonance at  $b_n=.2$  and  $\delta=10$  cm would occur at an energy of about 128 eV for  $B_x=10$  gauss, at about 650 eV for  $b_n=.3$  and when  $b_n$  is increased to .4 this energy increases to near 2 keV. Our primary energy operation range in the experiment varied from about 250 eV to several keV as is seen in the results of the next section.

### VL4 Experimental Results

The experimental results were obtained at three different grid current levels which produced three different levels of  $B_x$ . In each case the external Helmholtz field  $B_z$  was changed to produce a  $b_n$  variation.

#### VL4.1 Resonances

A dramatic example of the type of resonant behaviour observed during experimental cycles is provided by Figures (38) and (39) which show forward scattered current collection for the  $B_x = 12$  gauss field in Figure (38) and the highly structured coherence factors for the same data set in Figure (39). Note that the backscattered contribution is the complement of the forward scattered data. Both figures are plotted for two different values of the external Helmholtz coil field  $B_H$  increasing from the bottom of the page (Recall that  $B_H$  is not the same as the total  $B_z$  as covered in Section V.2 above and so one cannot generate  $b_n$  simply by dividing this value by  $B_x$ ). The shift of the primary forward scattered resonance peaks in Figure (38) from  $\hat{H}_D^{1/4} \sim 0.87$  (bottom panel) to  $\hat{H}_D^{1/4} \sim 0.97$  (top panel) is evident as  $B_H$  increases; also the backscattered peak seen in the  $C_r$  plots as the second enhancement near about  $\hat{H}_D^{1/4} \sim 0.93$  in the lower plot of Figure (39) increases in a similar manner to the rather broad peak extending from  $\hat{H}_D^{1/4} \sim 1.06$  to  $\hat{H}_D^{1/4} \sim 1.15$  in the upper panel. This feature of shifting peak position as the primary field varies is consistent throughout the experimental work. These two Figures may be compared to Figures (11) through (13) of the numerical simulation for the "quad grid" model described earlier. Figure (40) is a plot of  $C_r$  vs  $\hat{H}^{1/4}$  in order to allow one to compare to the numerical plots presented earlier and the primary Equation (15). In this case and for earlier definitions,  $N+1$  refers to the number of neutral sheet crossings so, for example, for  $N=1$  and electron injection on the backscattered side (by definition), one expects a peak in the backscattered current relative to the forward scattered side;  $N=2$  would imply resonance in forward scattered collection, etc; note that  $N=0$  would imply a single crossing.

A similar behaviour is seen in Figures (41) and (42) which are a plot of the normalized forward-scattered current for two different values of the external field  $B_z$  for the case in which  $B_x$  is 5.6 gauss. In these plots the peaks have been expanded to show more clearly the energy shift as the external Helmholtz coil field is varied.

It should be pointed out that the numerical values of  $\hat{H}^{1/4}$  seen in Figure (40) cannot be used as the primary basis of comparisons to theory. Resonances on these scales are separated by  $\Delta\hat{H}^{1/4}$  values more on the order of 0.2 than 1 as predicted by the theory. The explicit dependence of  $N$  on the power of  $\hat{H}$  is closely associated with the perfectly realizable Harris field and is not expected to characterize scattering centers which in general show chaotic scattering dependence on initial conditions but do not have exactly this field form [Chen, 1993]. Also the normalized energy as seen in Equation (15) is a function not only of the field but also of the parameters  $b_n$  and  $\delta$  both of which are to some extent variable in the experiment;  $b_n$  varies with respect to position as discussed earlier and  $\delta$  is estimated to include finite effects of near-wire distortions in the field. The values of  $N$  are highly sensitive to the choices of these two parameters in the normalization; it is the resonance structuring itself and its dependence on the initial conditions of energy and magnetic field that determine chaotic scattering from the scattering center.

For comparison to predictions of the Harris model and the simulations we show in Figure (43) the explicit energy dependence of the first two scattering resonances on the ratio  $b_n$ . Figures 43(a) and 43(b) show numerical simulations and Figure 43(b) shows the analytic energy dependence of the Harris model. We note that the dependence of the energy separation of the two peaks on  $b_n$  is qualitatively similar to what is observed in the laboratory case explored above in Figure (38).

#### VL4.2 Collected Current as a Function of $y$

As the energy of the injected particle is increased the particles leave the current sheet at higher and higher values of the  $y$ -coordinate. This is due to the fact that increasing energy implies increasing numbers of neutral sheet crossings and therefore detected particles travel farther in the  $y$ -direction. This behaviour which was demonstrated in Table I for the numerical simulation in the quad grid model case can also be seen in Figure (44) in which we plot three different injection energies for the case of the Harris field simulation for  $B_x = 12$  gauss at low pitch angle. This figure shows the final  $y$ -position (whether collected by the back-scattered or the forward scattered plate) increasing with energy,  $E$ , and with  $N$ , where  $N+1$  is the number of  $z$ -plane crossings. These two quantities increase going from plate (a) through (c) of the Figure. The trajectories are stopped at the positions of the collector plates and with these dimensions one can see that even for the 5 keV case of part (c) the particle emerges within the boundaries of the grid region. Each of these injections corresponds to a nearly field aligned injection and the position of the electron gun is as it was in the experiment. Figure (45) shows the number of scattered particles at different  $y$ -levels of collection as a function of energy for the numerical simulation of the actual field configuration produced by the grid and shaping bar assembly. Again the current collection levels increase with increasing  $y$ . Plotted in Figure (46) is the centroid of experimental current collection as a function of beam energy. As mentioned earlier both forward and backward scattered collection plates are partitioned into 16 separate plates; for this study the plates were ganged into groups of four along the  $x$  direction producing 4 separate horizontal rows. Total collected current is then monitored to each row as a function of energy. For the case chosen Figure (46) shows the current collected by the first two (lowest) forward scattered collection plates. The straight lines drawn represent the best fit to indicate average behaviour. The behaviour of the centroid of current is a result of decreasing collected current as a percentage of total on the first plate while that collected on the upper plate shows a corresponding increase.

One might reasonably ask whether the observed increase in  $y$ -position is simply the result of an increased Larmor radius due to the energy increase. Since this increase should go as the square root of energy one would expect current collection to follow the  $1/2$  power law given by this equation and to observe a broadening of the average pattern of collected current but no shift in the center position. This is not consistent with the observations of Figure (46) which plot the centroid of collected current on the plate. Without the resonances as described above it is difficult to explain the shifting energy peak patterns observed.

Figure (47) shows a plot of the correlation factor  $C_r$  described above vs  $\hat{H}^{1/4}$  except that instead of plotting the back and forward scattered peaks as positive values, forward scattered peaks are plotted as negative values. In this presentation it is easier to isolate forward from back scattered contributions without suppressing either. The relatively high value of the external  $B_z$  field produces a small  $b_n$  component on the forward grid side and a much larger one on the backscattered side. This behaviour is seen in Figures (29) through (31) which are plotted for a different value of current in the grids.

### VII Scaling Considerations and Future Work

In making comparisons to the insitu measurements a key issue is how and to what extent the expected laboratory results may be related to the actual space environment. Although as mentioned we did not attempt to build a model system, the basic physical processes rely on scale sizes. The most



important quantities are the spatial scale lengths and their relationship to one another. The relevant physical parameters are: the particle gyroradius  $\rho$ , the radius of curvature of the field lines in the current sheet  $R_c$ , the current sheet thickness  $\delta$ , the field component ratio  $b_n$ , gyrofrequency  $\Omega_n$ , and the particle energy. Scaled values of typical neutral sheet parameters are listed in Table II using length scaling to the experimental basis [e.g., Faelthammar, 1974]. The particle dynamics is stochastic rather than adiabatic in the current sheet because the gyroradii of the particles can be comparable to the radius of curvature of the field lines in the current sheet. In the magnetotail, a large fraction of the ions are in the nonadiabatic regime under quiet-time conditions, a fact which has been known for some time [Speiser, 1965]. Some electrons are also in the nonadiabatic (and nonintegrable) regime [West et al., 1978a,b; Lyons, 1984]. For the modified Harris model, the radius of curvature at  $z = 0$  is  $R_c = b_n \delta$ . If  $\rho_n = R_c$ , then the motion is highly nonadiabatic. Note that  $R_c/\rho_n$  is a dimensionless statement. The resonance scaling law above is expressed in terms of the dimensionless normalized Hamiltonian. The relevant physical parameters are  $b_n$  which is the dimensionless ratio  $B_n/B_0$ ,  $\Omega_n = v/\rho_n$  and  $\delta$ . Thus the resonance condition can be directly scaled to the laboratory distribution functions. For example, the separation between two resonances  $N_1$  and  $N_2$  is, as treated in Section VI.1,  $\Delta(H'') = (mb_n^2 \Omega_n^2 \delta^2)^{1/4} (N_2 - N_1)$  [Burkhart and Chen, 1990]. It was also shown that the resonance peaks are strong for,  $H \leq H_1 = (1/2)b_n^{-2}$  and that the distribution resonance peaks should terminate for the condition  $H \geq H_2 = (1/2)b_n^{-4}$ . These properties are all expressed in terms of dimensionless parameters. Thus they are easily amenable to laboratory simulations.

In order to accomplish Objective (iii) of Section IIa, we point out that having once established the scaling law, Chen et al., [1990] have argued that the characteristic thickness of the current sheet could be measured by the particle distribution function outside the current sheet. For a thermal distribution of current carriers, they showed that,

$$\delta = \alpha^{-2} (8/\pi) \Gamma^2(7/4) \rho,$$

where  $\alpha$  is a factor of order unity to be determined,  $\Gamma$  is the gamma function and  $\rho$  is the Larmor radius of a thermal particle evaluated outside the current sheet ( $z > \delta$ ). This relationship is important because it relates the observed distribution function features obeying the scaling law to the thickness of the current sheet. The parameter  $\alpha$  will be calculated theoretically separately. Future laboratory experiment simulations can test this theoretical prediction under various controlled conditions. The result can be scaled straight forwardly to the magnetotail environment. Conversely, theoretical results can be scaled to the laboratory parameters to be tested. In this regard, we note that we have a computer code to construct surface of section plots for a given magnetic field configuration (not limited to the fields that may be generated in the space chamber). We expect to control surface of section plots for the experimental magnetic field geometry. In fact, we will run numerical studies of orbits in the laboratory fields.

We note that in the experimental setup, the magnetic field as seen in Figures (28) through (32) is not perfectly smooth and is  $x$ -dependent. Holland and Chen [1991], however, have shown that fluctuations in the magnetic and electric fields under quiet-time magnetotail conditions do not significantly affect the scaling behavior and that energy gain/loss ( $\Delta H$ ) for collisions comparable to the difference between two neighboring resonances must be present to significantly degrade the resonance effect. Relative to the  $x$ -dependence, Burkhardt and Chen [1991] have shown that if  $\rho_n < L_x$ , where  $L_x$  is the gradient scale length in the  $x$ -direction, then the scaling law is not affected. This condition again is expected to be well satisfied.

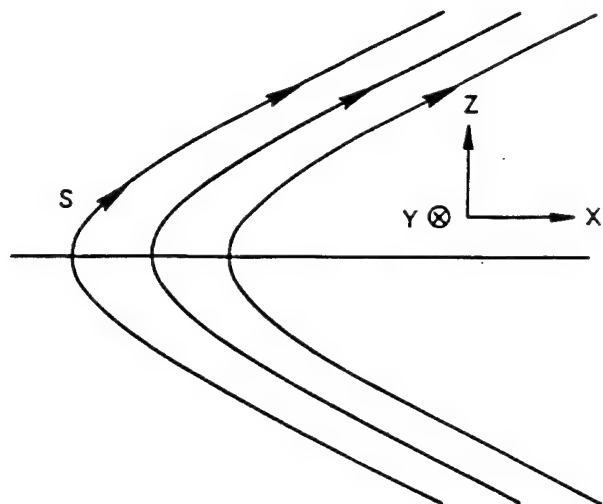
## ACKNOWLEDGEMENTS:

This work was funded by the Office of Naval Research. Also, we wish to acknowledge discussions with a number of people regarding this work. Useful suggestions were provided by Prof. D. Papadopolous, University of Maryland, Prof. W. Gekelman, UCLA and Prof. R. Kaufmann of the University of New Hampshire.

## VIII REFERENCES

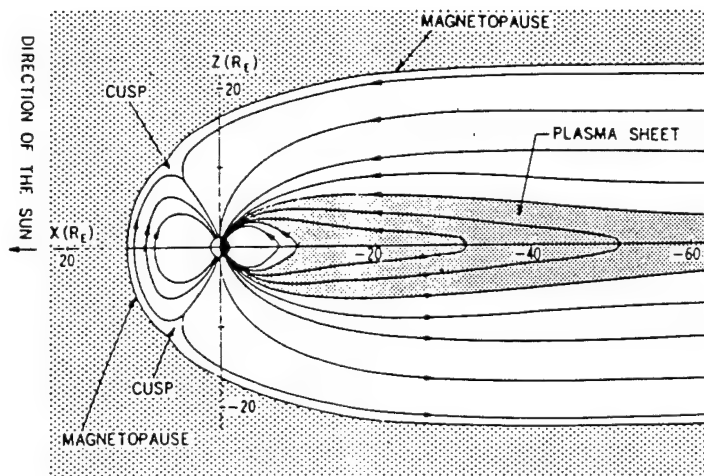
- Alekseyev, I.I., and A.P. Kropotkin, *Geomagn. Aeron., Engl. Transl.*, 10, 615, 1970.
- Alfven, H., L. Danielsson, C.-G. Faelthammar and L. Lindberg, *Proc. Plasma Space Sci. Symp.*, the Catholic University of America, Washington, DC, 1963.
- Alfven, H., NATO advanced study institute held in Bad Homburg, Germany, p.33, Plenum Press, New York, July 1964.
- Alport, M.J., S.L. Cartier, and R.L. Merlino, *J. Geophys. Res.*, 91, 1599, 1986.
- Ashour-Abdalla, M., J. Berchem, J. Buechner, and L.M. Zelenyi, *Geophys. Res. Lett.*, 17, 2317, 1990.
- Block, L.P., *Planet. Sp. Sci.*, 15, 1479, 1967.
- Block, L.P., *Tellus*, 7, 65, 1955.
- Block, L.P., *Tellus*, 8, 234, 1956.
- Buechner, J. and L.M. Zelenyi, *Phys. Lett. A*, 18, 395, 1986.
- Buechner, J. and L.M. Zelenyi, *J. Geophys. Res.*, 94, 11821, 1989.
- Burkhart, G.R. and J. Chen, *J. Geophys. Res.*, 96, 14033, 1991.
- Chen, J. and P.J. Palmadesso, *J. Geophys. Res.*, 91, 1499, 1986.
- Chen, J., G.R. Burkhart, and C.Y. Huang, *Geophys. Res. Lett.*, 17, 2237, 1990a.
- Chen, J., H.G. Mitchell, and P.J. Palmadesso, *J. Geophys. Res.*, 95, 15141, 1990b.
- Chen, J., *Phys. Fluids B*, 5, 2663, 1993.
- Cowley, S.H.W., *Cosmic Electrodyn.*, 2, 90, 1971.
- Doxas, I., W. Horton, K. Sandusky, T. Tajima, and R. Steinolfson, *J. Geophys. Res.*, 95, 12033, 1990.
- Eastwood, J.W., *Planet. Sp. Sci.*, 20, 1555, 1972.
- Faelthammar, C.-G., *Sp. Sci. Rev.*, 15, 803, 1974.
- Fahleson, U., *Planet. Sp. Sci.*, 15, 1489, 1967.
- Gekelman, W., 86, 659, 1981.
- Hairapetian, G. and R.L. Stenzel, *Phys. Rev. Lett.*, 65, 175, 1990.
- Holland, D.L. and J. Chen, *Geophys. Res. Lett.*, 18, 1579, 1991.
- Horton, W. and T. Tajima, *Geophys. Res. Lett.*, 17, 123(1990).
- Huba, J.D., J. Chen, and R.R. Anderson, *J. Geophys. Res.* (1991).
- Hutchinson, I.H., *Principles of Plasma Diagnostics*, Cambridge Univ. Press, 1987.
- Kaufmann, R.L., D.J. Larson, P. Beidel and C. Lu, *J. Geophys. Res.*, 98, 9307, 1993.
- Kaufmann, R.L., D.J. Larson, P. Beidel and C. Lu, *J. Geophys. Res.*, 98, 9321, 1993.
- Kaufmann, R.L. and C. Lu, *J. Geophys. Res.*, 98, 15447, 1993.
- Kawashima, N. and S. Mori, *Phys. Fl.*, 8, 378, 1965.
- Koepke, M. and W.A. Amatucci, *Phys. Rev. Lett.*, 72, 3355, 1994.
- Lyons, L.R., *J. Geophys. Res.*, 89, 5479, 1984.
- Lyons, L.R. and T.W. Speiser, *J. Geophys. Res.*, 87, 2276, 1982.
- Martin, R.F., *J. Geophys. Res.*, 91, 11985, 1986.

Pellat, R., Phys. Fluids, 22, 381, 1979.  
 Schindler, K., Rev. Geophys., 7, 51, 1969.  
 Sonnerup, B.U.O., J. Geophys. Res., 76, 8211, 1971.  
 Speiser, T.W., J. Geophys. Res., 70, 4219, 1965.  
 Speiser, T.W., J. Geophys. Res., 72, 3919, 1967.  
 Speiser, T.W., and L.R. Lyons, J. Geophys. Res., 89, 147, 1984.  
 Stenzel, R.L. and W. Gekelman, J. Geophys. Res., 86, 649, 1981.  
 Stern, D., and P. Palmadesso, J. Geophys. Res., 80, 4244, 1975.  
 Swift, D., J. Geophys. Res., 82, 1288, 1977.  
 Wagner, J.S., J.R. Kan, and S.I. Akasofu, J. Geophys. Res., 84, 891, 1979.  
 Walker, D.N., J. Geophys. Res., 91, 3305, 1986.  
 Walker, D.N., P.K. Chaturvedi, M. Singh, P. Rodriguez and C.L. Siefring, J. Geophys. Res., 96, 3589, 1991.  
 West, H.I., R.M. Buck, and M.G. Kivelson, J. Geophys. Res., 83, 3805, 1978a.  
 West, H.I., R.M. Buck, and M.G. Kivelson, J. Geophys. Res., 83, 3819, 1978b.



Schematic drawing of the Harris-type magnetic field (equation (1)) and the coordinate system. The line segment  $s$  measures the distance from  $Z = 0$  along the magnetic field lines.

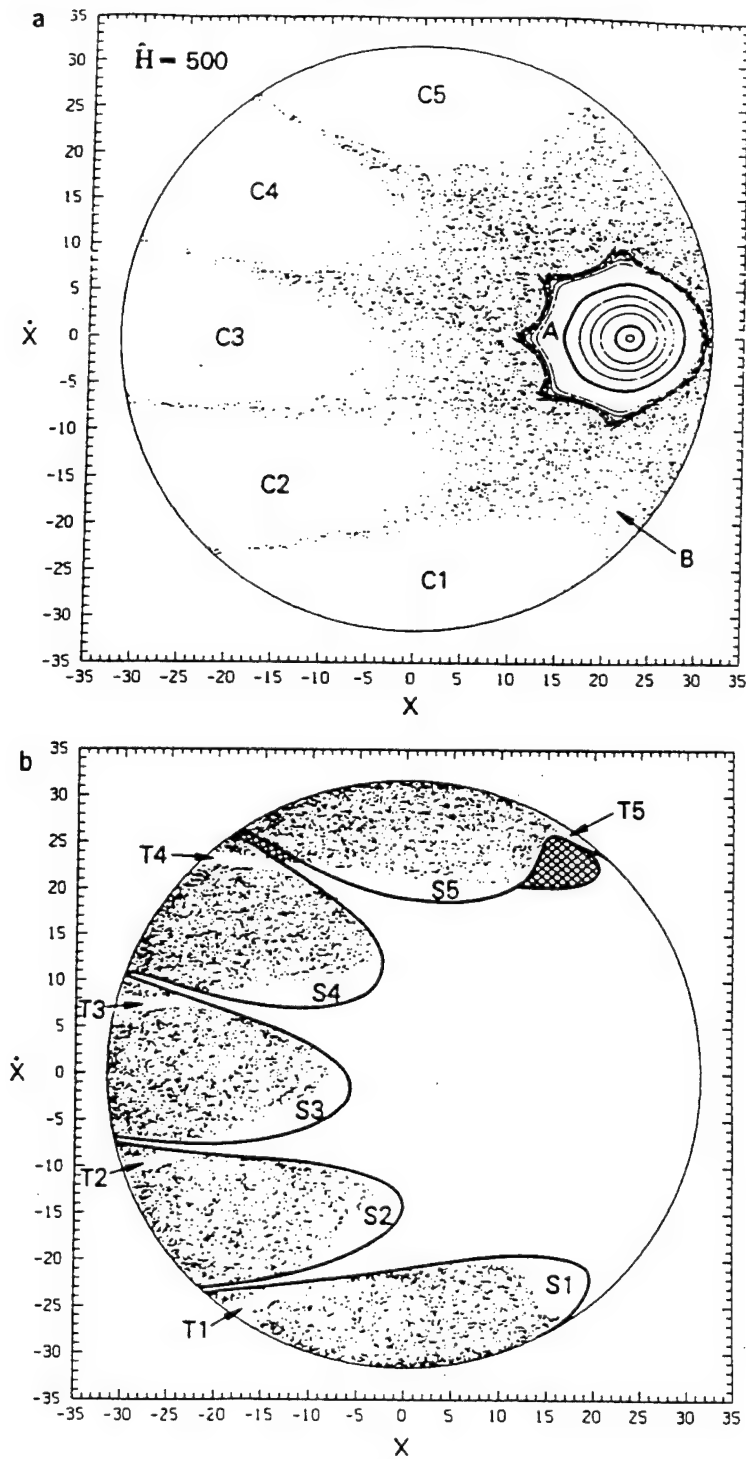
Figure (1)



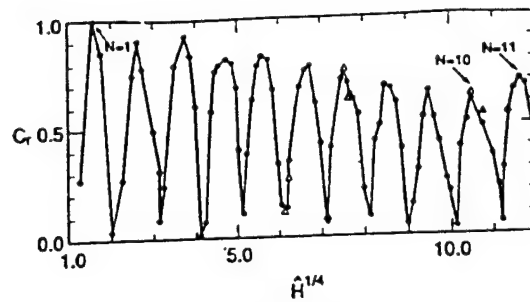
Schematic illustration of the noon-midnight section of the magnetosphere.

Figure (2)

Figure (3)

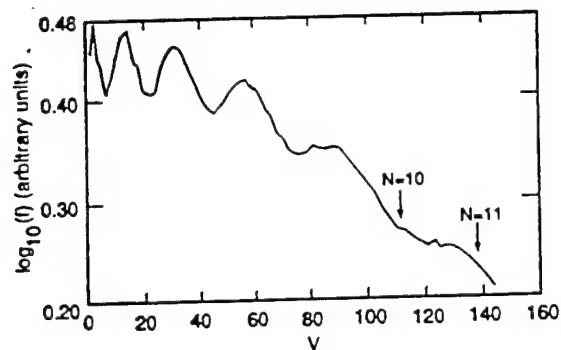


Surface of section plots for the Harria-type field with  $b_s = 0.1$  and  $\hat{H} = 500$ . (a) Representative integrable orbits in region A and stochastic orbits in region B; 60,000 points. (b) Transient orbits, showing the substructures in regions C1-C5; 42,000 points.



Plot of the coherence factor  $C_r$  versus  $\hat{H}^{1/4}$ .  $b_n = 0.05$ . The number of orbits for each energy is 355 (solid circle) or 598 (triangle). Straight lines are drawn between points. Peaks for  $N = 1, 10$  and  $11$  are shown.

Figure (4)



A model steady-state distribution function  $f(v)$  at  $z = +38$  with  $b_n = 0.05$ .  $f_1 > f_2$  is assumed.

Figure (5)

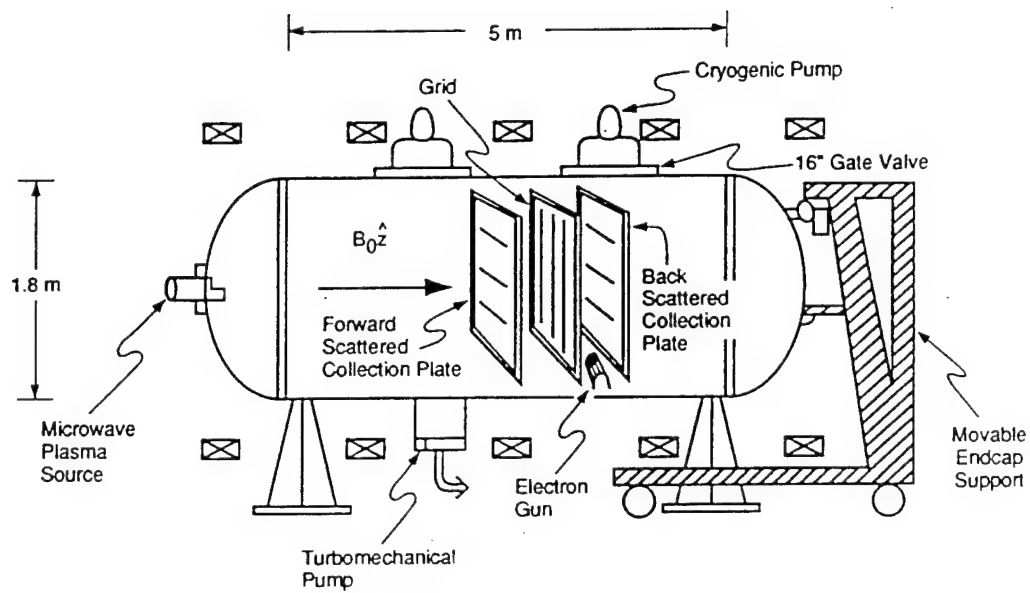


Figure (6)



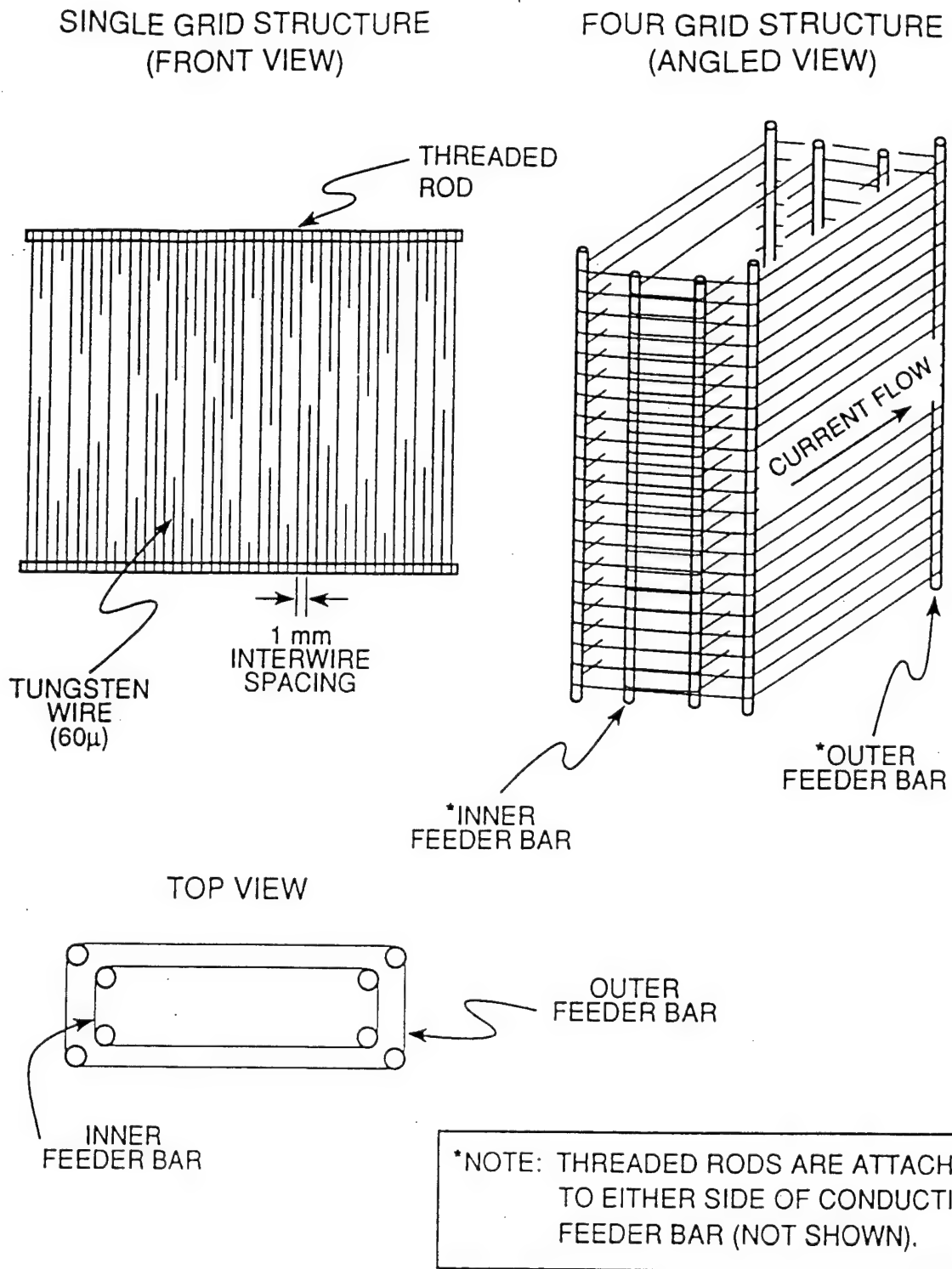
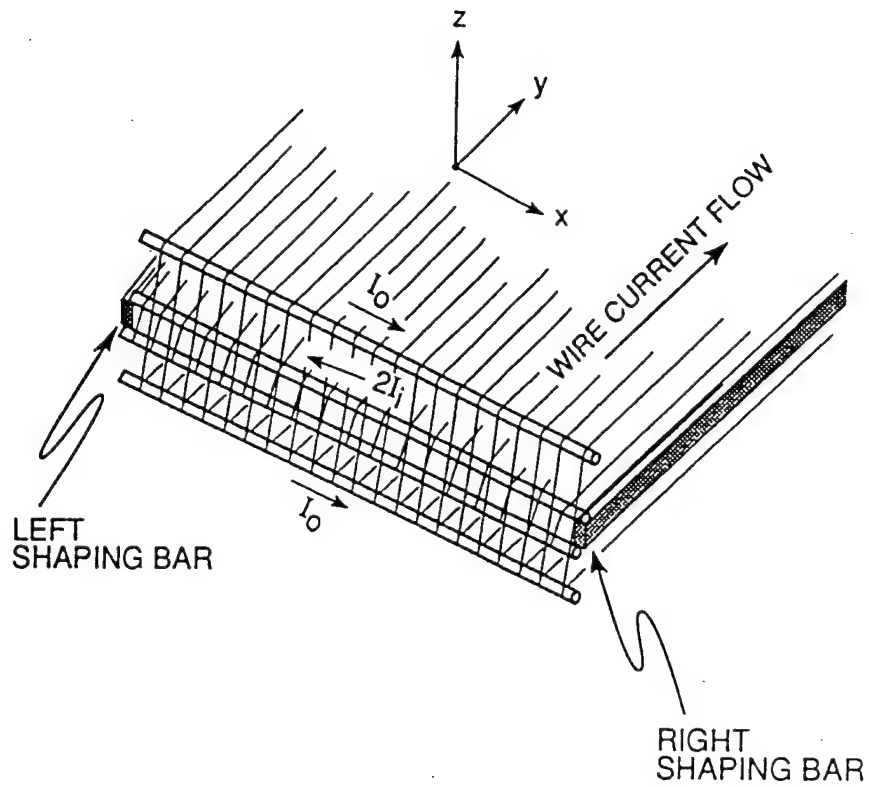


Figure (7)



Grid showing shaping bars,  
feeder bar current directions, and  
orientation.  $z$  is along chamber  $z$  axis.  
Feeder bars are not shown.

Figure (8)

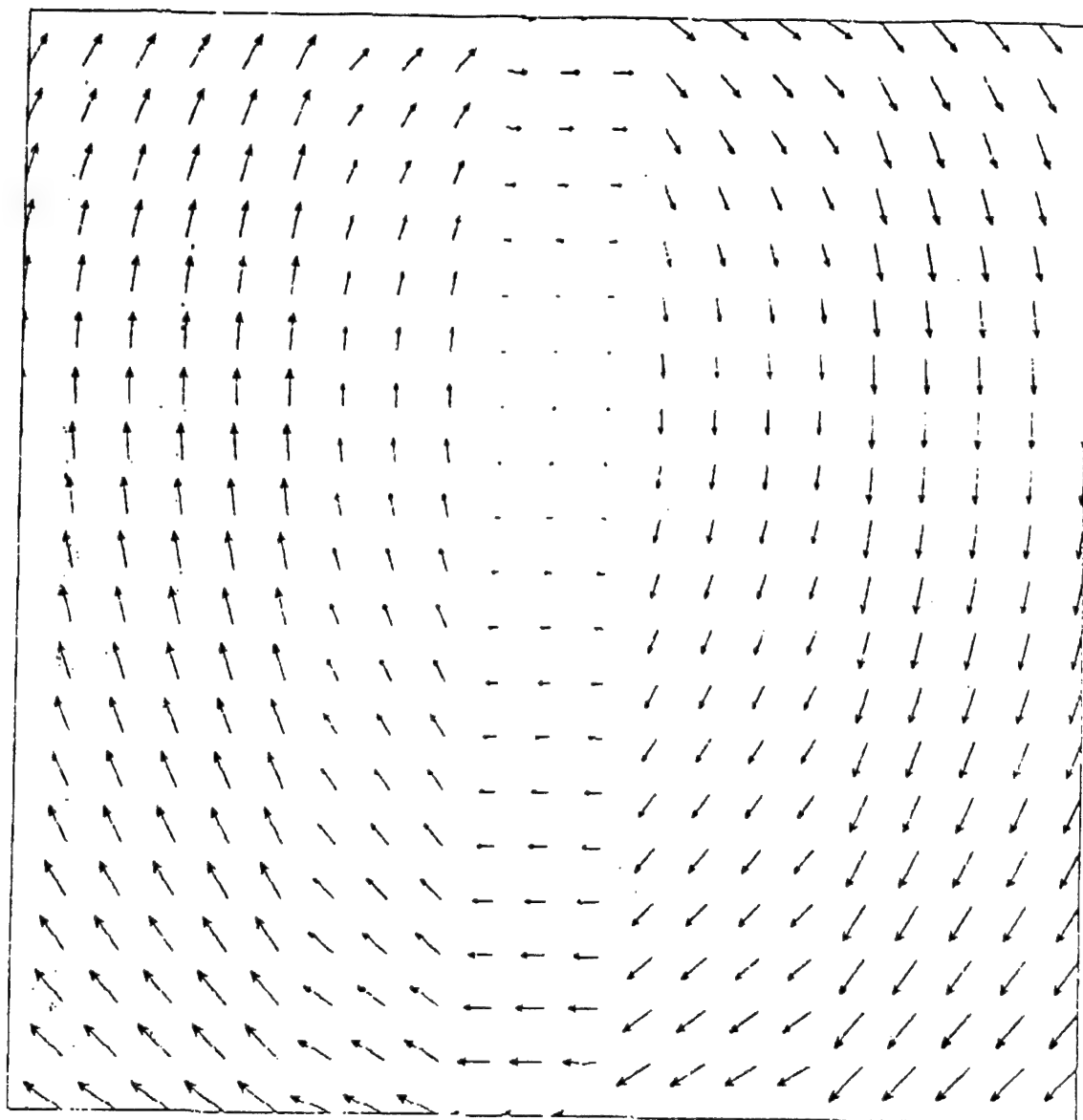


Figure (9)

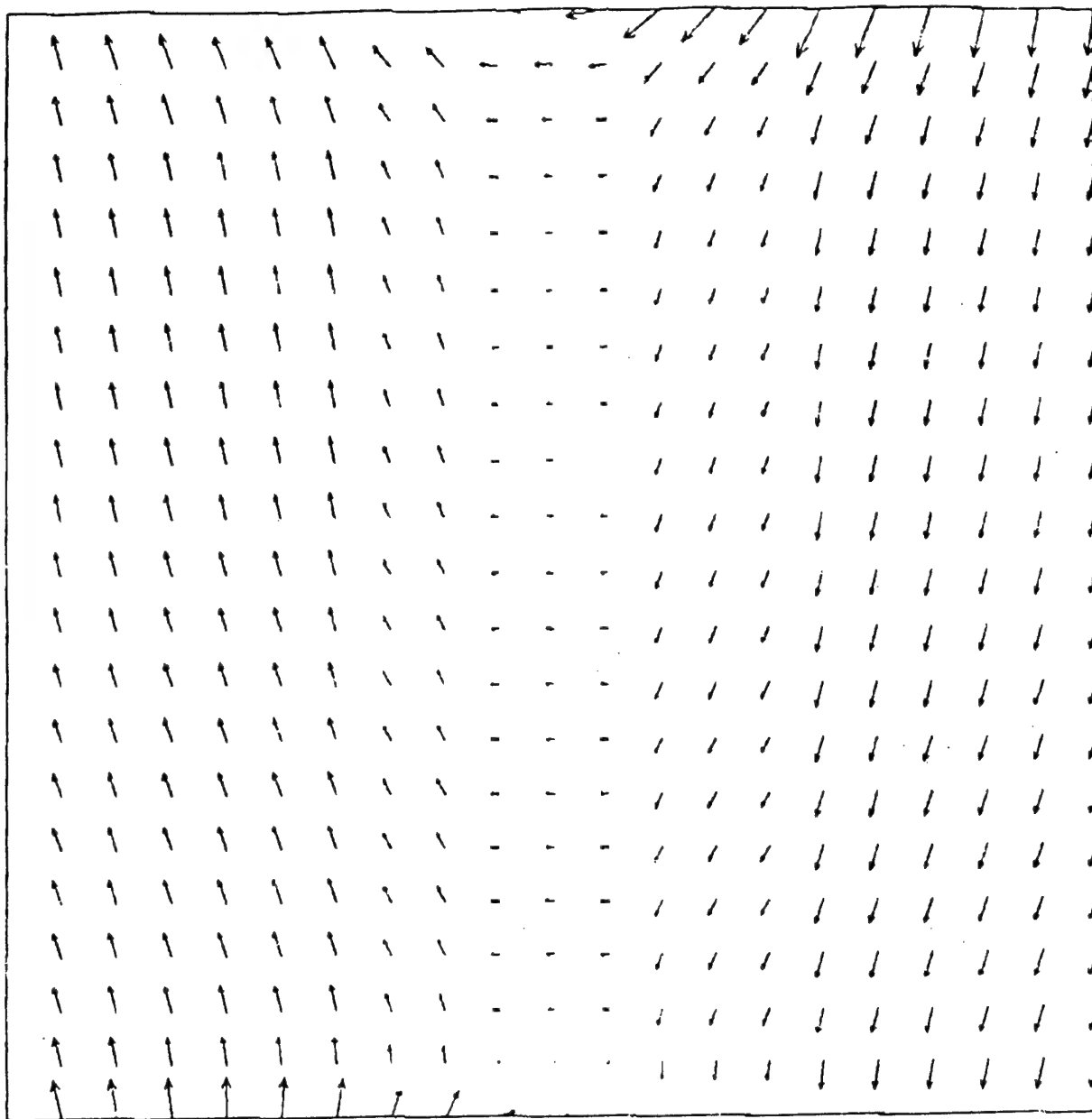
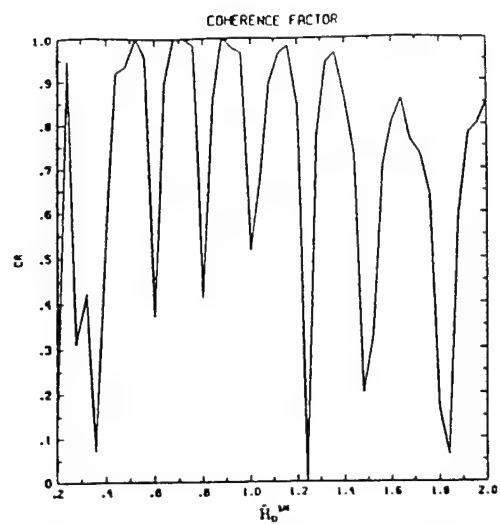
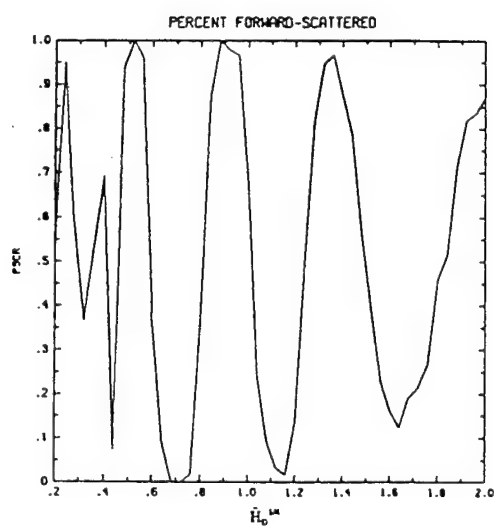


Figure (10)



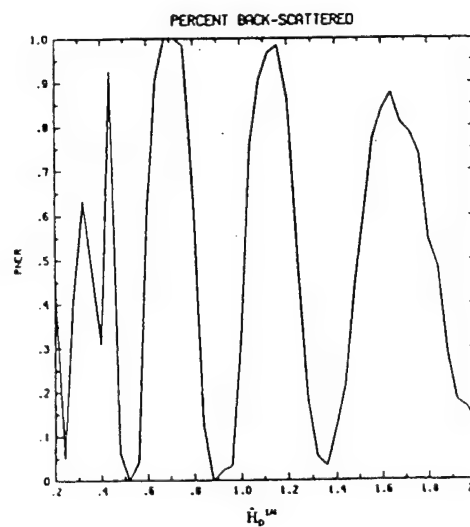
Plot of Coherence factor CR versus  $\hat{H}_0^{1/4}$

Figure (11)



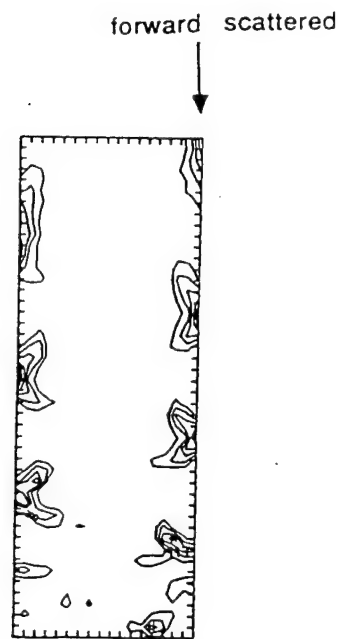
Percentage of particles forward scattered versus  $\hat{H}_0^{1/4}$

Figure (12)



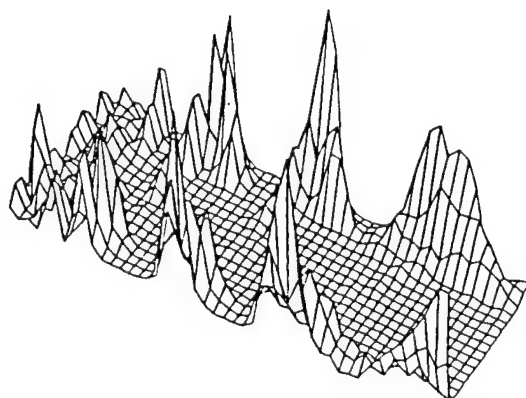
Percentage of particles backward scattered versus  $\hat{H}_0^{1/4}$

Figure (13)



Electron scattering amplitudes versus  
pitch angle

Figure (14)



Electron scattering amplitudes versus  
pitch angle - 3 dimensional view

Figure (15)

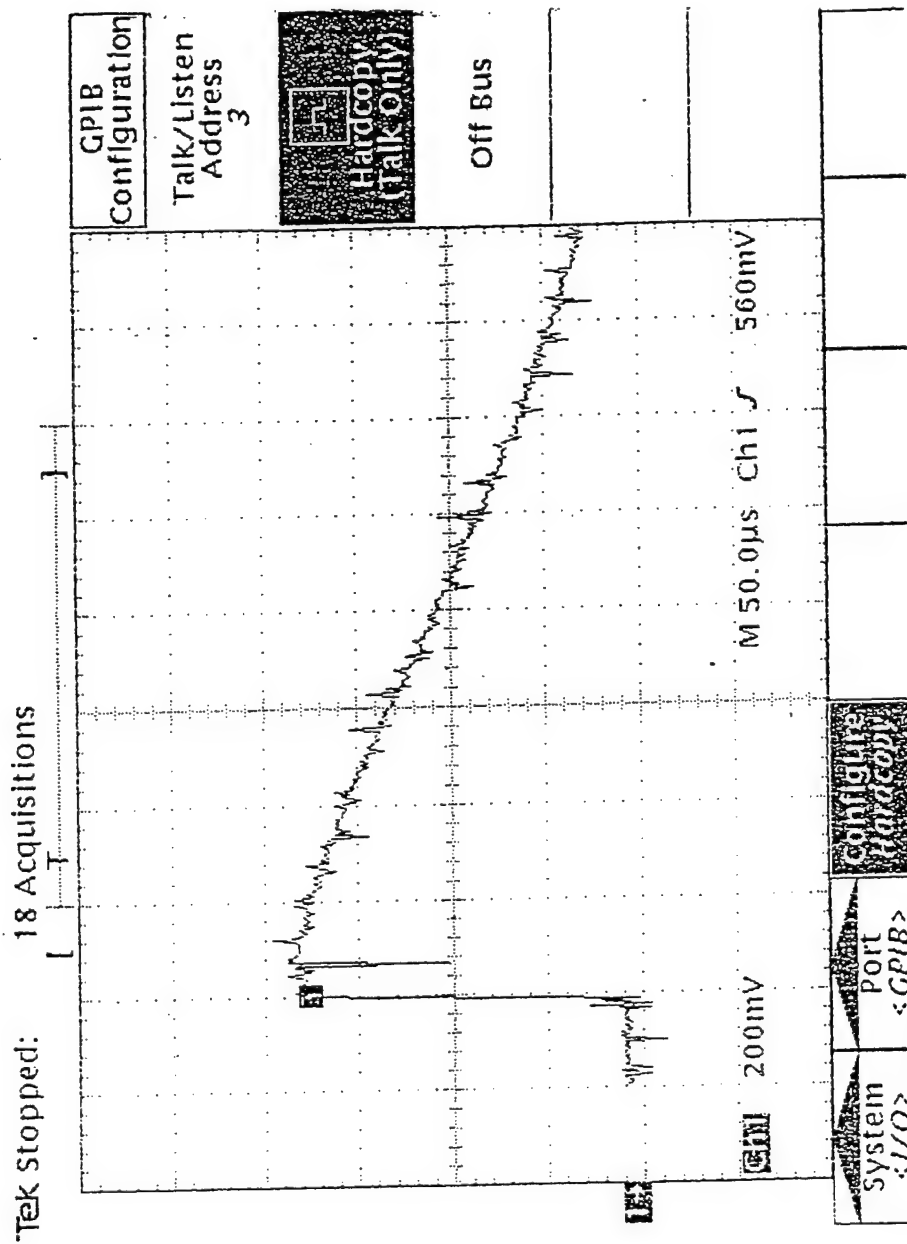


Figure (16)

# SPSC SCHEMATIC WITH HARRIS TYPE FIELD

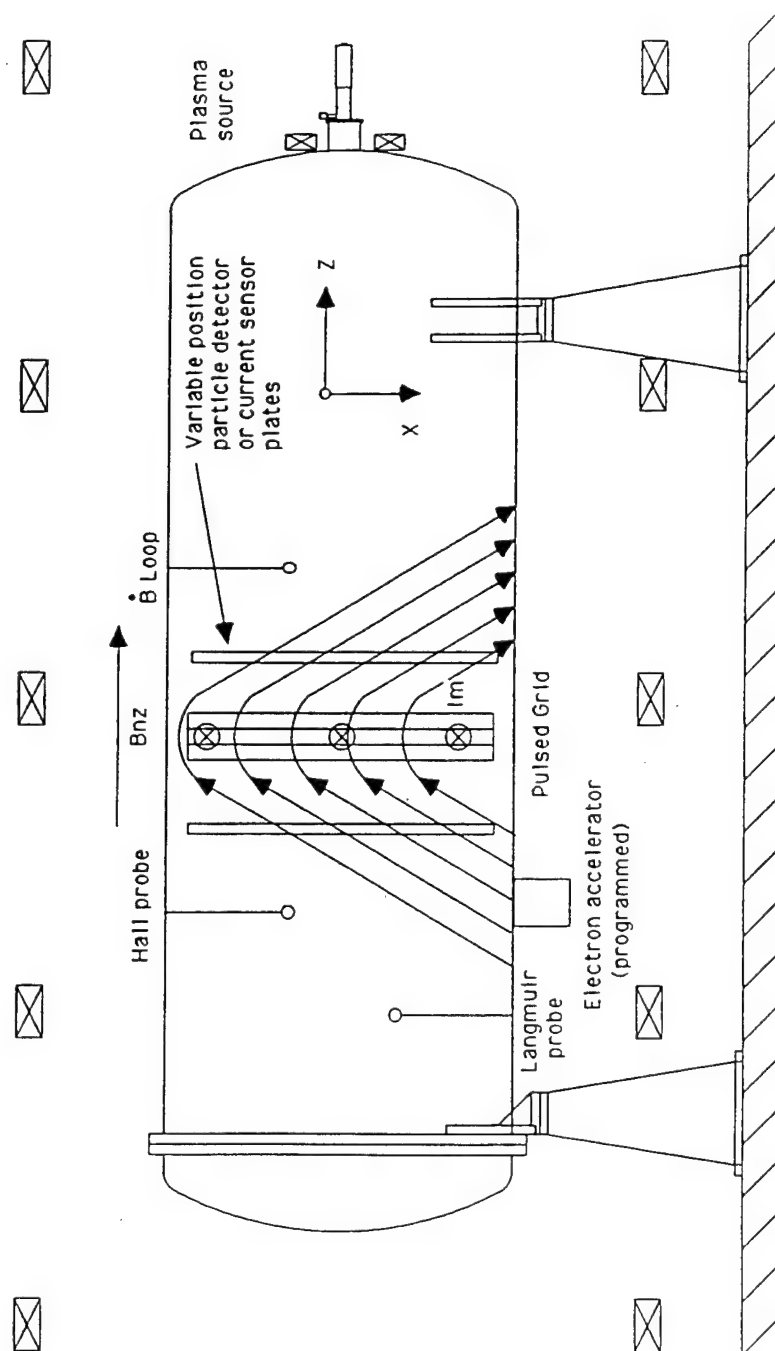
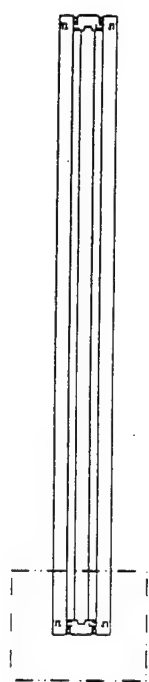
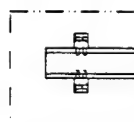
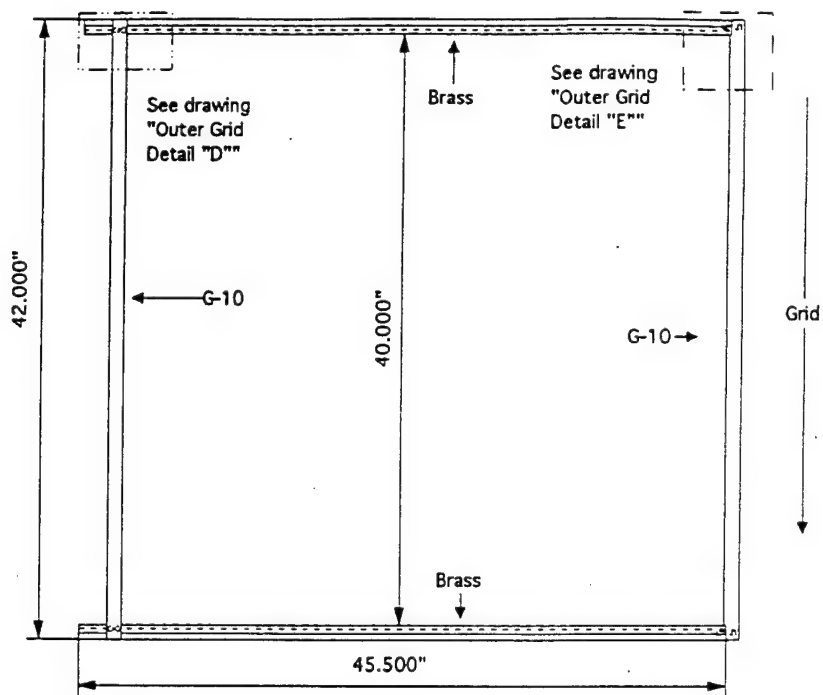


Figure (17)

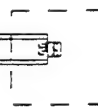




See drawing  
"Outer Grid  
Detail "A""



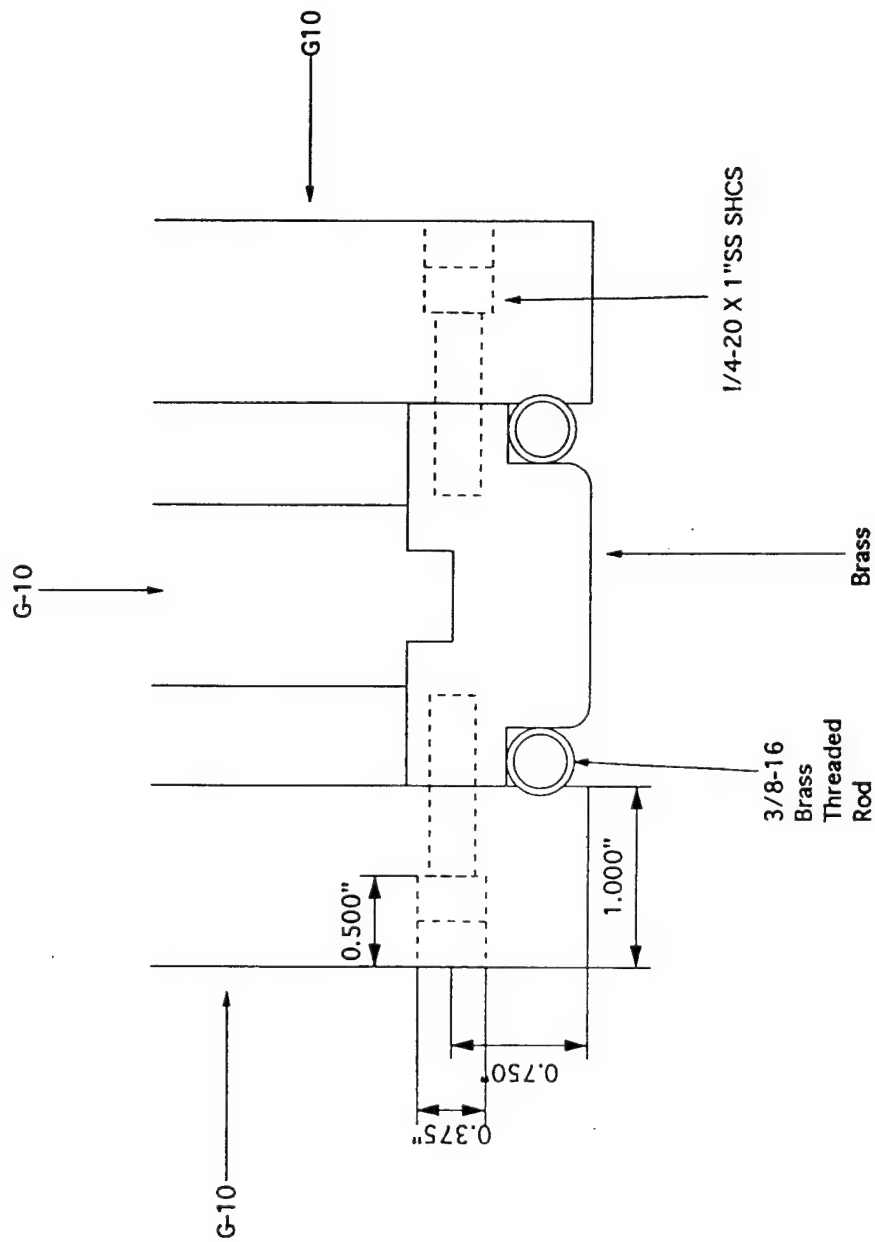
See drawing  
"Outer Grid  
Detail "B""



See drawing  
"Outer Grid  
Detail "C""

Figure (18)

Outer Grid I



Outer Grid  
Detail "A"

Figure (19)

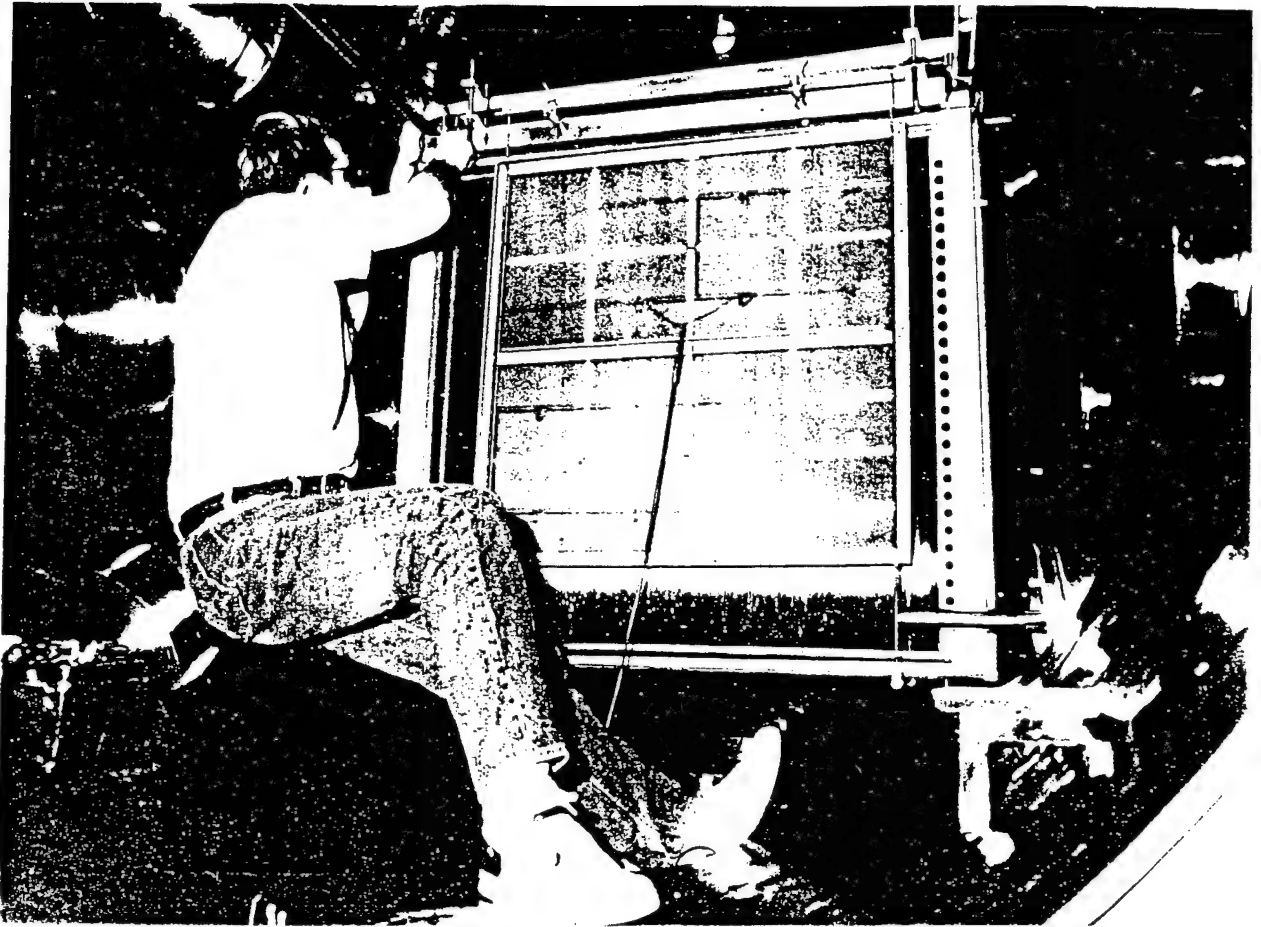
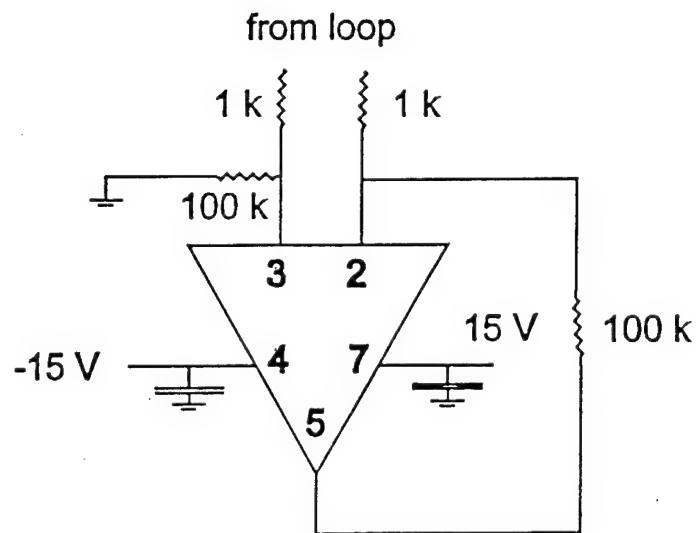
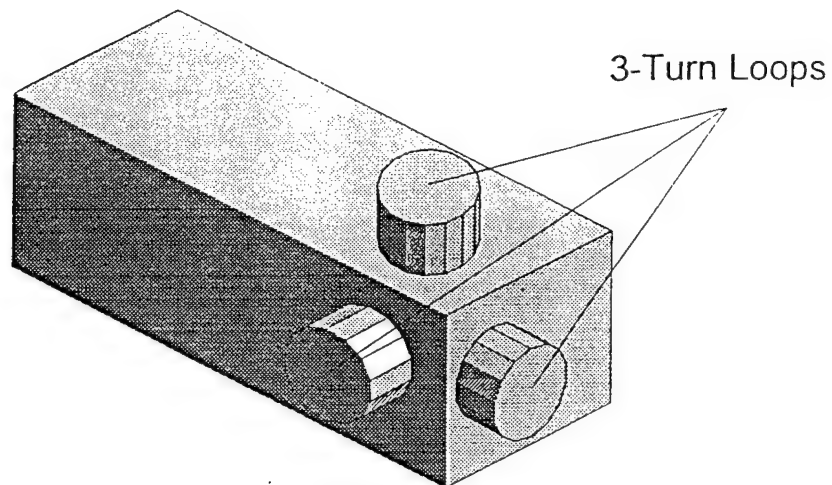


Figure (20)

# 3 Axis B-dot Probe



Op Amp is Burr Brown  
opa 620  
All resistors 1%

Figure (21)

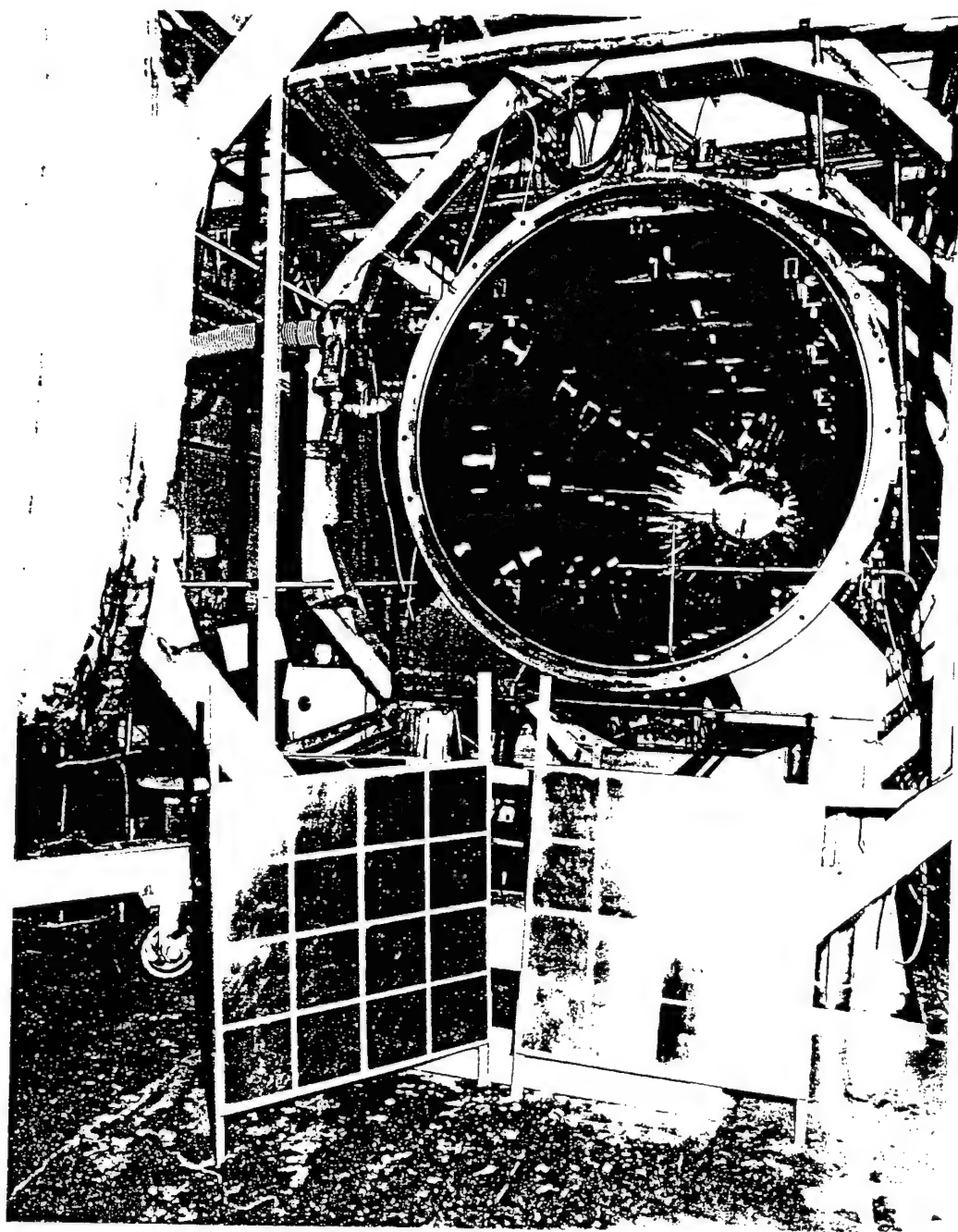


Figure (22)

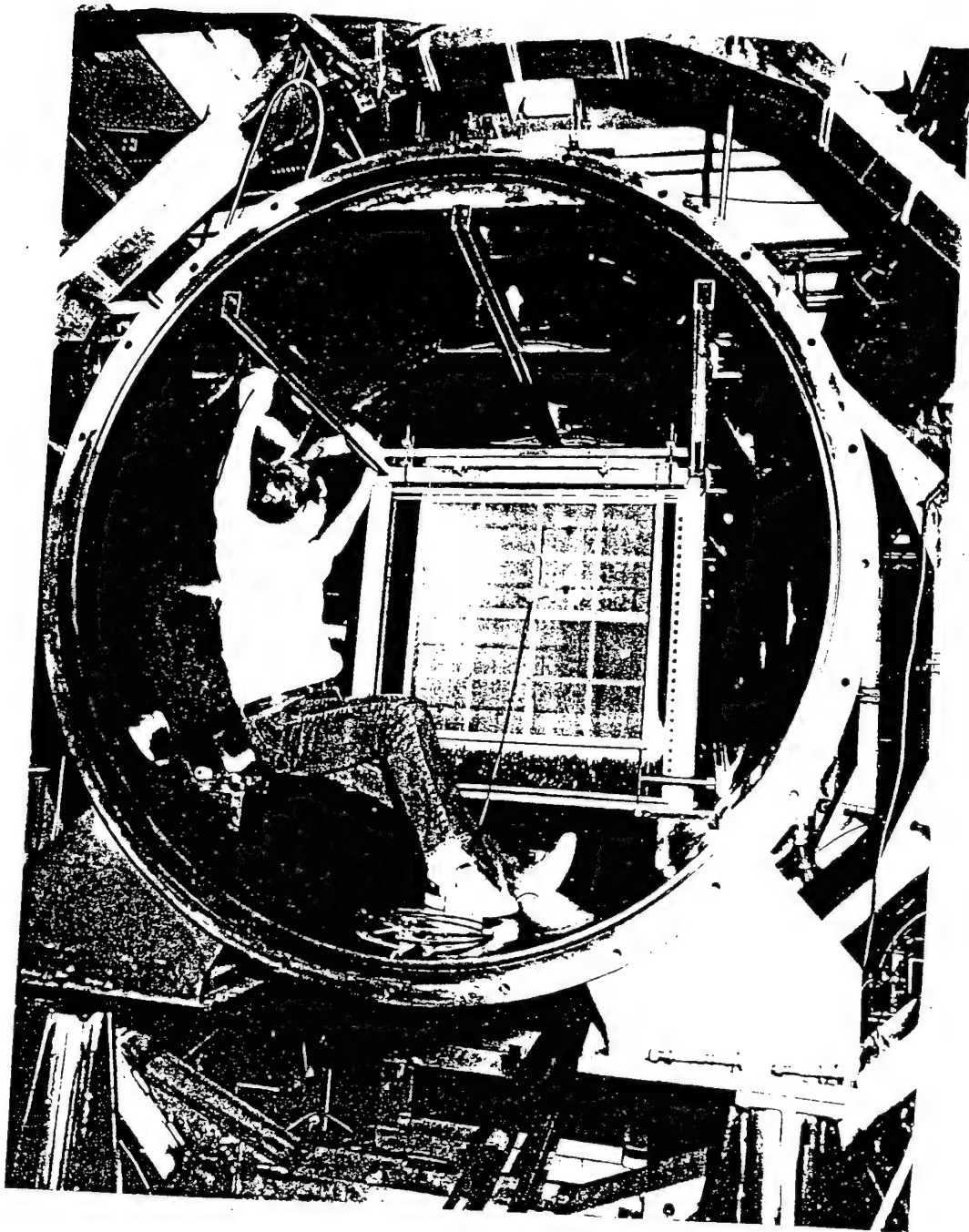
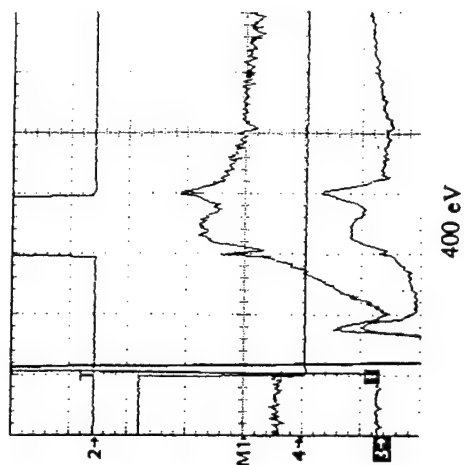


Figure (23)



$B_H = 4$  gauss  
 $B_A = 5$  gauss

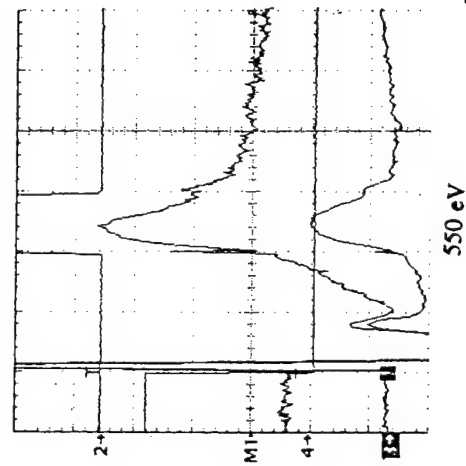
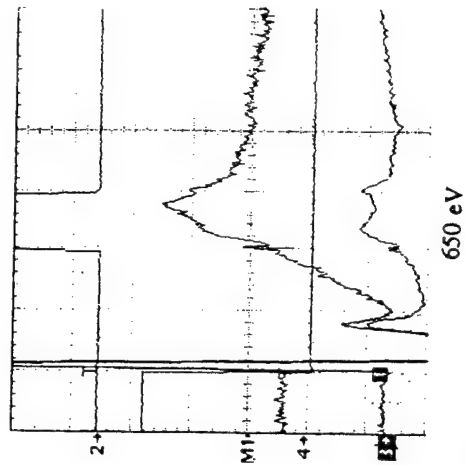


Figure (24)

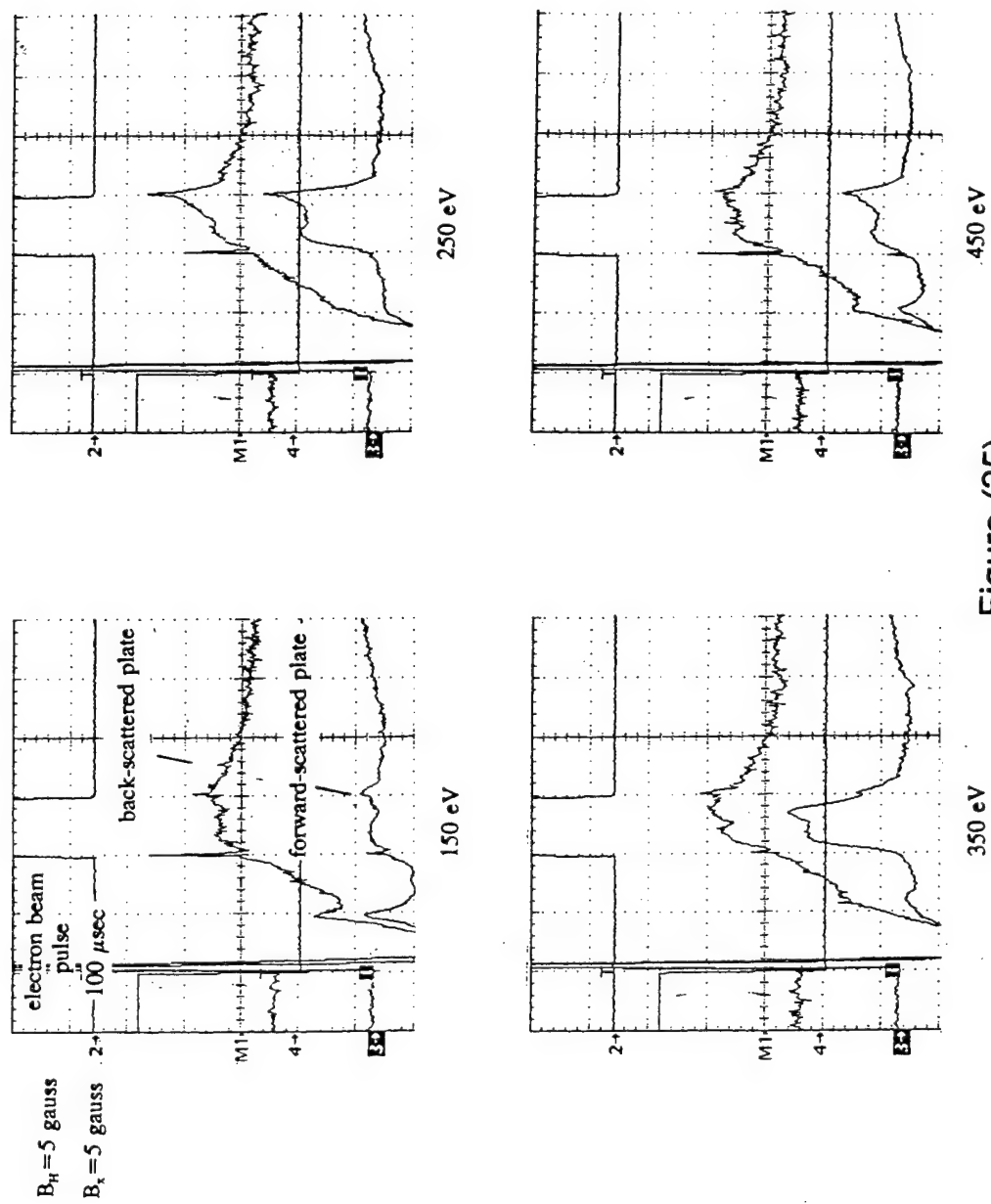
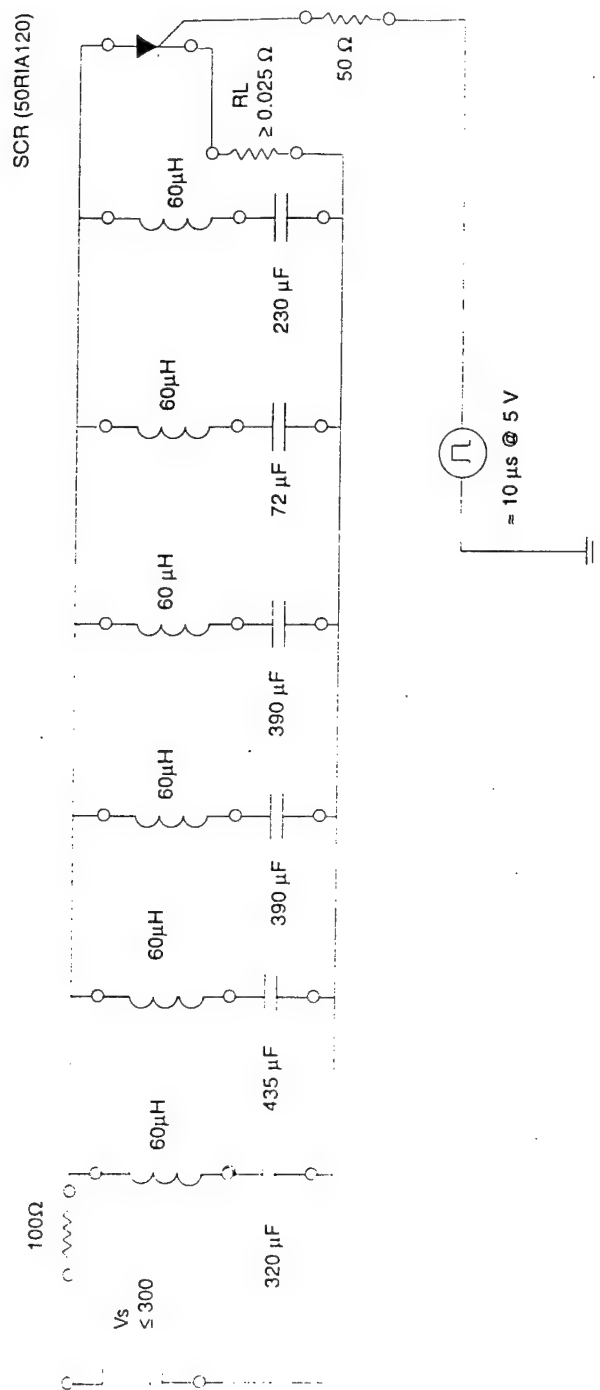


Figure (25)



PULSE FORMING NETWORK FOR B FIELD GRIDS  
USED IN CHAOS EXPERIMENT



Dwight Duncan  
4/12/93

Figure (26)

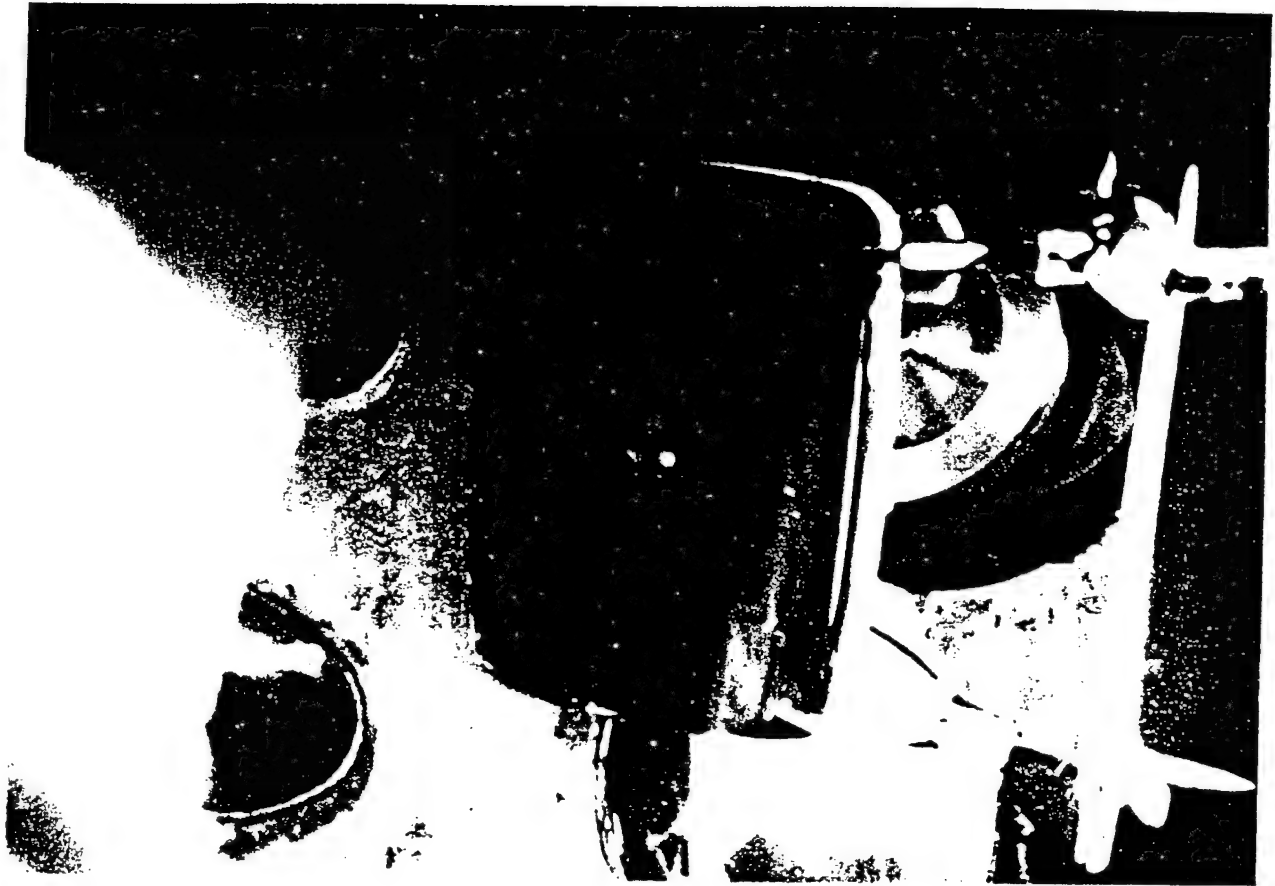


Figure (27)

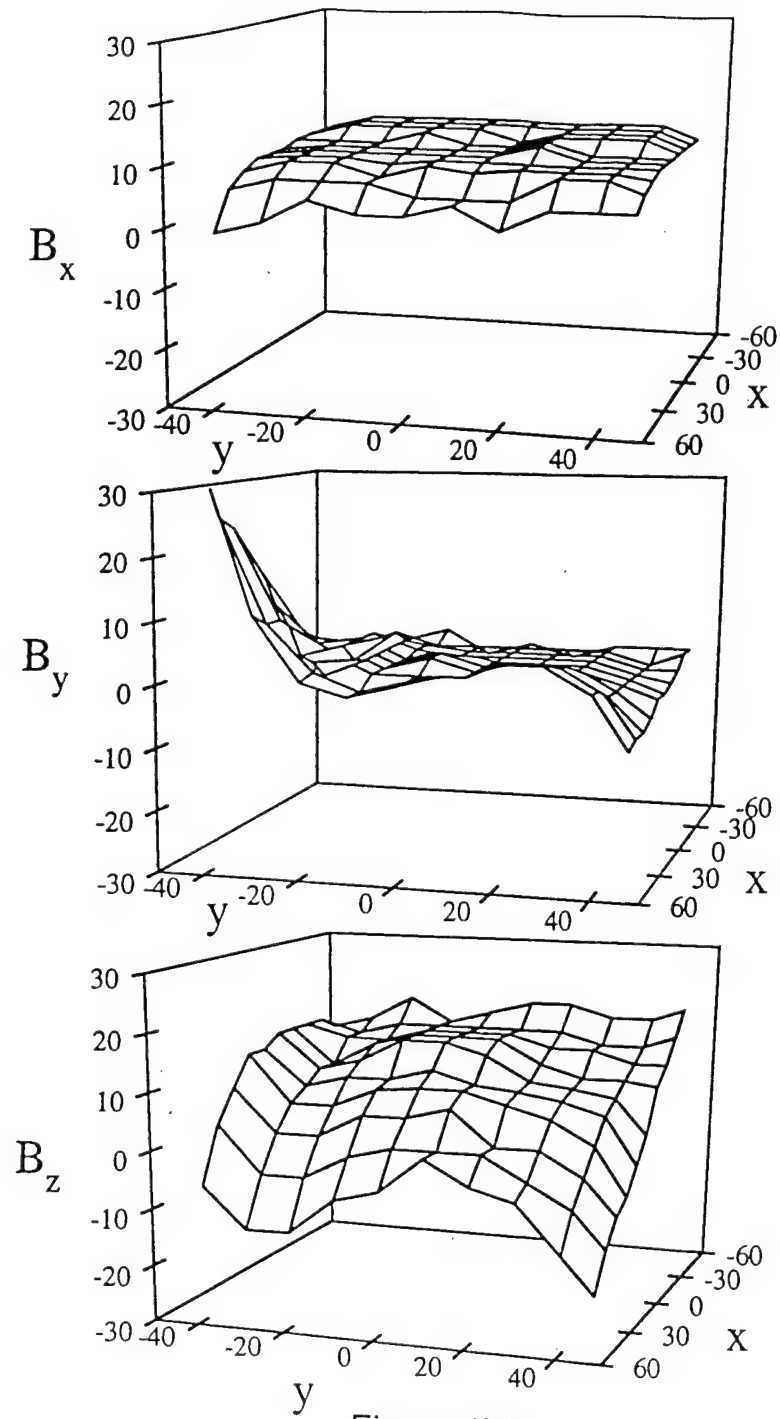


Figure (28)

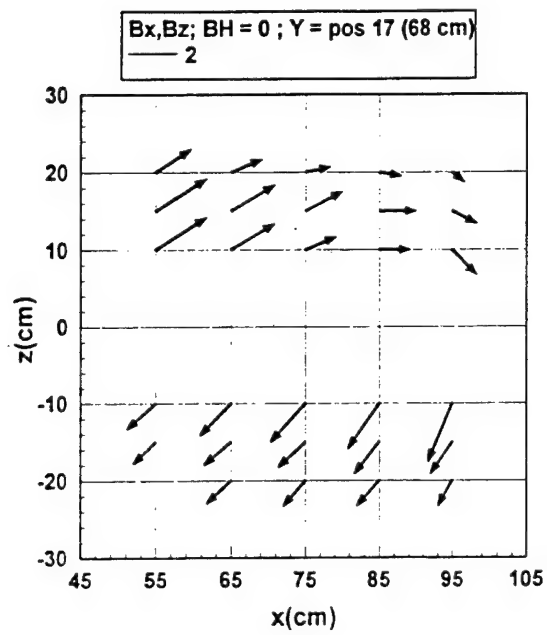
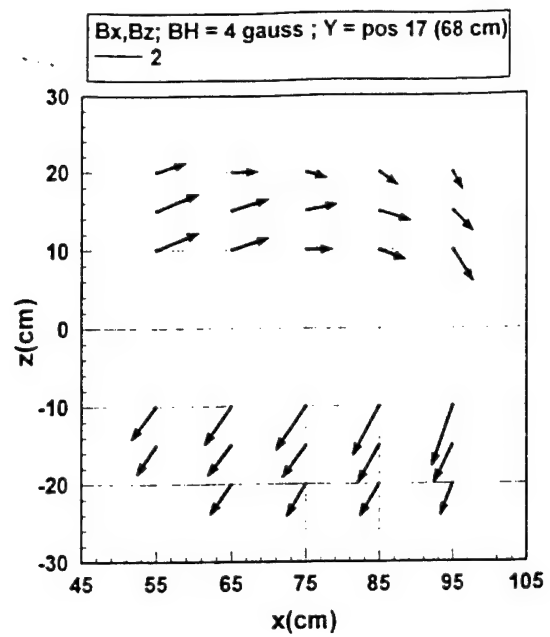
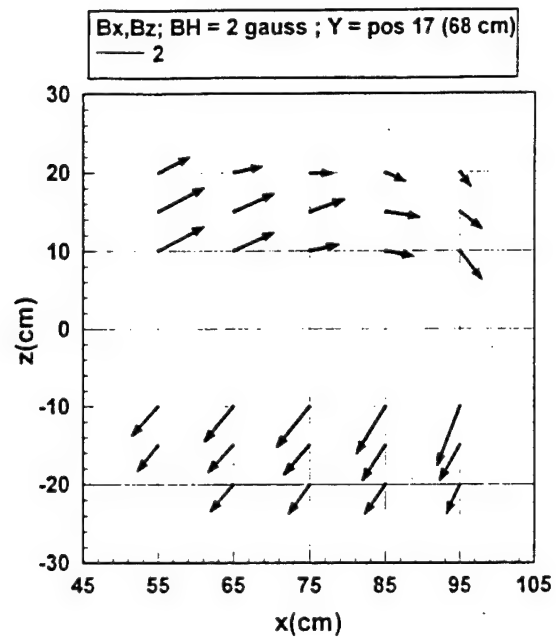


Figure (29)



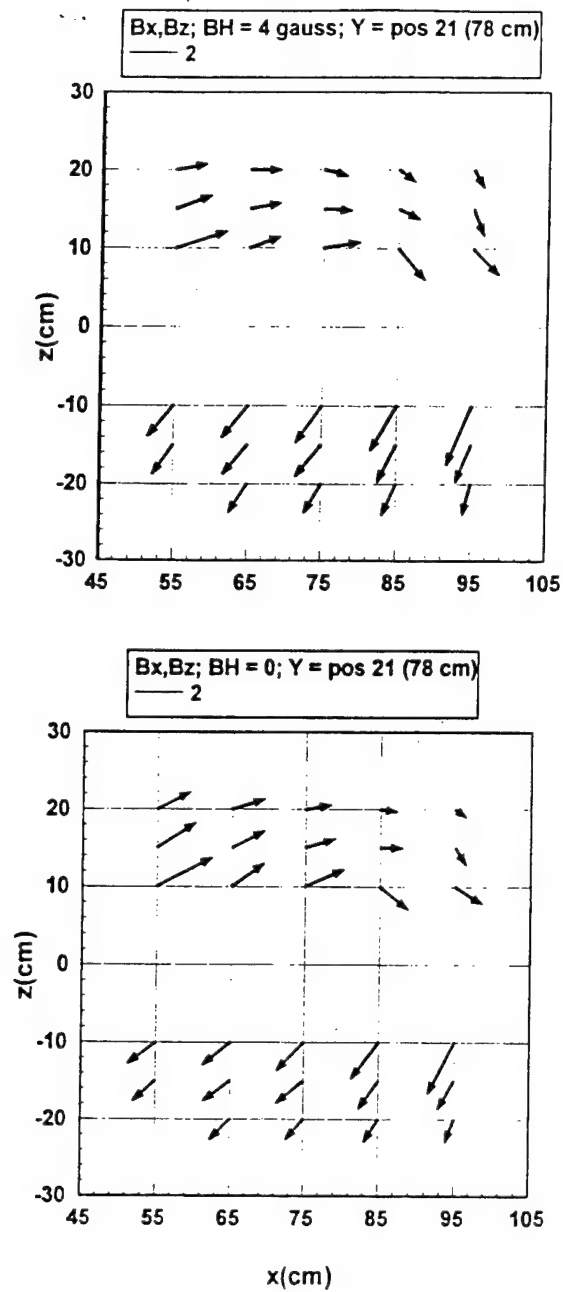


Figure (30)

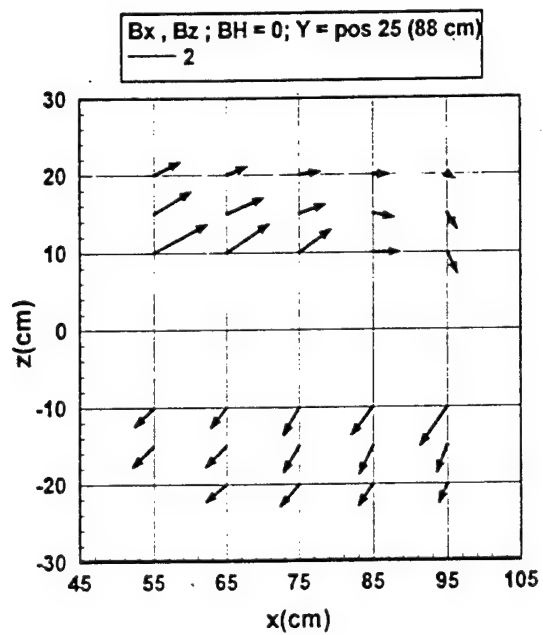
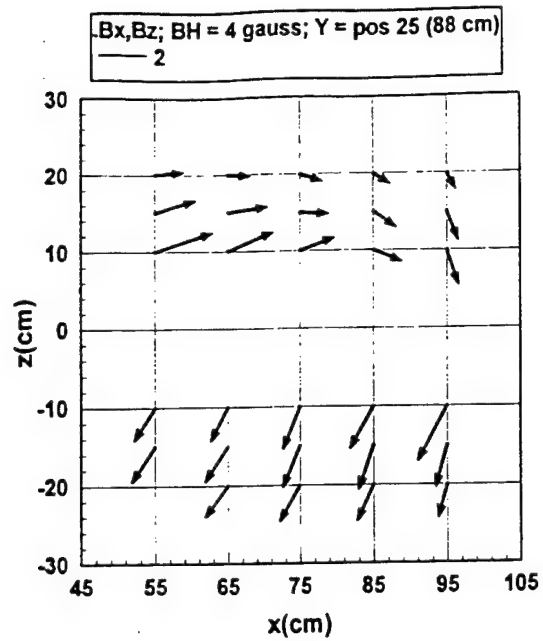


Figure (31)

B MMT - B(DOT) LOOPS-XZ PLANE

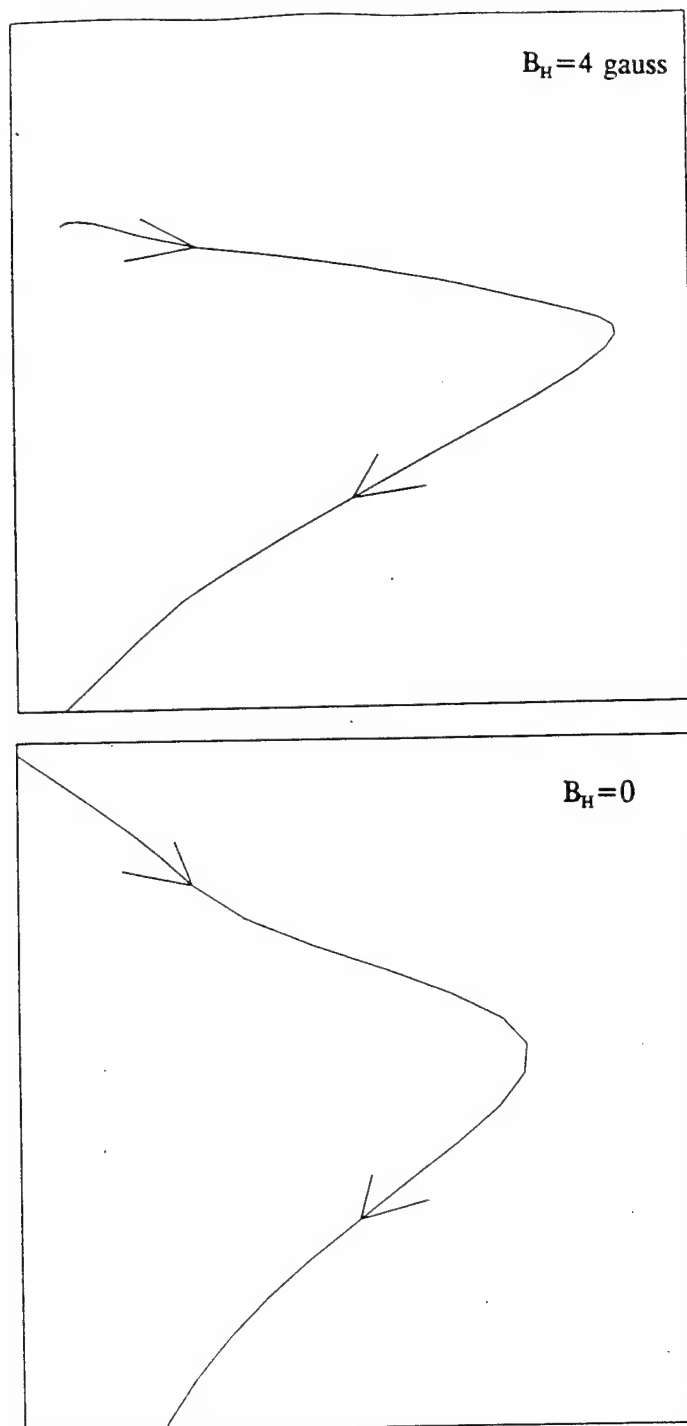


Figure (32)



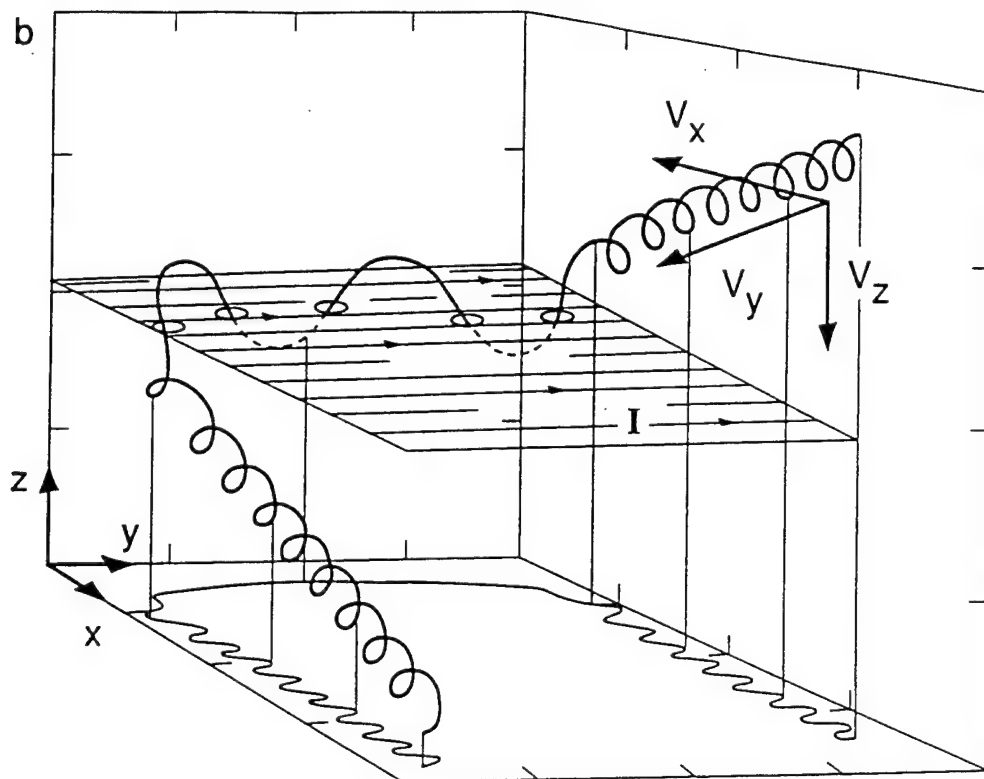


Figure (33)

Z-Y PLANE PROJECTION OF INJECTION  
VELOCITY NORMAL TO B

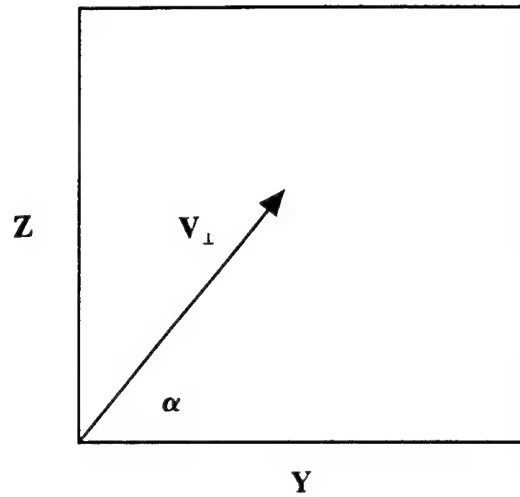


Figure (34)

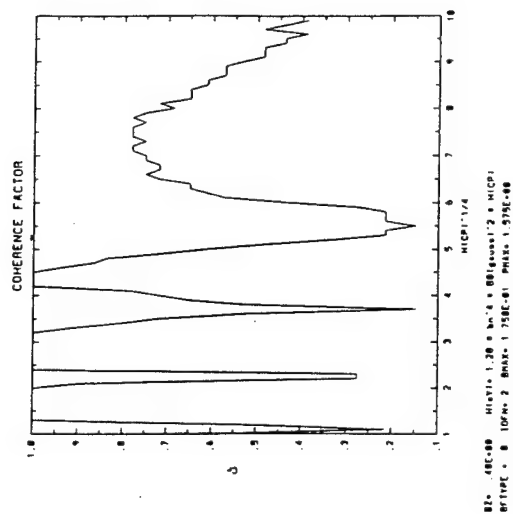
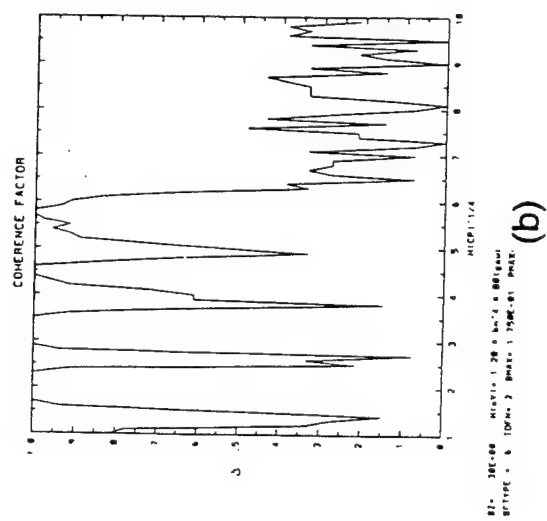
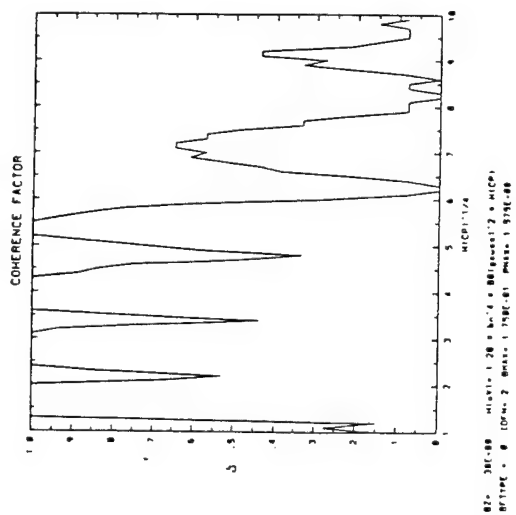
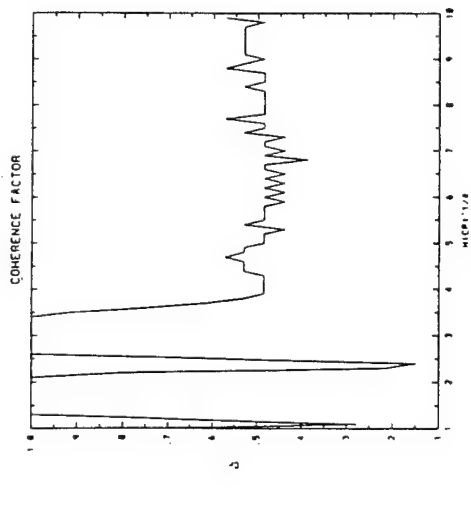
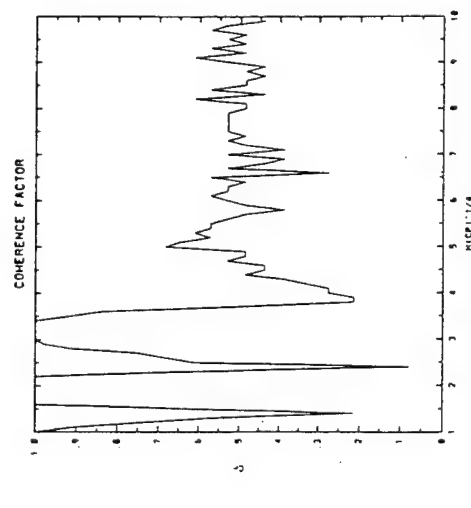


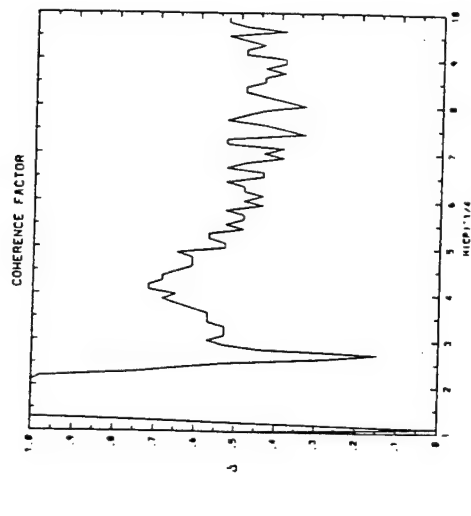
Figure (35)



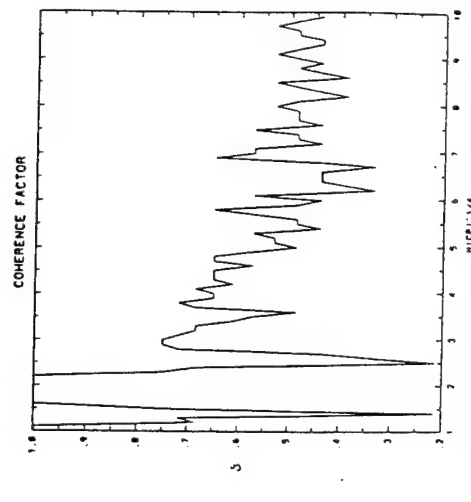
(a)



(b)

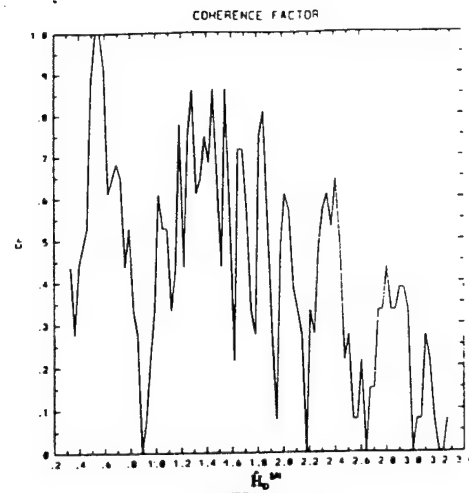


(c)

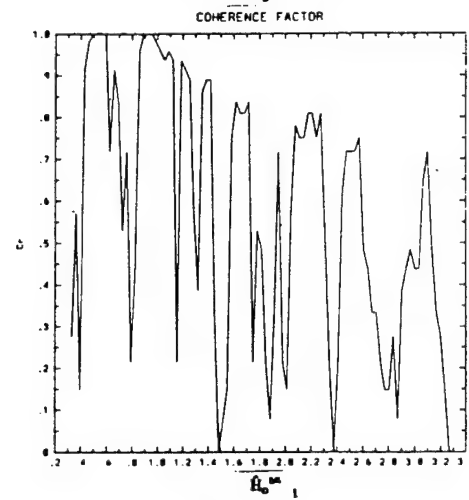


(d)

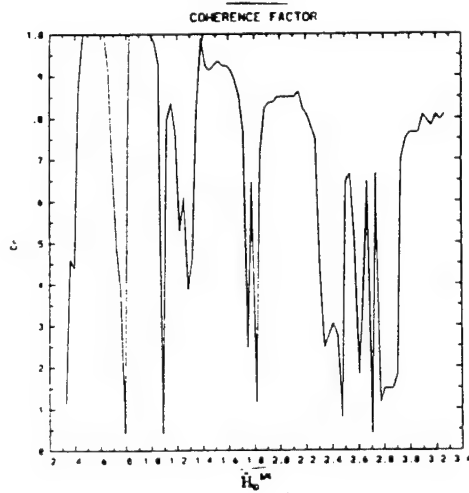
Figure (36)



$\alpha=50$  deg



$\alpha=30$  deg



$\alpha=20$  deg

Figure (37)

# Percent Forward-Scattered

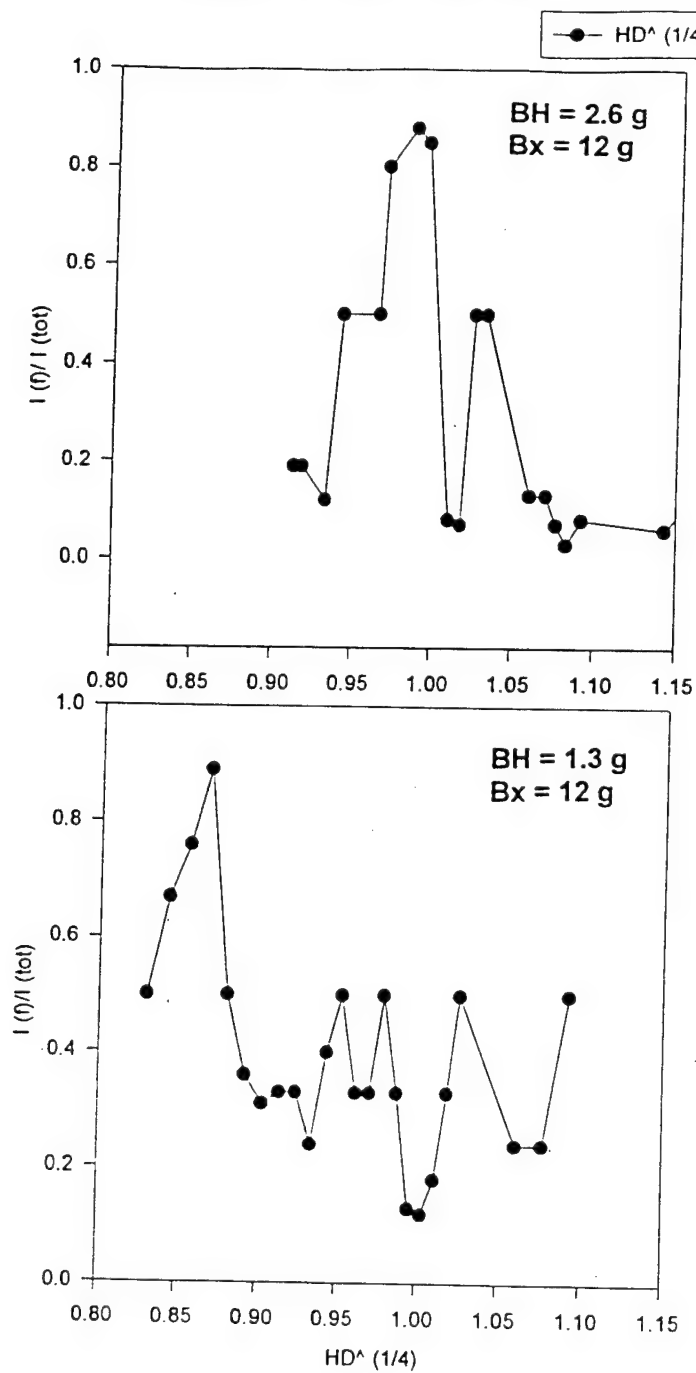


Figure (38)

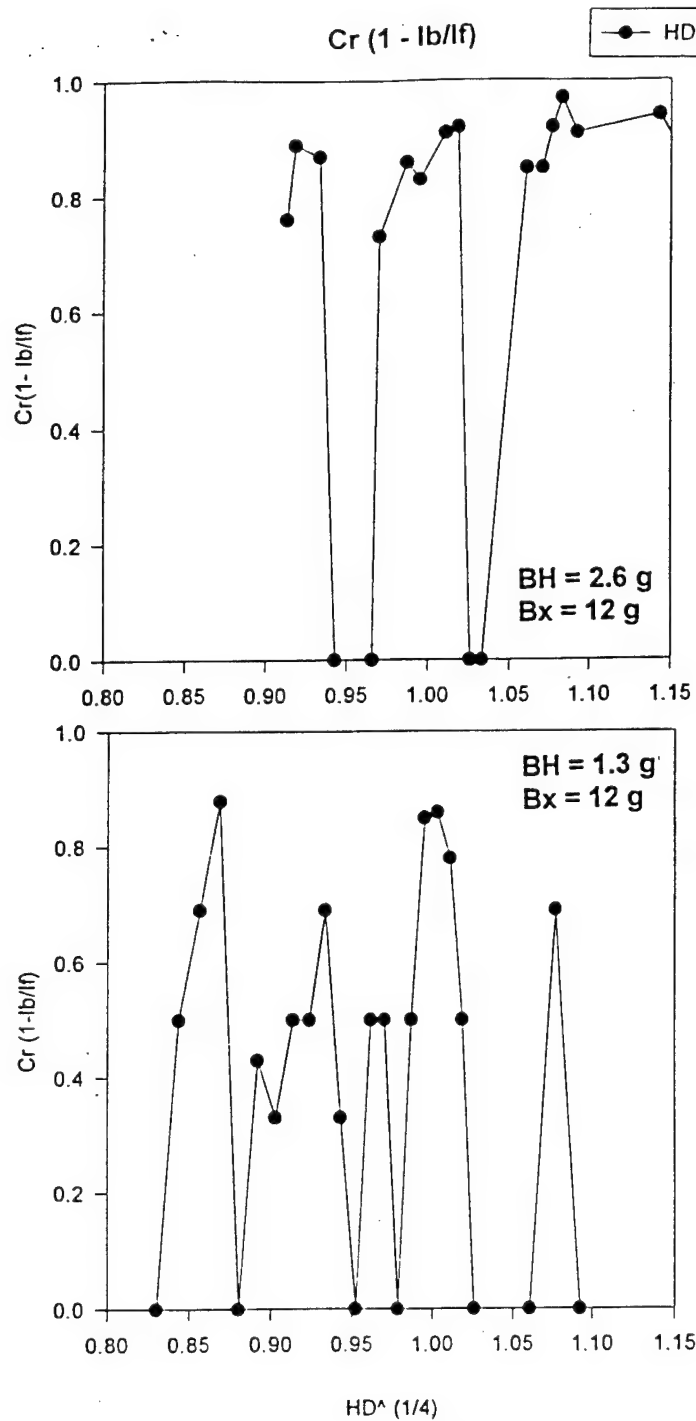


Figure (39)

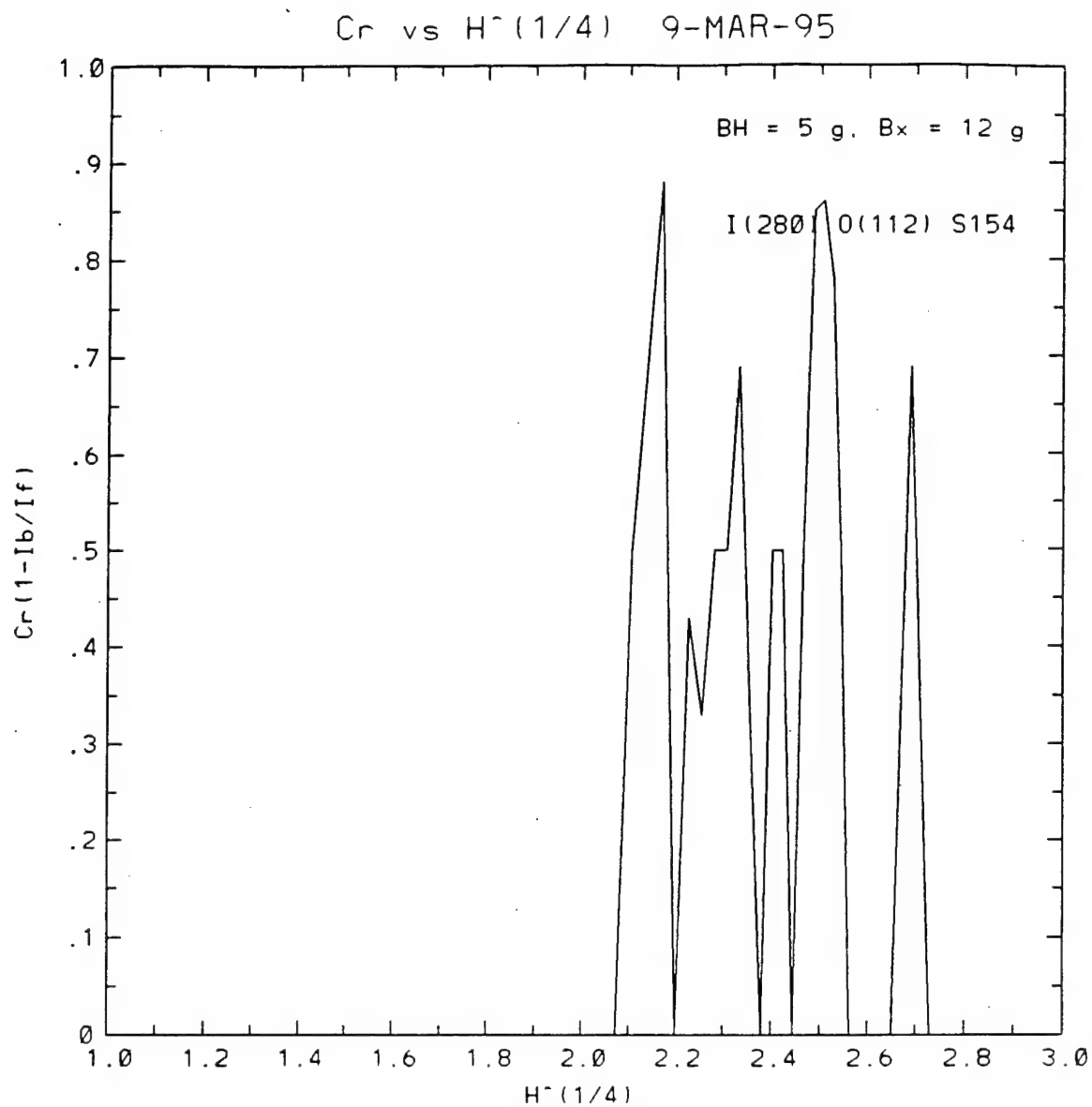


Figure (40)



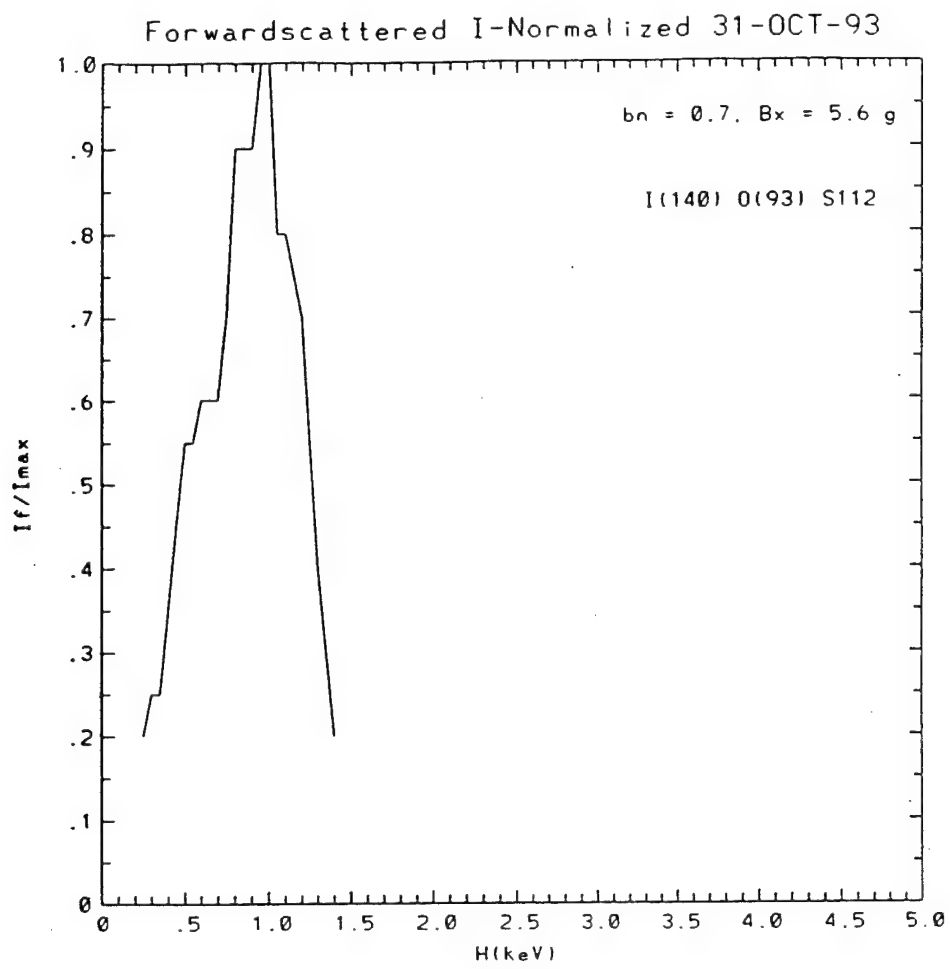


Figure (41)

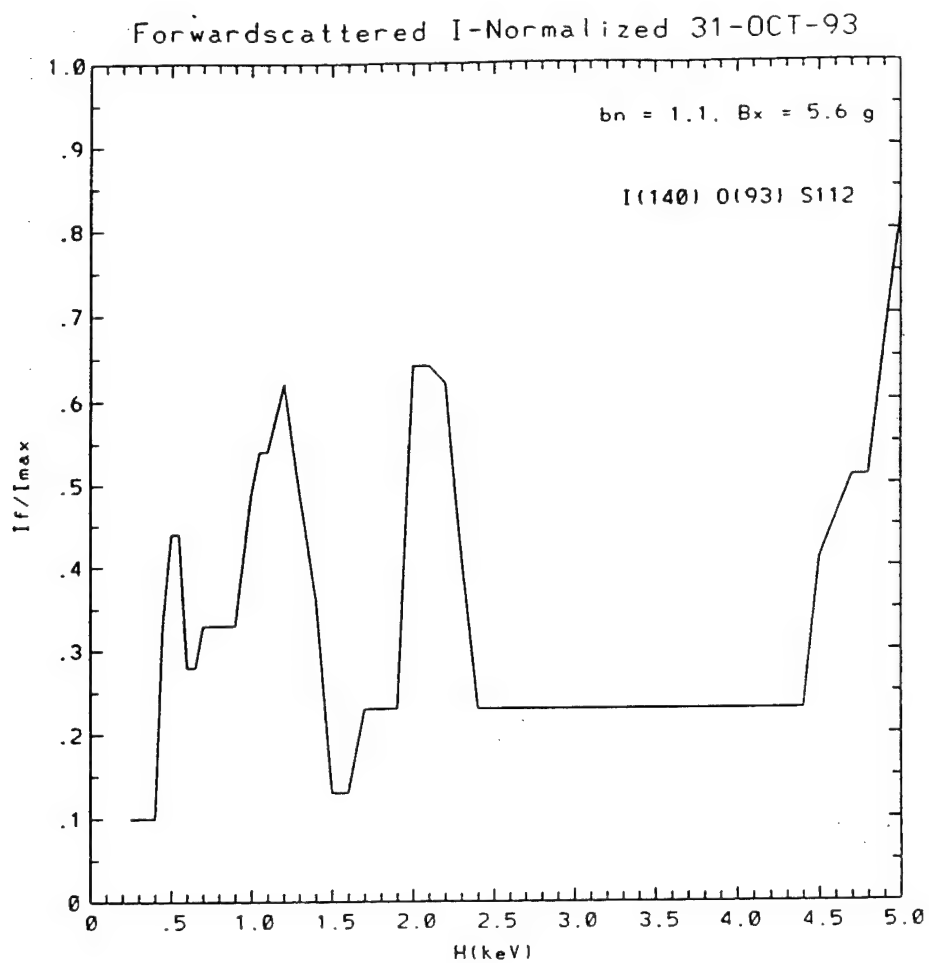


Figure (42)

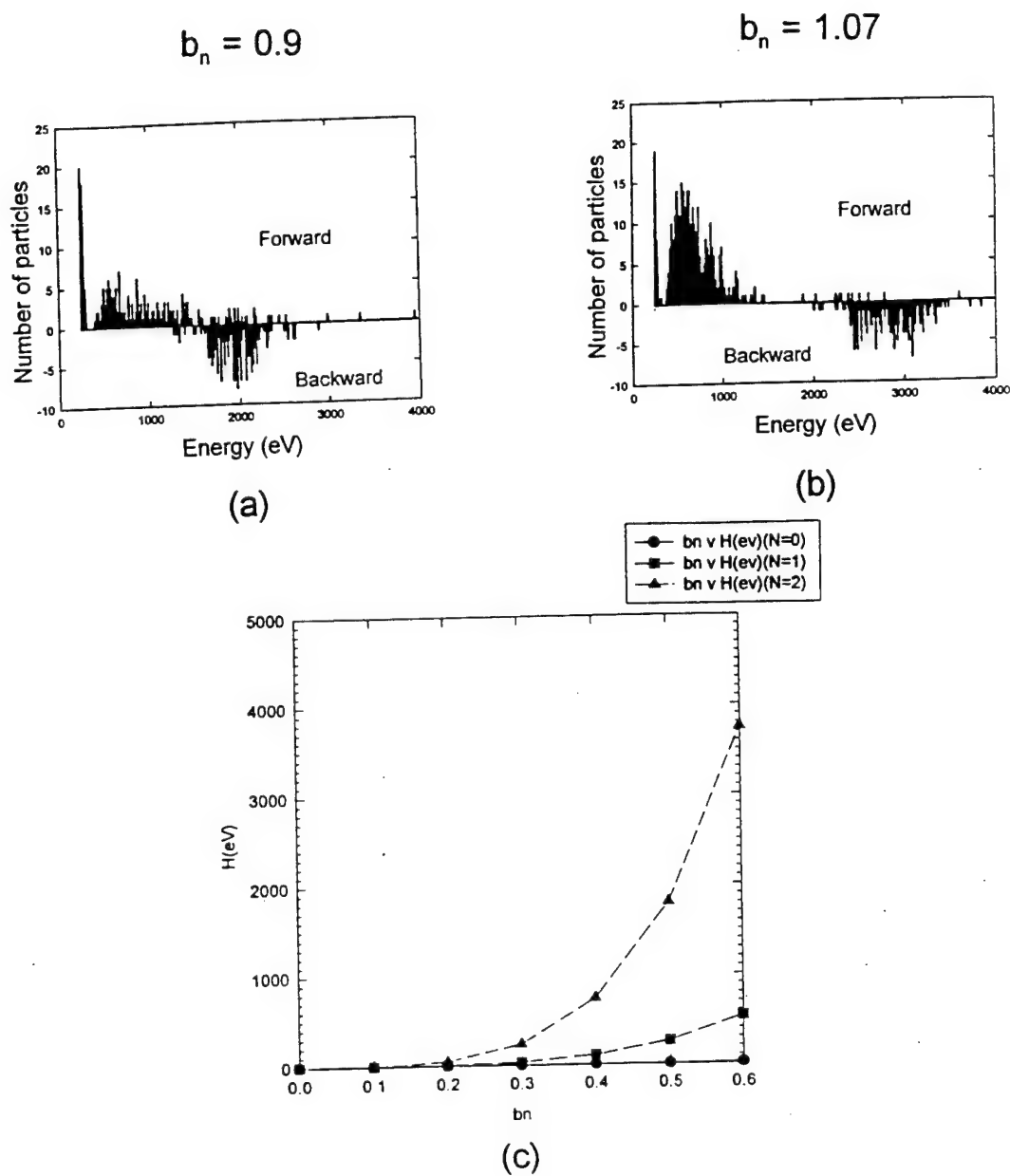
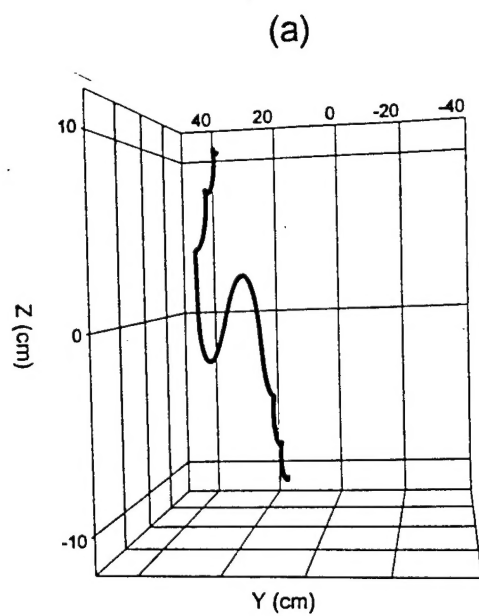
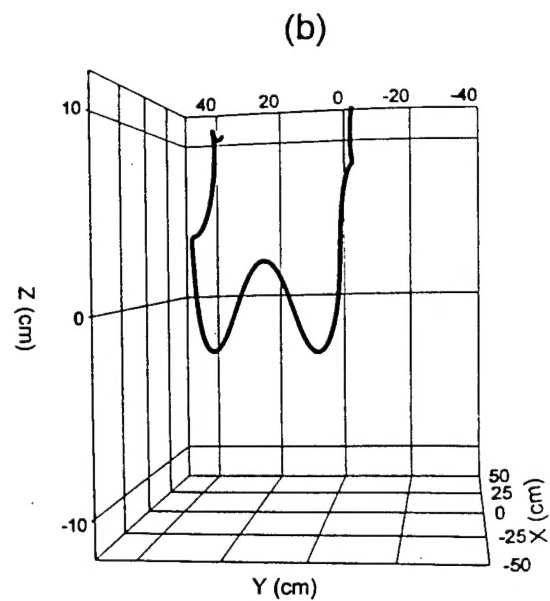


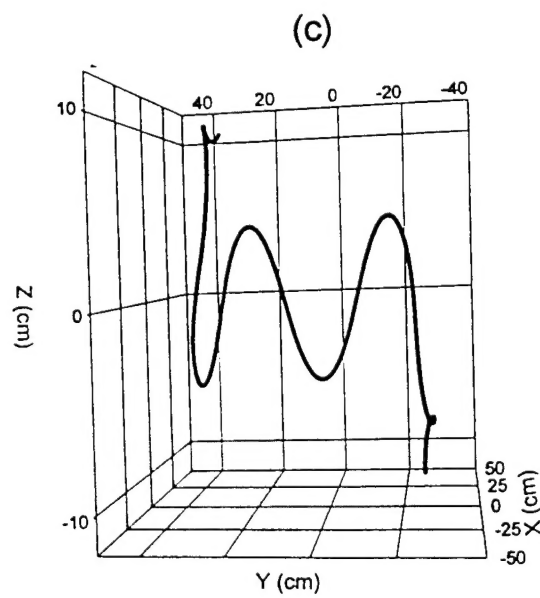
Figure (43)



$N = 2, E = 500 \text{ eV}$



$N = 3, E = 2 \text{ keV}$



$N = 4, E = 5 \text{ keV}$

$\delta = 5 \text{ cm}$

Figure (44)

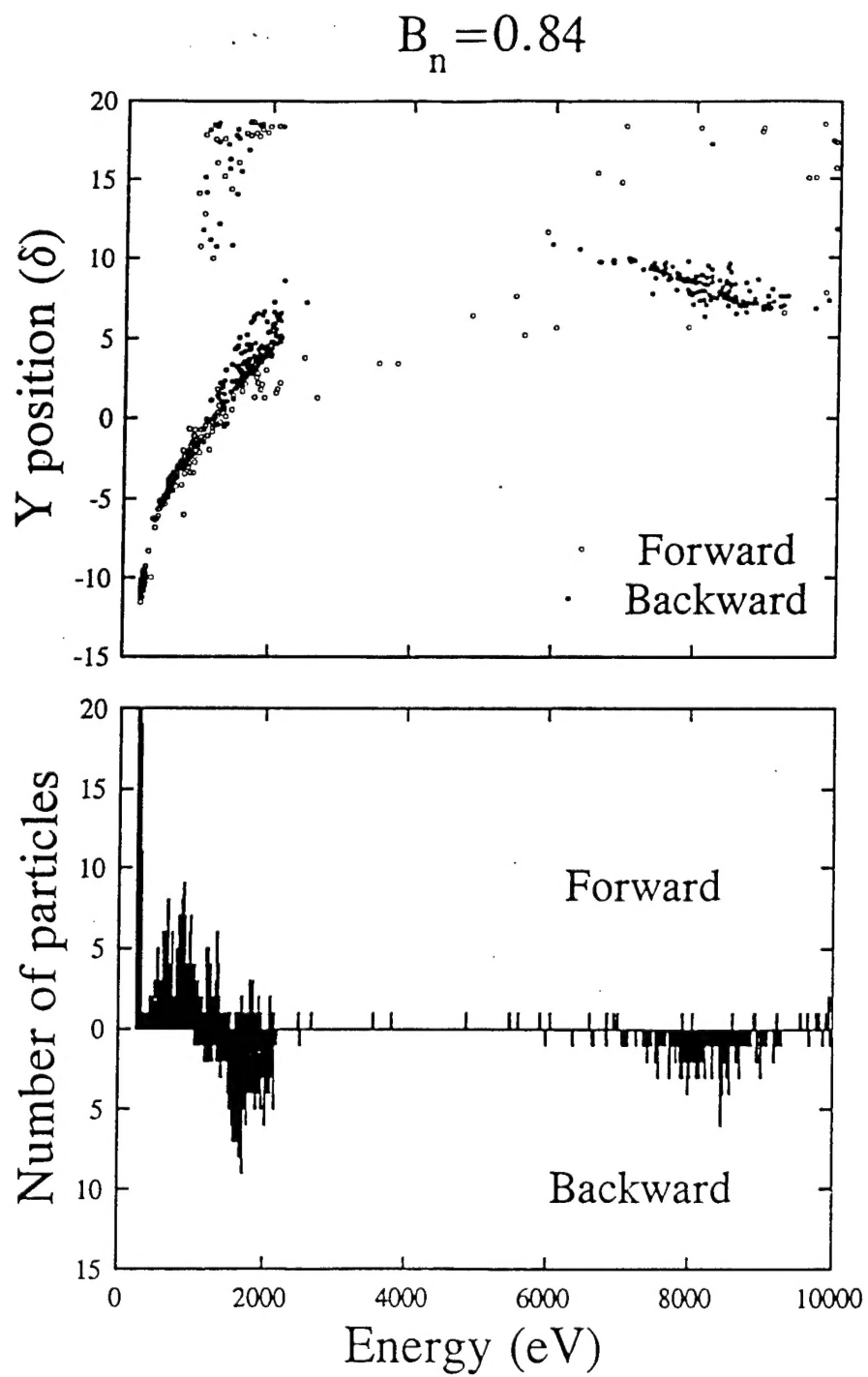


Figure (45)

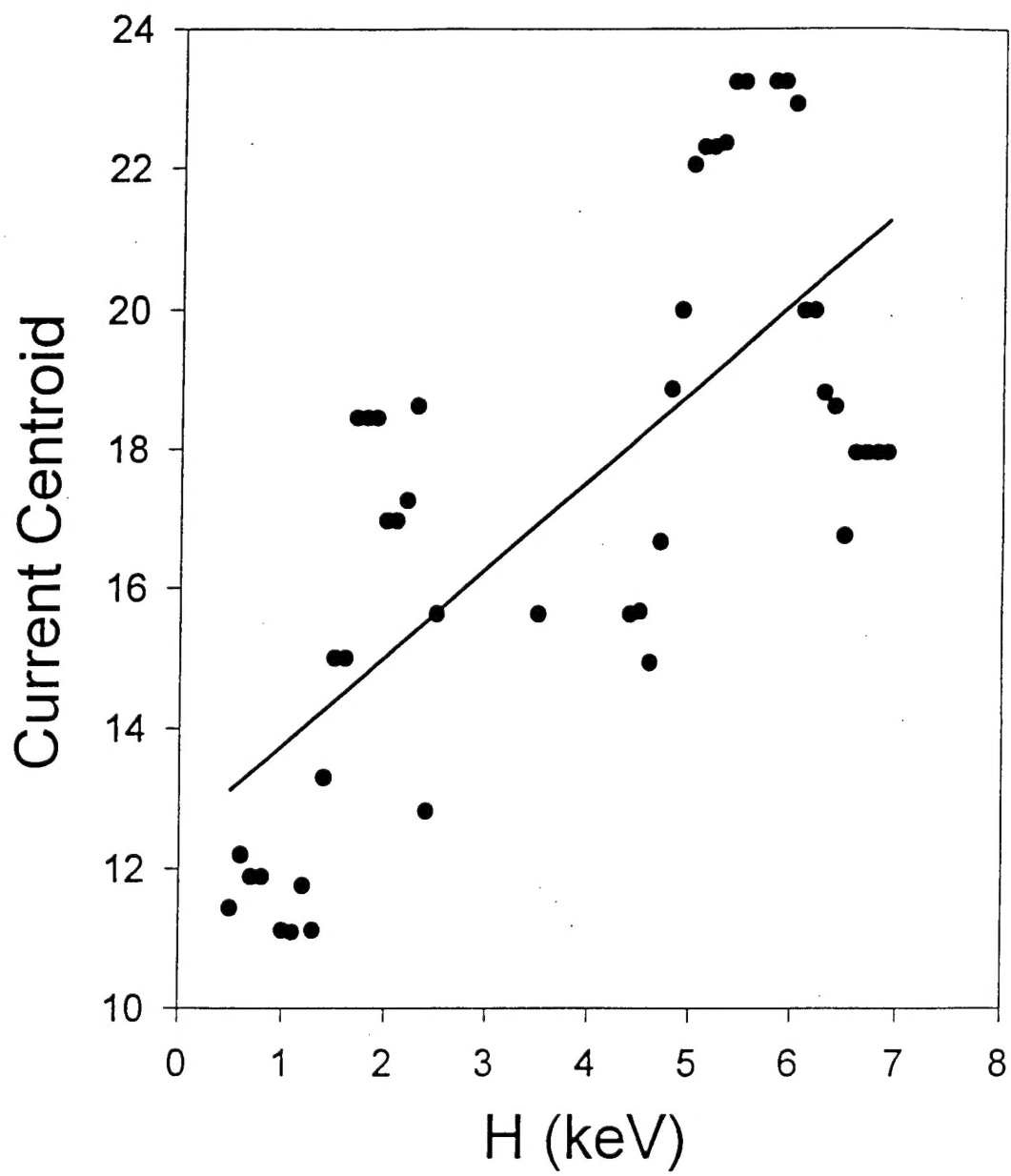


Figure (46)

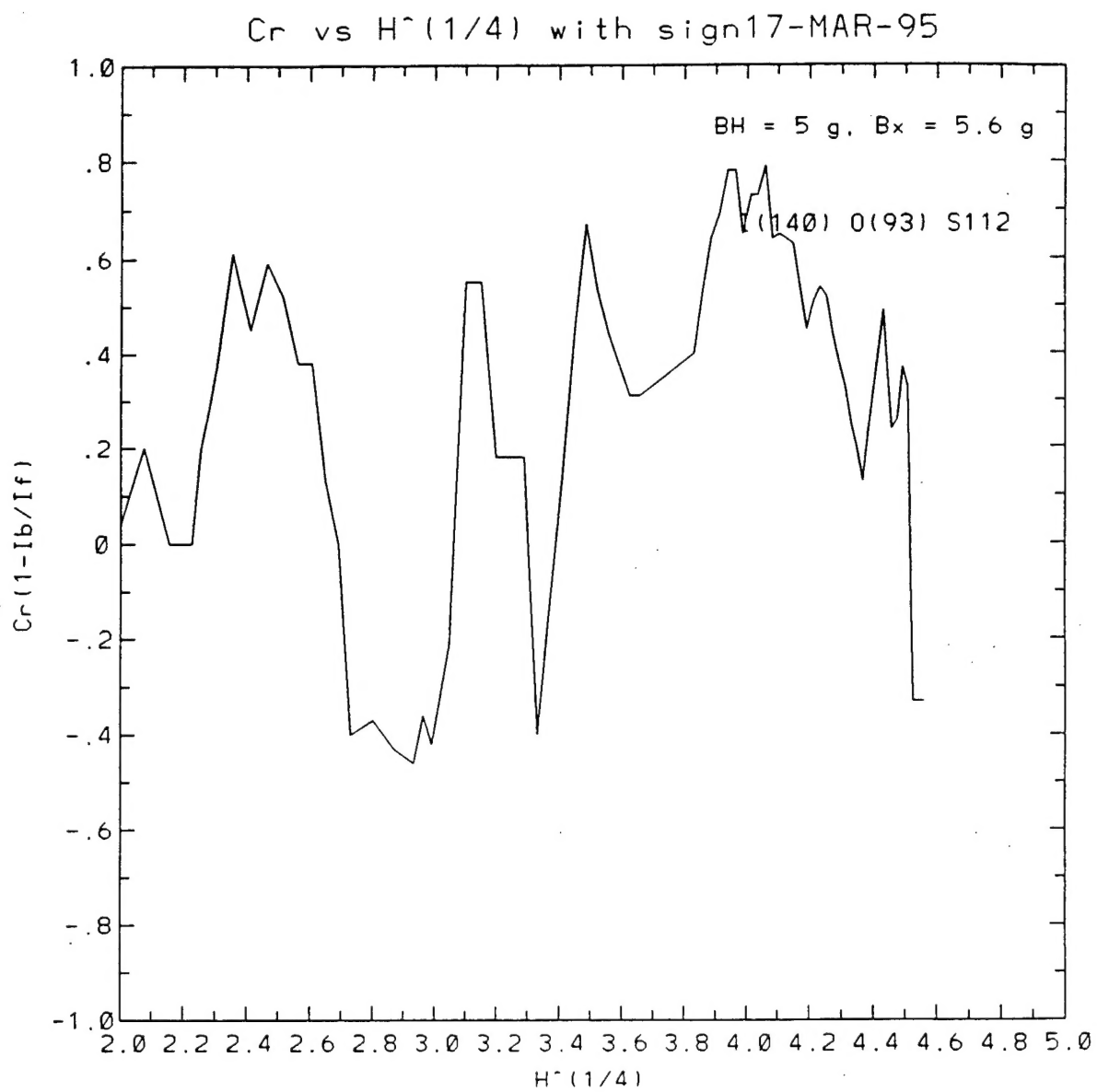


Figure (47)